



HAL
open science

Investigation of the thermal conductivity tuning of solid materials for energy-efficient systems using scanning thermal microscopy

Wenxiang Sun

► **To cite this version:**

Wenxiang Sun. Investigation of the thermal conductivity tuning of solid materials for energy-efficient systems using scanning thermal microscopy. Thermics [physics.class-ph]. INSA de Lyon, 2023. English. NNT : 2023ISAL0031 . tel-04246472

HAL Id: tel-04246472

<https://theses.hal.science/tel-04246472v1>

Submitted on 17 Oct 2023

HAL is a multi-disciplinary open access archive for the deposit and dissemination of scientific research documents, whether they are published or not. The documents may come from teaching and research institutions in France or abroad, or from public or private research centers.

L'archive ouverte pluridisciplinaire **HAL**, est destinée au dépôt et à la diffusion de documents scientifiques de niveau recherche, publiés ou non, émanant des établissements d'enseignement et de recherche français ou étrangers, des laboratoires publics ou privés.



INSA

N°d'ordre NNT : 2023ISAL0031

THESE de DOCTORAT DE L'INSA LYON, membre de l'Université de Lyon

Ecole Doctorale N° ED 162
MÉCANIQUE, ÉNERGÉTIQUE, GÉNIE CIVIL, ACOUSTIQUE

Spécialité/ discipline de doctorat :
Thermique Energétique

Soutenue publiquement le 11/05/2023, par :
Wenxiang SUN

Investigation of the thermal conductivity tuning of solid materials for energy-efficient systems using scanning thermal microscopy

Devant le jury composé de :

GRAUBY, Stéphane	Professeur des Universités/Univ. BORDEAUX	Président
GRAUBY, Stéphane	Professeur des Universités/Univ. BORDEAUX	Rapporteur
YASSAR, Abderrahim	Directeur de Recherche/École Polytechnique	Rapporteur
DELMAS, Agnès	Maître de Conférences HDR/INSA-LYON	Examinatrice
PERNOT, Gilles	Maître de Conférences/Univ. LORRAINE	Examineur
GOMÈS, Séverine	Directrice de Recherche CNRS/INSA-LYON	Directrice de thèse
HAMAOUÏ, Georges	Enseignant-Chercheur/Univ. Gustave Eiffel	Co-encadrant de thèse

Référence : TH0963_Wenxiang SUN

L'INSA Lyon a mis en place une procédure de contrôle systématique via un outil de détection de similitudes (logiciel Compilatio). Après le dépôt du manuscrit de thèse, celui-ci est analysé par l'outil. Pour tout taux de similarité supérieur à 10%, le manuscrit est vérifié par l'équipe de FEDORA. Il s'agit notamment d'exclure les auto-citations, à condition qu'elles soient correctement référencées avec citation expresse dans le manuscrit.

Par ce document, il est attesté que ce manuscrit, dans la forme communiquée par la personne doctorante à l'INSA Lyon, satisfait aux exigences de l'Établissement concernant le taux maximal de similitude admissible.



Département FEDORA – INSA Lyon - Ecoles Doctorales

SIGLE	ECOLE DOCTORALE	NOM ET COORDONNEES DU RESPONSABLE
CHIMIE	CHIMIE DE LYON https://www.edchimie-lyon.fr Sec. : Renée EL MELHEM Bât. Blaise PASCAL, 3e étage secretariat@edchimie-lyon.fr	M. Stéphane DANIELE C2P2-CPE LYON-UMR 5265 Bâtiment F308, BP 2077 43 Boulevard du 11 novembre 1918 69616 Villeurbanne directeur@edchimie-lyon.fr
E.E.A.	ÉLECTRONIQUE, ÉLECTROTECHNIQUE, AUTOMATIQUE https://edeea.universite-lyon.fr Sec. : Stéphanie CAUVIN Bâtiment Direction INSA Lyon Tél : 04.72.43.71.70 secretariat.edeea@insa-lyon.fr	M. Philippe DELACHARTRE INSA LYON Laboratoire CREATIS Bâtiment Blaise Pascal, 7 avenue Jean Capelle 69621 Villeurbanne CEDEX Tél : 04.72.43.88.63 philippe.delachartre@insa-lyon.fr
E2M2	ÉVOLUTION, ÉCOSYSTÈME, MICROBIOLOGIE, MODÉLISATION http://e2m2.universite-lyon.fr Sec. : Bénédicte LANZA Bât. Atrium, UCB Lyon 1 Tél : 04.72.44.83.62 secretariat.e2m2@univ-lyon1.fr	Mme Sandrine CHARLES Université Claude Bernard Lyon 1 UFR Biosciences Bâtiment Mendel 43, boulevard du 11 Novembre 1918 69622 Villeurbanne CEDEX sandrine.charles@univ-lyon1.fr
EDISS	INTERDISCIPLINAIRE SCIENCES-SANTÉ http://ediss.universite-lyon.fr Sec. : Bénédicte LANZA Bât. Atrium, UCB Lyon 1 Tél : 04.72.44.83.62 secretariat.ediss@univ-lyon1.fr	Mme Sylvie RICARD-BLUM Institut de Chimie et Biochimie Moléculaires et Supramoléculaires (ICBMS) - UMR 5246 CNRS - Université Lyon 1 Bâtiment Raulin - 2ème étage Nord 43 Boulevard du 11 novembre 1918 69622 Villeurbanne Cedex Tél : +33(0)4 72 44 82 32 sylvie.ricard-blum@univ-lyon1.fr
INFOMATHS	INFORMATIQUE ET MATHÉMATIQUES http://edinfomaths.universite-lyon.fr Sec. : Renée EL MELHEM Bât. Blaise PASCAL, 3e étage Tél : 04.72.43.80.46 infomaths@univ-lyon1.fr	M. Hamamache KHEDDOUCI Université Claude Bernard Lyon 1 Bât. Nautibus 43, Boulevard du 11 novembre 1918 69 622 Villeurbanne Cedex France Tél : 04.72.44.83.69 hamamache.kheddouci@univ-lyon1.fr
Matériaux	MATÉRIAUX DE LYON http://ed34.universite-lyon.fr Sec. : Yann DE ORDENANA Tél : 04.72.18.62.44 yann.de-ordenana@ec-lyon.fr	M. Stéphane BENAYOUN Ecole Centrale de Lyon Laboratoire LTDS 36 avenue Guy de Collongue 69134 Ecully CEDEX Tél : 04.72.18.64.37 stephane.benayoun@ec-lyon.fr
MEGA	MÉCANIQUE, ÉNERGÉTIQUE, GÉNIE CIVIL, ACOUSTIQUE http://edmega.universite-lyon.fr Sec. : Stéphanie CAUVIN Tél : 04.72.43.71.70 Bâtiment Direction INSA Lyon mega@insa-lyon.fr	M. Jocelyn BONJOUR INSA Lyon Laboratoire CETHIL Bâtiment Sadi-Carnot 9, rue de la Physique 69621 Villeurbanne CEDEX jocelyn.bonjour@insa-lyon.fr
ScSo	ScSo* https://edsciencessociales.universite-lyon.fr Sec. : Mélina FAVETON INSA : J.Y. TOUSSAINT Tél : 04.78.69.77.79 melina.faveton@univ-lyon2.fr	M. Bruno MILLY Université Lumière Lyon 2 86 Rue Pasteur 69365 Lyon CEDEX 07 bruno.milly@univ-lyon2.fr

*ScSo : Histoire, Géographie, Aménagement, Urbanisme, Archéologie, Science politique, Sociologie, Anthropologie

Acknowledgments

I would like to express my deepest gratitude and appreciation to all the individuals who have supported and contributed to the completion of this doctoral thesis.

First and foremost, I am immensely grateful to my supervisors, Professor Séverine GOMES and Georges HAMAOU, for their invaluable guidance, unwavering support, and exceptional mentorship throughout my research journey. Their expertise, enthusiasm, and dedication have been instrumental in shaping my research direction and enhancing the quality of this thesis. I am truly fortunate to have had the opportunity to work under their supervision.

I would also like to extend my sincere thanks to the members of my thesis committee, Professor Stéphane GRAUBY, Professor Abderrahim YASSAR, Professor Agnès DELMAS, and Professor Gilles PERNOT, for their insightful comments, valuable suggestions, and critical feedback. Their expertise and constructive criticism have greatly contributed to the improvement and refinement of this work.

I am grateful to the faculty and staff of the Institut National des Sciences Appliquées Lyon, for providing a conducive academic environment and research resources that have facilitated my studies. Their unwavering support and encouragement have been integral to my personal and professional development.

I would like to acknowledge the invaluable contributions of my colleagues and fellow researchers at laboratory CETHIL, group Micro et Nano Thermique (MINT). Their collaboration, discussions, and shared experiences have broadened my perspective and enriched my research endeavors. I am truly grateful for the stimulating intellectual environment that we have fostered together.

Furthermore, I am deeply indebted to my family for their unwavering love, encouragement, and belief in my abilities. Their constant support and understanding have been a source of strength and motivation throughout my academic pursuits.

Last but not least, I would like to express my heartfelt appreciation to all my friends who have stood by me during this challenging journey. Their encouragement, companionship, and unwavering belief in me have provided the necessary inspiration to overcome obstacles and persevere.

Although it is not possible to mention everyone individually, please know that your contribution, whether big or small, has played an integral role in the completion of this thesis. I am sincerely grateful for your support.

In conclusion, I extend my deepest gratitude to all those who have supported me in various ways, enabling the successful completion of this doctoral thesis. Your contributions have been invaluable, and I am honored to have had the privilege of working with such remarkable individuals.

Thank you.

Wenxiang SUN

Abstract

One potential solution for system thermal management is to utilize or create nanostructured or nanocomposite materials, as they can exhibit a tuned thermal conductivity. Two types of materials developed in this direction were studied in this thesis. They are amorphous chromium disilicide (CrSi_2) thin films on substrate that were modified by implantation with Ne and Al ions at room temperature and at 250°C for thermoelectric applications, and bulk polymer nanocomposites where nanofillers (expanded graphite (EG), multiwall carbon nanotubes (MWCNTs), and MXene) are used to enhance the polymer thermal conductivity for electronic applications (as an example). Scanning thermal microscopy (SThM) is used to analyze the heat conduction within both the types of material as a function of their microstructure change. Estimations of the contribution of phonons and electrons to the heat conduction in CrSi_2 in its amorphous phase and for ion-implanted amorphous CrSi_2 were obtained. These results combined with the analyses of the material microstructure show a decrease of the material thermal conductivity for all the studied CrSi_2 samples, more pronounced for ion-implantation at 250°C . Based on scientific literature this decrease is attributed to implantation induced defects clusters that are energy carrier scattering centers, phonon path disruption by atom mass contrast and nanocrystallites, created due to a radiation-enhanced phase transformation process at 250°C , with depletion zones for electrons located at their boundaries. For the case of Ne-implantations, observed Ne bubbles that are additionally induced by the ion-implantation also lead to phonon scattering. For polymer nanocomposites, thermal conductivity SThM measurements combined with the analyses of the material microstructure allow to verify that the introduction of carbonaceous fillers increases the heat conduction in materials while the filler concentration increases. A new analytical model, which allows the thermal conductivity estimation in the case of MWCNTs- multiphase PVDF based composites, is proposed and results are compared with SThM measurements. Main findings show that the β phase of PVDF, created because MWCNTs introduced in the PVDF matrix act as nucleation centers for β phase-PVDF, explains the increase of the thermal conductivity of the nanocomposite.

Keywords: thermal conduction tuning, amorphous chromium disilicide, carbon filler-based polymer nanocomposites, scanning thermal microscopy

Résumé

Une solution potentielle pour la gestion thermique de systèmes consiste à utiliser ou à créer des matériaux nanostructurés ou nanocomposites, car ils peuvent présenter une conductivité thermique ajustée. Cette thèse analyse l'ajustement de la conductivité thermique de deux types de matériaux développés dans cet objectif: des couches minces de disilicure de chrome amorphe (CrSi_2) sur substrat modifiées par implantation avec des ions de néon (Ne) et d'aluminium (Al) à température ambiante et à 250°C pour des applications thermoélectriques, et des polymères nanocomposites massifs où des nanocharges (nanotubes de carbone multiparois (NTCMPs), graphite expansé (GE) et MXene) sont utilisées pour améliorer la conductivité thermique du polymère pour des applications électroniques (par exemple). La microscopie thermique à balayage (S_{Th}M) est utilisée pour analyser la conduction thermique dans les deux types de matériaux en fonction de leur changement de microstructure, induit par l'implantation ionique dans diverses conditions pour le CrSi_2 et par l'ajout de nanocharges pour les polymères nanocomposites. Des estimations de la contribution des phonons et des électrons à la conduction thermique dans le CrSi_2 dans sa phase amorphe et pour des échantillons de CrSi_2 amorphe implantés par des ions ont été obtenues. Ces résultats, combinés à des analyses de la microstructure des matériaux, montrent une diminution de la conductivité thermique du CrSi_2 pour tous les échantillons étudiés. Cette diminution est plus prononcée pour les implantations avec des ions à 250°C . D'après la littérature scientifique, cette diminution est attribuée aux amas de défauts, induits par l'implantation, qui agissent comme des centres de diffusion des porteurs d'énergie, à la perturbation du trajet des phonons du fait d'un contraste de masse atomique entre les ions implantés et ceux du CrSi_2 et à des nanocristallites, créées grâce à un processus de transformation de phase (cristallisation de la phase amorphe du CrSi_2) à 250°C et ayant des zones de déplétion pour les électrons situés à leur frontière. Dans le cas des implantations avec des ions Ne, les bulles de gaz observées et induites par l'implantation ionique conduisent également à la diffusion des phonons. Pour les nanocomposites polymères, les mesures S_{Th}M de conductivité thermique, combinées à des analyses de la microstructure permettent de vérifier que l'introduction de charges carbonées augmente la conduction thermique dans les matériaux lorsque la concentration de charge augmente. Un nouveau modèle analytique qui permet l'estimation de la conductivité thermique des nanocomposites de PVDF multiphasiques à base NTCMPs, est proposé et les résultats sont comparés aux mesures S_{Th}M. Les principaux résultats montrent que la phase β du PVDF, créée parce que les NTCMPs sont introduits dans la matrice PVDF agissent comme des centres de nucléation pour la phase β du PVDF, expliquent l'augmentation de la conductivité thermique du nanocomposite.

Mots clés : ajustement de la conduction thermique, disilicure de chrome amorphe, polymères nanocomposites à base de charges de carbone, microscopie thermique à balayage



Table of contents

Acknowledgments.....	3
Abstract.....	5
Résumé	7
Table of contents	9
List of Figures	13
List of Tables	19
Acronyms	21
General introduction	29
Chapter I. CONTEXT AND SCIENTIFIC STATE OF ART	33
I. A. Introduction	33
I. A. 1. Global context	33
I. A. 2. Main challenge of the oriented-application materials of the thesis	36
I. A. 2. a) Materials for thermoelectricity	36
I. A. 2. b) Materials for heat dissipation	38
I. B. Thermal conduction in solid materials: fundamentals	39
I. B. 1. Thermal conduction in solids	40
I. B. 1. a) Fourier’s law and thermal conductivity.....	40
I. B. 1. b) Thermal resistance and thermal conductance	41
I. C. Heat conduction energy carriers	43
I. C. 1. Heat conduction by electrons	43
I. C. 2. Heat conduction by lattice vibrations	44
I. C. 3. Energy carriers in amorphous structure.....	46
I. D. Heat transfer through interfaces	48
I. E. Thermal conductivity tuning by modifying microstructure and geometry of solid materials	51
I. F. Techniques for investigating the thermal conductivity of solid materials....	55
I. F. 1. Thermoreflectance	55
I. F. 2. Photothermal radiometry	56
I. F. 3. 3 ω method	56
I. F. 4. Scanning thermal microscopy (SThM)	56

I. G.	Associated measurement modelling - generalities	59
I. H.	Conclusions	60
Chapter II.	MEASUREMENT SETUP AND PROCEDURE.....	63
II. A.	Scanning thermal microscope	63
II. A. 1.	Instrumentation and principle.....	63
II. A. 1. a)	Atomic Force Microscope instrument.....	63
II. A. 1. b)	Wollaston probe	64
II. A. 2.	Thermal control unit	66
II. A. 2. a)	Unbalanced Wheatstone bridge.....	67
II. A. 2. b)	Balanced Wheatstone bridge.....	68
II. B.	Temperature and electrical calibrations of the probe	69
II. B. 1.	Temperature calibration.....	70
II. B. 2.	Electrical calibration.....	72
II. B. 2. a)	Experimental part.....	72
II. B. 2. b)	Model for balanced Wheatstone bridge.....	73
II. B. 2. c)	Associated model	74
II. C.	Calibration for thermal conductivity measurement.....	76
II. C. 1.	Point thermal conductivity measurement methodology	76
II. C. 2.	Calibration curve	78
II. C. 2. a)	Case of the unbalanced Wheatstone bridge	78
II. C. 3.	Model for balanced Wheatstone bridge.....	81
II. C. 4.	Measurement protocol for imaging	83
II. D.	SThM measurement modelling – bulk and two layered samples.....	84
II. E.	Summary	85
Chapter III.	THERMAL CHARACTERIZATION OF ION IMPLANTED CrSi₂ THIN FILMS	87
III. A.	Context	87
III. B.	Sample description	89
III. B. 1.	Sample preparation	89
III. B. 2.	Microstructure of samples	91
III. B. 2. a)	As deposited (or pristine) CrSi ₂ film.....	91
III. B. 2. b)	Samples implanted at room temperature	93
III. B. 2. c)	Ne implanted CrSi ₂ at 250 °C.....	95
III. B. 3.	Thickness characterization	97
III. B. 4.	Electrical resistivity measurements	97
III. B. 5.	Roughness measurement	98
III. C.	Thermal conductivity determination	99

III. C. 1.	Effective thermal conductivity measurement	100
III. C. 2.	Contact radius determination.....	103
III. C. 3.	Thermal boundary resistance (TBR) characterization.....	105
III. C. 4.	The other input parameter in analytical model.....	106
III. D.	Results and discussion.....	108
III. E.	Conclusions and perspectives.....	113
Chapter IV. THERMAL CONDUCTIVITY ENHANCEMENT MECHANISM OF POLYMER COMPOSITES WITH CARBON-BASED FILLERS.....		115
IV. A.	Context	115
IV. B.	Sample description and characterization.....	117
IV. B. 1.	HDPE/EG Composites	117
IV. B. 1. a)	Measurement results for HDPE/EG composites.....	118
IV. B. 2.	PVDF/MWCNTs composites	122
IV. B. 2. a)	Structural characterization of PVDF matrix	125
IV. B. 2. b)	Nanostructure analysis.....	129
IV. B. 2. c)	Measurement results for PVDF/MWCNTs samples.....	131
IV. B. 2. d)	Analytical thermal modeling of the PVDF/MWCNTs nanocomposites	134
IV. B. 2. d. (i)	State-of-the art	134
IV. B. 2. d. (ii)	Proposed model and its application to sample analysis.....	138
IV. C.	Conclusions and perspectives.....	141
Chapter V. THERMAL CHARACTERIZATION OF POLYMER COMPOSITES WITH MXene-BASED FILLERS		145
V. A.	Context	145
V. B.	Sample description	146
V. C.	Thermal conductivity determination	147
V. C. 1.	Roughness measurement	147
V. C. 2.	Measurement results for PMMA samples	148
V. D.	Conclusions and perspectives.....	151
General conclusion and perspectives.....		153
References		159
Appendix 1: Theoretical calculations		187
Appendix 2. Uncertainty calculation of unbalanced TCU.....		192

Appendix 3. Previous techniques used for the sample analysis from ref [123].....	194
Appendix 4. Sensitivity of fitted k of CrSi2 layer by analytical model	195
Appendix 5. SEM image of PVDF composites.....	199
Appendix 6. FT-IR spectra of PVDF composites.....	200
Appendix 7. DSC results of PVDF composites	201
Appendix 8. Preparation procedure of PMMA composites filled with MXene and MWCNTs.....	203

List of Figures

Figure I-1. Primary energy consumption measured in terawatt-hours (TWh). From [9].....	33
Figure I-2. Qualitative representation of the thermoelectric parameters as a function of the charge carrier concentration (n) in materials. From [16].	37
Figure I-3. Schematic of thermal resistance in a solid.	42
Figure I-4. Schematic of harmonic approximation.	45
Figure I-5. Schematic of Phonon gas model.	46
Figure I-6. Density of vibration state and division of three type of energy carriers in amorphous silicon. Adapted with permission [23]. Copyright 1999, Taylor & Francis Ltd.....	48
Figure I-7. Temperature profile in function of sample depth for two layered materials [29].	49
Figure I-8. Schematic of probe-sample thermal contact (a) and equivalent thermal contact conductance G_c (b).....	59
Figure II-1. Schematic diagram of an AFM-based SThM used.....	64
Figure II-2. Optical image of Wollaston probe.	65
Figure II-3. Schematic diagram of an unbalanced Wheatstone bridge.	68
Figure II-4. Schematic diagram of a balanced Wheatstone bridge.	69
Figure II-5. Schematic of Wollaston probe components.....	70
Figure II-6. Variation of the electrical resistance as a function of temperature of a Wollaston probe, which is heated in an oven with no self-heating by Joule effect.....	72
Figure II-7. Variation of the electrical resistance ($R_{el, pt}$) as a function of power dissipated on the heating element Pt (P_p), (a): in air, (b): in vacuum; and temperature difference between ambient and heat element Pt as a function of P_p , (c): in air, (d): in vacuum.....	74
Figure II-8. Diagram of the existing heat transfers within the SThM probe while out of contact and the associated equivalent thermal conductance.....	75
Figure II-9. The protocol of measurement and associated equivalent thermal conductance while the probe is out- and in- contact with sample.....	77
Figure II-10. Thermal conductance G_s in function of thermal conductivity k_{ref} . Fitting parameters are: $A = 8.38 \cdot 10^{-6}$, $B = 2.08$, $C = 1.07 \cdot 10^{-5}$. The red fill area indicates the	

uncertainty of reference curve.....	81
Figure II-11. Calibration curve obtained experimentally from the measurement of reference samples [83]: PMMA ($k_{PMMA} = 0.187 \text{ W.m} - 1.\text{K} - 1$), POM-C ($k_{POM} - C = 0.329 \text{ W.m} - 1.\text{K} - 1$), Glass ($k_{Glass} = 1.11 \text{ W.m} - 1.\text{K} - 1$) and SiO ₂ ($k_{SiO2} = 1.28 \text{ W.m} - 1.\text{K} - 1$). The equation in red is the expression of the fitting curve of the measurements.....	83
Figure II-12. Contact spot of radius a , on an infinite half-plane with surface coating of thickness t	85
Figure III-1. Schematic of studied CrSi ₂ samples.....	90
Figure III-2. (a) Cross-Section-TEM micrograph showing the as-deposited CrSi ₂ thin film, where the S vector points to the surface of the film. The Si substrate and the SiO ₂ layer are also indicated in the image. (b) SAED pattern of the as-deposited CrSi ₂ sample shown in (a).	93
Figure III-3. Cross-section TEM micrograph for the CrSi ₂ sample implanted at room temperature with (a) Ne and (b) Al. EDX spectrum appears superimposed with SRIM ion concentration-depth-profile simulation for (c) Ne and (d) Al implantation.	94
Figure III-4. (a) Cross-section TEM micrographs of the CrSi ₂ sample implanted with Ne at 250 °C; (b) same sample at a higher magnification and (c) Ne EDX profile as a function of distance in the film.	95
Figure III-5. (a) SAED pattern superimposed with the theoretical planes of crystalline CrSi ₂ . (b) Dark Field contrast micrograph from the same area shown in Fig. 3(a) of the CrSi ₂ sample implanted with Ne at 250 °C.	96
Figure III-6. Electrical resistivity ρ measurements as a function of the temperature of as deposited and implanted CrSi ₂ samples. The lines serve as a guide for the eyes. Measurements error bars are within the symbol size.	98
Figure III-7. Measured thermal conductance G_s in function of thermal conductivity k . The embedded image is an enlarged display of CrSi ₂ samples results. Reference curve fitting parameters are: $A = 8.38 \cdot 10^{-6}$, $B = 2.08$, $C = 1.07 \cdot 10^{-5}$. The red fill area indicates the uncertainty of reference curve.....	101
Figure III-8. Effective thermal conductivity of CrSi ₂ samples. Diamond shapes represent data	

for each repetition of measurement. Error bar is the standard deviation (SD) of all repetition of each sample. The solid curves represent the distribution of the experimental set of data. 102

Figure III-9. (a) Thermal radius as a function of the sample step effective thermal conductivity k_{eff} for the Wollaston probe. [74]..... 103

Figure III-10. Fitted k of $CrSi_2$ layer by analytical model in function of input contact radius a 105

Figure III-11. Fitted k of $CrSi_2$ layer by analytical model in function of input TBR. 106

Figure III-12. Fitted k of $CrSi_2$ layer by analytical model in function of input thickness.. 107

Figure III-13. Fitted k of $CrSi_2$ layer by analytical model in function of input k_{Si} 108

Figure III-14. Thermal conductivity of as deposited and implanted $CrSi_2$ film calculated from model..... 109

Figure IV-1. Structure of HDPE from [170]. 117

Figure IV-2. Optical image of HDPE-EG composite..... 118

Figure IV-3. SThM images for HDPE composite containing 2 % (a, b) and 10 % (c, d) weight fractions of EG. Topography (a, c) and thermal) signal (b, d). 118

Figure IV-4. Effective thermal conductivity of HDPE/EG composite with 10 wt.% filler charge measured at different locations on the sample that are precised in **Figure IV. 3** (c). The root mean square was considered as the uncertainty and used to estimate the error bar. 120

Figure IV-5. Topography image (a) and thermal image (b) of 10 % weight fraction of EG-HDPE sample. (c) and (d): associated histograms giving the distribution of the height and thermal signal values respectively..... 121

Figure IV-6. Molecular formula of PVDF..... 123

Figure IV-7. Different crystalline phase molecular structures of PVDF [179]. 124

Figure IV-8. DSC results of PVDF composites, line 2 (black), 4 (red) and 6 (blue) indicate the first heating process, cooling process and the second heating process, respectively. 127

Figure IV-9. ωc and $\beta\%$ of samples calculated from line 2 in **Figure IV. 8** as a function of MWCNTs weight fraction. Solid lines are not fitting curves but guide for eyes to compare the tendency of data. 129

Figure IV-10. TEM images of PVDF matrix. 130

Figure IV-11. TEM images of PVDF/8 wt.% MWCNTs sample.....	131
Figure IV-12. Topography and thermal images for the PVDF composite containing 4 wt.% MWCNTs.	132
Figure IV-13. k_{eff} , $\beta r\%$ and $\beta\%$ of PVDF/MWCNTs composite versus weight fraction % of MWCNTs). Solid lines are not fitting curves but guide for eyes to compare the tendency of data.	133
Figure IV-14. Schematic of series model and parallel model.	135
Figure IV-15. Schematic of PVDF composite filled with MWCNTs	139
Figure IV-16. Experimental thermal conductivity, model fitting results and predicted results for fully crystallization of PVDF/MWCNTs composite versus weight fraction % of MWCNTs). Solid lines are not fitting curves but guides for eyes to compare the tendency of data.	140
Figure IV-17. Model fitting results for four arbitrarily selected values of k_{MWCNTs} . Solid lines are not fitting curves but guides for eyes to compare the tendency of data.....	141
Figure V-1. Molecular formula of PMMA.	146
Figure V-2. Calibration curve obtained experimentally from the measurement of reference samples [83]: PMMA ($k_{PMMA} = 0.187 \text{ W. m}^{-1} \text{ K}^{-1}$), POM-C ($k_{POM-C} = 0.329 \text{ W. m}^{-1} \text{ K}^{-1}$), Glass ($k_{Glass} = 1.11 \text{ W. m}^{-1} \text{ K}^{-1}$) and SiO ₂ ($k_{SiO2} = 1.28 \text{ W. m}^{-1} \text{ K}^{-1}$). The equation in red is the expression of the fitting curve of the measurements.	149
Figure V-3. Effective thermal conductivity of PMMA composites deduced by calibration curve.	150
Figure V-4. Schematic of contact condition of a Wollaston probe with a sample without (left) or with (right) significant topography.	151
Figure A1. 1. Contact spot of radius a , on an infinite half-plane with surface coating of thickness t	187
Figure A4. 1. Fitted k of CrSi ₂ layer by analytical model in function of input contact radius	

<i>a</i>	195
Figure A4. 2. Fitted k of CrSi ₂ layer by analytical model in function of input TBR.	196
Figure A4. 3. Fitted k of CrSi ₂ layer by analytical model in function of input thickness...	197
Figure A4. 4. Fitted k of CrSi ₂ layer by analytical model in function of input kSi	198
Figure A5. 1. SEM picture of (a), (b) PVDF matrix; (c), (d) PVDF/1.25 wt.% MWCNTs composite and (e), (f) PVDF/3.0 wt.% MWCNTs composite.....	199
Figure A6. 1. IR image of PVDF matrix and composites with MWCNTs fillers.	200



List of Tables

Table I-1. Characteristics of Wollaston probe, Kelvin nanotechnology probe and doped silicon probe [70].	57
Table II-1. Main characteristics of the Wollaston probe.	65
Table II-2. Thermal conductivity and roughness RMS of reference samples.	79
Table III-1. Ion implantation parameters	90
Table III-2. Thickness of CrSi ₂ film.	97
Table III-3. Roughness of samples where <i>std</i> is the standard deviation.	99
Table III-4. Input parameters in the analytical model	104
Table III-5. Phononic and electronic contribution to the thermal conductivity at room temperature	110
Table IV-1. Relative β phase percentage ($\beta r\%$) in PVDF nanocomposites containing different concentration of MWCNTs.	124
Table IV-2. The experimental and theoretical enthalpy of samples obtained from DSC and corresponding crystallinity and β phase percentage in total composite component of PVDF composites	128
Table IV-3. Summary of some analytical and empirical models from literature.	136
Table V-1. Roughness of PMMA composite samples	147
Table V-2. Topography of PMMA composite samples obtained by Wollaston probe.	148



Acronyms

Abbreviation	Denotation
AC	Alternating current
AFM	Atomic force microscopy
AMM	Acoustic Mismatch Model
CrSi ₂	Chromium disilicide
DC	Direct current
DMM	Diffuse Mismatch Models
DSC	Differential scanning calorimetry
EDX	Energy dispersive X-ray spectroscopy
EG	Expanded graphite
FDTR	Frequency domain thermoreflectance
FIB	Focused ion beam
FTIR	Fourier Transform infra-red spectrometry
GNP	Graphene nanoplatelet
HDPE	High-density polyethylene matrix
HF	Hydrogen fluoride
IR	Infrared
KNT	Kelvin nanotechnology probe
MD	Molecular dynamics
MFP	Mean free path

MWCNTs	Multiwall carbon nanotubes
PGEC	Phononic glass/electronic crystal
PGM	Phonon gas model
PMMA	Poly (methyl methacrylate) matrices
POM-C	Acetal copolymer
PTR	Photothermal radiometry
PVDF	Polyvinylidene difluoride
RMS	Root mean square
RT	Room temperature
rGO	Reduced graphene oxide
SAED	Selected Area Electron Diffraction
SEM	Scanning electron microscope
SRIM	Stopping and Range of Ions in Matter
STD	Standard deviation
STEM	Scanning transmission electron microscopy
SThM	Scanning thermal microscopy
TEM	Transmission electron microscopy
TBR	Thermal boundary resistance/ Kapitza resistance
TCR	Temperature coefficient of electrical resistance
TCU	Thermal control unit
TDTR	Time domain thermoreflectance
TPV	Thermophotovoltaic

XRD X-ray diffraction

ZT Figure of merit

2D Two dimensional



Nomenclature

Symbol	Meaning	Unit
A	Cross-sectional area,	$[m^2]$
a	Thermal contact radius,	$[m]$
C_v	Volumetric heat capacity,	$[J \cdot m^{-3} \cdot K^{-1}]$
D	Thermal diffusivity,	$[m^2 \cdot s^{-1}]$
e	Elementary charge,	$[C]$
f	Frequency,	$[Hz]$
G	Thermal conductance,	$[W \cdot K^{-1}]$
G_c	Contact thermal conductance,	$[W \cdot K^{-1}]$
G_{ic}	Thermal conductance of probe in contact with sample,	$[W \cdot K^{-1}]$
G_{oc}	Thermal conductance of probe out of contact with sample,	$[W \cdot K^{-1}]$
G_s	Global thermal conductance,	$[W \cdot K^{-1}]$
G_{ss}	Thermal conductance of sample system,	$[W \cdot K^{-1}]$
G_{wire}	Thermal conductance to Wollaston wire,	$[W \cdot K^{-1}]$
G_{env}	Out of contact thermal conductance to environment,	$[W \cdot K^{-1}]$
G'_{env}	In contact thermal conductance to environment,	$[W \cdot K^{-1}]$
I	Electrical current,	$[A]$
I_p	Electrical current on probe,	$[A]$
k	Thermal conductivity,	$[W \cdot m^{-1} \cdot K^{-1}]$
k_A	Thermal conductivity of amorphous PVDF,	$[W \cdot m^{-1} \cdot K^{-1}]$
$k_{x,y,z}$	Thermal conductivity in x,y,z direction,	$[W \cdot m^{-1} \cdot K^{-1}]$
k_B	Boltzmann Constant,	$[m^2 \cdot kg \cdot s^{-2} \cdot K^{-1}]$
k_c	Effective thermal conductivity of composite,	$[W \cdot m^{-1} \cdot K^{-1}]$
k_{eff}	Effective thermal conductivity,	$[W \cdot m^{-1} \cdot K^{-1}]$
k_e	Electronic contribution of thermal conductivity,	$[W \cdot m^{-1} \cdot K^{-1}]$
k_f	Thermal conductivity of filler,	$[W \cdot m^{-1} \cdot K^{-1}]$
k_L	Lattice thermal conductivity,	$[W \cdot m^{-1} \cdot K^{-1}]$

k_m	Thermal conductivity of matrix,	$[\text{W}\cdot\text{m}^{-1}\cdot\text{K}^{-1}]$
k_{ph}	Phononic thermal conductivity,	$[\text{W}\cdot\text{m}^{-1}\cdot\text{K}^{-1}]$
k_{sample}	Thermal conductivity of studied samples,	$[\text{W}\cdot\text{m}^{-1}\cdot\text{K}^{-1}]$
k_1	Thermal conductivity of first layer,	$[\text{W}\cdot\text{m}^{-1}\cdot\text{K}^{-1}]$
k_{sub}	Thermal conductivity of substrate,	$[\text{W}\cdot\text{m}^{-1}\cdot\text{K}^{-1}]$
k_{MWCNTs}	Thermal conductivity of MWCNTs,	$[\text{W}\cdot\text{m}^{-1}\cdot\text{K}^{-1}]$
k_α	Thermal conductivity of α phase PVDF,	$[\text{W}\cdot\text{m}^{-1}\cdot\text{K}^{-1}]$
k_β	Thermal conductivity of β phase PVDF,	$[\text{W}\cdot\text{m}^{-1}\cdot\text{K}^{-1}]$
L	Lorenz number,	$[\text{W}\cdot\Omega\cdot\text{K}^{-2}]$
l	Mean free path,	[m]
l_e	Electron mean free path,	[m]
l_L	Phonon mean free path,	[m]
n	Concentration of charge carriers,	$[\text{cm}^{-3}]$
P_p	Electrical power dissipated on heat element,	[W]
q	Rate of heat transfer,	[W]
$q_{x,y,z}$	Rate of heat transfer in positive x,y,z direction,	[W]
q_L	Wavevector of lattice vibration,	$[\text{m}^{-1}]$
R	Thermal resistance,	$[\text{K}\cdot\text{W}^{-1}]$
R_{th}	Thermal boundary resistance (TBR) / Kapitza resistance,	$[\text{m}^2\cdot\text{K}\cdot\text{W}^{-1}]$
$R_{th,i}$	Interface thermal resistance,	$[\text{m}^2\cdot\text{K}\cdot\text{W}^{-1}]$
$R_{th,s}$	Sample thermal resistance,	$[\text{m}^2\cdot\text{K}\cdot\text{W}^{-1}]$
$R_{el,p}$	Probe electrical resistance,	$[\Omega]$
$R_{el,Pt}$	Pt Heat element electrical resistance,	$[\Omega]$
R_v	Variable electrical resistance,	$[\Omega]$
R_0	Probe electrical resistance at 0°C ,	$[\Omega]$
R_{Ag0}	Wollaston wire electrical resistance at 0°C ,	$[\Omega]$
R_{Pt0}	Pt Heat element electrical resistance at 0°C ,	$[\Omega]$
R_{Pt30}	Pt Heat element electrical resistance at 30°C ,	$[\Omega]$
Rq	Root mean square roughness,	[nm]

S	Seebeck coefficient,	$[\text{V}\cdot\text{K}^{-1}]$
Sq	Extension to a plane of root mean square roughness,	$[\text{nm}]$
std_{Sq}	Standard deviation of Sq ,	$[\text{nm}]$
T_0	Reference temperature,	$[\text{K}]$
T	Generic temperature,	$[\text{K}]$
T_{Pt}	Mean temperature of the Pt element,	$[\text{K}]$
t	Film thickness,	$[\text{m}]$
t_{eff}	Effective thickness,	$[\text{m}]$
t_{eq-TBR}	Equivalent thickness of TBR,	$[\text{m}]$
V	Electrical voltage,	$[\text{V}]$
v_g	Phonon group velocity,	$[\text{m}\cdot\text{s}^{-1}]$
x,y,z	Dimensional Cartesian coordinate system,	$[\text{m}]$
ZT	Figure of merit,	
α	Temperature coefficient of electrical resistance,	$[\text{K}^{-1}]$
α_0	Temperature coefficient of electrical resistance at 0°C ,	$[\text{K}^{-1}]$
α_{p0}	Temperature coefficient of probe at 0°C ,	$[\text{K}^{-1}]$
α_{Pt0}	Temperature coefficient of Pt Heat element at 0°C ,	$[\text{K}^{-1}]$
α_{Ag0}	Temperature coefficient of Wollaston wire at 0°C ,	$[\text{K}^{-1}]$
$\beta\%$	Mass percentage of β phase,	
$\beta_r\%$	Relative β phase mass percentage,	
λ_L	Wavelength of lattice vibration,	$[\text{m}]$
ρ	Electrical resistivity,	$[\Omega\cdot\text{m}]$
σ	Electrical conductivity,	$[\text{S}\cdot\text{m}^{-1}]$
θ_D	Debye temperature	$[\text{K}]$
μ	Thermal diffusion length,	$[\text{m}]$
χ	Mass fraction,	
χ_α	Mass fraction of α phase PVDF,	
χ_β	Mass fraction of β phase PVDF,	

χ_A	Mass fraction of amorphous PVDF,	
χ_{MWCNTs}	Mass fraction of MWCNTs,	
Φ	Volume fraction of fillers,	
Φ'	Volume fraction of MWCNTs normalized by β phase PVDF,	
ω_α	Volume fraction of α phase PVDF normalized by PVDF matrix,	
ω_c	Crystallinity,	
ω_L	Angular frequency of lattice vibration,	$[\text{rad}\cdot\text{s}^{-1}]$
ΔH_m	Melting enthalpy,	$[\text{J}\cdot\text{g}^{-1}]$
ΔH_m^c	Reference melting enthalpy for fully crystalline PVDF,	$[\text{J}\cdot\text{g}^{-1}]$

General introduction

Thermal management is the process of controlling the temperature of a system or device to ensure it operates within safe temperature limits. This is important for several reasons like the device longevity, performance, safety, energy efficiency, and environmental impact. Thermal management plays a key role in improving the energy efficiency and sustainability of systems in numerous application domains including energy, transportation, building, and electronics. In order to better implement it in these practical applications, one of the first steps is the improvement of the physical phenomena efficiency used to confer to materials that constitute systems the most suitable properties for a given application.

In engineering, the efficiency factor, so-called figure of merit, is a quantity used to characterize the performance of a system or a material. This thesis analyses two approaches dedicated to the tuning of the thermal conductivity and the improvement of the figure of merit of two types of solid materials with potential physical properties either for thermoelectric applications or for heat dissipation within systems. For the case of a thermoelectric material, the figure of merit is defined by its ZT , which is all the higher as the thermal conductivity of the material is low. On the contrary, for a heat dissipation material, which is required to transfer and to dissipate heat away from components to prevent device overheating and damage, the thermal conductivity is desired to be high.

The development of new materials with controlled thermal conductivity, which surpasses that of the currently used materials is needed in order to influence the performances and reliability of the aforementioned applications. One potential solution is to utilize or create nanostructured or nanocomposite materials, as they can exhibit a tuned thermal conductivity. These advanced human-made materials are perceived as one of the most promising materials of the current generation. They require thermal engineering optimization and design laws. This also requires setting up dual approaches based on multiscale models for the prediction of material properties associated with specifically dimensioned experimental characterization techniques and methodologies.

This thesis was funded by the China Scholarship Council and took place at the laboratory Centre of Energy and Thermal Sciences of Lyon (CETHIL) of Lyon University in collaboration with the Electronic, Communication, Systems and Microsystems laboratory (ESYCOM) of Gustave Eiffel University, in France. Collaborations with the Physics Institute of the Federal University of Rio Grande do Sul (UFRGS) (Brazil), the Polymer Institute of the Slovak Republic (Slovakia), and Dokuz Eylul University (Turkey), who provide the thesis samples were also established.

This thesis aims to address the particular problematic of the thermal conductivity tuning of new materials. Two types of specific materials are focused on:

- 1- amorphous chromium disilicide (CrSi_2) modified by ion implantation that have promising properties for thermoelectric applications,
- 2- polymer nanocomposites where nanofillers (multiwall carbon nanotubes (MWCNTs), expanded graphite (EG), $\text{Ti}_3\text{C}_2\text{T}_x$ Mxene) are used to enhance the polymer thermal conductivity for many industrial applications.

Scanning thermal microscopy (SThM), which is a key characterization tool for the local thermal analysis of materials, has been developed at CETHIL for a long time. The technique was used in the thesis and analytical models accounting for the microstructure and geometry of samples were used and/or developed for identifying the sample thermal conductivity as well as interpreting the obtained results.

This manuscript reports the works and main results of my thesis and is split in five chapters:

Chapter I first briefly discusses the context of the thesis. It then reminds the basic knowledge of heat conduction in solids (dielectric materials, metals, and semiconductors, crystalline and amorphous) with a focus on the ways to tune the thermal conduction of thermoelectric solid materials and nanocomposite polymers. The chapter then addresses the principle of some thermal characterization methods nowadays available, including a focus on the SThM technique, used for the estimation of the thermal conductivity of materials; before

ending with the main scientific problematics of the thesis.

Chapter II presents in detail the experimental SThM setups and the methodology used for the determination of the thermal conductance of samples. Samples that were studied in the thesis are thin films of amorphous CrSi_2 deposited on a substrate and bulk nanocomposite polymers. The models that correspond with these geometries of samples and that were developed and/or used to estimate the material thermal conductivity from SThM measurements are given.

Chapter III gives a brief state of the art on the physical properties, the applications, and the potential of CrSi_2 as thermoelectric material. It then reports on the study of the effect of different ion species and implantation conditions on the heat transport within amorphous CrSi_2 thin films on substrate. The description of the amorphous CrSi_2 samples studied and the results of their microstructural and electrical characterization provided by the Physics Institute of Porto Alegre are given and discussed. This is followed by the results of the complementary analyses I have done for making it possible the sample study using SThM. Results of SThM measurements are then exposed and suggestions given for their interpretation.

Chapter IV continues with the investigation of the thermal conductivity enhancement mechanism of polymer composites modified with carbon-based fillers. Studied samples consist of high-density polyethylene (HDPE) matrix filled with 50 μm expanded graphite (EG) particles and polyvinylidene difluoride (PVDF) matrix containing multiwall carbon nanotubes (MWCNTs). Samples that were provided by the SlovakPolymer Institute are described, the results of their microstructural characterization given and the results of SThM measurements as a function of the filler concentration reported. For interpreting the thermal conductivity variation obtained for MWCNTs – PVDF composites, a new analytical model was developed in the thesis to assist in understanding the effect of the carbon-based nanofillers in the PVDF matrix on the nanocomposite thermal conductivity. This model is described in detail.

Chapters V gives the first results we got concerning the study of the thermal conductivity variation of Polymethylmethacrylate (PMMA) composites as a function of

Mxene/MWCNTs fraction.

The manuscript ends with a **General conclusions** that summarises the main findings of my works and gives the **Perspectives** of my works.

Chapter I. CONTEXT AND SCIENTIFIC STATE OF ART

I. A. Introduction

I. A. 1. Global context

Global climate change is becoming increasingly evident and irreversible due to historic and current human activities [1]. Climate change has impacted many aspects of the natural and human environment including rising temperatures, rising sea levels, agricultural problems [2]–[5] and acute human health complications [6]–[8]. One of the most important causes of climate change is the persistent reliance on fossil fuels throughout time, which emits high level of greenhouses gases as seen in **Figure I-1**. It can be observed that fossil fuels, mainly consisting of coal, oil, and gas, remain the primary source of energy for human society. As of 2021, their proportion in energy consumption exceeds 80%. However, due to the escalating increase in energy consumption, an energy crisis is going to become another challenge that human society must face.

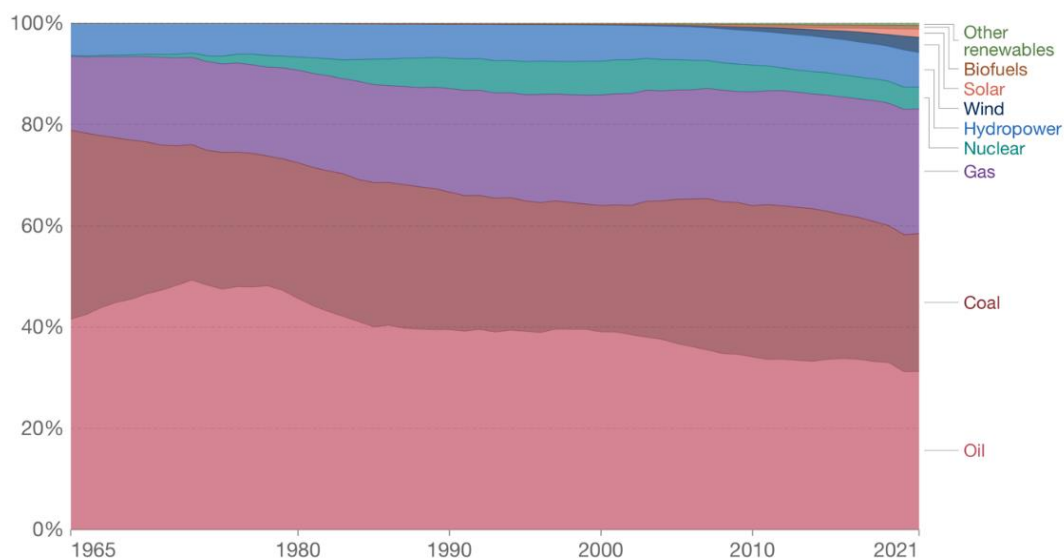


Figure I-1. Primary energy consumption measured in terawatt-hours (TWh). From [9]

Recent studies [1] prove that approximately all of the world's energy consumption involves the production or manipulation of heat over a wide temperature range. As a result, thermal energy and heat management are a central point in our energy production/consumption. At this crucial juncture in human societal development, the implementation of new energy solutions is hence desperately needed.

For the sake of reducing the energy losses and recycling energy, thermal management of devices has received widespread attention and unprecedented development in this era because heat is one of the most ubiquitous forms of energy. Technically, thermal management primarily encompasses three areas of content: i) energy generation and dissipation, ii) energy conversion, and iii) energy storage.

Energy generation includes both the more efficient extraction of energy from fossil or renewable resources and the minimization of unnecessary heat by product generated in the same process. Heat dissipation materials can be required in industry to transfer and to dissipate heat away from equipment and machinery to prevent overheating and damage. They are commonly used in electronics, automobiles, and industrial machinery to ensure proper functioning and prolong the lifespan of the equipment. Additionally, these materials can be used to dissipate heat generated by power generators, engines, and other equipment to protect personnel and the surrounding environment from excessive heat exposure. Thus, a higher thermal conductivity is desired for heat dissipation materials.

Nevertheless, thermal energy can also be effectively converted into other forms of energy such as electricity. It can be done by photovoltaic or thermoelectric conversions, for examples. Photovoltaic cells are made of semiconductor materials like silicon (Si) and are used to capture the energy from sunlight and convert it into electricity. Thermoelectricity, on the other hand, requires maintaining a temperature difference between the two faces of a solid component, a so-called thermoelectric material. This is known as the Seebeck effect. A thermoelectric generator uses this effect to convert heat into electricity, or vice versa. These generators can be used to convert waste heat into usable electricity. Another promising

alternative is thermophotovoltaic conversion (TPV) [10]–[14], which converts the radiative heat flux from a hot body, which can be removed from a recuperator, via a photovoltaic cell that operates in the infrared spectral range. Multiple sources of heat (vehicle engines, factories, etc.) could be put to use.

Consequently, as the world continues to increase its reliance on renewable energy sources, it becomes increasingly important to find efficient and cost-effective ways to store excess energy for later use.

Heat management endeavors intend to control and reduce heat losses in new components and materials where the downsizing of devices towards micro- and nanoscales and the increase of power requirements for electric devices and infrastructures (e.g., data centers and smaller scale digital infrastructures, computers, smartphones and portable devices, electric engines, 5G, etc.) lead to extremely high heat dissipation levels. Many physical phenomena can be used for heat management like the principles of thermoelectricity and TPV, which are very convenient ways to recycle the misused thermal energies [15]. The figure of merit of these phenomena varies with the materials used because it depends on their thermal and electrical properties. Therefore, effective thermal management requires the development of new materials with controlled properties that will influence the performances and reliability of systems.

As mentioned in the general introduction, one potential solution to optimize the efficiency of thermal management systems is to utilize or create nanostructured or nanocomposite materials, as they can exhibit tuned physical properties. They can exhibit unique chemical and physical (mechanical, electrical, thermal...) properties that differ from those of bulk materials. Due to the nanometric length scale of involved structures and multiple interfaces within materials, these properties include high surface area-to-volume ratios, enhanced reactivity, and unique optical, electrical, and magnetic characteristics, etc. These distinctive properties make these materials useful in a wide range of applications, from medicine to electronics including thermal management of systems [16]. They are perceived as one of the most promising materials of the current generation. Their integration in a system for a given

application is however a complex task as their optimization must answer to specifications that consider the multiscale and multiphysical behavior of the global system. This concerns both applications dealt with in this thesis, i.e., **thermoelectric transport** and **heat dissipation in systems**. While being aware of this, the thesis mainly concerns the thermal conductivity tuning of nanostructured and nanocomposite materials for each of these two applications.

I. A. 2. Main challenge of the oriented-application materials of the thesis

I. A. 2. a) Materials for thermoelectricity

For thermoelectric materials, the efficiency is given by ZT (unitless merit factor), which is defined as [16]:

$$ZT = T S^2 \sigma / k \quad (\text{I-1})$$

where T denotes the absolute temperature (K), S^1 denotes the Seebeck coefficient representing the thermoelectric power (V/K), σ the electrical conductivity (S/m) and k the thermal conductivity of the material (W/ (m.K)).

Achieving a high thermoelectric efficiency requires a high ZT value, which further requires a high-power factor ($S^2\sigma$) and a low k of materials. This is because an ideal thermoelectric material behaves like a "phononic glass/electronic crystal" (PGEC) material, with superior electrical properties similar to a crystalline material and poor thermal properties similar to an amorphous or glass-like material. However, S , σ and k are highly related to the concentration of charge carriers (n) (**Figure I-2**), resulting their interaction and conflict with each other, hence makes it challenging to achieve a high ZT . Up to now, the two strategies to develop highly efficient thermoelectric materials are the research for new materials with an inherent high ZT and the optimization of thermoelectric characteristics. The greatest choices

¹ Seebeck coefficient S is an intrinsic property of a material and corresponds to a measurement of the voltage generated in response to a temperature difference of 1 K.

for such situation are semiconductor materials since metals have a too low S while insulators are poor in terms of σ (**Figure I-2**).

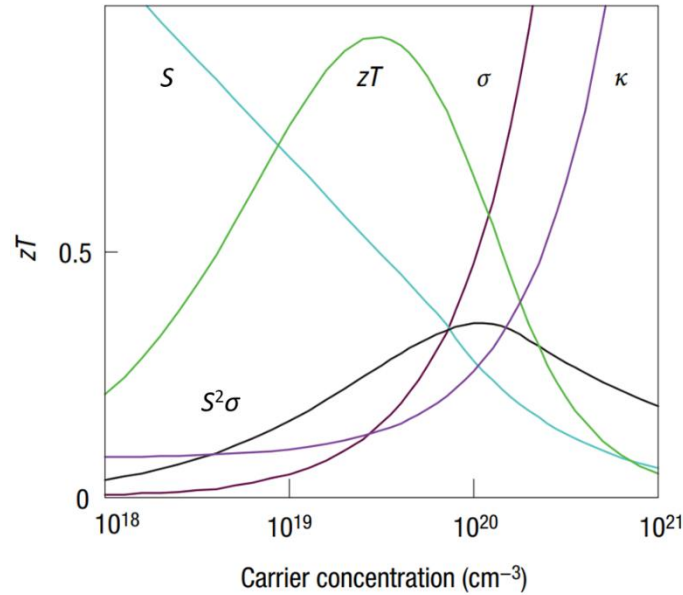


Figure I-2. Qualitative representation of the thermoelectric parameters as a function of the charge carrier concentration (n) in materials. From [16].

The component of the thermal conductivity k corresponding to heat conduction by electrons in a material is directly proportional to its electrical conductivity as stated by the Wiedemann–Franz law (see section **I. C. 1 Heat conduction by electrons**). Current strategies are focused on minimizing the thermal conductivity of materials without affecting electrical transport in order to maximize ZT . To achieve this goal, different methods are employed to reduce only the heat conduction caused by the lattice vibrations (phonons) of the material. These methods are given in the section **I. E Thermal conductivity tuning by modifying microstructure and geometry of solid materials**.

Among thermoelectric materials, those that are made amorphous naturally give rise to extensive phonon scattering, which is still a challenge for crystalline thermoelectrics. A bright future is expected for these materials, but we will see later that modelling of transport properties is challenging enough without breaking the long-range order so that design of amorphous thermoelectrics is at its infancy. A part of this thesis (**Chapter III**) is dedicated to the

experimental analysis of the heat transfer in such a thermoelectric material: the amorphous chromium disilicide (CrSi_2). It is studied in its pristine form but also after implantation with ions at different temperatures in order to verify if such material treatment can reduce the material thermal conductivity and improve the ZT .

I. A. 2. b) Materials for heat dissipation

In the case of applications requiring heat dissipation, it is desired to increase the thermal conductivity of materials. Such materials comprise metals, metallic alloys and polymer-based materials.

Polymer-based materials have particularly gained significant attention in recent years due to their low cost, excellent process ability, lightweight, and excellent flexibility. They are widely used in various industrial fields such as the electrical industry, fuel cells, packaging industry, and architectural engineering. With the rapid development of the microelectronic device industry, the demand for improved heat dissipation components has also risen. However, due to energy carrier scattering, most polymers have low thermal conductivity, typically in the range of 0.1 to 0.5 W/(m.K) [17]. As a result, enhancing the thermal conductivity of polymer-based systems has become a highly area of interest. Among the strategies developed in this direction, adding some micro and nanoscale thermal conductive fillers into polymer matrix is a popular method for enhancing its thermal conductivity but it is clear that heat conduction in such polymer nanocomposites is not well understood. To go further the thesis has also addressed the heat conductivity of different polymer composites including different volume fractions of nanofillers (multiwall carbon nanotubes (MWCNTs), expanded graphite (EG), $\text{Ti}_3\text{C}_2\text{T}_x$ Mxene). The goal was not here to enhance the thermal conductivity of the studied polymers but rather to better understand the mechanisms of this enhancement.

The physics of the heat conduction depends on the material considered. The next part of the manuscript reminds and gives the fundamentals of the thermal conduction in solid materials that are used later to analyze heat transfer in the materials studied in the thesis.

I. B. Thermal conduction in solid materials: fundamentals

Heat can be transferred via three distinct manners known as the thermal conduction, thermal convection, and thermal radiation [18]. Heat can transfer through any of those manners depending on the state and type of matter.

Thermal conduction is the transfer of heat energy through matter by the collisions of particles and heat carriers without matter displacement. It is a physical process that occurs in solids, liquids, and gases. In solids, the thermal transport is achieved through conduction, which is the vibration of both the lattice and the electrons (principle explained in detail in the next section). Simply put, in solids, heat is transported via material lattice vibrations that can be described as particles, known as phonons, where the transport theory can be described by the phonon gas model (PGM) [19]–[21]. The excessive presence of electrons inside metals, makes the electron-conduction the dominating heat channel [22].

Thermal convection takes place on the interface between a solid and a fluid flowing over it, which have different temperatures. The convection is caused by the fluid motion relative to the solid surface.

Thermal radiation represents the emission of energy in the form of electromagnetic waves due to the thermal motion of charged particles (for example electrons) in matter, i.e., at any temperature different than 0 K. It is emitted in all directions from the surface of an object and is the result of its temperature. Specifically, in vacuum, heat can only transfer between two bodies through thermal radiation manner.

Each of these heat transfer mechanisms is described by a specific law: Fourier's law for conduction, Newton's law for convection and Stefan-Boltzmann's law for radiation. As the thesis only studies the thermal conduction in solid materials, we will only detail this heat transfer mechanism in the following.

I. B. 1. Thermal conduction in solids

I. B. 1. a) *Fourier's law and thermal conductivity*

Fourier's law of heat conduction states that the rate of heat flow through a material is proportional to the negative gradient in the temperature and the thermal conductivity of the material. Mathematically, it can be expressed as:

$$q_x = -k_x A \frac{\partial T}{\partial x} \quad (\text{I-2})$$

where q_x (W) is the rate of heat transfer in positive x direction, k_x (W/mK) is the thermal conductivity in x direction, A (m²) is the cross-sectional area, and $\frac{\partial T}{\partial x}$ (K/m) is the temperature gradient in positive x direction. Similarly, the same form of the equation can be written in y and z directions for the case of a right-angle coordinate system:

$$q_y = -k_y A \frac{\partial T}{\partial y} \quad (\text{I-3})$$

$$q_z = -k_z A \frac{\partial T}{\partial z} \quad (\text{I-4})$$

For a three-dimensional system, the rate of heat transfer q (W) is the sum of the heat flux vectors transferred along x , y and z directions. In the case of material with isotropic thermal conductivity, which means $k_x = k_y = k_z$, q can be expressed as:

$$q = -kA\nabla T \quad (\text{I-5})$$

where k is the isotropic effective thermal conductivity of material, A is the cross-sectional area, and ∇T is the temperature gradient vector.

It is worth to mention that Fourier's law is just valid for a diffusion process. Whereas, when the studied system is out of the local thermodynamic equilibrium, the Fourier's regime will not be sufficient to explain the heat transport, and new laws should be used instead like

non-Fourier solutions or Boltzmann transport theory.

Concretely, the thermal conductivity k is an intrinsic property of a material that determines how easily heat is transferred through this material. It can be affected by effects of reduced size (defects, isotopes, impurities, nanopores, interfaces, nanostructures, etc...) within a solid.

In the case of composite materials an effective thermal conductivity (k_{eff}), which is an overall thermal conductivity including the contribution from all components to heat transport, can be used. k_{eff} can be determined experimentally and from Eq. I-5 or be predicted using a global model that describes the heat dissipation within the sample while taking into account its geometry, internal interfaces....

Heat transfer in some systems can also be described using a network of thermal resistances (thermal resistance of the material components and of the interfaces).

I. B. 1. b) Thermal resistance and thermal conductance

In analogy to the electrical conduction, heat flux can be approximated as a current in a circuit. While heat flows through an object, the instinct parameter of the object to resist this heat flux is called thermal resistance R (K/W). The presence of thermal resistance causes a temperature gradient in the path of the heat flow. For a given two points as shown in **Figure I-3**, the relationship between heat flux q , the temperature different of these two points $\Delta T = T_1 - T_2$, and the thermal resistance can be written by analogy with Ohm's law:

$$q = \frac{\Delta T}{R} \quad (\text{I-6})$$

By combining Fourier's Law for heat conduction, R could be written in the following form:

$$R = \frac{\Delta x}{kA} \quad (\text{I-7})$$

where Δx (m) represents the thickness measured on a path parallel to the heat flow, k (W/(m.K)) is assumed a constant parameter throughout the material, A (m²) is the cross-sectional area (**Figure I-3**). Additionally, the reciprocal of R is defined as the thermal conductance G (W/K), which is positively correlated with thermal conductivity:

$$G = \frac{kA}{\Delta x} \quad (\text{I-8})$$

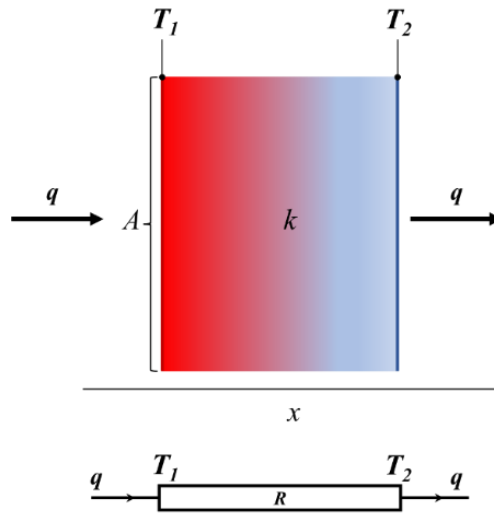


Figure I-3. Schematic of thermal resistance in a solid.

The characterization of heat conduction within nanostructured thin films of amorphous material on substrate and bulk nanocomposite materials has been made in this thesis at the steady state. Consequently, the heat conduction in the studied samples has been considered purely in the diffusive regime (samples' descriptions are detailed in each following chapter), Fourier's law has been applied and the effective thermal conductivity of the studied materials identified and used as an important parameter to evaluate the heat transfer performance. Understanding heat conduction in materials and through interfaces needs to consider the physics of the involved heat carriers.

I. C. Heat conduction energy carriers

As mentioned in the previous section, heat conduction in solids is governed by the propagation and collisions of many types of energy carriers. For a given material, the energy carriers involved in heat transfer depend on the chemical composition and structure (crystalline or amorphous) of the material.

Case of crystalline materials: Generally, the heat energy carrier concept in solid mainly accounts for the vibration of lattice (phonons) and electrons. Often, a single type of heat energy carrier may dominate the heat transfer. For example, the heat channel inside metals and heavily doped semiconductors is governed by electron-conduction while phonon-conduction dominates in dielectric and many light-to-moderately doped crystalline semiconductors. In some other cases, multiple types of heat energy carriers contribute collectively to the thermal conduction such as in thermoelectric materials where both lattice vibrations and electrons contribute to heat transport.

Case of disordered materials: Especially, some sophisticated heat energy carriers [23] have been proposed to illustrate the heat conduction in structurally disordered materials, i.e., amorphous materials. Heat transfer involves the propagation and collisions of propagons, the diffusion and collisions of diffusons and the vibration of locons.

In this thesis, amorphous semiconductor-like materials and polymer composites will be studied. Thus, the involved heat energy carriers in such materials will be featured in the following part.

I. C. 1. Heat conduction by electrons

Free electrons play a crucial role in the thermal conductivity of metals, semimetals and heavily doped semiconductors (also called degenerated semiconductors). For high quality metals around or above room temperature, electron MFP is dominated by the electron-phonon interaction and the scattering of electrons by impurities and defects [24]. A noteworthy feature

about electrons is that electron is capable to act as energy carrier for both heat and electrical charge. For a free electron gas with a parabolic dispersion near the Fermi energy (such as most metals and degenerate semiconductors) with only elastic scattering [25], the relationship between the electrical conductivity σ (S/m) (inverse of the electrical resistivity ρ ($\Omega\cdot\text{m}$)) and the electronic contribution of thermal conductivity k_e follows the Wiedemann-Franz law [16]:

$$k_e = LT\sigma \quad (\text{I-9})$$

where T is temperature, L is known as Lorenz number. At 300K, L is equal to:

$$L = \frac{\pi^2}{3} \left(\frac{k_B}{e} \right)^2 = 2.45 \times 10^{-8} \text{ (W}\Omega/\text{K}^2) \quad (\text{I-10})$$

where $k_B = 1.38 \times 10^{-23}$ ($\text{m}^2\text{kg}/\text{s}^2\text{K}$) is Boltzmann's constant and $e = 1.60 \times 10^{-19}$ (C) is the elementary charge.

The elastic scattering assumption is reasonable for scattering of electrons by impurities and point defects at all temperatures as well as for scattering of electrons by phonons at temperatures near and above Debye temperature² (θ_D), due to the energy exchanged with a phonon is sufficiently small compared to $k_B T$ [25]. With Eq. I-9 and for a given material, k_e can be estimated from the measurement of σ .

I. C. 2. Heat conduction by lattice vibrations

Lattice vibration is the dominant heat energy carrier in dielectric solids, including light-to-moderately doped semiconductors and insulators [25]. For crystalline solids, the atoms in the lattice are tied together through chemical bonds. Each atom vibrates around its own equilibrium location and affects neighboring atoms. With the harmonic approximation as shown in **Figure I-4**, interatomic interactions can be viewed as a mass-spring system. Thus, a single

² The Debye temperature θ_D is the temperature of a crystal's highest normal mode of vibration, and it correlates the elastic properties with the thermodynamic properties such as phonons, thermal expansion, thermal conductivity, specific heat, and lattice enthalpy.

atom's vibration can create lattice waves throughout the entire system.

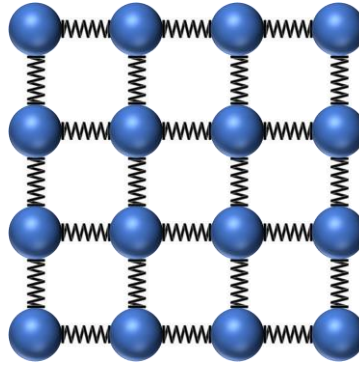


Figure I-4. Schematic of harmonic approximation.

Quantized lattice vibrations are defined as heat energy carriers called phonons, which can be modeled as particles that have each their own angular frequency (ω_L), wavevector (q_L) (direction is same as the direction of wave, size is equal to $2\pi/\lambda_L$ where λ_L is the wavelength) and moves at a specific velocity [26]. In reality, phonons are not independent as described in harmonic approximation, which leads to phonon-phonon interaction.

Phonon gas model [27] describes the transport of phonon as shown in **Figure I-5**, where each particle represents a wave packet constituted of phonons with different frequencies. Likewise, to gas molecules, phonons carry heat energy and travel inside the material. In reality, phonons are not independent as described in harmonic approximation, which leads to phonon-phonon interaction.

An important parameter to characterize the motion of heat energy carriers is their mean free path (MFP) l : l_e and l_L and l_e for electrons and phonons, respectively. In the description of energy carriers as particles, this mean free path is the average distance traveled by the particle between collisions. In the case of phonons, their scattering with defects, imperfections, material boundaries, and the Umklapp scattering [28] between phonons determines l_L and leads to a thermal resistance to heat conduction.

According to the kinetic theory of gases, the lattice thermal conductivity (k_L) of a crystalline solid can be represented mathematically as:

$$k_L = \frac{1}{3} C_V v_g l_L \quad (\text{I-11})$$

where C_V is the volumetric heat capacity ($\text{J}/(\text{m}^3\text{K})$), v_g is the phonon group velocity (m/s), l_L is the mean free path of phonon (m). This equation is also valid for heat conduction electrons.

The key to understand the variation of the thermal conductivity of a material is then to figure out the influence on C_V , v_g and l_L on its value.

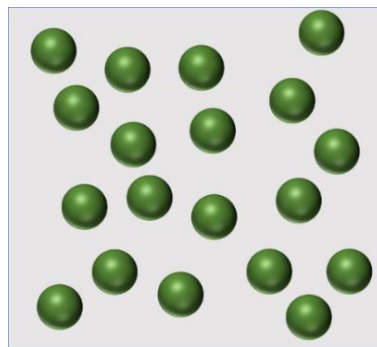


Figure I-5. Schematic of Phonon gas model.

I. C. 3. Energy carriers in amorphous structure

An amorphous material is a solid that lacks long-range order in its atomic or molecular structure. Unlike crystalline materials, which have a well-defined arrangement of atoms or molecules, the atoms or molecules in amorphous materials are arranged in a random or disordered fashion. This gives amorphous materials a glass-like or non-crystalline appearance. Examples of amorphous materials include glass, plastic, and some ceramics. Amorphous materials have different physical and mechanical properties than crystalline materials, such as lower mechanical strength, higher thermal and electrical insulation, and higher chemical resistance.

Regarding heat transfer by electrons in amorphous materials (metallic glasses...), the situation is different compared to crystalline metals because the mean free path of conduction

electrons is so short due to structural and compositional disorder that the Wiedemann-Franz law should hold in the whole temperature range.

Regarding heat transfer by phonons, due to the lack of periodicity in the atomic or molecular structure, phonons in amorphous materials are not able to propagate as far as in crystalline materials. In this limit, Eq. I-11 is no longer effective because it becomes questionable to treat phonon as a particle whose MFP is much longer compared to wavelength λ_L [25]. In 1979, Slack developed the “minimum thermal conductivity” model [29]. In this model, half of wavelength is employed as MFP of phonons. The prediction from “minimum thermal conductivity” model usually underestimates the thermal conductivity compared to experiment data [30] and thus is defined as a conceptual lower bound of k_L .

Many attempts have been made to better understand the physical mechanism of heat conduction in amorphous materials [31]–[33]. In 1993, Allen and Feldman [31] proposed to use propagons, diffusons, and locons as three novel heat energy carriers to describe the vibrational modes in amorphous structure, as illustrated in **Figure I-6**. Simply put, propagons is a plane-wave-like non-localized thermal carrier with an identifiable wavevector in the low frequency range. Propagons broadly resemble the traditional definition of phonons. Diffusons are also non-localized vibrational modes but do not exhibit the characteristics of a plane wave. Diffusons conduct heat via the coupling with each other. Locons are localized vibrational modes and their contribution to thermal conductivity is commonly considered to be negligible. It is generally believed that propagons and diffusons are jointly responsible for the heat conduction in amorphous materials due to the relatively large MFP of propagons and the large proportion of diffusons. However, it is very challenging to distinguish propagons and diffusons from each other because they are both non-localized. Additionally, the quantitative quantification of the contribution of propagons and diffusons is in fact significantly affected by the chosen propagon-to-diffuson transition frequency [34].

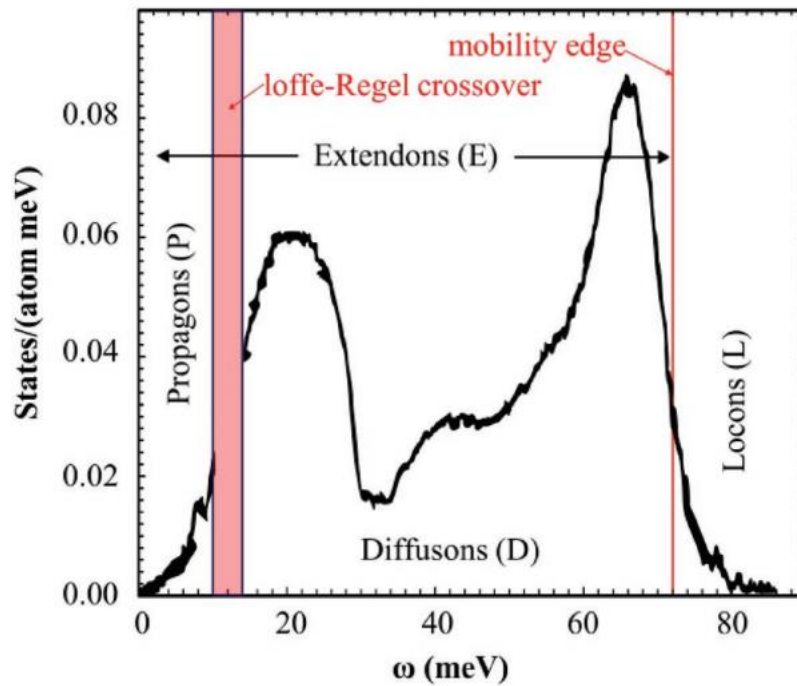


Figure I-6. Density of vibration state and division of three type of energy carriers in amorphous silicon. Adapted with permission [23]. Copyright 1999, Taylor & Francis Ltd.

Some researchers have shown that the “minimum thermal conductivity” model where phonon is responsible for heat conduction is roughly consistent with the method that regard diffusons as the most important vibrational modes in amorphous solids [23], [25]. Considering that the behaviors of phonons is better understood and studied, the term “phonon” is used as one of heat energy carriers of the studied samples (amorphous CrSi_2 and polymers) in this thesis. This is an integrated concept, which also includes the heat transfer mechanisms of propagons and diffusons. In any case the thermal conductivity corresponding to this phonon heat transport will be written as k_{ph} instead of k_L used for crystalline materials.

I. D. Heat transfer through interfaces

In this thesis, heat transfer through interfaces is described using thermal resistances of interfaces and thermal boundary resistances.

The interfacial thermal resistance (also known as thermal boundary resistance **TBR**)

R_{th} (Km^2/W) refers to the thermal resistance that occurs at every interface between materials with same or different phonon density of states. This phenomenon was named after Kapitza due to his observation of a temperature jump at the interface between heated metal and He II superfluid phase [35]. The presence of the TBR affects the thermal conduction across the interface and results in a temperature difference at both sides of the interface as shown in **Figure I-7**. The value of TBR is given by:

$$R_{th} = \frac{\Delta T}{q/A} \quad (\text{I-12})$$

where ΔT (K) refers to the temperature difference at the interface between the adjacent media, q (W) is the heat flux across the interface, and A (m^2) is the cross-sectional area.

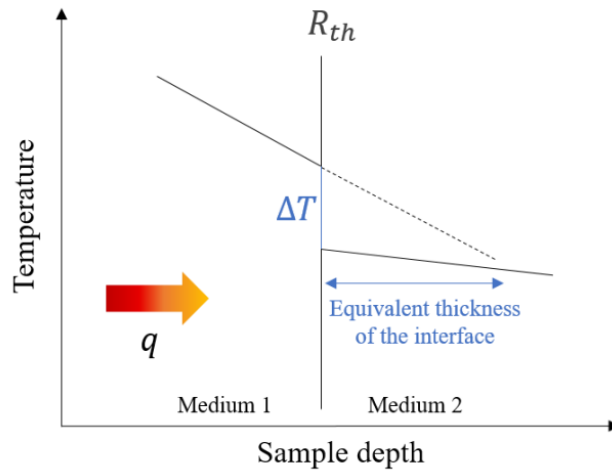


Figure I-7. Temperature profile in function of sample depth for two layered materials [29].

One should note that even though the mechanical condition on interface is perfect, heat carriers (for example phonons) may scatter or localize on the interface due to mismatch of atomic vibrational spectra [34]. Thus, the TBR is mainly attributed to the imperfect contact and phonon scattering. On the one hand, the roughness on the surface of a solid material may induce an imperfect contact between two mediums. In reality, only a limit number of bonds connects both lattices allowing the thermal conduction of heat flux through solid-solid contacts. The voids between two imperfect surfaces are filled by the surrounding fluid such as air. Air is

generally considered as a poor conductor of heat with thermal conductivity of $0.026\sim 0.067$ (W/(m.K)) in the temperature range of 300 K to 900 K [36]. Thus, the voids filled with air contribute to an additional thermal resistance while heat fluxes across the interface. Nonetheless, an extra interfacial resistance is generated due to this barrier effect. Such phenomenon is generally explained using acoustic mismatch model (AMM) and diffusive mismatch model (DMM) [37]. AMM model supposes a specular scattering on the interface while DMM model assumes a diffusive scattering. Much effort have been put into the research about thermal resistance on the interface using extensions of these two theoretical methods [38]–[40].

In particularly, TBR at the interface between two amorphous materials, presents some unexpected phenomena. Unlike the defects at interfaces between two crystalline structures that cause more scattering and thus increase the TBR, the introduction of structural defects (such as introduction of nitrogen defects [41]) to amorphous interface may facilitate the heat transfer across the interface. This suggests that the contact thermal conduction mechanism at crystalline/crystalline (crystalline interfaces) and amorphous/amorphous interfaces (amorphous interfaces) are very different. Apart from that, a lower TBR at amorphous interfaces than its crystalline counterparts have been found both in experiments [42] and molecular dynamics (MD) simulations [43], [44]. The reason behind such phenomenon contrary to intuition is still not understood sufficiently. The idea that a broader frequency range of vibrations could contribute to the thermal transport at amorphous interface is proposed by Gordiz and Henry [45] to explain this phenomenon. Some other researchers believe that the disorder at amorphous interfaces can disrupt vibrational modes, resulting in higher frequency vibrations near the interface which could “bridge” vibrational modes on either side of the interface [46].

In this thesis, due to the presence of substrate under the sample of nanometric thickness to be studied (detailed in subsequent chapters), TBR between sample and substrate must be taken into account.

Almost all the cases covered in this thesis are about amorphous interfaces between films

of thickness ranging from 250 nm to macroscale. The determination of the values of the involved TBR is rather difficult because the actual situation at the interfaces is very complex and uncertain. A common way to decide TBR is to refer to TBR values for a specific couple of materials in literature. However, some combinations of components to create an interface have never been studied or the conditions of components (different fabrication processes, stoichiometry...) are not completely identical. In that way, a possible range of TBR in general within $10^{-8} \sim 10^{-6}$ (Km^2/W), which is the possible value for R_{th} [47], [48] will be considered.

To simplify the case, sometimes TBR R_{th} (Km^2/W) is equivalent to an additional layer with an equivalent thickness t_{eq-TBR} , which is determined by:

$$t_{eq-TBR} = R_{th} k_{sample} \quad (\text{I-13})$$

where k_{sample} is usually the thermal conductivity of studied samples. More details can be found in **Chapter II** and in the Appendix 1.

According to the above discussion one can see that the thermal resistance of a material can be modulated by introducing or reducing interfaces, thereby achieving the desired tuning of the thermal conductivity of material.

I. E. Thermal conductivity tuning by modifying microstructure and geometry of solid materials

The thermal conductivity of a material is dominated by its volumetric heat capacity C_V , the group velocity of heat energy carriers v_g and their mean free path l as presented in Eq. I-11. It is challenging to modify v_g experimentally. Thus, to tune the thermal conductivity of materials in order to achieve an expected performance, the modification of C_V and l is needed.

In the case of thermoelectric materials, a higher energy conversion efficiency requires a lower thermal conductivity k coexisting with an unaffected or enhanced electrical

parameters. However, it is acknowledged that these properties are usually interdependent within materials, and it is challenging to independently manipulate one parameter [49]. As explained previously, the electronic contribution of thermal conductivity k_e is proportional to electrical conductivity σ .

The power factor ZT , which indicates the energy conversion efficiency of a material can be also written as Eq. I-14 by combining the Wiedmann-Franz law (Eq. I-9) with Eq. I-1:

$$ZT = \frac{S^2 \sigma}{k} T = \frac{S^2 / L}{1 + \frac{k_L}{k_e}} \quad (\text{I-14})$$

It could be noted that a low ratio between the lattice and electronic thermal conductivities, $\frac{k_L}{k_e}$, is desired in order to improve the thermoelectric efficiency. To attain this objective, many efforts have been focused only on reducing the lattice thermal conductivity of materials. The “phonon glass electron crystal” (PGEC) concept is henceforth proposed [50] and is considered as the ideal material to achieve maximum ZT . To obtain PGEC materials, various methods have been attempted.

Structuring by decreasing the size of the material's grains, by introducing interfaces between different regions or by amorphisation can enhance phonon scattering, reducing the thermal conductivity [51]. By efficiently controlling the introduced interfaces, the scattering intensity of electrons and phonons at the same interface differs dramatically [52]. The significant reduction of k_L and the conservation of σ lead to a satisfactory ZT .

Another method to form PGEC that has been proven to be very effective in the literature is **doping**, which can introduce **impurities or defects into the material**. As it will be seen in chapters III, the microstructure and the physical properties of a material can be tailored using ion implantation technique. As outlined in references [53]–[55], ion implantation technique enables the introduction of point defects, extended defects, and dangling bonds that can enhance the charge transport within the lattice. This technique also introduces vacancies and interstitials that serve as scattering centers for phonons, which affect k_L . Additionally, depending on the

experimental conditions, ion implantation can induce the recrystallization of amorphous materials, creating crystallites boundary that can also disrupt the phonon path, as stated in reference [56].

The utilization of isoelectronic elements in materials also allows for the preservation of the crystalline electronic structure while also increasing σ . This is accomplished by introducing elements with similar electronic configurations into the pristine material. The significant mass contrast created by these isoelectronic elements disrupts the phonon path, resulting in a decrease of k_L [55], [57].

Additional methods like, compositing by combining different materials with dissimilar thermal and electrical properties [58], [59]; phonon engineering by designing the material's lattice structure to selectively scatter certain phonon frequencies (phonon filtering) while preserving electronic transport [60], [61]; superlattice by creating a stacked structure of alternating materials with different thermal properties [62], are also possible routes to create PGEC. It's worth noting that the specific methods used to obtain a PGEC will depend on the specific material and desired properties.

In the case of applications requiring heat dissipation, polymers are highly desirable materials in widespread domains due to its low-cost, corrosion resistant, light weight and excellent processability. Whereas the inherently low thermal conductivity of polymers restricts heat dissipation, thereby limiting the performance of the materials in operation and shortening the lifespan of polymer-based materials. Many attempts have been made to enhance the thermal conductivity of polymer materials while minimize any adverse effects on the other properties.

Specifically, **nanocomposition by adding some nanoscale thermal conductive fillers into polymer matrix** is a popular method for enhancing its thermal conductivity. Common thermal conductive fillers include [63]: metallic fillers such as copper, aluminum, and silver, ceramic fillers such as boron nitride (BN), aluminum nitride (AlN) and silicon carbide (SiC), and carbon-based fillers such as expanded graphite (EG), carbon fiber, carbon black, carbon nanotubes and graphene. Most recently, a novel two-dimensional (2D) transition metal carbides

and nitrides, also known as MXene, is also used as functionalized fillers in polymer matrices [64].

Another way to enhance the thermal conductivity of polymer-based materials is by **altering the material's crystallinity**. Depending on the molecular chain structure, many polymers can be classified as semi-crystalline phase. A semi-crystalline polymer is a type of polymer that contains both crystalline and amorphous regions in their microstructure. These polymers are characterized by the presence of both ordered, highly packed regions (crystalline regions) and disordered, less densely packed regions (amorphous regions). The degree of crystallinity in a semi-crystalline polymer can vary widely, depending on the polymer type, processing conditions, and other factors. It has been demonstrated that k of polymer-based materials can be improved by increasing the crystallinity [65]. One should take note that in this thesis I will just use the term amorphous polymer in order to represent non-crystalline polymer. Whereas I will use the term crystalline polymer instead of semi-crystalline polymer.

However, a thorough examination of the literature reveals a significant scatter in the reported experimental data of thermal conductivity for these materials. The large variation in thermal conductivity values can be attributed to a number of factors including the purity and quality of the nanofillers and the polymer matrix, the dispersion of nanoparticles in the matrix, the measurement techniques and conditions, and the sample preparation method. Additionally, the presence of impurities, defects, and other microstructural features can also affect the thermal conductivity of crystalline polymers. Despite these challenges, it is clear that the thermal conductivity of polymer-based materials is an important property that can have a significant impact on their performance in various applications. Further research is thus needed to better understand the underlying mechanisms that govern the thermal conductivity of these materials.

It is also worth to mention that compared to any other kind of material, the scientific literature addressing heat transfer within polymers is not uniformly calibrated. Depending on the origin of their discipliner community, published articles may abuse the concept of term “phonons”, which is a common situation. It is clear that heat transfer within polymers and

particularly semi-crystalline polymers is not well-understood. We will see it in Chapter IV that the current models used to describe heat conduction are still mainly based on mixing law or empirical models.

A more complete state of the art on the properties of the materials of the study will be given while discussing the results we got on CrSi₂ and polymeric materials in Chapter III and IV respectively in order to avoid repetitions in the manuscript.

Some techniques for estimating the thermal conductivity of solid materials are summarized in the following section.

I. F. Techniques for investigating the thermal conductivity of solid materials

Various techniques can be used to investigate the thermal conductivity of solid materials. The main steps of the general principle of all these techniques are first to heat the sample with a source (laser or heated probe, etc.), and second to measure or follow the resulting sample temperature variation. A mathematical model, which describes the heat dissipation in the sample from the source, is then used to reproduce the measurement and results are compared to experimental data to determine the thermal conductivity of interest.

I. F. 1. Thermorefectance

Thermorefectance method [66] is based on the principle that when a material is heated, its temperature changes can be detected as a change in its reflectivity. This technique typically involves the focalization of a modulated pump laser beam onto the surface of the material and the measurement of the reflected light via a probe beam as a function of the modulation frequency. The change in the reflected light can then be used to determine the ratio of the temperature change of the material, which depends on the thermal conductivity. This technique is a non-contact method but requires the deposition of an optical transducer layer (mainly a

reflective metallic layer) on the film's surface in order to induce a surface heat absorption of the optical energy.

I. F. 2. Photothermal radiometry

Photothermal radiometry (PTR) [67] is another optical technique for characterizing the thermal conductivity of a material. The main difference between PTR and thermoreflectance technique is that PTR is based on the detection of the emitted infrared thermal radiation rather than the change in reflectivity induced by the temperature variation of the material. An optical transducer layer on the film's surface is also often needed for PTR to enhance the absorption of energy by the sample from the heating laser.

I. F. 3. 3ω method

3ω method is an electrical-based contact technique that requires the deposition of a micrometric in size metallic resistance (transducer) on the samples' surface when bulk or thin film samples are studied [68]. The transducer is used to heat the sample and as thermometer: its electrical resistance is linearly dependent of its temperature. Practically a small AC current is applied to the transducer, and the resulting modulation of the transducer temperature change as a function of the modulation frequency is measured. This temperature change depends on the thermal properties of sample.

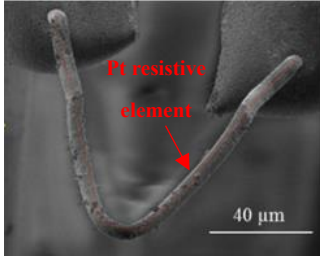
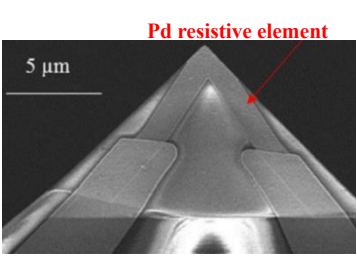
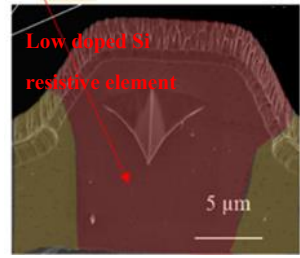
I. F. 4. Scanning thermal microscopy (SThM)

SThM technique is the technique that was used in these works. It is mainly based on the atomic force microscopy (AFM) technique equipped with a small thermal probe. For thermal property characterization, called active mode of SThM, the AFM probe, which is equipped with a resistive element, is self-heated by Joule effect in dc or in ac regime. As in the 3ω method, the probe is used as a local heating source for the sample and as a resistive thermometer simultaneously but contrarily to 3ω method, SThM does not require to cover the sample surface

with an electro-thermal transducer. This makes SThM less invasive than all the aforementioned techniques. The self-heated probe that is used in contact with the sample (in the conventional mode of SThM) can moreover be moved at the sample surface to image the thermal properties of samples. It is commercialized as a thermal imaging technique but has been developed for the thermophysical property measurement of materials for more than twenty years.

Several types of SThM resistive probes with different size [69]: Wollaston probe, Kelvin nanotechnology (KNT) probe and doped silicon probe, are presented in **Table I-1**.

Table I-1. Characteristics of Wollaston probe, Kelvin nanotechnology probe and doped silicon probe [70].

Scanning electron image of SThM probe	 <p style="text-align: center;">Wollaston probe</p>	 <p style="text-align: center;">Kelvin nanotechnology probe</p>	 <p style="text-align: center;">Doped silicon probe</p>
Resistive element: Curvature radius:	<ul style="list-style-type: none"> • 200 μm length and 5 μm diameter platinum/rhodium wire • few hundred nm 	<ul style="list-style-type: none"> • 18 μm length and 2 μm width Pladium ruban • Apex curvature radius: < 100 nm 	<ul style="list-style-type: none"> • few μm heigth low doped silicon pyramidal tip • 10-20 nm

We chose to use the Wollaston microprobe, described more in detail in **Chapter II** of the manuscript, because it allows the thermal investigation of the several μm^3 subsurface volumes in materials, more particularly in low thermal conductivity materials without any preliminary processing of the sample's surface [87]. Indeed, the contact radius may reach to more than 10 μm for the Wollaston probe operated in air conditions on polymeric materials [88], which is larger than the other kind of probe such as the KNT probe and doped silicon probe (a few hundred nanometers for both the probes). Such large contact radius is favorable to obtaining representative result while measuring thermal conductivity of low thermal conductivity composite materials considering that the size of fillers can be micron-sized and the dispersion may not be homogeneous. On the other hand, Wollaston probe is tougher during circuit

undulation. Metallic components also make it convenient to be calibrated.

An advantage of SThM is its capability to perform images of the thermal conductance of sample with a sub-micrometric thermospatial resolution. Furthermore, SThM can detect local thermal conductivity inhomogeneities and distributions [71] in materials with low thermal conductivity. This can provide more information to better understand the underlying factors that contribute to the heat transfer by conduction in materials. The main limits of this technique [69] are:

(1) the narrow range of sensitivity to thermal conductivity for bulk samples. It is limited at thermal conductivities lower than few W/(m.K) except for the Wollaston microprobe where thermal conductivities until twenty W/(m.K) can be measured depending on the shape of the probe.

(2) the complexity of the thermal contact between the probe and the sample, which involves heat transfer by conduction through the air, the water meniscus formed at the probe-sample contact, the probe-sample solid-solid contact (radiation can be neglected for measurements in air) (**Figure I-8** (a)). Many parameters define the thermal contact such as sample topography and roughness, hydrophobicity, surface contamination, etc. Our experiments were designed to minimize the effect of these parameters on our measurements: flat samples and very low roughness samples were studied; the operating temperature of the Wollaston probe was chosen larger than 100°C to evaporate the meniscus, samples were carefully cleaned before any measurement.

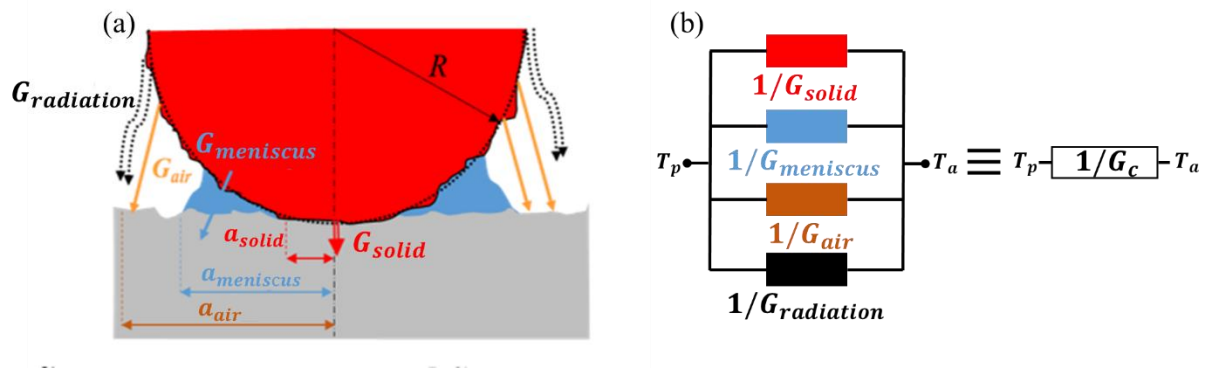


Figure I-8. Schematic of probe-sample thermal contact (a) and equivalent thermal contact conductance G_c (b).

I. G. Associated measurement modelling - generalities

As introduced previously the determination of the thermal conductivity of a material requires a mathematical model that describes the heat dissipation from the heating source in the material sample whatever the considered measurement technique is. This model then expresses the thermal conductance of the sample and takes into account the geometry (bulk sample, multilayered sample etc.) and the thermophysical properties of the sample components and interfaces between them. It also takes into account the sample heating process (steady state, transient or modulated regime, contact or no-contact technique), shape of the heating source and thermal resistance between the transducer (probe in the case of SThM) and the sample surface.

The heat equation, which is based on the Fourier law, need to be solved. As an example, for optical methods, such as thermorefectance and PTR techniques, some combination of the material's thermophysical properties (thermal conductivity, density, specific heat, and thermal resistance at interfaces) can be determined when these properties are not correlated. The designs of the experimental setups are based on the interplay between three characteristic lengths: the thermal diffusion length, μ (defined as $\mu = (D/\pi f)^{0,5}$, where f is the frequency of the excitation source and D is the thermal diffusivity of the material in question), the excitation spot radius, r_0 (laser pump beam at 1/e), and the detection spot radius, ϕ_0 (laser probe beam radius at 1/e or detector's opening radius). The last two parameters are finite and are fixed by

the experiment. The relationship between μ , r_0 , and ϕ_0 delineates the limit between a 1D and a 3D heat transfer resolution. Such resolutions were extensively studied in literature, where the 1D heat transfer resolution is mainly used in simple calculation cases (exhibiting good 1D signal to noise ratio) and the 3D resolution is used for more complex cases.

For SThM the modelling is more complex as it involves the thermal interaction between the probe and the sample. In the thesis, an effective thermal conductance (G_c), as represented in **Figure I-8** (b), will be used to overcome this issue. The following Chapter II addresses more in detail the technique and the methodology I used for thermal conductivity estimation.

I. H. Conclusions

The thesis is in the frame of the establishment of treatment processes of materials dedicated to the tuning of the thermal conductivity (k) of materials for oriented applications that are in strong link with the thermal management of systems. The focus was made on two types of materials:

- (1) amorphous CrSi_2 , which is a semiconductor-like material and part of the transition metal silicides studied for thermoelectric applications. In this case, the material treatment process to be evaluated consisted in its implantation with ions and expected results were a decrease of the amorphous CrSi_2 thermal conductivity;
- (2) polymeric materials that are involved in many applications where heat transfer has to be improved or optimized. For these materials the treatment was the introduction of carbon –based nanofillers in the polymer-based matrix.

For both the types of materials studied, the goals were to measure the thermal conductivity of the materials previously treated in different conditions to evaluate the treatment process, to improve the understanding of the mechanisms of the thermal conductivity variations observed as a function of the treatment conditions and to propose ways to improve the treatment process.

In this chapter are reminded the basic knowledge of heat conduction in solids (dielectric

materials, metals, and semiconductors, crystalline or amorphous) that we used to discuss and interpret the thermal conductivity values measured in the thesis. The main approaches used for tuning the thermal conductivity of materials are reviewed. They mainly consist for thermoelectric materials in introducing scattering centres for energy carriers for reducing k , but it is also found that nanocrystallites in an amorphous matrix can also contribute to the filtering of energy carriers and decrease k . In the case of polymeric materials, the adding of highly conductive charges and the improvement of the polymer crystallinity are the main ways to improve k . Let us here remark that the state of the art for the materials that were studied in the thesis are reported in the **Chapters III, IV and V**, which are dedicated to the material measurement for avoiding repetitions and making it more fluent the discussion of the results.

This **Chapter I** also gives the main advantages and limits of the SThM technique used for thermal conductivity measurements in the thesis. SThM is less invasive than other thermal techniques. It also precises the aspects of the methodology that we followed to overcome the SThM disadvantages: choice of the Wollaston probe, which can probe large material volume, use of a measurement modeling using an effective thermal conductance to describe the heat transfer between the probe and the sample without accounting for its complexity, design of our experiments to minimize artifacts in our measurements.

The SThM equipment and the measurement methodology used in the thesis are given in detail in the following **Chapter II**.



Chapter II. MEASUREMENT SETUP AND PROCEDURE

II. A. Scanning thermal microscope

II. A. 1. Instrumentation and principle

The SThM instrument used in this work combines an AFM with a thermal control unit enabling electro-thermal measurements via a thermoresistive microsensor (the Wollaston probe) that constitutes the tip of the AFM probe. It was used in contact mode and force constant mode. The probe was heated by a dc electrical current. A schematic diagram of this AFM-based SThM is shown in **Figure II-1**.

II. A. 1. a) Atomic Force Microscope instrument

The AFM used in this thesis was a NTEGRA-Aura AFM from NT-MDT. As shown in **Figure II-1** a piezoelectric displacement system allows the sample to move horizontally (in the X, Y directions) and vertically (in the Z direction). A laser beam is focused on the reflecting mirror that is glued on the probe cantilever. It is reflected toward and detected by a photodetector allowing the detection of the probe cantilever bending, which is caused by the probe-sample interaction force when the probe is in near contact or in contact with the sample.

During imaging, the thermal probe is in contact with the sample's surface (equivalent to the AFM contact mode), and the contact force between the probe and the sample is maintained constant (AFM constant force mode). Hence, in order to obtain an image of the topography of the sample surface the probe scans the surface in the X, Y directions. During this scan of the sample surface, the variation of the contact force due to the sample topography induces a variation of the bending of the cantilever, hence a displacement of the laser spot on the photodetector. An electronic feedback loop allows the adjustment of the vertical positioning of the sample for maintaining constant the laser spot position at the photodetector, i.e., for

maintaining constant the contact force between the tip and the surface of the measured material. The variation of the voltage applied at the Z piezoelectric displacement ceramic is used to reconstruct the topography of the sample.

Furthermore, in conventional SThM point measurement, the probe also contacts the sample with a constant force (feedback loop on) in a particular location.

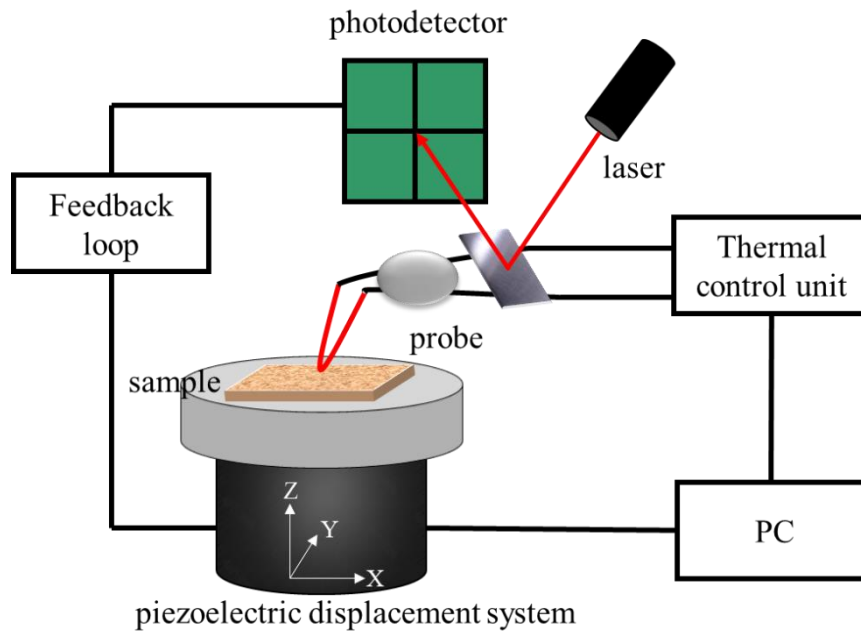


Figure II-1. Schematic diagram of an AFM-based SThM used.

In these works, this equipment was used as AFM for the analysis of the roughness and the topography of samples and as SThM in imaging and point measurement modes for their thermal analysis. Measurements were performed in ambient air environment.

II. A. 1. b) Wollaston probe

As shown in **Figure II-2**, the Wollaston probe consists of a cantilever made with a 5 μm diameter rhodium-plated (10%) platinum filament (90%) core and a 75 μm silver shell. The resistive element, which constitutes the tip, is obtained by electrochemical etching on the silver shell, allowing to strip a 200 μm segment rhodium-plated platinum filament core previously bended into V-shape. A mirror is glued on the Wollaston wire cantilever to reflect the laser

toward the photodetector. The Wollaston probes used in this work were supplied by the Czech Metrology Institute (CMI) or Bruker company.

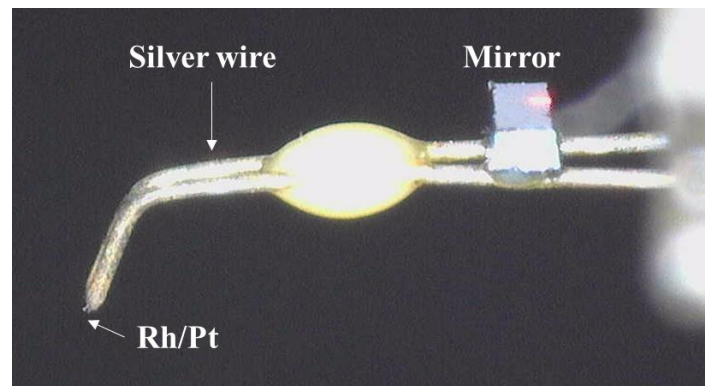


Figure II-2. Optical image of Wollaston probe.

Table II-1 gives the approximate values of the main characteristics of the Wollaston probe as AFM and thermal probe. However, as Wollaston probes are made manually it is strongly recommended to experimentally determined these parameters for each probe used when quantitative measurements are required.

Table II-1. Main characteristics of the Wollaston probe.

Stiffness coefficient	5-20 N/m
Curvature radius	V shape 15 -20 μ m but curvature radius of the apex is rather of few hundred nanometers due to roughness of the apex.
Temperature coefficient of electrical resistance (TCR)	$1.66 \cdot 10^{-3}$ 1/K
Approximate electrical resistance	2-5 ohms
Operating temperature range	50°C-800°C

The measurement with this metallic probe is an electro-thermal measurement which is

based on the linear relationship between the probe electrical resistance $R_{el,p}$ and the probe mean temperature T :

$$R_{el,p} = R_0(1 + \alpha_0(T - T_0)) = R_0(1 + \alpha_0\Delta T) \quad (\text{II-1})$$

where R_0 is the probe electrical resistance at a reference temperature T_0 (0°C); $\Delta T = T - T_0$; and α_0 is the temperature coefficient of electrical resistance (TCR) at T_0 , describing the relative change of electrical resistance that is associated with a given change in temperature. The subscript 0 is used to indicate the reference temperature 0°C .

In active mode, the SThM probe is used as a thermometer and as a heater simultaneously. The electrical current that supplies the probe is then sufficiently high (several tens of mA) to heat the resistive element of the probe by Joule effect. When the probe and the sample are in contact a part of the power generated by Joule effect in the probe is transferred to the sample. This leads to a cooling of the probe. Depending on the thermal control unit used, the corresponding variation of the probe's electrical resistance is measured or compensated to keep constant the probe at a mean temperature. In the latter case, the compensation is obtained by adjustment of the current applied to the probe and the measured signal is the variation of the current. Therefore, using such setup it is possible to obtain simultaneously the topography of the studied sample and an electro-thermal image. As explained in **Chapter I** the contrast of electro-thermal image strongly depends on the thermal conductance of the sample and of the thermal interaction between the probe and the sample. The contrast of the electro-thermal image or the voltage recorded in point measurements may be then related to the thermal conductivity of the sample. A model that will be presented in the third part of this chapter is used to establish this relation. The inputs in this model must be representative as precisely as possible of the system studied and particularly of the probe. A calibration of the probe is henceforth required.

II. A. 2. Thermal control unit

Two types of Thermal Control Unit (TCU) (see in **Figure II-1**) were used. Both the

units are based on a Wheatstone bridge where the resistive SThM probe is included in one of the branches of the bridge (**Figure II-3** and **Figure II-4**).

II. A. 2. a) Unbalanced Wheatstone bridge

One of our TCU is based on a home-made unbalanced Wheatstone bridge. In this configuration, a Keithley 6221 current source is used for its more stable power supply. The bridge is used to detect the variation of the probe's electrical resistance. As mentioned previously, the electrical resistance of the probe ($R_{el,p}$) constitutes one of the branches of the bridge, while the other three branches are composed of two fixed electrical resistors (R_1 and R_2) and a variable resistance (R_v), as shown in **Figure II-3**. R_1 and R_2 are set respectively as approximately 10 times higher than $R_{el,p}$ to limit the variation of the current flowing through the whole circuit while $R_{el,p}$ shifts during the experiment process. A constant current I is supplied by the current source. The bridge is balanced before any measurements by adjusting R_v to be equal to $R_{el,p}$ to make ΔV as close to $0 V$ as possible (experimentally less than 10^{-4} mV), leading to the detection of the variation of $R_{el,p}$ ($\Delta R_{el,p}$). In real case, limited by the accuracy of the component, R_v cannot be exactly equal to $R_{el,p}$, this was taken into account in the determination of measurement uncertainty. Considering that the ΔV is usually a weak signal (less than 5 mV), a pre-amplifier is used between points A and B (in **Figure II-3**) in order to amplify the signal and extract its value. It is assumed in our calculation that the current is equally separated into two branches. Thus, the variation of $R_{el,p}$ during the measurement is given by:

$$\Delta R_{el,p} = R_{el,p} - R_v = \Delta V / \frac{I}{2} \quad (\text{II-2})$$

The corresponding uncertainty that must be taken into account for the calculation of $\Delta R_{el,p}$ is estimated of approximately 4% (See Appendix 2),

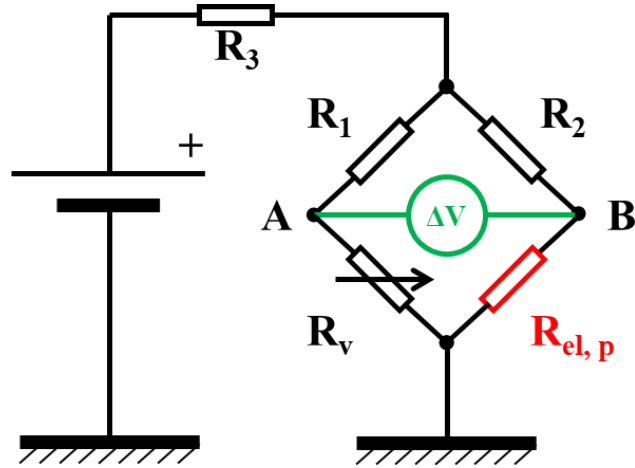


Figure II-3. Schematic diagram of an unbalanced Wheatstone bridge.

II. A. 2. b) *Balanced Wheatstone bridge*

The second TCU is a commercial unit [72] and is based on a balanced Wheatstone bridge technique. The schematic diagram of such circuit is shown in **Figure II-4**. With such unit the bridge is always kept balanced by a feedback loop that monitors the current applied to the bridge so that the electrical resistance of the probe is constant. While the probe is heated by Joule effect (active mode of a resistive probe) and the heat spreads from the probe to the sample during the measurement of the thermal properties of materials, the electrical power dissipated to the sample is increased to maintain the bridge balanced ($\Delta V = 0$). This power can be derived by measuring the voltage V applied on whole bridge and that is measured. The mean temperature of the probe ($T \approx 140^\circ\text{C}$), which is linearly dependent to the electrical resistance of the probe can be chosen by adjusting the variable resistance R_v . For this TCU $R_v = 5R_{el,p}$.

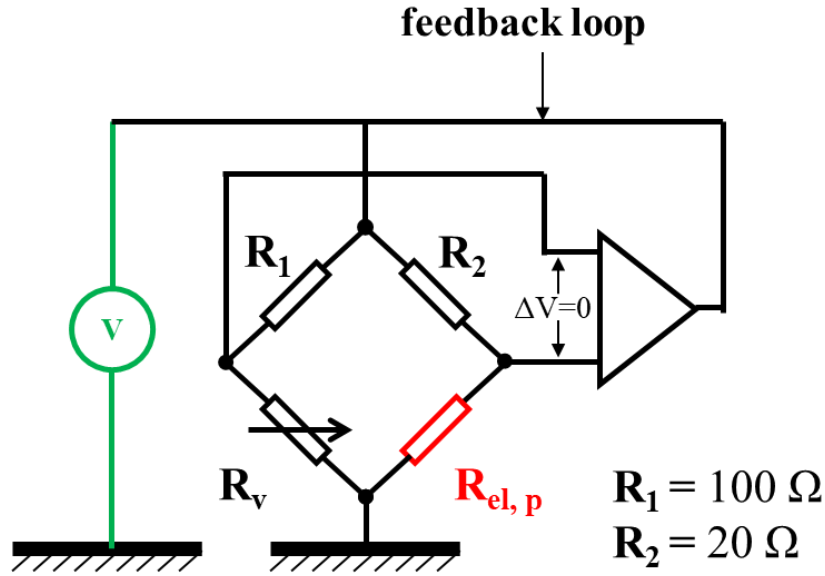


Figure II-4. Schematic diagram of a balanced Wheatstone bridge.

In this TCU, $R_{el,p}$ can be directly calculated from input R_v . I_p is deduced by $I_p = \frac{V}{R_2 + R_{el,p}}$.

II. B. Temperature and electrical calibrations of the probe

The Wollaston probes are home-made sensors. They are made manually and are not reproducible. Their physical properties and characteristics are different from one probe to another. Then before quantitatively characterizing a tip-sample system using a model, it is necessary to calibrate each probe while it is out of contact with a sample. This calibration is made in different steps.

The first step is a temperature calibration. In this step, the relationship of probe electrical resistance in function of temperature, i.e., the TCR of the probe (α_0), is characterized. The electrical resistance and TCR of each probe component (Pt wire, Wollaston wire, electrical cables as represented in **Figure II-5**) is also specified in this step.

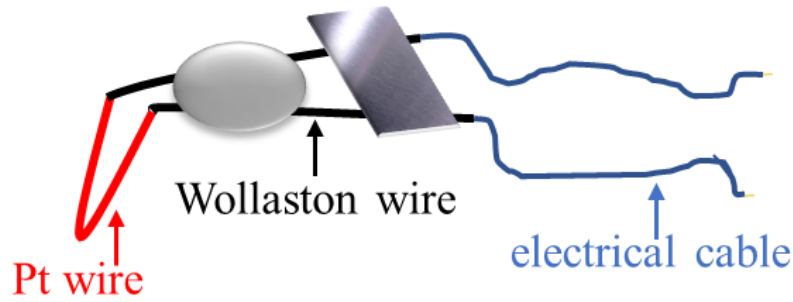


Figure II-5. Schematic of Wollaston probe components.

The second step is an electrical calibration. This step is dedicated to establishing the expression of the probe electrical resistance, i.e., its mean temperature, as a function of the power electrically dissipated in its resistive Pt element. This step notably allows the estimation of the electrical resistance of the probe at the ambient and from electrical calibration performed in air and in vacuum the determination of the thermal conductances corresponding to the heat transfer from the heated resistive element to the ambient environment and that to the probe cantilever.

II. B. 1. Temperature calibration

The temperature calibration for the probe is dedicated to characterizing $R_{el,p}$ at a given temperature. It was performed using a thermostatic oven. In this case, all the components of the probe are heated to the same temperature with no self-heating by Joule effect ($I < 0.1$ mA). In other words, the whole probe can be considered isothermal. R_0 and α_0 of the studied probe can then be calculated from the curve of $R_{el,p}$ as a function of T (Eq. II-1). As a reminder: $R_{el,p} = R_0(1 + \alpha_0(T - T_0))$.

Figure II-6 gives an example of the temperature calibration curve for one Wollaston probe used during this thesis. The electrical resistance of the cable of the probe ($R_{el,cable}$) also was measured under the same heating and cooling conditions in order to eliminate the contribution from cable in the probe electrical resistance. In this analysis procedure, 0°C was chosen as T_0 , so R_0 has the same value with the interception of curve with y axis. The slope

of the curve is equal to the product of R_0 and α_0 . In this work, the mean value of calibration curves get from heating and cooling progress is used. Furthermore, since the electrical resistance of the probe $R_{el,p}$ is the sum of all the probe component' electrical resistances (the one of the Pt resistive elements and the one of the Wollaston cantilevers). Thus, a system of two equations can be used for this calculation as follows:

$$\begin{cases} R_{p0} = R_{Ag0} + R_{Pt0} \\ R_{p0}\alpha_{p0} = R_{Ag0}\alpha_{Ag0} + R_{Pt0}\alpha_{Pt0} \end{cases} \quad (\text{II-3})$$

with R and α representing the electrical resistance and the TCR and the subscripts p , Ag, and Pt, are for probe, Wollaston cantilever and Pt heater, respectively. In this work the cantilever is assumed in Ag. The subscripts 0 is used to indicate the reference temperature 0°C .

Therefore, from the oven calibration it is possible to measure both R_{Ag0} and R_{Pt0} with the Eq. II-4 (deduced from Eq. II-1 and II-3):

$$\begin{cases} R_{Ag0} = \frac{R_{p0}(\alpha_{p0} - \alpha_{Pt0})}{\alpha_{Ag0} - \alpha_{Pt0}} \\ R_{Pt0} = \frac{R_{p0}(\alpha_{p0} - \alpha_{Ag0})}{\alpha_{Pt0} - \alpha_{Ag0}} \end{cases} \quad (\text{II-4})$$

By applying $\alpha_{Ag0} = 0.0041 (K^{-1})$ [73] and $\alpha_{Pt0} = 0.00166 (K^{-1})$ [73], $R_{Ag0} = 0.043 \Omega$ and $R_{Pt0} = 2.198 \Omega$ can be calculated from above equation. It can be also known that the electrical resistance of Pt heater at experiment temperature 30°C is equal to $R_{Pt30} = 2.308 \Omega$, which will be used later to determine the temperature of heater part during the measurements. All the above parameters are in good accordance with ones from literature [70]. The uncertainty of results is estimated as 5% measurement error of the instrument.

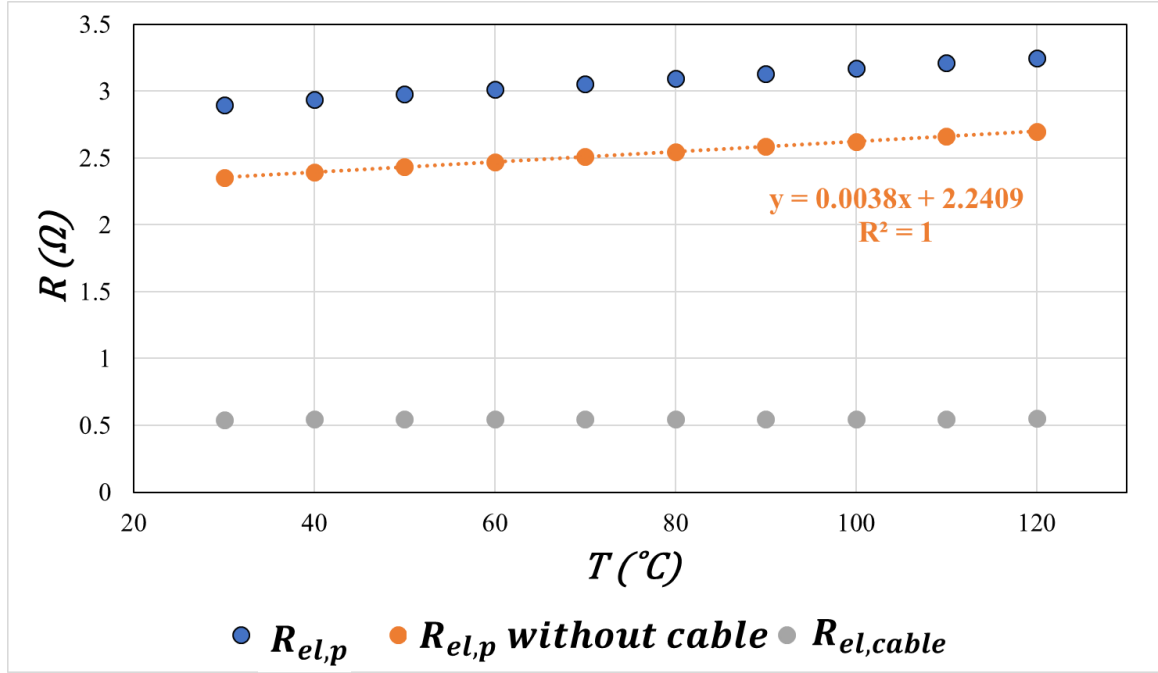


Figure II-6. Variation of the electrical resistance as a function of temperature of a Wollaston probe, which is heated in an oven with no self-heating by Joule effect.

II. B. 2. Electrical calibration

II. B. 2. a) Experimental part

In this calibration the probe is heated by Joule effect using a DC electrical current as in a measurement in active mode with our setup. Out of contact measurements are performed in air and in vacuum so that the thermal conductance corresponding to the heat transfer from the heated resistive element to the ambient environment and the thermal conductance corresponding of the probe cantilever can be determined (see **Section I. G Associated measurement modelling - generalities**).

It is here considered that only the heater part of the probe (V shaped Pt wire) is heated resulting in an increase of the overall electrical resistance of the probe. Therefore, for the electrical calibration, different DC currents (I_p increase from 0 mA up to 50 mA) are applied to the probe.

For balanced bridge TCU, R_v is increased from R_0 . The input R_v while V just starts to vary is recorded and is equal to 5 time of $R_{el,p}$ at room temperature. For such TCU, electrical calibration is not necessary as explained in **Section II. A. 2. b) Balanced Wheatstone bridge.**

II. B. 2. b) Model for balanced Wheatstone bridge.

For unbalanced bridge TCU, the electrical voltage (V_p) of the tip alongside the variable electrical resistance R_v , which is supposed to be equal to $R_{el,p}$ (when the Wheatstone bridge is balanced) are measured. **Figure II-7** gives an example of electrical calibration results for one Wollaston probe performed in air (a, c) and in vacuum (b, d) with an unbalanced bridge. By subtracting the contribution of Wollaston silver wire R_{Ag30} and cable $R_{el,cable}$, we can plot $R_{el,pt}$ as a function of the power dissipated on heat element (P_p), where $P_p = I_p^2 R_{el,pt}$ after removing the inherent offset of the system, as shown in **Figure II-7** (a), (b). With the temperature calibration, we may convert the electrical resistance into the mean temperature of the heated Pt element, as plotted in **Figure II-7** (c) and (d), where ΔT is the difference between the temperature of Pt and ambient temperature, which is equal to 0°C without any applied power. The thermal conductance of the probe G can then be calculated then by equation $G = \frac{P_p}{\Delta T}$, which is equal to the slope of the curve in **Figure II-7** (c) and (d).

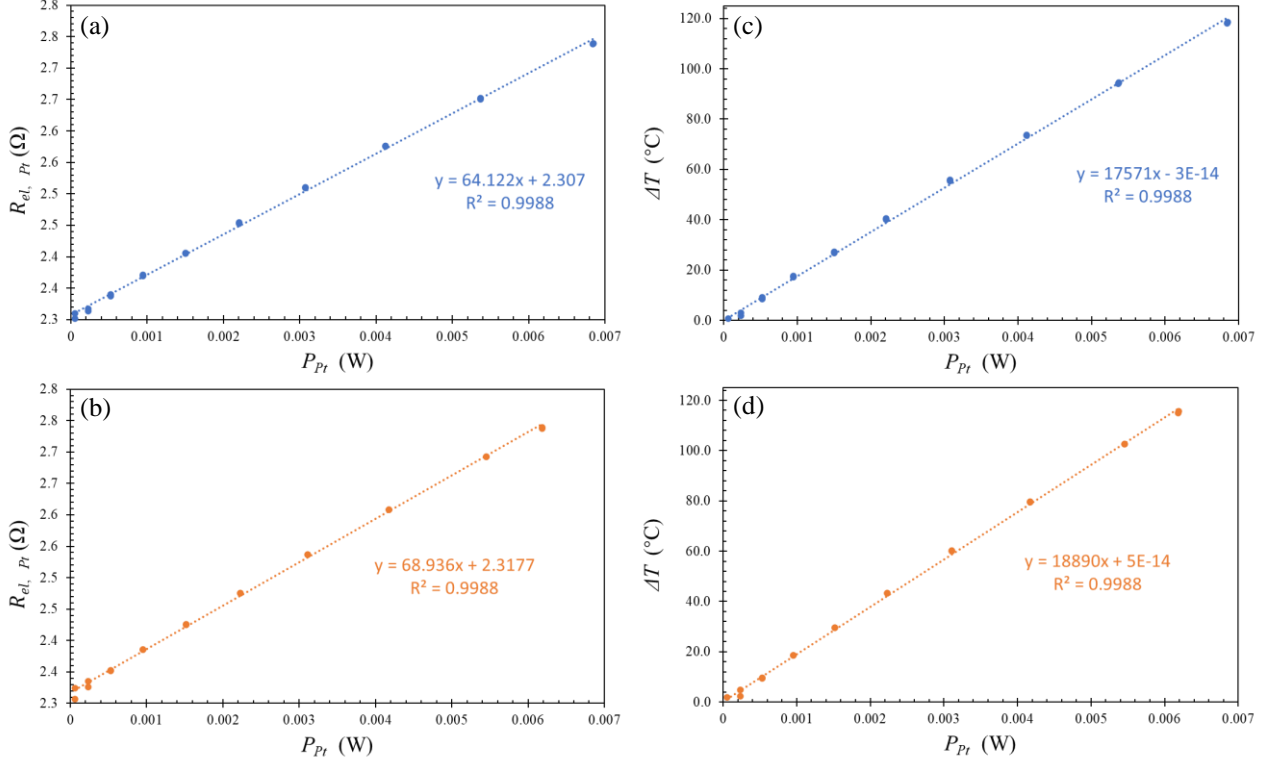


Figure II-7. Variation of the electrical resistance ($R_{el,pt}$) as a function of power dissipated on the heating element Pt (P_p), (a): in air, (b): in vacuum; and temperature difference between ambient and heat element Pt as a function of P_p , (c): in air, (d): in vacuum.

II. B. 2. c) Associated model

Figure II-8 is a simplified diagram to describe the thermal conductance network of the probe corresponding to the configuration of the electrical calibration. T_a is the temperature of ambient and T_{Pt} is the mean temperature of the Pt element. The temperature at the apex of the Pt/Rh tip has been proved to be around 1.5 time of the mean temperature of the resistive wire [74]. However, it is very difficult to determine experimentally the tip apex part and its dimension. Furthermore, when not in vacuum and in contact with the sample, the tip-sample thermal contact area is not just limited in the tip apex due to heat conduction through the gas [74]. Therefore, we consider that the whole Pt/Rh wire is isothermal and that the mean temperature T_{Pt} was used to calculate the thermal conductance of the elements of the probe.

Two main heat transfer channels constitute the system when probe is out of contact with sample:

- 1) G_{wire} corresponds to the heat conduction to the silver wire.
- 2) G_{env} corresponds to the heat lost by the Pt wire to the environment. Thermal conduction is included, and radiation effect is small enough to be neglected [75].

R_{wire} and R_{env} are the thermal resistances that are the inverse of G_{wire} and G_{env} , respectively. The measurements were performed both in ambient conditions and under primary vacuum ($\sim 1.8 \cdot 10^{-1}$ mbar) in this calibration step. G_{wire} exists both in air and vacuum while there is no G_{env} under vacuum. So we may deduce $G_{wire} = 5.29 \pm 0.79 \cdot 10^{-5}$ W/K from **Figure II-7 (d)** and $G_{env} = 3.97 \pm 0.60 \cdot 10^{-6}$ W/K from the difference between the slope of the two curves in **Figure II-7 (c)** and (d). This is in the same magnitude as $G_{wire} = 3.62 \pm 1.16 \cdot 10^{-5}$ W/K and $G_{env} = 8.05 \pm 3.64 \cdot 10^{-6}$ W/K measured in Ref [70]. These parameters will be used later to calculate the thermal conductance of samples.

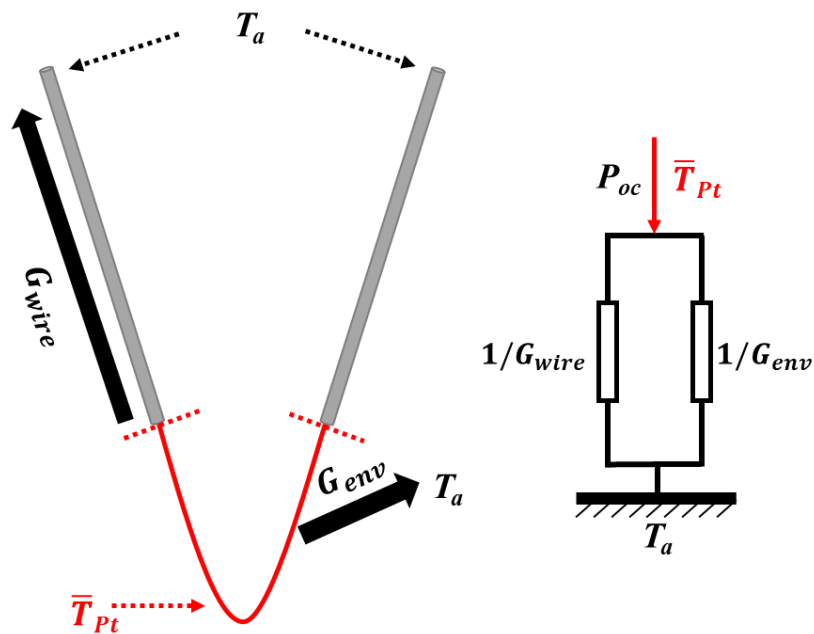


Figure II-8. Diagram of the existing heat transfers within the SThM probe while out of contact and the associated equivalent thermal conductance.

$$G = G_{wire} + G_{env} \quad (\text{II-5})$$

II. C. Calibration for thermal conductivity measurement

This calibration must be made in the same experimental conditions than measurement of unknown samples. In this thesis, it was made from point measurements using reference samples with known thermal conductivity and known roughness. These measurements were performed in ambient air conditions with a chosen current applied to the probe, heating the probe to around 148°C to make sure that there is no water meniscus between apex and sample.

II. C. 1. Point thermal conductivity measurement methodology

The measurements are made in two steps for a given sample:

- First the probe is out of contact. Its apex is then 2 mm far away from the surface of sample to prevent a heat transfer to it. Wheatstone bridge is balanced ($\Delta V < 1 \mu V$).
- Second the probe is in contact with the sample with a probe-sample force of 100 nN. The variation of ΔV is recorded when the probe-sample contact is established. This voltage variation corresponds with the decrease of the probe temperature from T_{Pt} to $T_{Pt,IC}$.

Knowing the corresponding ΔT and P_p parameters from calibration, the thermal conductance of probe in contact with sample G_{ic} can be determined by the general equation $G = \frac{P}{\Delta T}$. The whole process of testing is presented in the form of a simplified diagram in **Figure II-9**.

It can be seen that $G_{ic} = G_s + G'_{env} + G_{wire}$, where G'_{env} is associated to the heat dissipated to the environment when probe is in contact with sample.

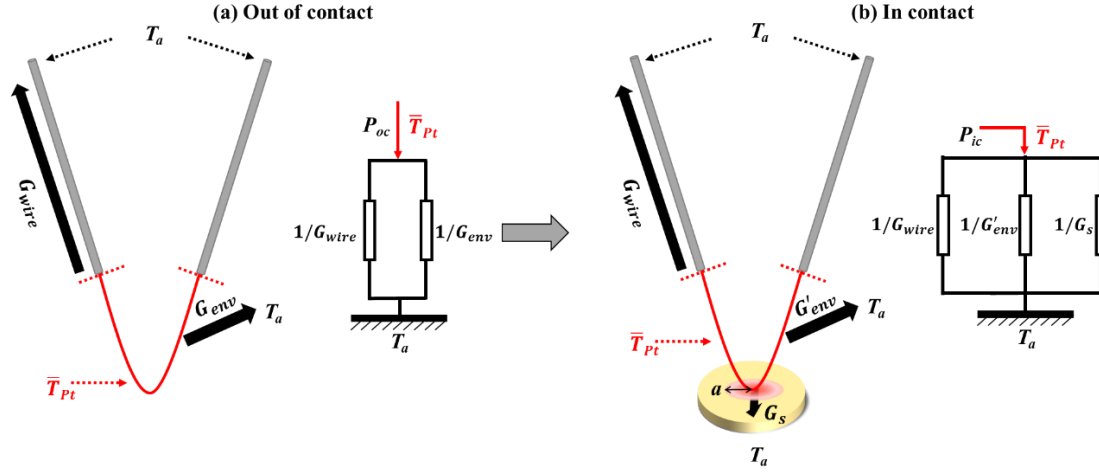


Figure II-9. The protocol of measurement and associated equivalent thermal conductance while the probe is out- and in- contact with sample.

Thus, G_S can then be given by Eq. II-6.

$$G_S = G_{ic} - G_{wire} - G'_{env} \quad (\text{II-6})$$

G_S is the parallel connection of the apex-sample contact thermal conductance G_C (associated to heat transfer between the Pt wire and the sample by conduction through the air, the water meniscus and through solid-solid contact) and thermal conductance of sample system G_{SS} , detailed analysis of probe thermal conductance network can be found in [76]. G_S can be expressed as:

$$G_S = \frac{G_{SS}G_C}{G_{SS} + G_C} \quad (\text{II-7})$$

In the case of diffusive samples, G_{SS} is proportional both with sample effective thermal conductivity k_{eff} and effective radius a of the thermal contact assumed discoidal (as exposed in **Figure II-9**), G_{SS} can be expressed as [74]:

$$G_{SS} = 4k_{eff}a \quad (\text{II-8})$$

One should note that in order to minimize the influence of the thermal drift; a flat and homogeneous Si sample is used as a reference sample. Each time before and after measuring

the studied sample, this reference Si sample is measured and used for the normalization of calculated thermal conductance. To take into account the diversity of sample surface and reduce the random error, for each sample, measurements are performed at 5 different points and repeated 10 times per point. Generally speaking, a larger number of experimental measurements can help to reduce the uncertainty associated with the measurements. This is because the more measurements we take, the more data we have to work with, and the more confident you can be in the results. The standard deviation tends to decrease, because we are getting a more accurate representation of the true value of the quantity we are measuring. However, it's important to keep in mind that simply taking more measurements is not always the best way to reduce uncertainty. In some cases, there may be systematic errors or other sources of uncertainty that cannot be reduced by taking more measurements. Additionally, it's important to make sure that the measurements are taken under consistent conditions, and that the equipment and methods used to take the measurements are reliable and accurate.

Hence standard deviation rather than extreme values of the measured ΔV was used while determining the error bar of the estimated thermal conductance.

II. C. 2. Calibration curve

II. C. 2. a) Case of the unbalanced Wheatstone bridge

For an unbalanced Wheatstone bridge as described in **section II. A. 2. a) Unbalanced Wheatstone bridge**, a constant I_p chosen according to the expected probe mean temperature is applied to the circuit. The variation of the probe electrical resistance between out of contact (balanced bridge) and in contact (unbalanced bridge) configurations can be calculated from: $\Delta R_{el,p} = \frac{\Delta V}{I_p}$, where ΔV is directly output by unbalanced Wheatstone bridge. G_{ic} then can be determined as explained above. Eq. II-9 is obtained by combining Eq. II-6 to Eq. II-8,

$$G_s = G_{ic} - G_{wire} - G_{env}' = \frac{4kaG_c}{4ka+G_c} = \frac{G_c}{1 + \frac{G_c}{4ka}} \quad (\text{II-9})$$

With the assumptions that a and G_c are invariable with k [77]–[80], G_s can be then plotted in function of $G_s = \frac{A}{1+\frac{B}{k}}$. However, it has already been demonstrated that this assumption is not valid when measurements are performed under ambient air conditions and the out of contact measurements are made while the probe is at a large distance of the sample surface (i.e., 2mm): notably a can strongly increase when k decreases [81], [82]. Additionally, there still is some heat flow from probe toward environment while probe is in contact with sample, which may make the hypothesis that $G_{env}' = 0$ not entirely correct. Consequently, a constant parameter C is added and a formula of type $G_s = \frac{A}{1+\frac{B}{k}} + C$ is currently used [74].

A series of bulk reference sample as shown in **Table II-2** with well-known thermal conductivities has been measured to establish the calibration curve. Thermal conductivity and roughness of these samples were measured with an uncertainty of 5% at the French National Laboratory (LNE) and at Czech metrology institute (CMI) respectively as described in [70]. A fitting curve using above form is demonstrated with the Wollaston probe used as shown in **Figure II-10** and can be used to find the effective thermal conductivity of studied samples (k_{eff}). The edge of red fill area around the fitting curve is calculated using the measured thermal conductance plus or minus uncertainty. Those uncertainty are caused by the measurement fluctuation. The point of germanium is out of curve due to the low sensitivity of SThM at the range of thermal conductivity more than 20 W/(m.K).

Table II-2. Thermal conductivity and roughness RMS of reference samples.

	Materials	Thermal conductivity k (W/(m.K))	Roughness RMS (nm)

1	Poly (methyl methacrylate)	PMMA	0.187	6.43
2	Acetal copolymer	POM-C	0.329	15.7
3	Borosilicate glass	Glass	1.11	1.90
4	Silica glass	SiO ₂	1.28	0.73
5	Zirconium dioxide	ZrO ₂	1.95	1.58
6	Zirconium dioxide and Magnesium oxide	ZrO ₂ /MgO	3.09	2.8
7	Titanium dioxide	TiO ₂	9.15	0.3
8	Germanium	Ge	52	0.57
9	Silicon	Si	148	1.47

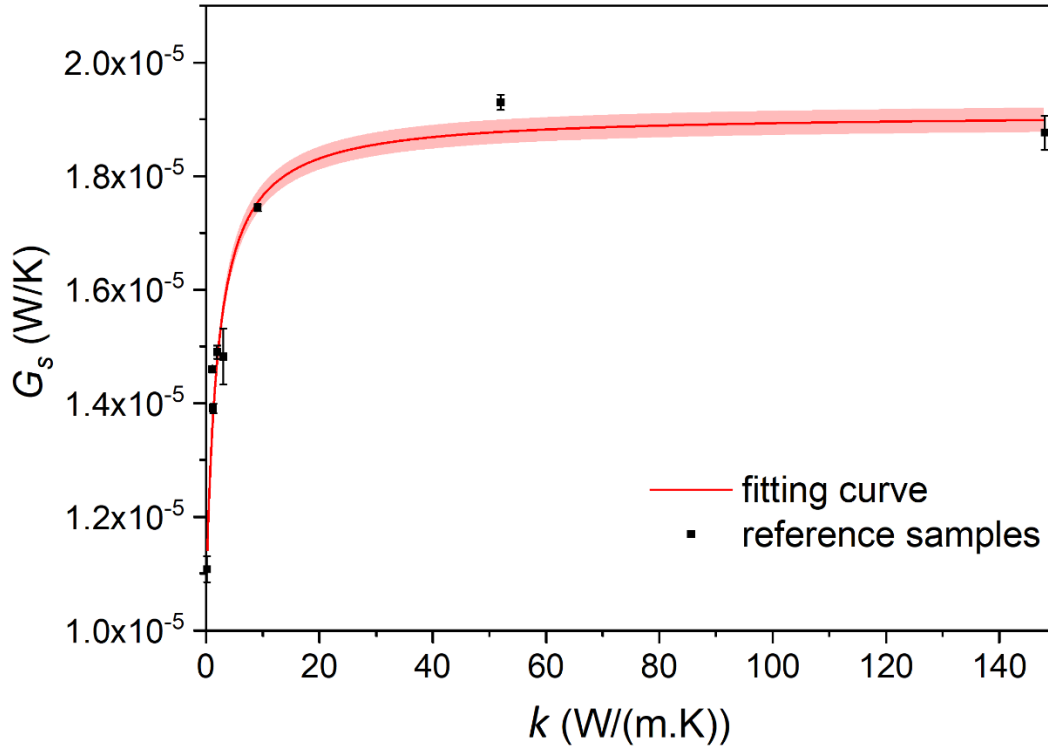


Figure II-10. Thermal conductance G_s in function of thermal conductivity k_{ref} . Fitting parameters are: $A = 8.38 \cdot 10^{-6}$, $B = 2.08$, $C = 1.07 \cdot 10^{-5}$. The red fill area indicates the uncertainty of reference curve.

II. C. 3. Model for balanced Wheatstone bridge

For a balanced Wheatstone bridge, the voltage difference $V_{ic} - V_{oc}$ represents the variation of the thermal conductance of the probe G between out of contact (G_{oc}) and in contact (G_{ic}) configurations:

$$G_{ic} - G_{oc} = \frac{P_{Pt-ic} - P_{Pt-oc}}{\Delta T} \quad (\text{II-10})$$

where $P_{Pt-ic} = R_{Pt} I_{ic}^2$ and $P_{Pt-oc} = R_{Pt} I_{oc}^2$ are the electrical power dissipated in the resistive element while the probe is out of contact and in contact with sample, respectively. For balanced Wheatstone bridge, ΔT is kept constant throughout the measurement. Eq. II-11 and II-12 can be calculated by further deduce Eq. II-10,

$$G_{ic} - G_{oc} = G_s + G'_{env} - G_{env} = \frac{G_c}{1 + \frac{G_c}{4ka}} + G'_{env} - G_{env} \quad (\text{II-11})$$

$$P_{ic} - P_{oc} = \frac{G_c \Delta T}{1 + \frac{G_c}{4ka}} + (G'_{env} - G_{env}) \Delta T \quad (\text{II-12})$$

Considering ΔT is a constant, with the same assumption that a and G_c are invariable with k . We may plot $P_{ic} - P_{oc}$ in a curve with the shape $P_{ic} - P_{oc} = \frac{A}{1 + \frac{B}{k}} + C$, which can be used in the probe calibration for thermal conductivity measurements [74].

Figure II-11 gives the calibration curve experimentally obtained using our SThM with a selected series of bulk reference samples with well-known thermal conductivity in the range 0.187-1.28 W/(m.K) and well-known roughness (lower than 15 nm) [83]. This range is selected specially for studying polymeric material due to that for most polymer the k is low, in the range of 0.1 to 0.5 W/(m.K) [17]. The good fitting of experimental data using the above formula is demonstrated. The corresponding curve was used to find the effective thermal conductivity of the studied samples (k_{eff}) in **Chapter IV** and **V**.

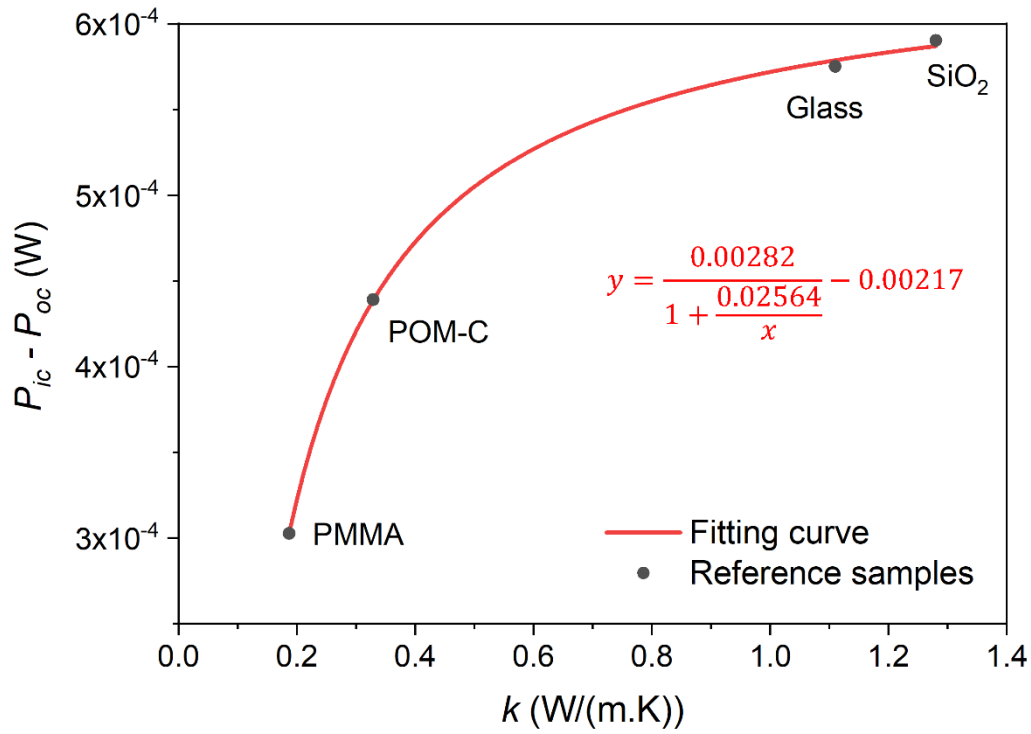


Figure II-11. Calibration curve obtained experimentally from the measurement of reference samples [83]: PMMA ($k_{PMMA} = 0.187 \text{ W} \cdot \text{m}^{-1} \cdot \text{K}^{-1}$), POM-C ($k_{POM-C} = 0.329 \text{ W} \cdot \text{m}^{-1} \cdot \text{K}^{-1}$), Glass ($k_{Glass} = 1.11 \text{ W} \cdot \text{m}^{-1} \cdot \text{K}^{-1}$) and SiO₂ ($k_{SiO_2} = 1.28 \text{ W} \cdot \text{m}^{-1} \cdot \text{K}^{-1}$). The equation in red is the expression of the fitting curve of the measurements.

II. C. 4. Measurement protocol for imaging

Systematical topography analysis is important for properly interpreting the SThM measurements. On one hand, thermal contact radius a and G_c strongly depend on the mechanical contact between the probe and the sample's surface, which can be affected by its roughness [84]. In order to make the hypothesis that a and G_c are constant as valid as possible, the selected area with a flat surface is preferable for measuring accurately the thermophysical properties of the samples without topography artifact. On the other hand, it has been well demonstrated in literature that the heat dissipation towards samples strongly depends on the contact area and the air gap between probe and sample [85]–[87]. To avoid the artificial thermal signal variation induced by such effects in our measurements, the thermal and topography images of samples were performed simultaneously with the same Wollaston probe at scanning frequencies of 0.1-0.4 Hz, which ensures that the scan time for each pixel is much

larger than the thermal response time of the probe (which is 1 ms). The scan was performed on an area of $100 \mu\text{m}^2$ initially to obtain the overall information of sample surface. For the samples that show a mismatch between the topography and the thermal image, additional investigation was performed on the interested zone using a smaller scan area size, allowing to avoid topography artifact in the thermal signal. To study the thermal conductivity of a specific area, an average value of in contact voltage (V_{ic}) for balanced TCU inside a square containing at least 25 pixels was recorded. For the case of the samples with homogeneous k_{eff} distribution, five of such squares with low roughness were selected and taken into average.

II. D. SThM measurement modelling – bulk and two layered samples

Calibration curves are used to determine the k_{eff} of any unknown sample. In the case of bulk materials, we identify directly the sample thermal conductivity in this way.

For an unknown material in form of a thin layer deposited on substrate a model is required to derive from the measured k_{eff} the thermal conductivity of interested layer k_1 . The model that we used (given in detail in Appendix 1) is based on the Drydren model [88] and expresses the sample thermal resistance $R_{th,s}$, see Eq. II-13. It is specifically adapted to thick substrate that can be assumed semi-infinite (**Figure II-12**) and takes into account the thermophysical properties of the sample components (k_1 and k_{sub} the thermal conductivity of the film and the substrate respectively) and interfaces ($R_{th,i}$, interface thermal resistance) between them. It also takes into account the sample heating process, i.e. the fact of measurements was performed at the steady state and involved a small heating source at the sample surface. This source is described as a hot disc with radius a in Eq. II-13.

$$R_{th,s} = \frac{1}{\pi k_1 a} \int_{\xi=0}^{\infty} \frac{1 + Ke^{-2\xi t_{eff}/a}}{1 - Ke^{-2\xi t_{eff}/a}} J_1(\xi) \frac{\sin(\xi)}{\xi^2} d\xi \quad (\text{II-13})$$

With $t_{eff} = t + R_{th}k_1$ where t is the film thickness, $K = \frac{1 - \frac{k_{sub}}{k_1}}{1 + \frac{k_{sub}}{k_1}}$, J_1 is

the Bessel functions of the first kind of order 1.

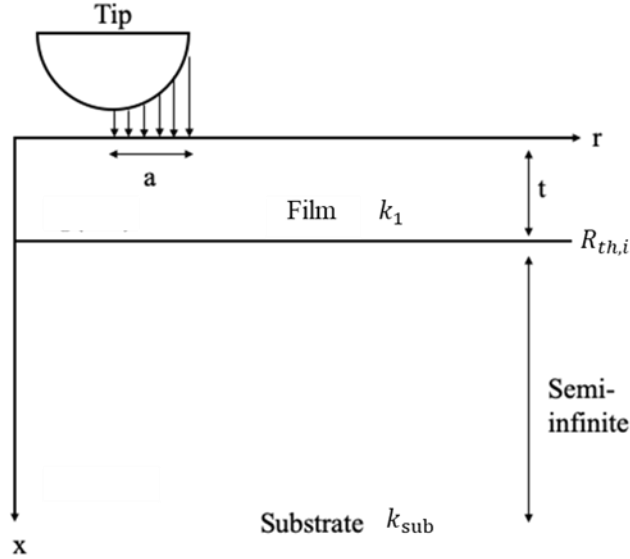


Figure II-12. Contact spot of radius a , on an infinite half-plane with surface coating of thickness t .

The information of this model can be found in Appendix 1. For the post-treatment of experimental data, a Matlab code was established.

II. E. Summary

This chapter introduced and detailed the experimental setup used for the thermophysical characterization of the samples that were studied in this thesis. Mainly, the SThM measurement setup alongside the calibration and thermal conductivity protocols used in this work are presented.

Because Wollaston probes are not reproducible, each probe must be calibrated. The probe calibration consists of three steps: (1) a temperature calibration, (2) an electrical calibration and (3) a thermal conductivity calibration while the probe is in contact with reference samples. Both the calibration steps (1) and (2) allows the determination of the

thermoelectric and thermal properties of the probe resistive sensor while the probe is out of contact with a sample. Through the temperature calibration, the relationship between temperature and electrical resistance of probe is established. While the electrical calibration goes on monitoring the variation of electrical resistance of probe in function of the electrical power dissipated on it. The thermal conductivity calibration and its associated model provides the calibration curve to be used for the determination of the thermal conductance G_s or the effective thermal conductivity k_{eff} of an unknown sample. In case of a bulk sample, the material thermal conductivity equals k_{eff} .

The ion implanted amorphous CrSi_2 samples that were measured are not bulk samples but are in shape of thin films on a substrate. The modelling used to derive the film thermal conductivity from G_s or k_{eff} (determined with the calibration curve) is then also provided for this geometry of samples.

The following **Chapter III** gives and analyses the results that we obtained on ion implanted amorphous CrSi_2 samples. **Chapters IV** and **V** concerns those obtained on the polymeric nanocomposites studied in the thesis.

Chapter III. THERMAL CHARACTERIZATION OF ION IMPLANTED CrSi₂ THIN FILMS

This chapter analyses the effect of ion implantation on the heat conduction within a chromium disilicide (CrSi₂) material. A part of the analysis has been published as *Ion implantation effects on the microstructure, electrical resistivity and thermal conductivity of amorphous CrSi₂ thin films* on Journal of Materials Science, 2022, 57(2): 1174-1185. This work was performed in collaboration with M. M. Timm (from the Physics Institute of UFRGS, in Brazil), who fabricated the sample and performed the microstructure and electrical resistivity characterizations of samples.

III. A. Context

Transition metal (TM) silicides have favorable physical properties: thermal and structural stability, high electrical conductivity and thermoelectric power at elevated temperature, and natural abundance of their constituent elements, that make them suitable for applications in Si-based microelectronics [89], ceramics [90], spintronic [91], and thermoelectricity [92], [93]. Among them, CrSi₂ that is a degenerate p-type semiconducting material with a high electrical conductivity ($\sigma \sim 1.2 \text{ m}\Omega\cdot\text{cm}$ at 300 K) has been considered for a wide range of applications, from electro-optic interconnects [94], Schottky junctions [95], [96], to IR detection devices [97], [98]. Furthermore, CrSi₂ is chemically and thermally stable at high temperatures and its constituent elements are naturally abundant and non-toxic. Combined with its high electrical conductivity and medium Seebeck coefficient ($S \sim 110 \text{ }\mu\text{V/K}$ at 300 K), crystalline CrSi₂ has become an engaging material for potential use in thermoelectric applications [99]–[102]. However, CrSi₂ in its crystalline form has a high thermal conductivity ($k \sim 16 \text{ W/(m}\cdot\text{K)}$ [103] at 300 K), which negatively affects its figure of merit ZT and hinders its use as practical thermoelectric devices [99], [104].

Many studies have been performed in single and polycrystalline CrSi₂, including bulk and thin films. It has been shown, for example, that the electrical properties of CrSi₂ are pretty

sensitive to variations in the composite stoichiometry [105], deposition methods [106], [107], thermal treatments [19], and the nature of the substrate [109], [110]. Most these studies have focused on crystalline CrSi₂.

In its amorphous form, CrSi₂ should also present interesting behaviors. As an example, ZT increasing was accomplished in Cu-Ge-Te, NbO₂, In-Ga-Zn-O, Zr-Ni-Sn, Si-Au, and Ti-Pb-V-O amorphous systems [111]. Naturally, amorphous thermoelectrics give rise to extensive phonon scattering, which is still a challenge for crystalline thermoelectrics. It has been suggested that some amorphous semiconductors can attain good thermoelectric properties due to their modest to good electrical conductivity (σ) and poor thermal conductivity (k), improving the σ/k ratio as required by the energy conversion figure of merit [112]–[114]. A bright future is expected for these materials. Another main benefit of amorphous materials is that they can be deposited using common fabrication techniques such as sputtering at room temperatures.

In this sense, we have explored heat transfer in amorphous CrSi₂ and the use of ion implantation to modify its electrical and thermal properties. The combination of ion implantation and *in-situ* or *ex-situ* thermal treatments indeed allows tailoring several properties of semiconductors. This includes not only the electrical conductivity [115]–[117] but also the microstructure configuration to provide, for example, impurity gettering [118], [119], end-of-range defect engineering [120], or even strain relaxation effects [121], [122]. Ion beam modification techniques are explored to improve crystalline materials' electric and thermal properties via doping or by forming point and extended defects to act as phonon scattering centers, thus reducing the phonon contribution to the thermal conductivity. However, for amorphous materials, the situation is different. Ion implantation can still be used for doping, but the microstructure modification requires a different approach. Amorphous materials provide an extra degree of freedom concerning ion implantation experiments. Since the ion implantation/irradiation processes can occur at non-thermal equilibrium conditions, it allows modifying the compaction degree of the amorphous lattices or enables the formation of crystalline clusters and even the promotion of complete recrystallization resulting in a highly defective crystal lattice.

In this chapter, the influence of different ion species and implantation conditions on the thermal conductivity k of amorphous CrSi_2 thin films is investigated. The effects on the microstructure and electrical properties were also characterized [123] and provides some information that can be used to interpret thermal property results.

The implants were done at different fluences in substrates that were kept at room temperature or heated at 250 °C. The microstructure of the samples was characterized via transmission electron microscopy (TEM) and scanning transmission electron microscopy associated with energy dispersive X-ray spectroscopy (STEM-EDX). We also use Electrical Resistivity and Scanning Thermal Microscopy (SThM) measurements to assess electrical and thermal conductivities of the samples. The discussions consider Ne as an inert element and how the matrix responds to the implantation-induced atomic displacements, causing, for example, the formation of nanosized Ne bubbles and CrSi_2 crystallites. Al is a common dopant in crystalline CrSi_2 . Here we investigate its doping and irradiation effects throughout the amorphous CrSi_2 films. The results obtained demonstrate that the ion implantation/irradiation process causes significant modifications to the electrical and thermal properties of amorphous CrSi_2 thin films.

III. B. Sample description

III. B. 1. Sample preparation

CrSi_2 amorphous films with an average thickness of 260 nm were deposited on Si (100) substrates by radio-frequency magnetron sputtering technique in a high vacuum chamber (base pressure of 2×10^{-6} mbar) with a high purity CrSi_2 target (3", 99.95%, Neyco) using an experimental protocol developed previously [124]. The sputtering targets were operated at 120 W under a pressure of 0.51 Pa with a high purity Ar flow (99.99%). A SiO_2 sublayer with a thickness of 25 nm was deposited by sputtering before the CrSi_2 layer. The schematic of the sample geometry is shown in **Figure III-1**. The depositions were done at room temperature

with a multi-target Plassys MP4505 equipment available at the “Centrale de Technologie de Montpellier” (CTM, Montpellier University, France).

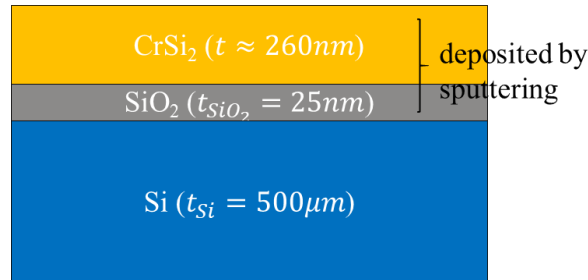


Figure III-1. Schematic of studied CrSi₂ samples.

One series of samples contains Ne implants in a uniform concentration-depth distribution. A second sample series has Al implants at distinct energies, calculated to produce a uniform concentration-depth distribution along with the film (details are given in **Table III-1**). The Ne and Al implants were done at room temperature and at 250 °C. The fluences of the Ne and Al implantations at 250 °C were adjusted to produce similar damage levels, computed in displacement per atom (dpa) units [125]. The implantation profiles and fluences, simulated using the SRIM code [126], lead to atomic concentrations of ≈ 0.008 at.% for Al (room temperature implantation), of ≈ 0.64 at.% for Al (250 °C implantation) and ≈ 1 at.% for Ne. All the implantation experiments were done using a 500 kV HVEE ion implanter (Laboratório de Implantação Iônica, Instituto de Física, UFRGS Brazil) maintaining the beam current below 500 nA/cm² to avoid the heating of the substrate that could affect the sample microstructure. The sample's temperature during implantations was kept constant, feedback-controlled using a type K thermocouple and a Tantalum resistance attached to the sample holder. **Table III-1** summarizes the implantation parameters.

Table III-1. Ion implantation parameters

Ne		Al			
Room Temperature and T=250 °C		Room temperature		$T = 250 \text{ }^\circ\text{C}$	
Energy	Fluence	Energy	Fluence	Energy	Fluence

(keV)	(at/cm ²)	(keV)	(at/cm ²)	(keV)	(at/cm ²)
250	1x10 ¹⁶	200	1x10 ¹⁴	200	8x10 ¹⁵
120	7x10 ¹⁵	90	4.5x10 ¹³	90	3.6x10 ¹⁵
50	4x10 ¹⁵	40	1x10 ¹³	40	8x10 ¹⁴
20	1.5x10 ¹⁵	30	1x10 ¹³	30	8x10 ¹⁴
Concentration (at.%)					
~1.0		~0.008		~0.64	

The various techniques that were used to characterize the samples [123] are given in Appendix 3. In the next section, the characterization results gotten on microstructure and electrical resistivity are presented. They are essential for the interpretation of the variation of the thermal conductivity measured as a function of the implantation conditions and understand the heat transport in our CrSi₂ samples. As reminded in **Chapter I** the microstructure of a material indeed influences the mean free path of energy carriers, which include electrons for CrSi₂, and the contribution of electrons to heat conduction can be calculated following the Wiedemann- Franz law from the material electrical resistivity.

III. B. 2. Microstructure of samples

III. B. 2. a) *As deposited (or pristine) CrSi₂ film*

Figure III-2 (a) shows cross-section TEM micrographs of the as-deposited, non-implanted CrSi₂ sample. The film was deposited over a Si wafer layered with a 25 nm SiO₂ layer. The S white arrow (in **Figure III-2** (a)) points to the surface of the film. The thickness of CrSi₂ film is approximately indicated as 269 nm. For the focused ion beam (FIB) sample preparation, the film was covered by a thin carbon layer and then by a Pt film also appearing in the micrograph. The CrSi₂ film deposition process results in columnar structures due to the low

mobility of the atoms adsorbed by the substrate surface during the sputtering deposition process. This type of growth is predicted for room temperature depositions by the Thornton model [127], [128]. The crystallinity of the CrSi₂ samples considered in this study was assessed via the Selected Area Electron Diffraction (SAED) technique. **Figure III-2** (b) shows the SAED pattern from the CrSi₂ film depicted in **Figure III-2** (a). In cross-section TEM specimens, SAED measurements are sensitive to the formation of small crystallites with characteristic dimensions above 1 nm. The observation of a diffuse and broad ring pattern indicates that the sample can be considered amorphous within the sensitivity level of the technique. It is also worth to mention that the diffuse ring is corresponding to the metallic glasses local atomic structure rather than oxide glasses (such as SiO₂) whose SAED pattern is a halo ring adjacent to the central beam spot as shown in [129]. Similar electron diffraction pattern is observed for amorphous metal structure [130]. It is generally believed that the atomic arrangements of metallic glasses follow a certain regular manner i.e., short-range order and medium-range order. Despite of the classification of crystalline phases as a p-type semiconductor, the amorphous CrSi₂ is described as an amorphous metal with a higher carrier concentration due to its metallic like behavior of conductive properties [131]. In fact, CrSi₂ could be fabricated through mechanical alloying procedure [132]. Therefore, the amorphous CrSi₂ studied in this work is considered as an amorphous metal where both electrons and phonons will be regarded as the energy carriers responsible for heat transfer.

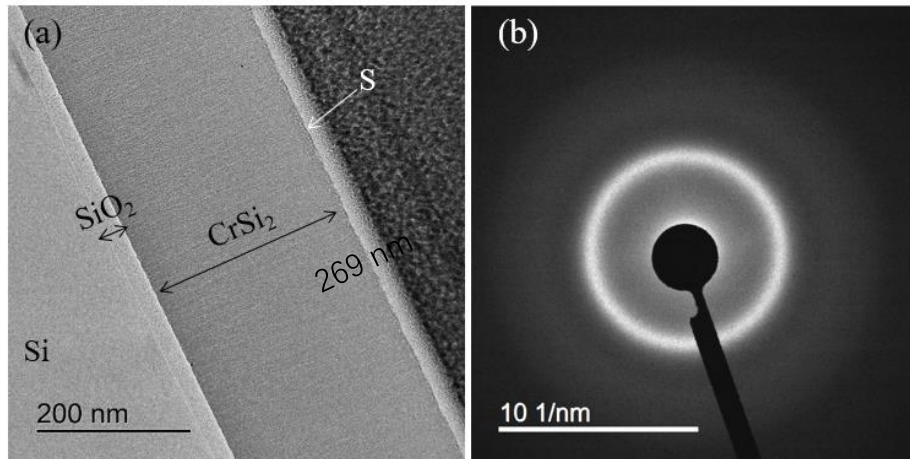


Figure III-2. (a) Cross-Section-TEM micrograph showing the as-deposited CrSi_2 thin film, where the S vector points to the surface of the film. The Si substrate and the SiO_2 layer are also indicated in the image. (b) SAED pattern of the as-deposited CrSi_2 sample shown in (a).

III. B. 2. b) *Samples implanted at room temperature*

Figure III-3 (a) and (b) show cross-section TEM micrographs of room temperature (RT) Ne and Al implanted CrSi_2 samples. The Ne implantation to a concentration of ≈ 1 at.% triggered the formation of a dense array of Ne-filled cavities (i.e., bubbles) distributed throughout the film (white disks surrounded by a dark ring produced by bright-field under focus imaging conditions). We can infer from **Figure III-3** (a) that Ne bubble formation preferentially occurs along with the columnar structures of the film. The Al implantation to a concentration of ≈ 0.008 at.% (**Figure III-3** (b)) does not affect the columnar structure arrangement. Also, it does not cause any other observable microstructure modification concerning the pristine structure shown in **Figure III-2** (a). The approximate thickness of CrSi_2 layers can be inferred from TEM images.

The scattered points in **Figure III-3** (c) and (d) represent the EDX signals for Ne and Al as a function of distance along with the film, respectively. The dash-dotted lines correspond to the Ne and Al concentration-depth profiles predicted by SRIM simulations [126]. The EDX measurements indicate that the concentration-depth profile of the implanted Ne ions did not diffuse much into the CrSi_2 layer due to the trapping of Ne by bubbles. Differently, Al has diffused along with the film due to implantation enhanced diffusion and knock-on by successive

ions. The corresponding SAED patterns of Ne and Al implanted samples (not shown) remain similar to the one in **Figure III-2** (b). These measurements indicate that the RT implantations preserved the amorphous structure of the film. Another notable aspect worth mentioning is that the implanted depth shown in EDX signals -depth profiles is larger than corresponding CrSi₂ layer thickness, particularly for Ne implanted sample (**Figure III-3** (c)). This suggests that the interface between CrSi₂ layer and SiO₂ and a part of the SiO₂/Si substrate is also implanted.

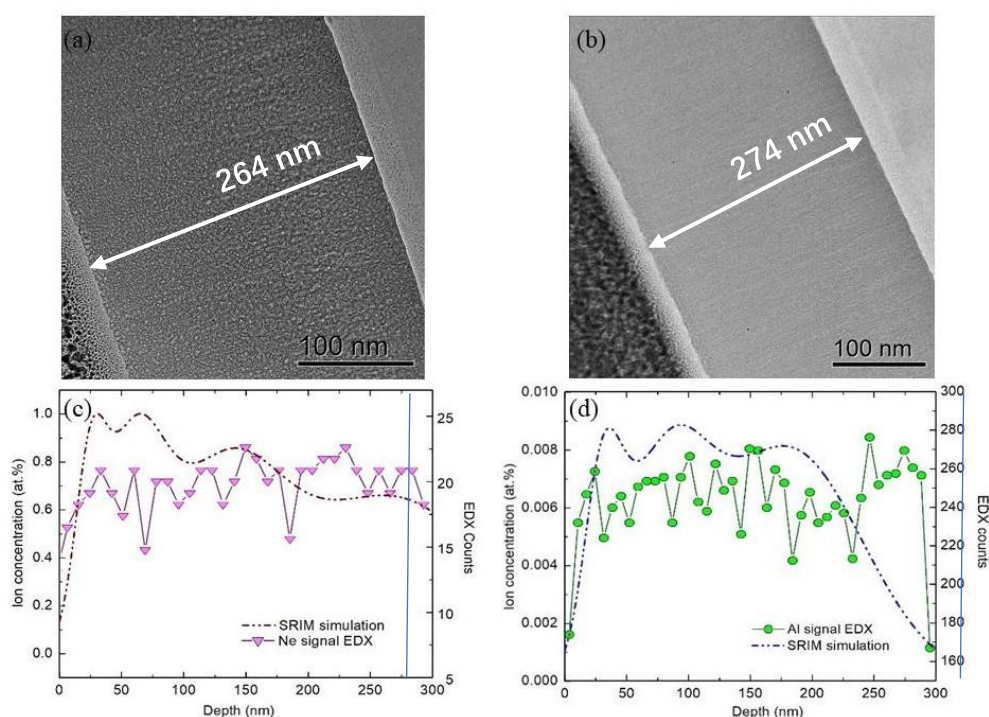


Figure III-3. Cross-section TEM micrograph for the CrSi₂ sample implanted at room temperature with (a) Ne and (b) Al. EDX spectrum appears superimposed with SRIM ion concentration-depth-profile simulation for (c) Ne and (d) Al implantation.

Inert gases have an extremely low solubility limit and tend to agglomerate into more stable gas-vacancy complexes leading to bubble formation [133]–[135]. The same behavior also occurs in amorphous structures where the concept of vacancies correlates with small free volume pockets in the network structure [136]. The resolution limit for under-focus phase-contrast imaging conditions in TEM observations is about 0.7 nm. Therefore **Figure III-3** (a) reveals only the visible bubbles, coarsened by getting additional Ne atoms or by interacting with other surrounding bubbles via, for example, irradiation-induced bubble migration and

coalescence process [137]. The same atomic mobility behavior discussed for the Ne atoms may also occur for the Al implanted sample. In this case, the atomic mobility can be inferred by the difference in the Al concentration-depth profile measured by EDX and predicted by the SRIM code (**Figure III-3 (d)**).

III. B. 2. c) Ne implanted CrSi₂ at 250 °C

The effects of the Ne implantation at 250 °C in the CrSi₂ film structure can be inferred by the TEM micrographs presented in **Figure III-4 (a)**, which shows that the implantation effects are quite similar within the entire film thickness.

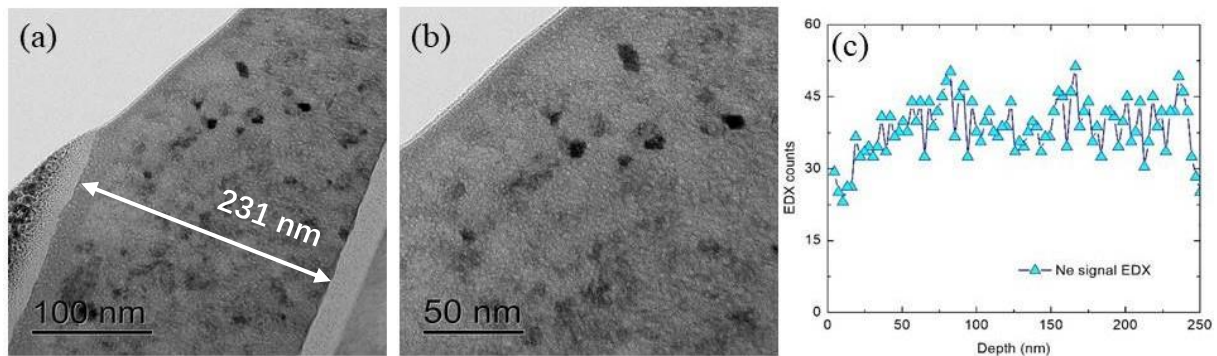


Figure III-4. (a) Cross-section TEM micrographs of the CrSi₂ sample implanted with Ne at 250 °C; (b) same sample at a higher magnification and (c) Ne EDX profile as a function of distance in the film.

Figure III-4 (b) shows an enlarged micrograph from a region of **Figure III-4 (a)**. This figure better illustrates the presence of crystal grains (darker domains obtained via bright field diffraction contrast) and the homogeneously dispersed Ne bubbles (depicted in bright field under focus imaging conditions). The micrograph also suggests that the columnar grain structure has been smoothed out. These features are quite distinct from those observed for the RT implantation case (**Figure III-3 (a)**). **Figure III-4 (c)** shows the EDX measurement for Ne distribution as a function of distance in the film. The depth-distribution of the Ne content is very similar to the one obtained by implantation at room temperature (**Figure III-3 (c)**). As previously stated, the same occurrence of implantation depth exceeding sample thickness also takes place in the sample implanted at 250 °C.

We can infer from **Figure III-4** (a) and (b) that, for implantations at 250 °C, a significant fraction of the amorphous structure has been transformed into randomly oriented crystallites with diameters from 5 to about 20 nm. This phenomenon is also evidenced by the dense ring-like distribution of diffraction spots in the SAED pattern presented in **Figure III-5** (a). The ring pattern is well fitted using the hexagonal structure of the CrSi_2 crystal lattice (space group $P6_222$, lattice parameters $a = 4.42758 \text{ \AA}$ and $c = 6.36805 \text{ \AA}$, Wyckoff positions $3d$ (Cr) and $6j$ (Si)) [138]. The (h, k, l) index of the rings is presented in the figure. Additional rings formed by rather weak spots are observed, showing that other phases have been produced in a minor volume fraction. **Figure III-5** (b) shows a dark field TEM micrograph produced by selecting a spot from the innermost ring of the SAED pattern. The dark-field micrograph was taken in the same region as the bright-field ones from **Figure III-5** (a) and (b).

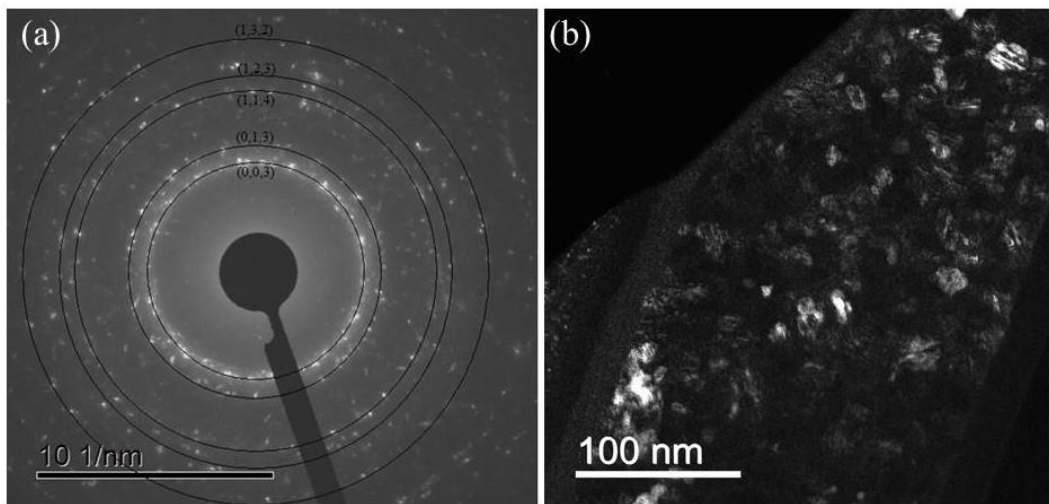


Figure III-5. (a) SAED pattern superimposed with the theoretical planes of crystalline CrSi_2 . (b) Dark Field contrast micrograph from the same area shown in Fig. 3(a) of the CrSi_2 sample implanted with Ne at 250 °C.

It seems worth noting that the Ne implantation at 250 °C induced local crystallization reactions at a temperature about eighty degrees lower than the crystallization temperature $T = 327 \text{ °C}$ expected by thermal treatments [139]. This phenomenon is typically expected in ion implanted/irradiated samples and is usually interpreted as a radiation-enhanced phase transformation process [140]. The formation of a dense array of nanocrystallites is probably connected to the bubbles and the remaining columnar grain boundaries, which may act as

inhomogeneous nucleation sites for the amorphous-crystalline phase transition.

III. B. 3. Thickness characterization

The thicknesses of all five samples were identified from TEM images directly and summarized in **Table III-2**. Due to the utilization of sputtering technology, the sample thickness distribution is not entirely uniform with an uncertainty of roughly 30 nm.

Table III-2. Thickness of CrSi₂ film

Sample	CrSi ₂	CrSi ₂ Ne RT	CrSi ₂ Ne 250 °C	CrSi ₂ Al RT	CrSi ₂ Al 250 °C
<i>t</i> (nm)	269	264	231	274	260

III. B. 4. Electrical resistivity measurements

The electrical resistivity ρ measurements on implanted and non-implanted CrSi₂ thin layers were carried out between 80 K and 330 K with a magnetic field of 0.5T by the Van der Pauw method. The electric contacts were made using In droplets, and the measurements were done with an Ecopia HMS 5000 four-point probe equipment (CTM, Université de Montpellier, France).

Figure III-6 shows the electrical resistivity ρ measurements as a function of temperature T for the as deposited and implanted samples. The behavior of the $\rho(T)$ curve for the as-deposited sample is in good agreement with previous measurements in CrSi₂ [138], [141].

The $\rho(T)$ curves for the RT Ne and Al implantations present a shift towards lower ρ values compared to the one of pristine CrSi₂. The curves show similar temperature dependence to the pristine deposited film for the measured temperature range from 60 to 330 K. The

electrical resistivity values for the Ne implantation at 250 °C are about 70% larger than the as-deposited film value (**Figure III-6**). And the Al 250 °C case presents similar electrical resistivity values. The detailed discussion and explanation could be checked in [142].

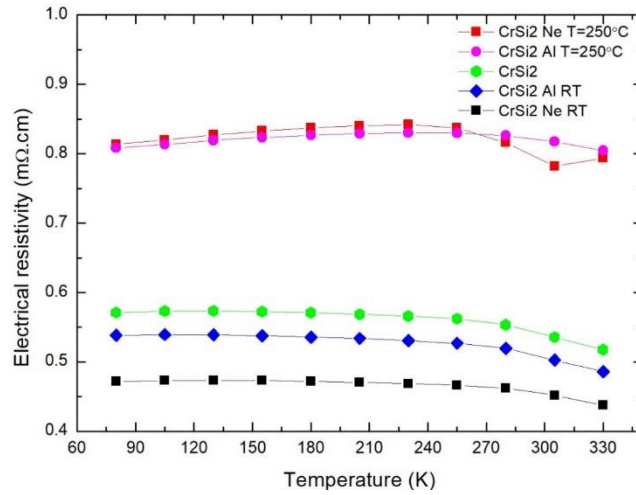


Figure III-6. Electrical resistivity ρ measurements as a function of the temperature of as deposited and implanted CrSi_2 samples. The lines serve as a guide for the eyes. Measurements error bars are within the symbol size.

III. B. 5. Roughness measurement

The root mean square (RMS) roughness (R_q) of sample surface plays an important role on the heat transfer through the mechanical contact between the SThM probe and the sample [84]. Large roughness may reduce the contact thermal conductance. At roughness levels close to 10 nm, the reduction in thermal conductance at the microcontact level can be as high as 90%, while at the nanocontact level, it can reach approximately 50%. It has been discovered that heat transfer is not limited to diffusion, but that ballistic or boundary-limited heat conduction may also be present [84]. In order to estimate the possible influence on the SThM measurement, the determination of the CrSi_2 sample roughness was first performed with a NT-MDT AFM operated in the contact mode and with a SHOCONA AFM probe. The measured areas were chosen to cover the typical surface features for SThM measurement on each sample. The measurement was conducted at an area of size 1×1 , 2×2 and $20 \times 20 \mu\text{m}^2$, separately. Three images were scanned at different locations for the size $2 \times 2 \mu\text{m}^2$ because this size is

more representative of the real point measurement contact area while using a resistive probe. Results after the AFM analysis are shown in **Table III-3**, where **Sq** represents the root mean square roughness of the scanned area. This parameter **Sq** is an extension to a plane of the equation of **Rq** and given as:

$$Sq = \sqrt{\frac{1}{A} \iint_A Z(x, y)^2 dx dy} \quad (\text{III-1})$$

Data presented in bold are the average values calculated on the three measurements obtained on $2 \times 2 \mu\text{m}^2$.

By comparing the **Sq** averaged values of all 5 samples, it can be summarized that all the samples have a smooth surface (**$Sq \approx 1 \text{ nm}$**) and the difference between each sample is less than 1 nanometer. Therefore, the hypothesis that the impact of roughness on mechanical contact between probe and sample is neglectable is proposed according to the results in [84].

Table III-3. Roughness of samples where *std* is the standard deviation.

	Image n°	Area [μm^2]	CrSi ₂	CrSi ₂ Ne RT	CrSi ₂ Ne 250 °C	CrSi ₂ Al RT	CrSi ₂ Al 250 °C
Sq [nm]	1	1x1	1.35	0.67	1.50	1.34	1.01
Sq [nm]	2	2x2	1.64	1.11	1.58	1.14	1.18
Sq [nm]	3	2x2	1.45	0.74	1.55	0.85	1.41
Sq [nm]	4	2x2	1.37	0.80	1.57	1.68	1.36
Sq [nm]	5	20x20	2.90	0.85	5.00	2.75	4.22
Sq avg [nm]			1.49	0.88	1.57	1.23	1.32
std_{Sq} [nm]			0.11	0.16	0.01	0.35	0.10

III. C. Thermal conductivity determination

Following the structural characterization of the samples, SThM measurements were used in order to assess their thermal conductivity. Subsequently, calibrated SThM probes were

used to measure the effective thermal conductivity of CrSi₂ samples, which is still influenced by the substrate, contact resistance, etc. The analytical model used to extract the thermal conductivity of CrSi₂ layer separately is given in **Chapter II** and detailed in Appendix 1. This model depends on many parameters describing the experiment configuration (sample and heating source geometry and sample thermal properties). In the following section, the details of each step followed to get the value of these model parameters are given. The sensitivity of the thermal conductivity of CrSi₂ samples determined by model to each input parameter will also be discussed.

III. C. 1. Effective thermal conductivity measurement

SThM in ambient air conditions using the Wollaston wire probe operated in active mode was used to characterize the thermal conductivity k of the CrSi₂ films. The unbalanced TCU as described in **section II. A. 2. a) Unbalanced Wheatstone bridge** was used and the point measurement methodology was applied. The calibration, measurement and reference curve establishment procedure have already been explained in detail in **Chapter II**. The measured thermal conductance (G) results of reference samples are plotted in function of their thermal conductivity in **Figure III-7**. The uncertainty is due to a large number of repetitions. Eventually, the effective thermal conductivity (k_{eff}) of CrSi₂ samples can be derived from the SThM signal measured on CrSi₂ samples and a reference curve that is obtained by fitting the SThM signal measured on reference samples of thermal conductivity differing as described in **Chapter II**.

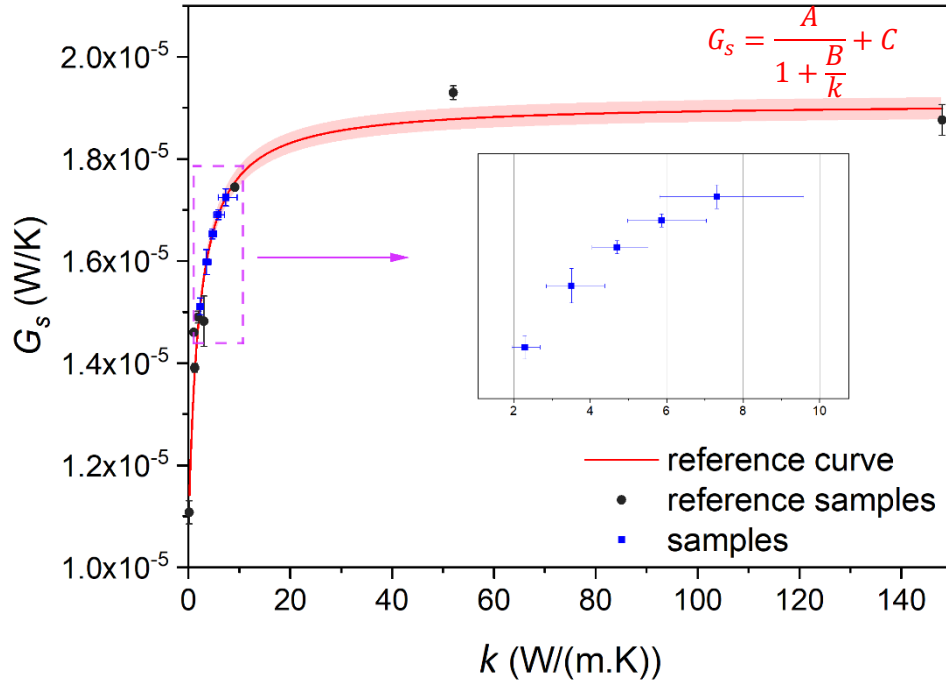


Figure III-7. Measured thermal conductance G_s in function of thermal conductivity k . The embedded image is an enlarged display of CrSi₂ samples results. Reference curve fitting parameters are: $A = 8.38 \cdot 10^{-6}$, $B = 2.08$, $C = 1.07 \cdot 10^{-5}$. The red fill area indicates the uncertainty of reference curve.

Results are shown in **Figure III-8**, where diamond shapes represent data for each repetition of measurement. Error bars are the standard deviation of all repetitions for each sample. The curves at the right of the mean values are the representation of the distribution of the experimental data. It can be noticed that the samples annealed at 250 °C have a narrower distribution of data and the standard deviation is significant smaller compared to pristine sample or RT implanted ones. One possible reason could be that the annealing may homogenize the thickness or defects of the samples due to the promotion in the mobility of defect when implanted at high temperature [143].

It is worth to mention that the effective thermal conductivity of the samples under investigation k_{eff} is that of a sample composed with three layers. It includes the information about the heat conduction within the CrSi₂ material in addition to the contribution of the sputtered SiO₂ layer and Si substrate as well as the interfacial thermal resistances between the layers. Therefore, a simulation model for two layered system mentioned in **section II. D SThM**

measurement modelling – bulk and two layered samples is applied using Matlab to extract the thermal conductivity of the studied CrSi₂ film separately.

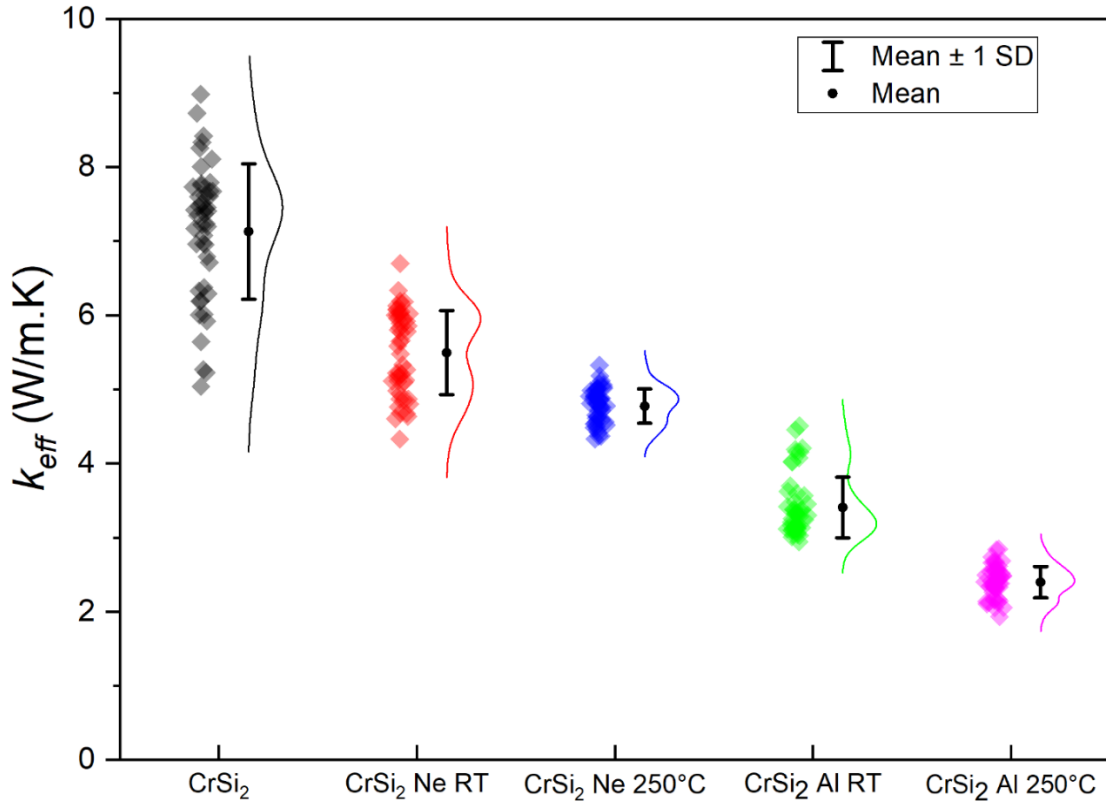


Figure III-8. Effective thermal conductivity of CrSi₂ samples. Diamond shapes represent data for each repetition of measurement. Error bar is the standard deviation (SD) of all repetition of each sample. The solid curves represent the distribution of the experimental set of data.

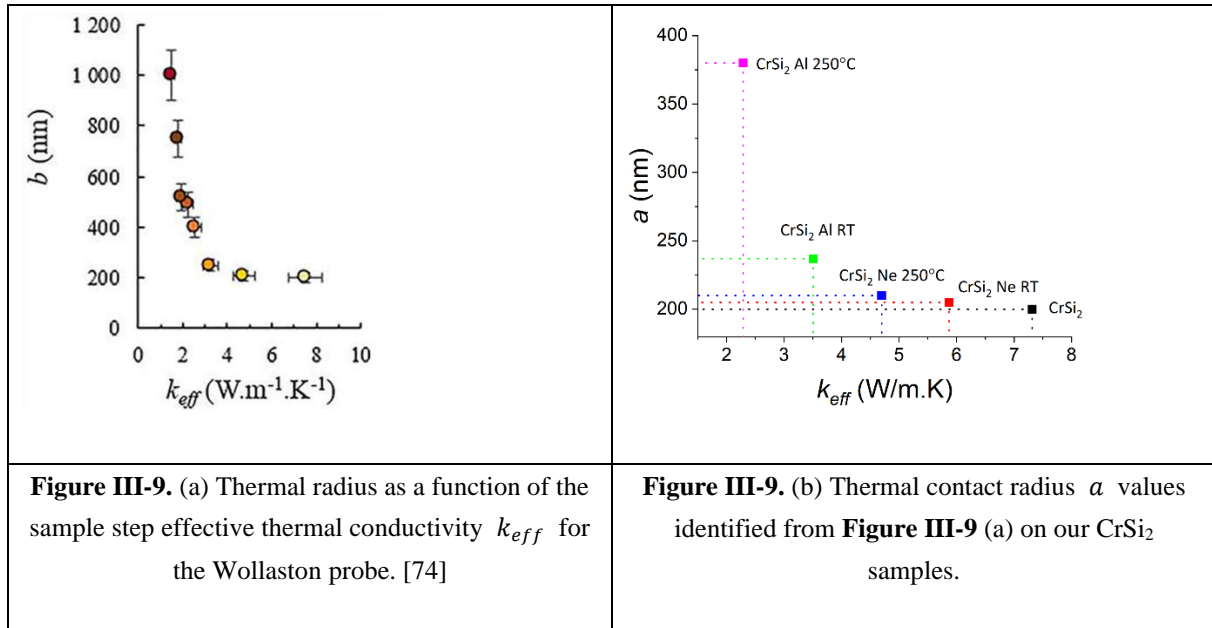
In this model, the thermal resistance of CrSi₂ layer ($R_{th,sample}$ (K/W)) is determined by:

$$R_{th,sample} = \frac{t}{k \times A} \quad (\text{III-2})$$

where t (m) represents the thickness of CrSi₂ film, k (W/(m.K)) is the thermal conductivity of CrSi₂ film and A is the cross-sectional area (m²) perpendicular to the path of heat flow. Hence, t and A are two of the required input parameters of the model (more details can be checked in Appendix 1, which must be determined before any use of the model for the identification of the CrSi₂ film thermal conductivity.

III. C. 2. Contact radius determination

Parameter A can be obtained from the probe-sample thermal contact radius a . It has been confirmed that more conductive material may act as a heat sink and leads to a greater constriction of heat flow lines, which means a smaller a . While the heat flow lines spread over the surface of materials with low thermal conductivity, making a large a [74]. The relationship of thermal radius a as a function of the effective thermal conductivity of samples for Wollaston probe is characterized in previous work by using a sample consisting of different thicknesses of silica layers standing on a single silicon wafer [74]. The relationship curve is presented in **Figure III-9** (a). Based on this Figure data, we can roughly estimate a of each CrSi_2 samples with their k_{eff} results obtained previously. The values of the parameter a is then evaluated approximately and shown in **Figure III-9** (b).



The reliability of fitted k of CrSi_2 layer by analytical model on input parameter, a , is also evaluated since the SThM measurement is strongly correlated to this parameter [144]. When evaluating the impact of one parameter on the overall outcome k , all other input parameters are the parameters listed in **Table III-4**. **Figure III-10** plots fitted k for pristine CrSi_2 in function of input thermal contact radius a . The same tendency of fitted k as function

of a could be observe for the other samples as shown in Appendix 4. It can be seen that a plays a crucial role in determining k . k decreases sharply with the increase of input a . It has to be mentioned that the environment and the probe's geometry have a significant impact on the a value [145]. Therefore, since a different probe was used than the one used to obtain the calibration curve presented in **Figure III-9**, this may have introduced some errors that have been taken into account in the calculations. Undoubtedly, the accuracy of the measurement can be greatly improved if the $a(k_{eff})$ curve can be reacquired using the probe used for the measurement.

Table III-4. Input parameters in the analytical model

Input parameters \ Sample	Sample				
	CrSi ₂	CrSi ₂ Ne RT	CrSi ₂ Ne 250 °C	CrSi ₂ Al RT	CrSi ₂ Al 250 °C
t (nm)	269	264	231	274	260
a (nm)	200	205	210	237	380
R_{th} (nK · m ² /W)	100	100	100	100	100
k_{Si} (W/(m. K))	130	130	130	130	130
k_{eff} (W/(m. K))	7.13	5.50	4.78	3.41	2.40

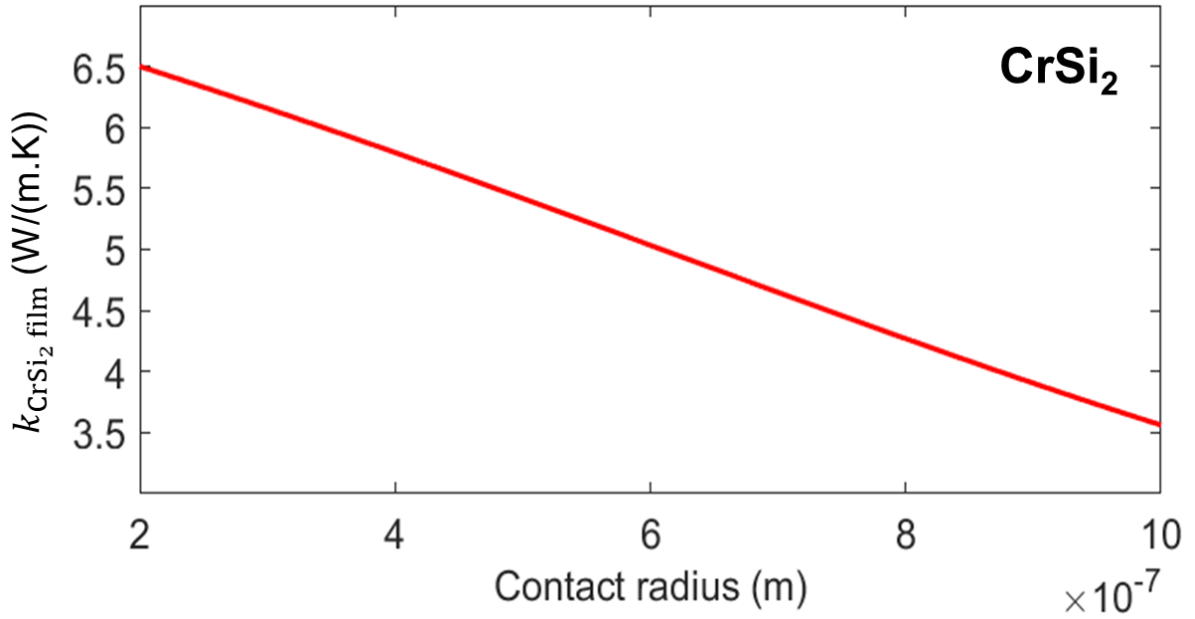


Figure III-10. Fitted k of CrSi₂ layer by analytical model in function of input contact radius a .

III. C. 3. Thermal boundary resistance (TBR) characterization

Thermal boundary resistance (TBR) between CrSi₂ film and Si substrate is another important input parameter as explained in **Chapters I and II**. For the studied samples, it is noted that there is a 25 nm SiO₂ layer sputtered between CrSi₂ film and Si substrate that introduces an additional thermal boundary resistance. Thus, in order to simplify the studied system, the TBR between CrSi₂ film and SiO₂ ($R_{th \text{ CrSi}_2/\text{SiO}_2}$), the thermal resistance of SiO₂ layer (R_{SiO_2}) and the TBR between SiO₂ and Si substrate ($R_{th \text{ SiO}_2/\text{Si}}$) are grouped in series as one effective thermal resistance R_{th} :

$$R_{th} = R_{CrSi_2/SiO_2} + R_{SiO_2} + R_{SiO_2/Si} \quad (\text{III-3})$$

It is noteworthy to remind that, as was stated earlier in **section III. B. 2. b) Samples implanted at room temperature**, some ion implantation exceeds the CrSi₂ film and arrived at the interstitial zone between CrSi₂ film and Si substrate and even reaches substrate layer. This may influence the property of SiO₂ and Si layer as well as the relevant interface. Thus, it becomes challenging to obtain an accurate R_{th} from the literature. The values of R_{th}

experimentally determined for solid–solid contacts close to room temperature typically lie in the range 10^{-9} to 10^{-6} $\text{m}^2\text{K}/\text{W}$ [146], [147]. **Figure III-11** plots the fitted k in function of input TBR of pristine CrSi_2 in this range. The same tendency could be also observed for the other samples as shown in Appendix 4. It could be concluded that TBR also has a certain degree of impact on fitted k . TBR was chosen as 10^{-7} $\text{m}^2\text{K}/\text{W}$ for all CrSi_2 samples for subsequent analytical model calculation, with an approximately 30% uncertainty taken into account.

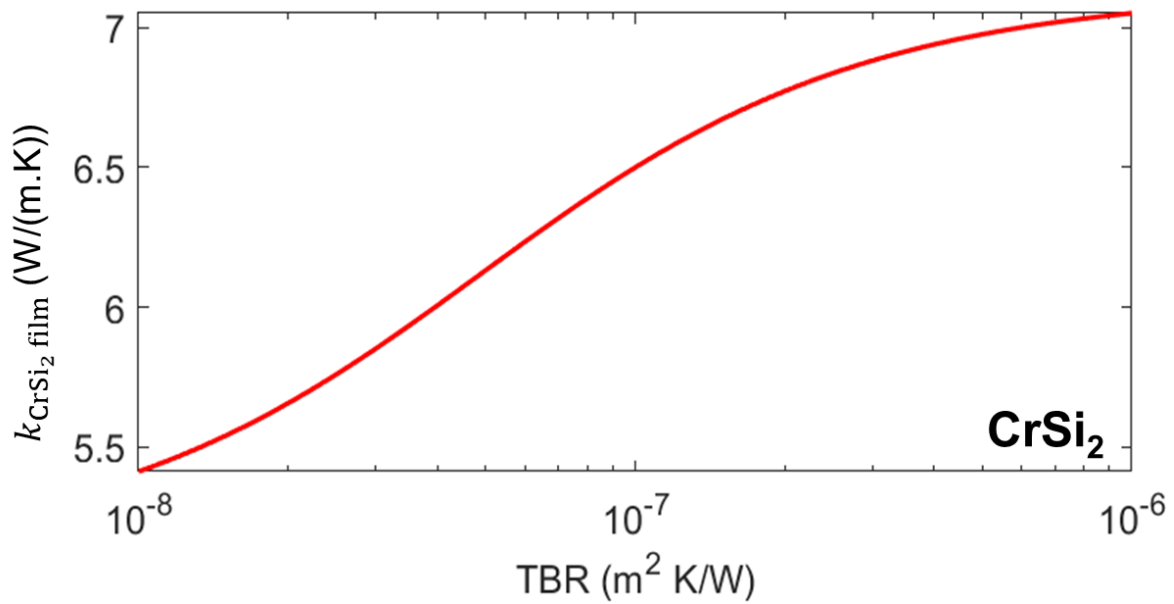


Figure III-11. Fitted k of CrSi_2 layer by analytical model in function of input TBR.

In order to quantify this TBR more precisely, measurements using another technique such as a frequency and a time domain thermoreflectance method (FDTR/TDTR) [148][149] could be favorable. A collaboration on this subject was initiated with the Laboratoire Ondes et Matière d'Aquitaine (LOMA, Bordeaux France). However, due to the significant errors and uncertainties in the thickness and thermal capacity of the sample, which are also important input parameters for FDTR/TDTR method, the aforementioned method cannot be used to accurately measure TBR in this work.

III. C. 4. The other input parameter in analytical model

The other input parameters for analytical model also include thickness (t (nm)) of CrSi_2

layer and thermal conductivity of Si substrate (k_{Si} (W/(m.K))). Fitted k of pristine CrSi₂ layer by analytical model in function of input t and k_{Si} are plotted in **Figure III-12** and **Figure III-13**, respectively. The same tendency could be also observed for the other samples as shown in Appendix 4. It could be seen that these two parameters slightly influence the fitted result, and the introduced uncertainty is approximately less than 3%. As final input parameter for analytical model, t is characterized through TEM as stated previously, k_{Si} is chosen as 130 W/(m.K) [150]. All parameters input in model is summarized in **Table III-4**.

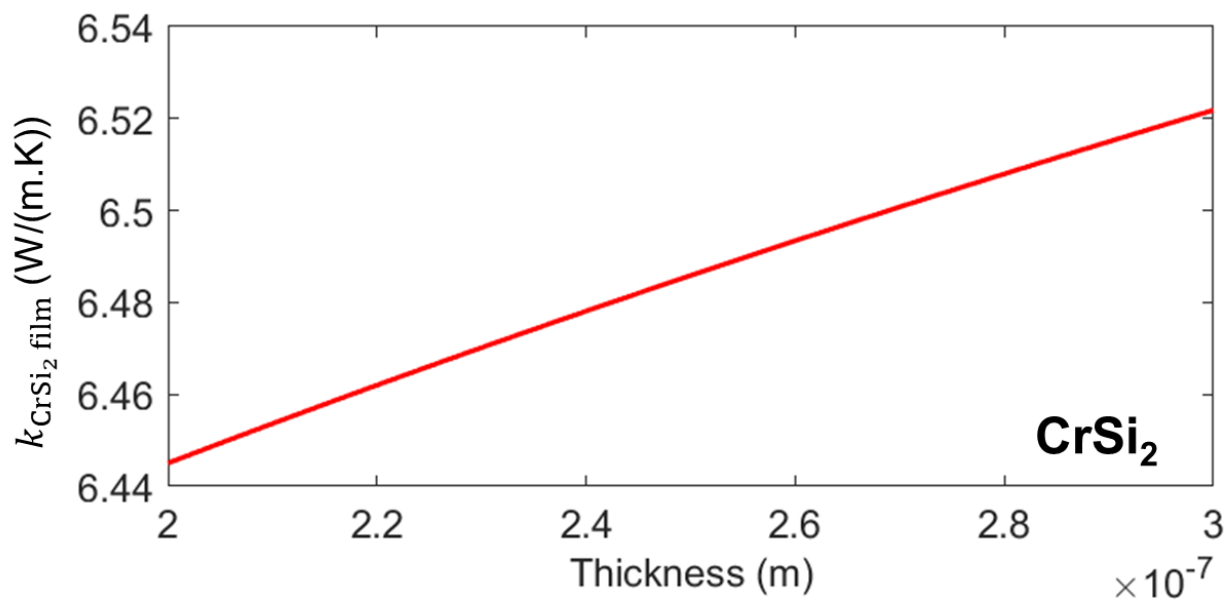


Figure III-12. Fitted k of CrSi₂ layer by analytical model in function of input thickness.

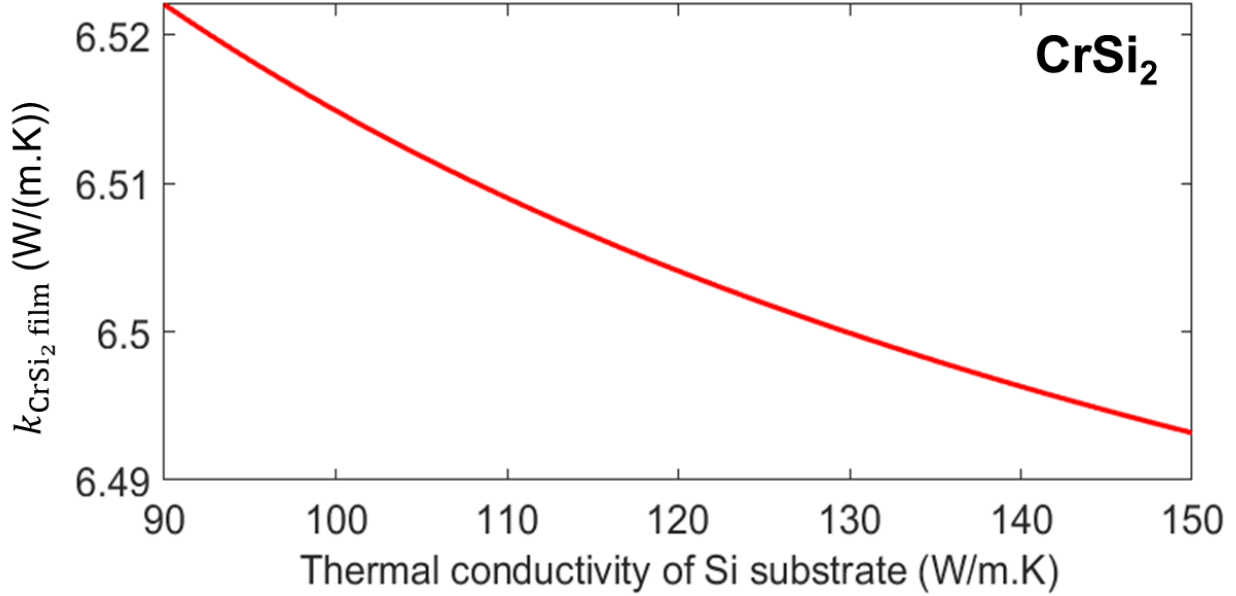


Figure III-13. Fitted k of CrSi_2 layer by analytical model in function of input k_{Si} .

III. D. Results and discussion

The thermal conductivity (k) value for our CrSi_2 films derived from k_{eff} by using the mentioned theoretical model are grouped in **Figure III-14**. The error bars represent the standard deviation of the measurements for both the CrSi_2 samples, and the reference samples mentioned in **Chapter II**. The significant uncertainties for the as-deposited CrSi_2 are linked to the fact that, as already introduced in **Chapter I**, the sensitivity of SThM technique decreases with the increase of thermal conductivity.

k determined for the as-deposited pristine sample (6.5 W/(m.K)) is lower compared to 16 W/(m.K), which is given by the scientific literature [103]. The lattice thermal conductivity k_L for polycrystalline CrSi_2 samples have been measured as 12 W/(m.K) at 300 K [151], which lies between the values of single-crystal CrSi_2 along the [100] and [001] directions [152]. This difference from our result is since the sample studied in this work exhibits an amorphous structure rather than a crystalline one. It may be problematic to use the term phonon for amorphous material because of the absence of periodic lattice in non-crystalline structure. But as introduced in **Chapter I**, here in this manuscript, the term phonon generalizes both the propagating and localized atomic oscillations.

In addition to the phononic thermal conductivity, the electrons in CrSi₂ also contribute to the thermal conductivity. Due to the high contact thermal resistance between probe and sample surface (in the order of 10⁶ magnitude) and the order of magnitude of the thermal conductivity, the temperature on the surface of sample does not change a lot compared to ambient temperature (approximately 300 K). It only significantly changes when measuring polymeric materials that have k , typically in the range of 0.1 to 0.5 W.m⁻¹.K⁻¹ [17]. Thus, the phononic and electronic contributions to the thermal conductivity, k_{ph} and k_e respectively can be presumably separated using the Wiedemann–Franz law at 300 K (Eq. (I-9)). According **Figure III-6** the value of k_e can be determined at 300 K for each samples. The remaining part of total thermal conductivity could be attributed to phononic thermal conductivity k_{ph} , the calculated results for all CrSi₂ samples are listed in **Table III-5**.

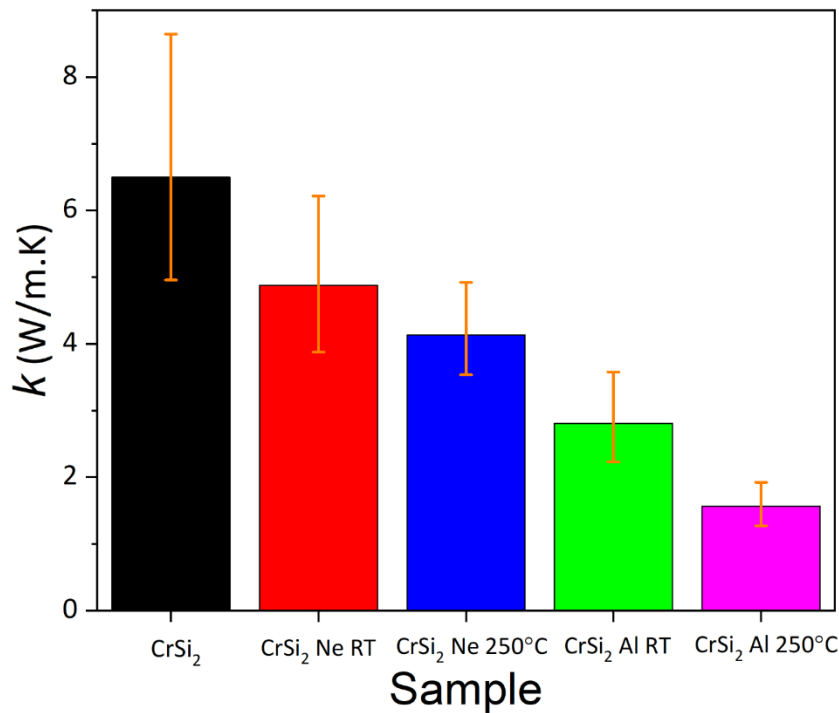


Figure III-14. Thermal conductivity of as deposited and implanted CrSi₂ film calculated from model.

Table III-5. Phononic and electronic contribution to the thermal conductivity at room temperature

Sample	Thermal conductivity, k (W/(m.K))			Ratio of phononic contribution to k (%)
	Total	Electronic, k_e	Phononic, k_{ph}	
CrSi ₂	6.50	1.37	5.13	79.0
CrSi ₂ Ne RT	4.88	1.62	3.26	66.8
CrSi ₂ Al RT	2.80	1.45	1.35	48.2
CrSi ₂ Ne 250 °C	4.13	0.93	3.20	77.4
CrSi ₂ Al 250 °C	1.60	0.90	0.67	42.7

Pristine CrSi₂

Thermal conductivity of 6.5 W/(m.K) is obtained for the pristine amorphous CrSi₂ film. As expected it is lower than the thermal conductivity of the crystalline CrSi₂ (16 W/(m.K) [103]). The k reduction is about 60% and it can be seen from **Table III-5** that heat is mainly propagated through phonons: the contribution of phonon to total thermal conductivity reaches 80%. k_{ph} is reduced of about 50 % compared to the value estimated for the crystalline CrSi₂ (10-12 W/(m.K) [103]) and k_e is reduced of 77%. In a first approach, these values could be surprising for an amorphous material where amorphisation is expected reducing k more strongly but the thermal conductivity of metallic glasses or amorphous alloy have been intensively investigated and could be higher than 5 W/(m.K) at 300 K [153], [154]. The contribution of phonon to total thermal conductivity may reach as high as 49% for some thin foil metallic glasses [155].

CrSi₂ implanted at RT

When compared to the pristine sample (6.5 W/(m.K)), all the implanted samples present a significant decrease in the thermal conductivity. The samples implanted at RT present a less pronounced reduction in their thermal conductivity than their 250 °C counterparts.

In the **case of the samples implanted with Ne**, the critical feature is the presence of Ne bubbles. We suggest that bubbles represent a discontinuity on the solid structure of the matrix and may act as efficient scattering centers for the phonons.

In the **case of the Al implantation at RT**, even though the implanted atomic concentration is very low compared to Ne at RT (see **Table III-1**), the formation of defect clusters resulting of the Al implantation could play a dominant role in controlling thermal conductivity behavior. It has been shown, for example, that even very low irradiation doses (as low as 0.00032 dpa – displacement per atom) decrease the thermal diffusivity of self-irradiated tungsten due to the formation of sub-nanometric defects [156]. The introduction of isoelectronic elements (such Al and Ne for Cr and Si) preserves the crystalline electronic structure while enhancing electrical conductivity and creating a mass contrast that disrupts the path of the heat carriers [139], [157]. In this sense, Perumal *et al.* showed that the introduction of Al and Mn as co-substitutors in CrSi₂ induces a decrease in thermal conductivity due to a mass fluctuation effect from the atomic weight difference between the solute (Al or Mn) and solvent atoms (Cr and Si) [158]. Choy *et al.* observed that the increasing number of chemical components in amorphous alloy increases disorderliness and leads to a decrease in phonon mean free path [155].

Therefore, the phononic component of the CrSi₂ thermal conductivity decreases, explaining the reduction observed on the k measurements for the two samples implanted at RT compared to the non-implanted CrSi₂ sample. As expected the thermal conduction electronic component is enhanced slightly for both the samples implanted at RT. However, the electron contribution to the thermal conduction is larger for the Al implantation than for the Ne implantation due to a larger decrease on k_{ph} .

CrSi₂ implanted at 250°C

The samples implanted with Ne and Al at a temperature of 250 °C present a more significant reduction in k than the RT Ne and Al implanted samples. In these cases, we can suggest that the nanocrystallites formed during the 250 °C implantations are effective scattering centers for the phonons and contribute to a more pronounced effect on k . Similarly, Novikov *et al.* have shown that nanocrystal interfaces in stoichiometric CrSi₂ amorphous thin films largely contribute to the decrease of the material thermal conductivity [159]. They have also demonstrated in the same study [159] that the nanocrystal boundaries lead to an increase of the CrSi₂ electrical resistivity compared to amorphous CrSi₂ without nanocrystals, which also happens in our case for the 250°C Ne-implanted CrSi₂ sample. The reason of the increase of the material electrical resistivity is the presence of depletion zones located in nanocrystal grains due to the band bending at their boundary. The depth of this depletion layer is evaluated to be in the range of 10 to 30 nm for CrSi₂ [159], which is of the same order of magnitude than the average crystallite size (15 nm) produced by implantation performed at 250 °C in our case (see **Figure III-4**). This means that a large part of the volume of nanocrystals in our sample will be greatly influenced by the band bending effects on their boundary interfaces. This region may act as an energy-filtering barrier so that only the energy carriers with large amounts of energy can penetrate the barrier at the boundary of nanocrystal grains.

This leads to a significant decrease on electronic component of the thermal conductivity for 250°C Ne-implanted CrSi₂ samples while no obvious phononic component variation is detected.

For the 250°C Al-implanted CrSi₂ sample, the combination of crystallites and the mass fluctuation effect discussed above could explain the significant decrease in the thermal conductivity by both electrons and phonons. Moreover, contrarily to the other samples, results in **Table III-5** could suggest an electron contribution to the heat transfer conduction larger than that of the phonons.

III. E. Conclusions and perspectives

State of the art shows that CrSi_2 has potential as thermoelectric material but its ZT is still too small to be competitive. Different approaches were used to reduce its thermal conductivity while CrSi_2 is in its crystalline form but ZT is still too small. The material amorphisation combined with the introduction of isoelectronic elements such as Ne and Al ions should help to decrease the phonon and electron components of the heat conduction in the material. However, CrSi_2 is still a material that is not well known in its amorphous state. Scientific literature furthermore shows that the temperature of the material during irradiation is also a parameter to be exploited to decrease the thermal conductivity as in a range of temperature larger than RT a part of the amorphous material crystallizes due to a radiation-enhanced phase transformation process.

We determined using SThM amorphous chromium disilicide (CrSi_2) modified by Ne and Al ion implantations at RT and 250°C. Our results give a new estimation of the thermal conductivity for the amorphous CrSi_2 of about 6.5 W/(m.K). As expected, it is lower than the thermal conductivity of the crystalline CrSi_2 [103]. The found k reduction is about 60% and heat conduction is shown mainly acting via phonons.

Changes of the microstructure of amorphous CrSi_2 as a function of the implantation irradiation conditions are in good accordance with those previously found elsewhere in the scientific literature. Identified thermal conductivity values show that ion implantation induces substantial modifications on the microstructure of amorphous CrSi_2 , which induce the decrease of the material thermal conductivity. The k reduction is more pronounced for the implantation at 250°C.

For Ne implantation at RT and 250°C Ne bubbles should act as efficient scattering centers for the phonons and phonon path should be disrupted by the mass contrast. For Al implantation at RT results should be due to the phonon scattering by defect clusters and the disruption of the phonon path by the mass contrast.

For implantation at 250°C, nanocrystallites formed during implantation mainly further reduces the heat conduction by electrons, which could be due to the presence of depletion zones located at the nanocrystallite boundaries. These nanocrystallites also lead to a decrease of the phonon contribution to heat conduction in the case of the implantation with Ne ions.

In a more general way, this work demonstrates that thermal conductivity behavior of amorphous structures can be tailored via ion implantation. This is done by exploring doping, amorphous to crystalline phase transitions and irradiation-induced void defects, providing new possibilities for applications in thermoelectrics.

One perspective could be to exploit the effect of the temperature during ion implantation for tuning the size of the induced crystallites in order to optimize the energy-filtering barrier at the crystallite boundaries for a more pronounced decrease of the material thermal conductivity.

Furthermore, the accuracy of fitted k result could be improved by a more accurate measurement of the model input parameters. As an example, the contact radius a could be obtained through an a - k_{eff} calibration, which is performed on a series of specially designed reference sample (i.e., reference samples of known low thermal conductivity with different thicknesses, deposited on a known thermal conductivity substrate, with the interface thermal resistance between them having been extensively studied.). Apart from that, TBR could be qualified via the other technique such as FDTR/TDTR.

Chapter IV. THERMAL CONDUCTIVITY ENHANCEMENT MECHANISM OF POLYMER COMPOSITES WITH CARBON-BASED FILLERS

This chapter presents an analysis of the heat transfer within two types of polymer composites containing carbonous fillers. It focusses on, first, the determination through SThM measurements (imaging or point measurements) and, second, the modeling of the effective thermal conductivity of polymeric nanocomposites. The goal is to elucidate the mechanism of enhancement of the heat transfer with the introduction of nanofillers in polymer matrices. Samples consist of high-density polyethylene (HDPE) matrix filled with 50 μm expanded graphite (EG) particles and polyvinylidene difluoride (PVDF) matrix containing multiwall carbon nanotubes (MWCNTs).

Experimental results of this part of the manuscript have been published as *Investigation of the thermal conductivity enhancement mechanism of polymer composites with carbon-based fillers by scanning thermal microscopy* in AIP Advances journal, **12**(10), 105303, (2022).

IV. A.Context

As mentioned in **Chapter I** polymers have potential for widespread applications where higher heat dissipation is desired (light emitting devices, batterie, electromagnetic shielding...) and the insertion of fillers such as ceramics materials, metallic materials and carbon-based materials is a popular strategy to enhance the thermal conductivity of polymer composites. Among all these fillers, carbon-based materials have aroused higher attention and interest of scholars due to their thermophysical properties exhibiting a thermal conductivity that can even reach values higher than several thousands of $\text{W}/(\text{m.K})$ for fillers such as carbon fibers and carbon nanotubes in their axial direction [160]. For such reasons, a large number of studies have been carried out to improve the polymer k using carbon-based nano-fillers [67], [161]–[166].

In this context, *Chirtoc et al.* [67] have introduced EG fillers into HDPE and achieved

increased thermal conductivity when the filler concentration increases in the range up to 0.06 graphite volume fraction. However, it was recognized from this study that the experimental results obtained using a back-detection modulated PTR method deviate from those predicted by the model of *Nan et al.* [167] for fillers at higher concentrations [67]. A proposed reason was that the non-interacting particle assumption of the model is not valid as the filler concentration increases.

PVDF is also a type of polymer that is widely employed as base matrix for nanocomposites, due to its excellent film formation, mechanical properties, high resistance towards chemicals, alongside a thermal, oxidative, and hydrolytic stability [168], [169]. Specifically, *Georgousis et al.* [166] have dispersed MWCNTs in PVDF and observed that the electrical and mechanical properties of the PVDF matrix improve after adding the MWCNTs, which gives an advantage of such polymer for prospective strain sensing applications. However, the effect of introducing MWCNTs on the thermal properties of these PVDF – based composites is still missing. The characterization of the thermophysical properties of the combination PVDF/MWCNTs would be favorable to supplement the understanding of the influence produced by MWCNTs on the polymer matrix and to suggest other applications of the material.

In order to verify the thermal conductivity PTR measurements obtained by *Chirtoc et al.* [67], and to obtain the complementary thermal conductivities for the samples of *Georgousis et al.* [166], we measured the effective thermal conductivity of the polymer composites studied by these two groups applying the methodology previously described in chapter II. A balanced TCU was used for these measurements. Furthermore, in order to better understand the experimental results, a model describing the samples of dispersed MWCNTs in PVDF was developed to support the inference on the mechanisms of thermal property tuning.

IV. B. Sample description and characterization

IV. B. 1. HDPE/EG Composites

HDPE BP 5740 3 VA, supplied by British Petroleum UK, was used as matrix. Expanded graphite, particle sizes of 50 μm (EG50), Ecophit G, supplied by SGL Technologies GmbH.

HDPE, with molecular chain structure as shown in **Figure IV-1**, was filled with 2 % (HDPE98-EG2) and 10 % (HDPE90-EG10) weight/mass fraction (χ (wt.%)) of 50 μm EG in a Brabender Plasticorder PLE 331 apparatus as described in [67]. HDPE is a thermoplastic polymer that has excellent processability and very low cost. The thickness of samples after compression molding was around 0.3 mm. Optical observation (**Figure IV-2**) shows the amorphous HDPE matrix and suggests that large EG flakes (50 μm in size) were broken during preparation process and formed fragments with observed size that can be less than 10 μm , which is consistent with the results proposed in the literature [67]. EG flakes are then smaller than the introduced EG fillers.

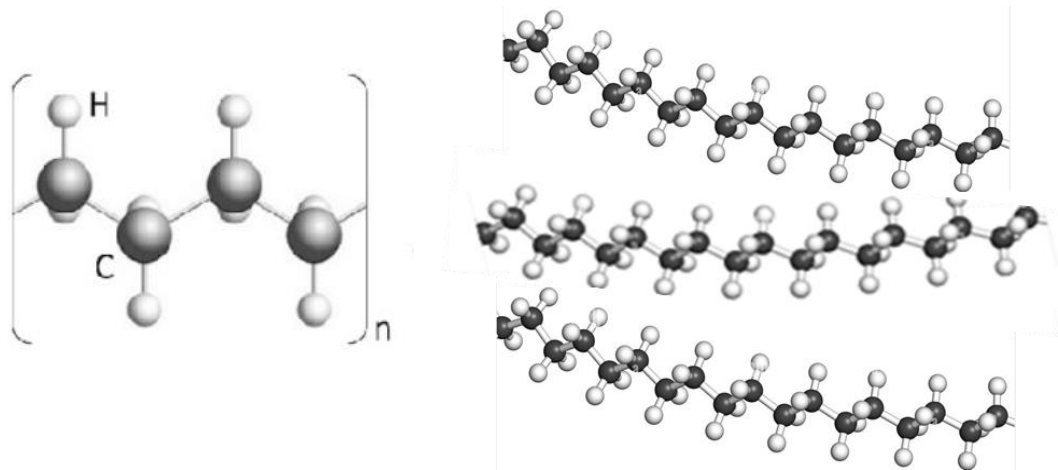


Figure IV-1. Structure of HDPE from [170].

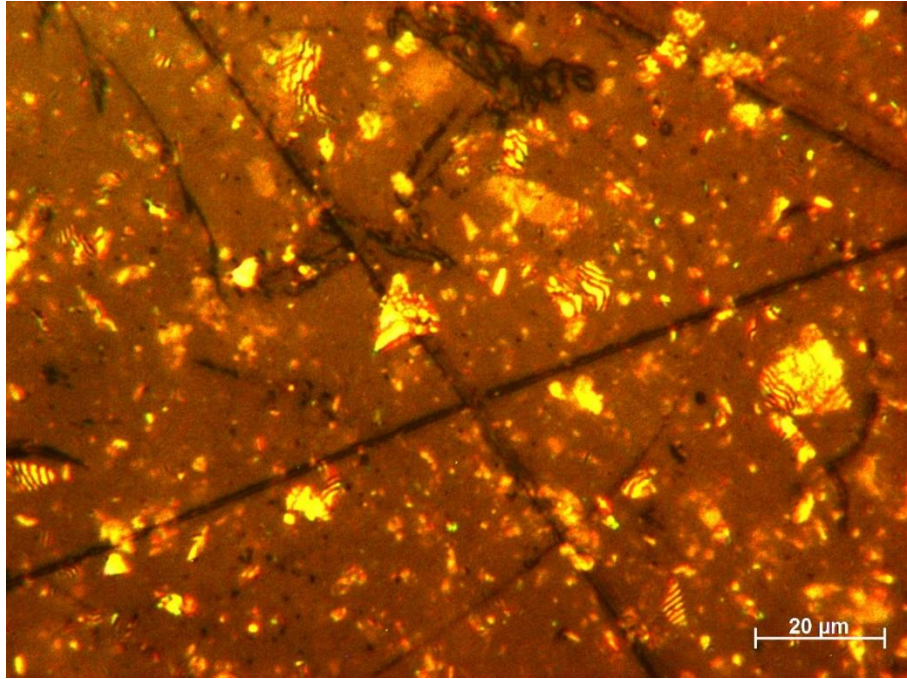


Figure IV-2. Optical image of HDPE-EG composite.

IV. B. 1. a) *Measurement results for HDPE/EG composites*

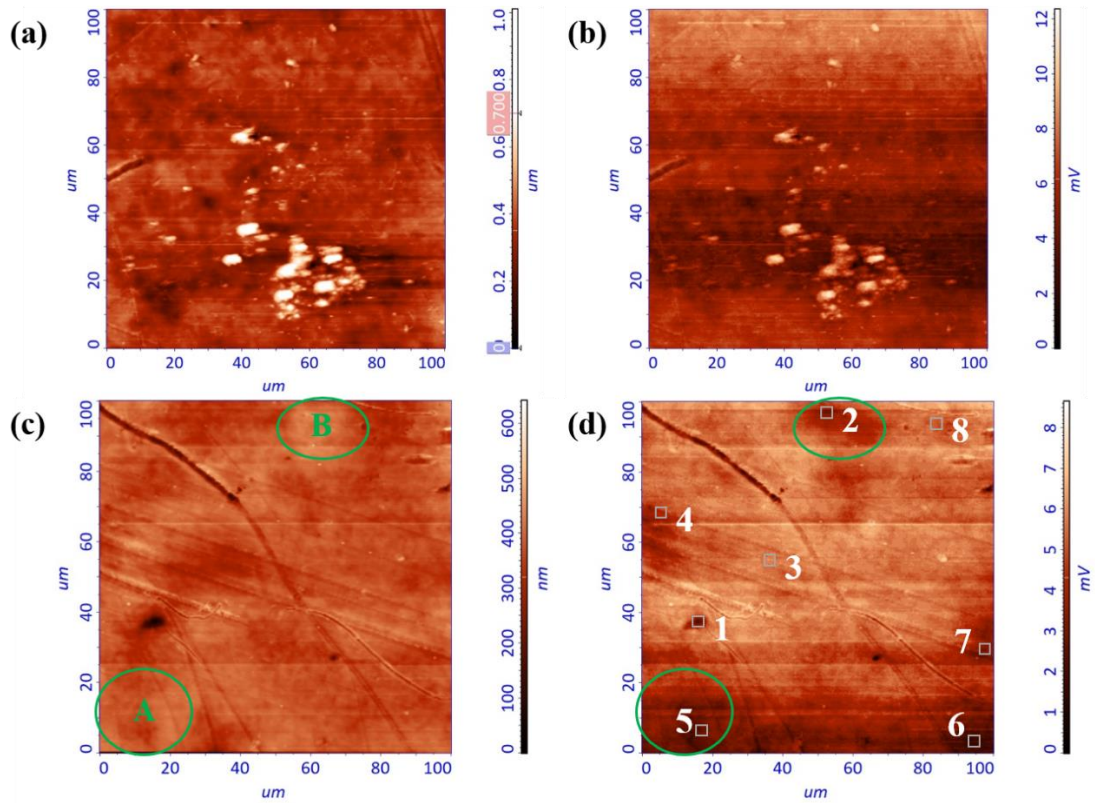


Figure IV-3. SThM images for HDPE composite containing 2 % (a, b) and 10 % (c, d) weight fractions of EG. Topography (a, c) and thermal) signal (b, d).

Figure IV-3 displays the topography and thermal images obtained simultaneously of HDPE composites filled with 2 and 10 wt.% of EG, respectively. Benefit from measuring simultaneously the morphological and thermal signals, it is possible to analyze these data from the exact same region. The topography (**Figure IV-3 (a)**) and thermal (**Figure IV-3 (b)**) images of 2 wt.% EG contained in a HDPE matrix present a high degree of consistency in contrast, which means the variation of heat loss flux is due to the topography features of the sample surface. The bright part indicating higher heights may be caused by the dust or surface defect formed during the fabrication.

By averaging the thermal signal from the flat part on the thermal image, $k_{eff} = 0.45 \pm 0.02$ W/(m.K) was determined by using the calibration curve shown in **Chapter II**. The uncertainty is calculated from the root mean square of U_{ic} . The identified k_{eff} value is lower than the result (0.59 W/(m.K)) measured on the same sample with back-detection PTR method but close to the result ~ 0.40 W/(m.K) for neat HDPE (pristine, without any fillers) [67]. The reason of the lower value from SThM measurements may come from the lack of EG fillers contained in limited probed volume, what is expected for a composite with low filler concentration such as 2 wt.%.

This result proves the reliable sensitivity of SThM in the studied thermal conductivity range. The deviation of the results obtained by SThM, and PTR techniques verifies the inhomogeneity of dispersion of EG fillers at low concentration. In ref. [67], it has been shown that the experimental result from PTR method fit well with the effective thermal conductivity of composite model of Nan et al. [167] when filler charge is less than 6 vol.%. It is worth to note that this model is effective with the assumption regarding non-interacting fillers. No agglomeration of EG observed from SThM is also favorable to the validation of this assumption.

On the contrary to 2 wt.% EG fraction sample, HDPE composite with 10 wt.% filler charge shows a different contrast pattern between thermal and topography images as circled in **Figure IV-3 (c)** (zones A and B). The dark area in thermal image indicates a higher heat transfer from the probe to the sample that corresponds to a higher local thermal conductance of the

sample. Meanwhile, the same position on topography image has a shallower color associated with higher heights.

Furthermore, as explained above, the topography of the sample surface may induce some artifacts in the thermal images. This can be linked to the fact that the contact radius may reach more than 5 μm for Wollaston probe on polymeric materials [171], which is comparable to the size of convex zones for the studied samples. The scanning with the SThM probe of a concave surface may induce more thermal exchange due to the increase of the probe-sample contact area through the air gap, which does not agree with our results. Therefore, the thermal signal contrast obtained can only be attributed to the variation of the thermal properties beneath the surface of the sample. Besides, these high thermal conductance regions are distributed as islands inside the sample. The agglomerations of EG fillers are supposed to be the reason behind this phenomenon.

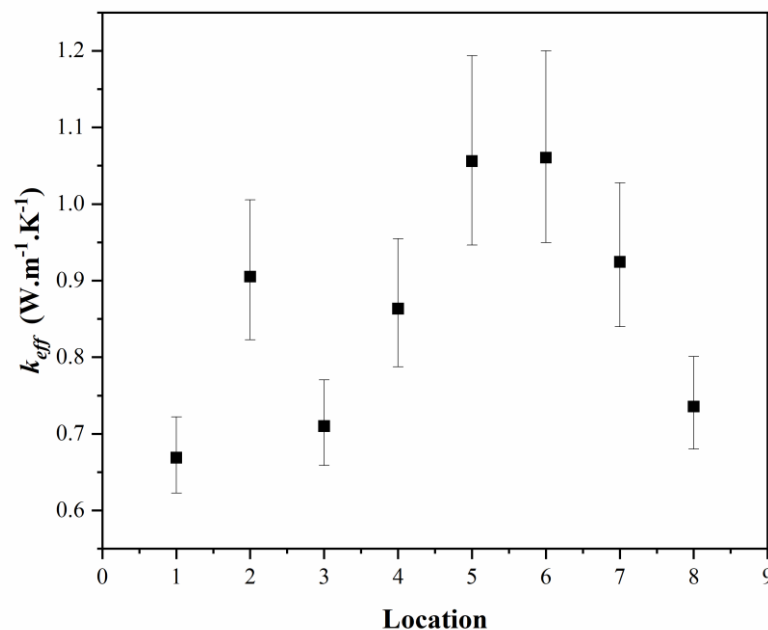


Figure IV-4. Effective thermal conductivity of HDPE/EG composite with 10 wt.% filler charge measured at different locations on the sample that are precised in 错误!未找到引用源。 (c). The root mean square was considered as the uncertainty and used to estimate the error bar.

After comparing the topography and the thermal images of the samples, the second step of the measurement was to identify k_{eff} of the polymeric-based nanocomposites. Eight locations were chosen randomly as indicated in **Figure IV-3** (c). For each location, SThM signal of at least 25 pixels were collected. The thermal conductivity was calculated using the averaged signal at each location according to the calibration curve presented in **Chapter II**. Results are given in **Figure IV-4**. All the results fall within the range from 0.67 to 1.06 W/(m.K), which is close but still lower than the k_{eff} values measured by other methods (1.27 W/(m.K) for PTR [67], 1.26 W/(m.K) for Flash method [172] and 1.23 W/(m.K) from modelling [67]). The reason that the SThM results are lower compared to those obtained with the other techniques could also be linked to the lack of fillers contained in the limited probed volume of the sample. One should keep in mind that the SThM area for investigation was $100 \mu\text{m} \times 100 \mu\text{m}$, and the original EG particle size was $50 \mu\text{m}$, which was broken during preparation to smaller fragments with size less than $10 \mu\text{m}$. This fact can also contribute to the inhomogeneity of measured thermal conductivity values. Nonetheless, the enhancement of the heat transfer along higher concentration of EG fillers can be clearly demonstrated by SThM.

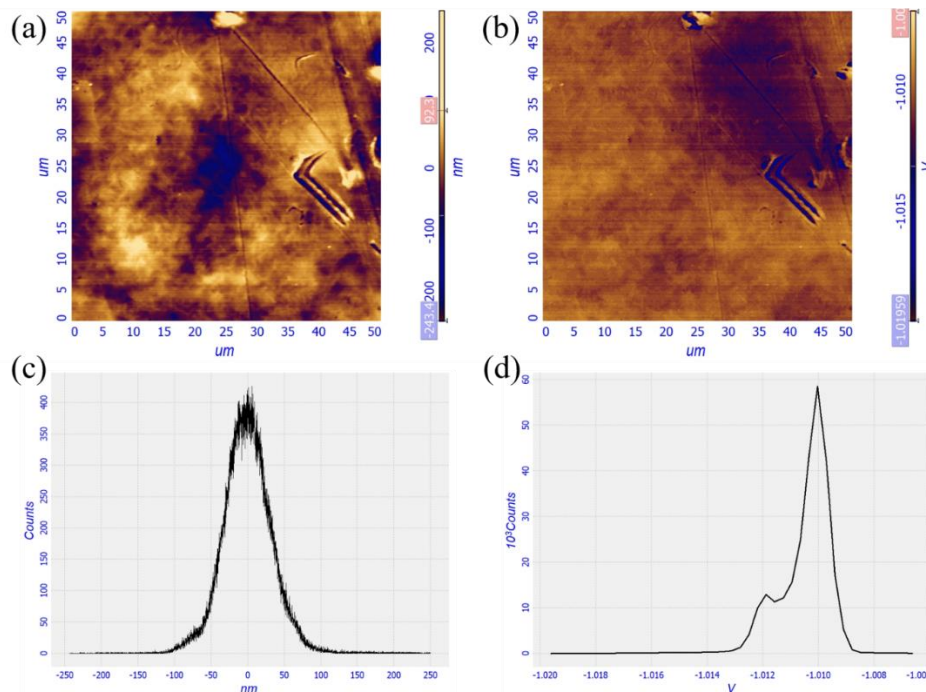


Figure IV-5. Topography image (a) and thermal image (b) of 10 % weight fraction of EG-HDPE sample. (c) and (d): associated histograms giving the distribution of the height and thermal signal values respectively.

To further investigate and demonstrate our conjecture, the same scanning procedure was performed on another zone of the sample HDPE90-EG10 with $50\ \mu\text{m}\times 50\ \mu\text{m}$ area size. The mismatch of the topography and thermal contrast also appears clearly on the obtained images as shown in **Figure IV-5**. The distribution curve of the signals is also represented in this figure. The distribution curve for the height of the sample presents only one peak, demonstrating that the surface is flat. Two peaks appear on the thermal signal distribution curve, indicating the existence of two levels of thermal conductance within the sample. These peaks cannot be correlated to the topography of the sample surface.

We can observe in the top right corner of **Figure IV-5** (b) a dark area where the sample thermal conductance is larger than elsewhere at the surface. This kind of relatively high thermal dissipation area with such large size only arises while the weight fraction of EG reaches 10 %. The estimated diameter of this area, which is around $20\ \mu\text{m}$ from thermal image, is larger than EG intercalation diameter $5\text{-}10\ \mu\text{m}$ that is observed under optical microscope for HDPE98-EG2 sample [67]. The possible reason of the formation of large heat sink area may be related to the agglomeration due to Van der Waals interaction between graphene platelets [173] of the EG with a high specific surface area [174]–[176].

All these results further prove the capability of SThM to detect the local thermal conductivity variation among different zones of the polymer composites, which is due to the fillers buried beneath the surface.

IV. B. 2. PVDF/MWCNTs composites

The PVDF (SOLEF1010, Solvay Solexis S.A., Belgium), molecular formula shown in **Figure IV-6**, was supplied in the form of pellets. The MWCNTs (Nanocyl 7000, Belgium; purity of 90%, outer diameter of $9.5\ \text{nm}$ and length $1.5\ \mu\text{m}$) were used as received.

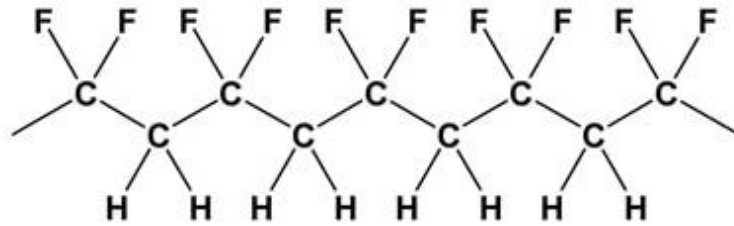


Figure IV-6. Molecular formula of PVDF.

PVDF matrix with MWCNT fillers of an outer diameter of 9.5 nm and length 1.5 μm were prepared by melt mixing in a micro-compounder DSM Xplore TM 15 (the Netherlands) using the parameters detailed in [166]. Composites containing 0.5, 1, 1.25, 1.5, 1.75, 2, 3, 4, 6, 8 wt.% MWCNTs have been studied. The thickness of PVDF/MWCNTs samples was around 0.5 mm.

The morphology was studied using scanning electron microscopy (SEM) and no large agglomeration of MWCNTs is observed as shown in Appendix 5. PVDF exhibits five crystalline phases (α , β , γ , δ and ε) due to the arrangement of $-\text{C}(\text{F})-$ dipoles, as presented in **Figure IV-7**. Antiparallel composition of α and ε results in non-polar PVDF. The other three phases are polar and exhibit piezoelectric and ferroelectric properties [177]. The most electroactive phases are β and γ [178]. Thus, it is very important to monitor the variation of the different crystalline phase concentration to fully understand the thermophysical properties tuning in PVDF matrices. The relative percentage of each phase for our samples was characterized by Fourier Transform infrared spectrometry (FTIR) and differential scanning calorimetry (DSC) techniques.

FTIR spectra of pure PVDF and PVDF/MWCNTs nanocomposite films were acquired with NICOLETE 8700 (Thermo Scientific, Madison USA) in Micro-ATR mode, with resolution 4 cm^{-1} , 320 scans, in the range between 4000 and 650 cm^{-1} . The absorbance peak of vibration bands indicating both the α (763 cm^{-1}) and β (840 cm^{-1}) phases can be observed as shown in Appendix 6, proving the existence of these phases. The relative β phase percentage $\beta_r\%$ in the whole crystalline phases portion, defined as $\beta_r\% = \frac{\chi_\beta}{\chi_\alpha + \chi_\beta}$, where χ_α and χ_β are crystalline mass fraction of α and β phase respectively, is calculated using

corresponding absorbance of vibration bands in FTIR as described in [166] and the result is shown in **Table IV-1**.

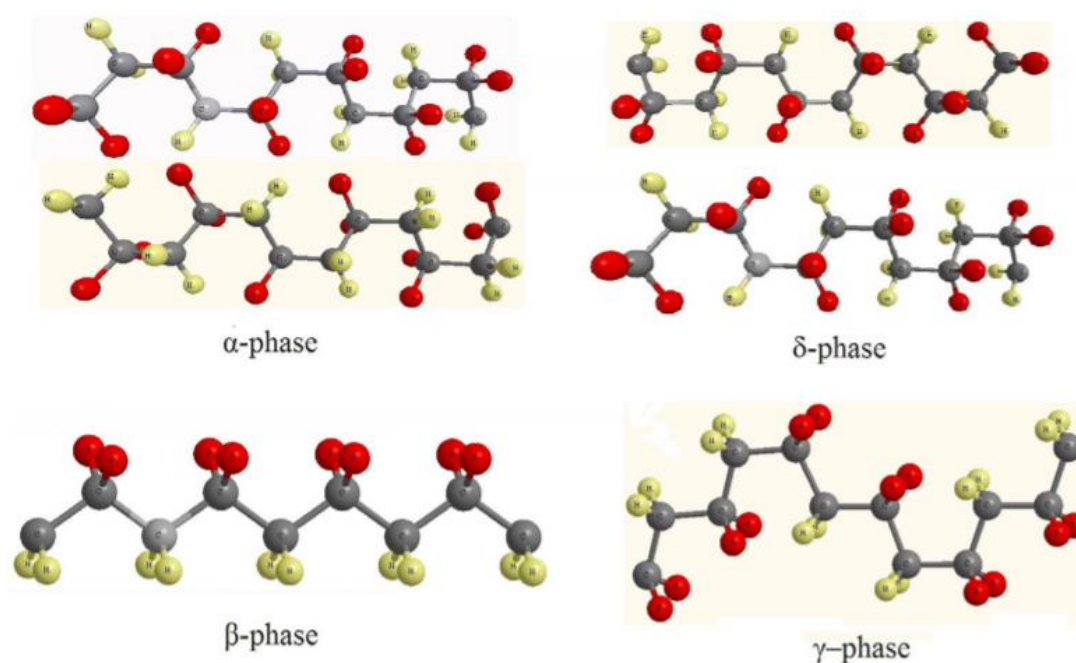


Figure IV-7. Different crystalline phase molecular structures of PVDF [179].

Table IV-1. Relative β phase percentage (β_r %) in PVDF nanocomposites containing different concentration of MWCNTs.

Sample	PVDF	PVDF/1.25 wt% MWCNTs	PVDF/2 wt% MWCNTs	PVDF/4 wt% MWCNTs	PVDF/8 wt% MWCNTs
β_r %	0	$15.8 \pm 1.0\%$	$10.3 \pm 0.5\%$	$36.9 \pm 0.8\%$	$47.9 \pm 6.1\%$

However, in order to obtain the specific fraction of each component in the overall composite material, the other existing portions of composite i.e., amorphous structure of PVDF and fillers MWCNTs have to be taken into account as well. Additional measurements using different techniques are recommended to acquire more comprehensive data. One of these possible techniques is the differential scanning calorimetry (DSC). DSC is a thermal analysis

technique used to measure the enthalpy change of the sample during the predetermined heating and cooling process alongside the evaluation of the melting temperatures of the crystallites. The peak area in DSC result is indicated to the melting or crystallization enthalpy of samples. In general, melting enthalpy is used to calculate the crystallinity. Thus, I used DSC to characterize the PVDF/MWCNTs nanocomposite samples following the steps described below.

The melting temperatures of α and β crystallites of PVDF are very close at 167-171°C, but γ crystallites melt at slightly higher temperatures around 175-180 °C [180], [181]. The crystallinity of samples was determined by DSC measurements, which were performed at Ingénierie des matériaux polymers (IMP, Lyon) using a DSC 3-star system (Mettler-Toledo, Greifensee, Switzerland). Samples weighing between 3.5 and 5 mg were placed in aluminum pan with a lid on. Nitrogen was used as a purging gas with a 50 ml.min⁻¹ flow rate. The samples were heated from 0 to 200 °C with a 5 °C.min⁻¹ ramping rate, then held for 5 min at each temperature. This initial heating step enables the determination of the enthalpy change of the polymer composites during the heating process, characterizing the crystallinity of the samples, while also eliminating the thermal history of the material. The samples were afterward cooled from 200 °C to 0 °C with a cooling rate and waiting time equal to that of the heating procedure. Well-controlled cooling process favorable to achieve a more complete crystallization than the sample fabricated following preparation process mentioned earlier, in order to attain the maximum possible crystallinity that the material can achieve. Finally, they were heated again using the same parameters to 200 °C for characterizing the maximum possible crystallinity of samples.

IV. B. 2. a) Structural characterization of PVDF matrix

The DSC result of PVDF matrix and PVDF/ 8 wt.% MWCNTs samples are shown in **Figure IV-8** while the result for the other samples is presented in Appendix 7. By using such structural characterization, the total crystallinity of PVDF materials was calculated knowing that $\omega_c = \frac{\Delta H_m}{\Delta H_m^c} \times 100\%$. ΔH_m (J/g) is the melting enthalpy of the sample given by DSC peak area as shown in **Figure IV-8** and ΔH_m^c (J/g) is the reference melting enthalpy for 100% fully

crystalline PVDF. Considering that the two crystalline phases α and β coexist at the same time, ΔH_m^c is calculated as:

$$\Delta H_m^c = \Delta H_{m\alpha}^c \times (1 - \beta_r\%) + \Delta H_{m\beta}^c \times \beta_r\% \quad (\text{IV-1})$$

where $\Delta H_{m\alpha}^c$ and $\Delta H_{m\beta}^c$ represent the melting enthalpy for 100% fully α or β crystalline PVDF, respectively. In this thesis, $\Delta H_{m\alpha}^c$ and $\Delta H_{m\beta}^c$ were assigned a value equal to 104.5 (J/g) [182] and 219.7 (J/g) [183], respectively, according to literature studies. In **Figure IV-8**, line 2 (black), 4 (red) and 6 (blue) indicate the enthalpy changes during first heating process, cooling process and the second heating process, respectively. The peak area of lines 2 and 6 gives the melting enthalpy ΔH_{m2} and ΔH_{m6} respectively. These values and ΔH_m^c as well for each sample are summarized in **Table IV-2**. The crystallinity (ω_c) and β phase percentage in total composite component ($\beta\%$) calculated from the data of the corresponding line is also listed in **Table IV-2**. Compared to $\beta_r\%$ which only considers crystalline phases portion of composite, $\beta\%$ is the mass percentage of β phase PVDF normalized to total mass of MWCNTs/PVDF composite which is given by $\beta\% = \frac{\chi_\beta}{\chi_\alpha + \chi_\beta + \chi_A + \chi_{MWCNTs}}$, where χ_A and χ_{MWCNTs} are the mass fraction of amorphous portion of PVDF and MWCNTs, respectively.

ω_c and $\beta\%$ of studied sample deduced from line 2 in **Figure IV-8** are presented in **Figure IV-9**. Line 2 indicates the melting enthalpy during first heating process, which is corresponding to the crystallization of the sample after processing. Generally, ω_c decreases while $\beta\%$ increases as a function of mass fraction of MWCNTs except for an inflection point observed at 2 wt.% MWCNTs. MWCNTs may absorb trans-trans conformations of PVDF chains while the latter acts as nucleating agents owing to the strong confining effect of MWCNTs, which results in the formation of the β phase during the crystallization of PVDF [184].

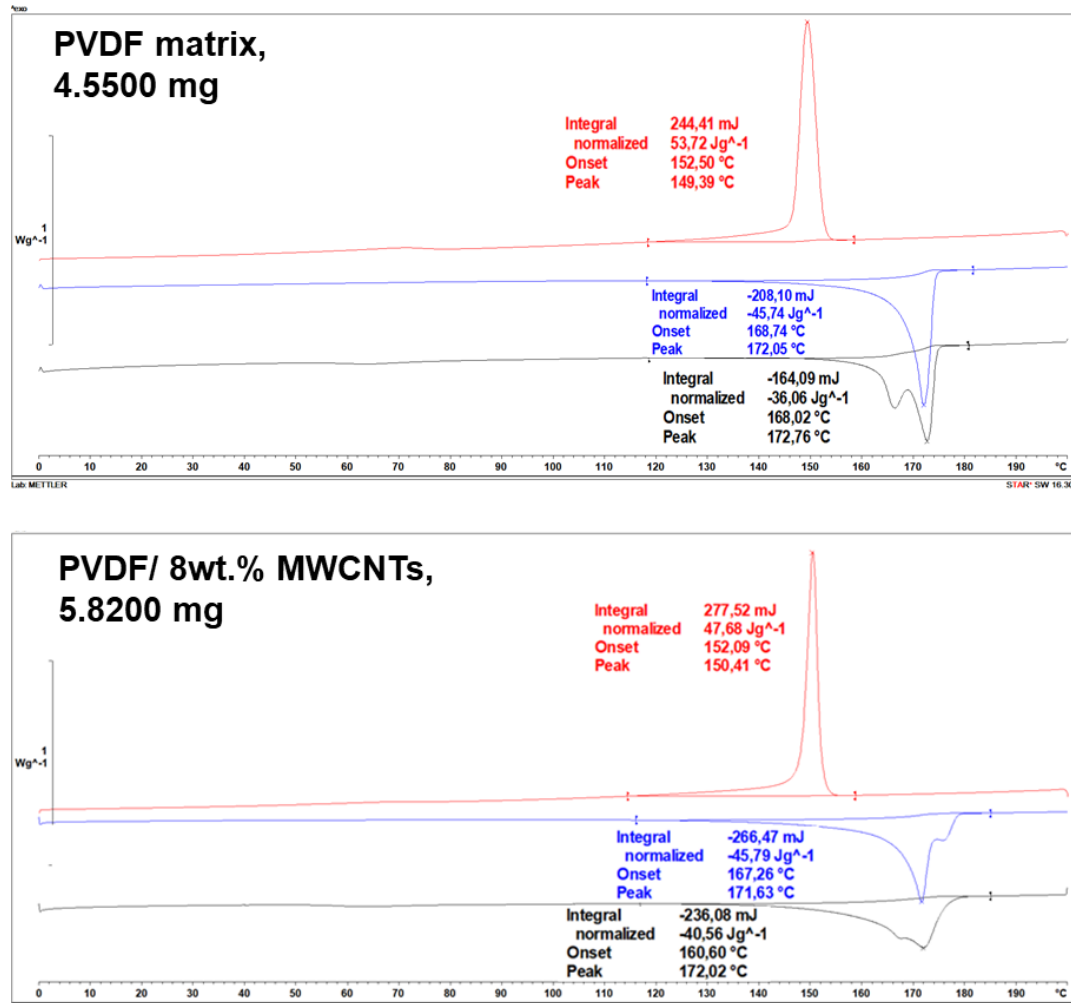


Figure IV-8. DSC results of PVDF composites, line 2 (black), 4 (red) and 6 (blue) indicate the first heating process, cooling process and the second heating process, respectively.

On the other hand, an increased concentration of nanoparticles can also impede the crystallization process by reducing polymer chain mobility, ultimately leading to a lower content of the crystalline structure [179].

Both of these antagonistic mechanisms exist simultaneously in our composite material, resulting in the increased formation of β phase and reduction of ω_c with the addition of MWCNTs. However, the formation of β phase in a blend composite not only depends on the weight fraction of MWCNTs but also on their synthesis process. The surface energy of MWCNTs is also influenced by persistence lengths within the matrix, diameter distribution, bundling characteristic etc., which makes the crystallinity of composite hard to be predict [179].

The result of 2 wt.% MWCNTs sample is also the outcome of the combined effects of all the aforementioned factors. Another thing can be concluded for **Figure IV-8** is that the supplement of MWCNTs has no influence on crystallization temperature, which is at 150 °C. This temperature is lower than melting temperature. One possible reason is that the nucleation happens at lower temperature compared to the frozen of polymer chains. The two visible peaks in line 2 in **Figure IV-8** are attributed to the crystallite with different sizes. The separation of them is rather difficult because of their overlap. It is only possible to assume their percentage in melting peaks. Line 6 in **Figure IV-8** indicates the enthalpy change during second heating process while the cooling rate of sample is well controlled. The obtained sample with such cooling procedure may reach its maximum possible crystallinity, with a very homogenous distribution of crystallite size. ω_{c6} and $\beta\%_6$ are results calculated based on line 6 in **Figure IV-8** and summarized in **Table IV-2**. An increase of both parameters compared to their first heat process counterparts could be observed as expected. This is just to show the potential of samples on crystallization. In reality, it is rather difficult to perform such cooling procedure during the fabrication of polymer composites.

Table IV-2. The experimental and theoretical enthalpy of samples obtained from DSC and corresponding crystallinity and β phase percentage in total composite component of PVDF composites

Sample	PVDF	PVDF/1.25 wt% MWCNTs	PVDF/2 wt% MWCNTs	PVDF/4 wt% MWCNTs	PVDF/8 wt% MWCNTs
ΔH_{m2} (J/g)	36.06	41.32	41.37	40.73	40.56
ΔH_{m6} (J/g)	45.74	47.60	48.88	47.67	45.79
ΔH_m^c (J/g)	104.50	122.70	116.37	147.01	159.68
ω_{c2}	34.51%	33.67%	35.56%	27.70%	25.40%
$\beta\%_2$	0	5.32%	3.66%	10.22%	12.17%

ω_{c6}	43.77%	38.79%	42.01%	32.43%	28.67%
$\beta\%_6$	0	6.13%	4.33%	11.97%	13.73%

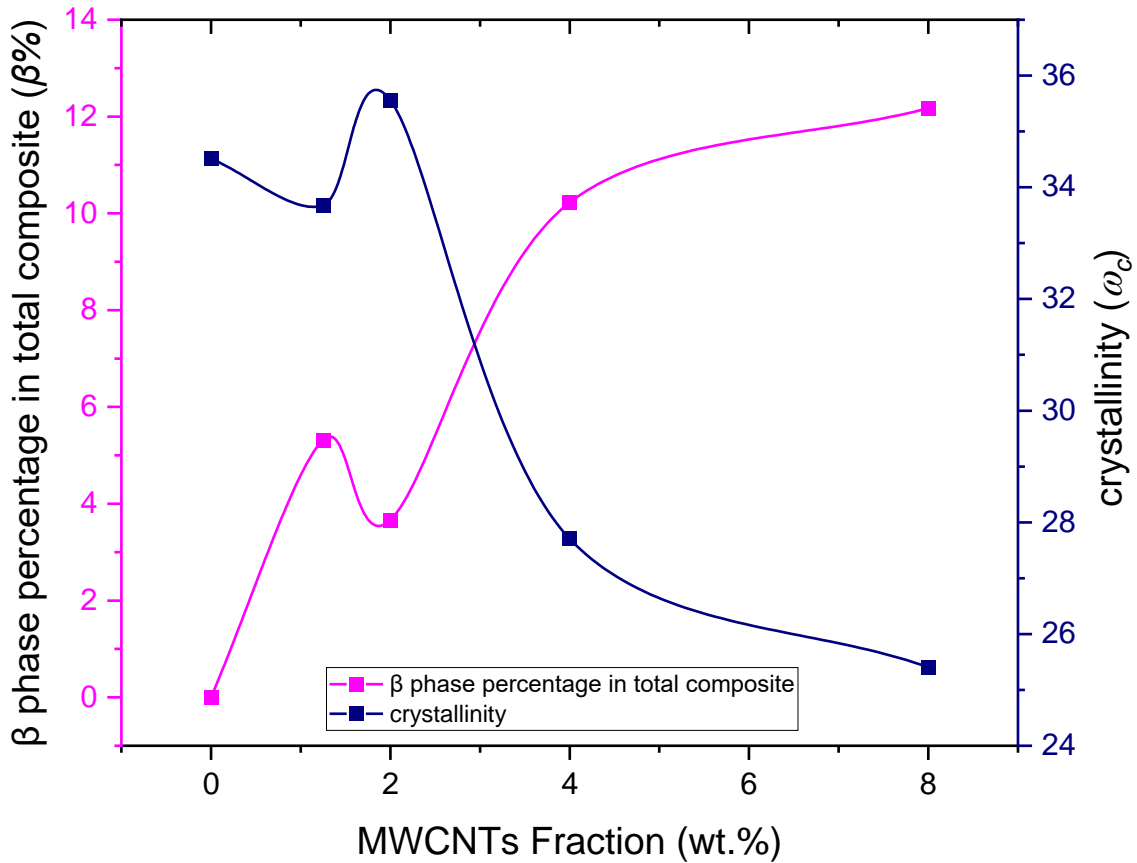


Figure IV-9. ω_c and $\beta\%$ of samples calculated from line 2 in **Figure IV-8** as a function of MWCNTs weight fraction. Solid lines are not fitting curves but guide for eyes to compare the tendency of data.

The formation of PVDF β phase starts to happen when MWCNTs are introduced, which is due to the nucleation effect [185]. MWCNTs may favor the formation of the PVDF β phase but the trend of $\beta\%$ is non-monotonic as a function of the filler fraction. To verify this transmission electron microscopy (TEM) images were performed.

IV. B. 2. b) Nanostructure analysis

The nanostructure of PVDF composite was studied through TEM technique in collaboration with Centre Technologique des Microstructures EZUS LYON (France). **Figure**

IV-10 presents the TEM images of PVDF matrix. Large crystalline regions called spherulites, can be observed from the figure. The boundaries of the lattice are not very clear, which is because PVDF is a semi-crystalline polymer (crystallinity= 34.5%), and there are still many amorphous parts in the matrix.

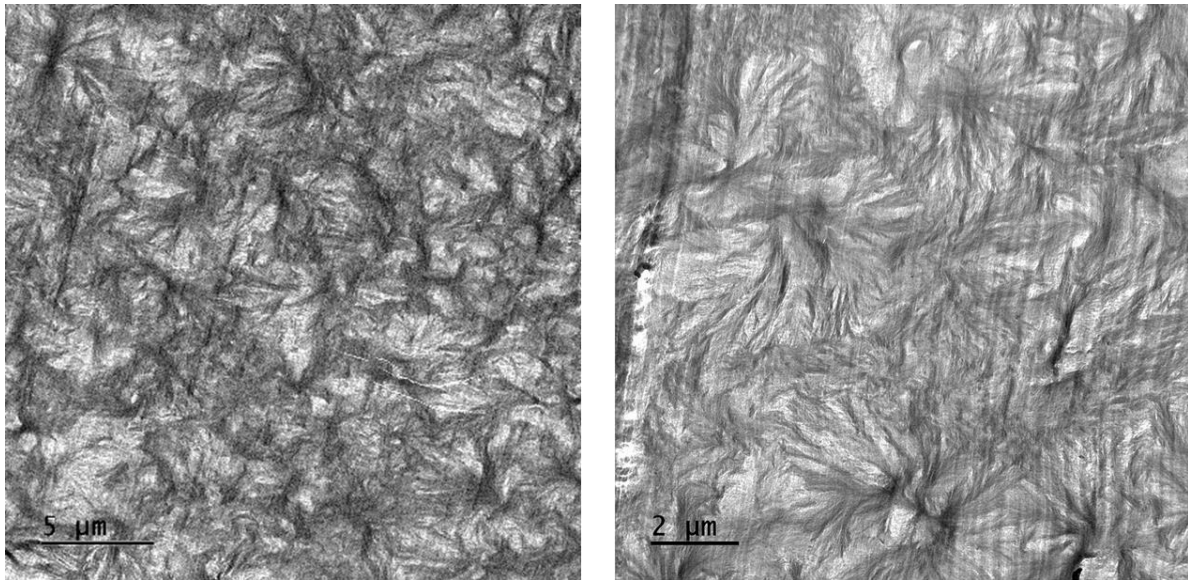


Figure IV-10. TEM images of PVDF matrix.

TEM images of PVDF/8 wt.% MWCNTs sample is shown in **Figure IV-11**. Compared to PVDF matrix, the smooth part, which indicated to amorphous PVDF noticeably increased, which is in agreement with the decrease of ω_c presented in **Figure IV-9**. This is due to the restriction effect of MWCNTs on mobility of polymer chains [179]. New crystalline phases can be clearly observed in the gaps between the entangled carbon nanotube networks. This shows that the addition of MWCNTS can promote the nucleation, thereby promoting the formation of PVDF β phases. The observation through TEM technique supplies some supportive information for the interpretation of our results in terms of thermal conductivity and the development of an analytical model to predict this property for our samples.

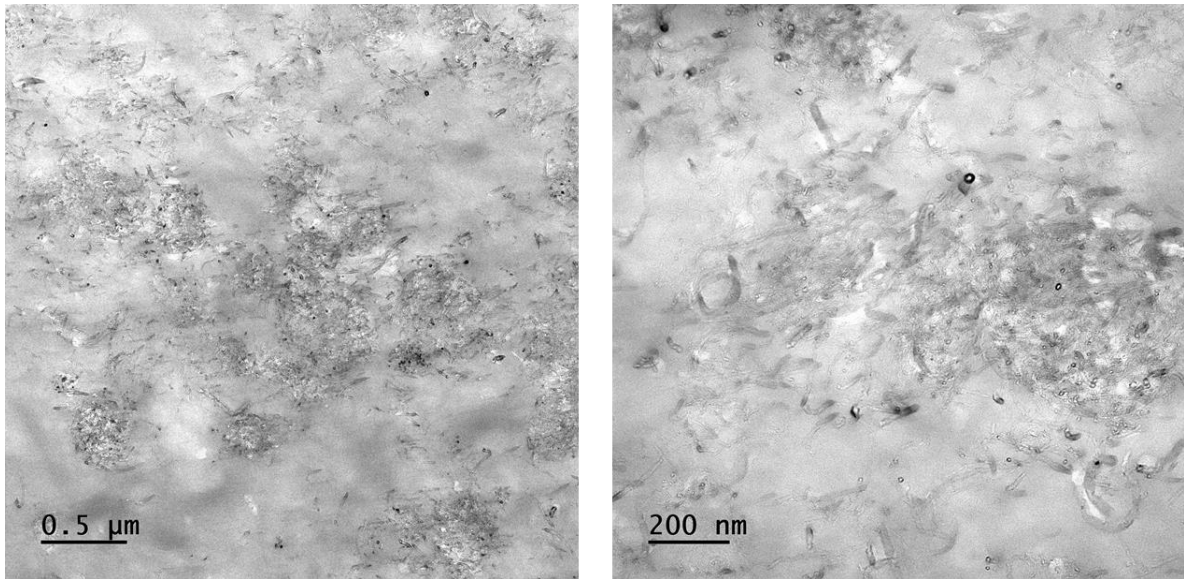


Figure IV-11. TEM images of PVDF/8 wt.% MWCNTs sample.

It is known that a polymer has a thermal conductivity larger when it has a high degree of crystallinity than when it is amorphous [186]. To bring answers to “What is the impact of the increase of the observed β phase when MWCNTs are added to the PVDF matrix on the heat transfer within the nanocomposite materials?”, we measured the thermal conductivity of our PVDF/MWCNTs nanocomposite samples.

IV. B. 2. c) Measurement results for PVDF/MWCNTs samples

Due to the rather high roughness on the surface of PVDF/MWCNTs samples, the contrast in thermal images is almost identical with the topography image. **Figure IV-12** shows the topography and thermal images for composite containing 4 wt.% MWCNTs as an example. No obvious difference can be observed from the two images, that is in good agreement with the well dispersion of MWCNTs inside the PVDF matrix proved by SEM images [166].

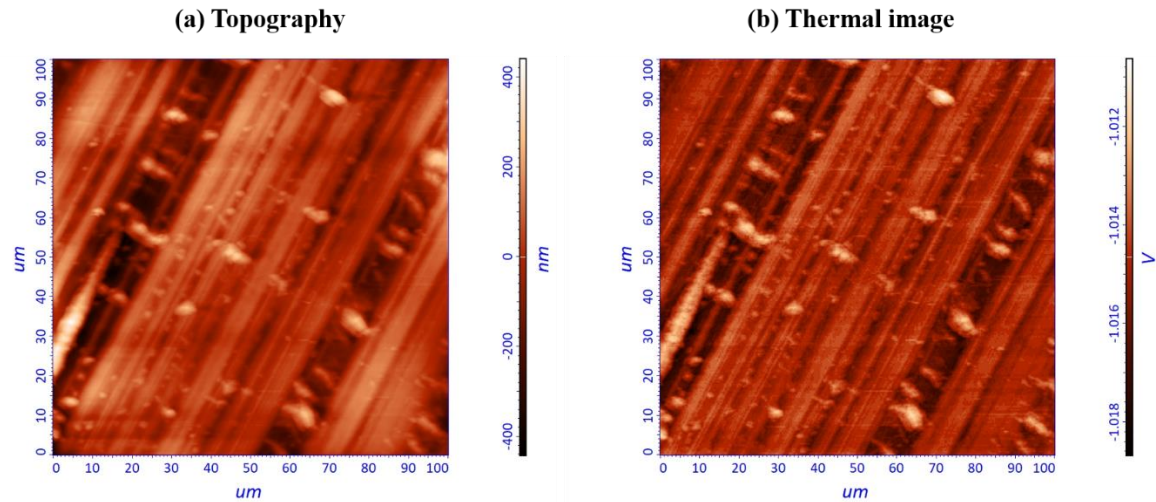


Figure IV-12. Topography and thermal images for the PVDF composite containing 4 wt.% MWCNTs.

The k_{eff} of the samples is calculated from the average value of the signal lying inside selected area that avoids the variation caused by roughness as much as possible. The results have been plotted as a function of MWCNTs weight fraction in **Figure IV-13**. The PVDF matrix displays a thermal conductivity of approximately 0.24 W/(m.K), which is very close to the value proposed by literature [187]. It can be seen that an enhancement of thermal conductivity is achieved with the addition of MWCNTs, which confirm the observation in literature [160]. No percolation behavior, as detected for the electrical conductivity results [166], appears for the thermal properties, which is in agreement with the results reported in literature [188]. The reason may be that the expansion of heat flux aroused by the formation of MWCNTs network is very slight due to relatively small thermal conductivity ratio ($\sim 10^4$) between MWCNTs and PVDF matrix compared to electrical issue ($\sim 10^{11}$). The heat dissipated through polymer matrix is still the main part of heat transfer [189]. Another possibility is the high thermal resistance at the interface between individual carbon nanotube, leading to the insufficient channel for heat transfer [190]. The k_{eff} reaches 0.36 W/(m.K) while the fillers loading is 8 wt.%, which is at the same level compared to PVDF filled with graphene (0.32 W/(m.K) for 10 wt.%) [191] or conducting carbon black (0.4 W/(m.K) for 10 wt.%) [192], but lower than the one filled with reduced graphene oxide (rGO) (0.89 W/(m.K) for 3 wt.%) [193]. The enhancement of thermal conductivity induced by rGO is explained as the crystallite size dependence on filler concentration [193]. It is worth to note that in our measurement, a

nonmonotonic trend of the thermal conductivity results versus MWCNTs weight fraction is observed. In addition, this trend is strongly in concurrence with the PVDF β phase relative percentage $\beta_r\%$ and PVDF β phase percentage in total composite $\beta\%$, as shown in **Figure IV-13**. This suggests that there may be a connection between the formation of PVDF β phase and the variation in thermal conductivity.

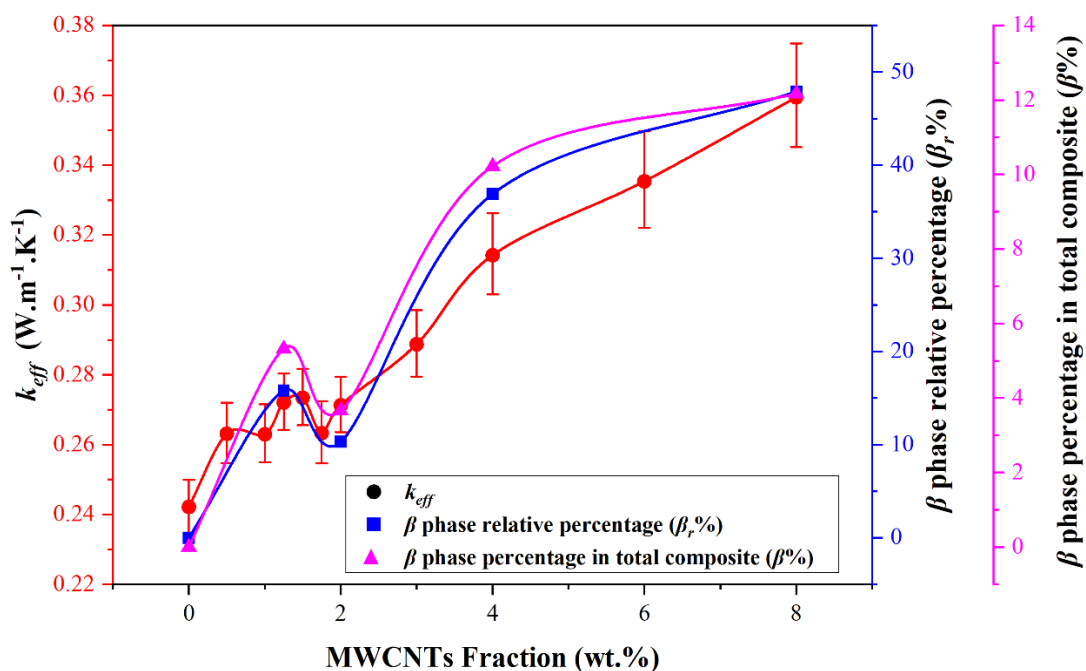


Figure IV-13. k_{eff} , $\beta_r\%$ and $\beta\%$ of PVDF/MWCNTs composite versus weight fraction % of MWCNTs). Solid lines are not fitting curves but guide for eyes to compare the tendency of data.

The formation of PVDF β phase is strongly linked to the fabrication condition and very complicated to be predicted. However, the β phase PVDF is a kind of crystalline polar polymer with an all-trans conformation, which is suggested to be favorable for the heat transfer by increasing the mean free path of energy carriers [194]. Consequently, it is reasonable to suppose that the formation of β phase PVDF may facilitate the thermal transport considering that the electric and thermal current flows at macroscopic dimensions share the same equation [189]. The high degree of overlap between k_{eff} and $\beta\%$ reinforces the hypothesis that MWCNTs improve the thermal behavior of polymer composite by affecting the crystalline phase of the PVDF matrix. This result provides powerful evidence for interpreting the non-monotonic trend

of thermal conductivity as a function of filler concentration by matrix crystallinity mechanism in addition to aggregation effect [195] and thermal interfacial resistance effect [196]. In summary, the formation of MWCNTs heat conduction paths and a relatively higher crystallinity of PVDF matrix leads to the enhancement of the composite k_{eff} .

To go further in our analysis of these results a modelling to reproduce the values of k_{eff} measured by SThM was developed.

IV. B. 2. d) Analytical thermal modeling of the PVDF/MWCNTs nanocomposites

IV. B. 2. d. (i) State-of-the art

To better understand the role of introduced carbonous fillers and the heat transfer tuning mechanism, an analytical model is required. This model is supposed to describe the polymer composite system properly. Different theoretical and empirical models have already been developed to calculate or predict the thermal conductivity of a composite material. The simplest ones among them are rules of mixture which are given by [197]:

Parallel model:

$$k_c = k_f \cdot \Phi + (1 - \Phi)k_m \quad (\text{IV-2})$$

Series model:

$$\frac{1}{k_c} = \frac{\Phi}{k_f} + \frac{(1 - \Phi)}{k_m} \quad (\text{IV-3})$$

Geometric mean model:

$$k_c = k_f^\Phi \cdot k_m^{(1-\Phi)} \quad (\text{IV-4})$$

where k_c , k_f , k_m represent the thermal conductivity of composite, fillers, and polymer matrix, respectively. Φ indicates the volume fraction of fillers.

The schematic of parallel model and series model is presented as **Figure IV-14**. Parallel model considers that the polymer matrix and the gathered fillers are arranged in parallel in the same direction of the heat flux, which is equivalent to the highest enhancement of the thermal conduction case. Meanwhile series model considers that the polymer matrix and the gathered fillers are arranged in series in the direction of the heat flux, which represents the less enhanced thermal conduction case. This leads to an overestimation or underestimation of composite's thermal conductivity. In addition, the hypothesis of both models about gathered fillers is against the fact that no agglomeration of fillers is observed in our PVDF composites.

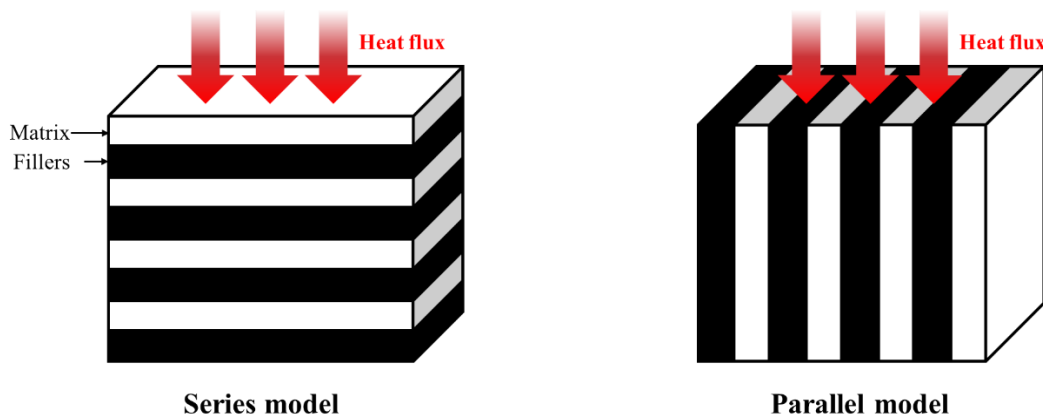


Figure IV-14. Schematic of series model and parallel model.

Furthermore, there are some other models that assume that there is no mutual interaction between fillers such as the Russell's model [198] and the Maxwell's model [199]. In these models, the shape of the fillers can be either treated as identical cubes or homogenous spheres as exposed by Russell's model or Maxwell's one, respectively. However, such models cannot be applied to the MWCNTs filler case study due to its cylinder structure and high aspect ratio.

Several other effects are taken into account in different other models like i) the effect of the filler's shape using the Hamilton-Crosser's Model [200], ii) the interfacial thermal barrier effect using Hasselman's model [201], and iii) the effect of dispersion of fillers via Cheng-Vachon's model [202]. Nevertheless, all the above models neglect the effect of the crystallinity

of the polymer matrix.

In the same prospect, many empirical models were also developed to predict the polymer composite thermal conductivity[203], [204]. Nevertheless, the know parameters, i.e., input parameters, of the model that are used to fit the experimental results are usually difficult to be explained physically. A summary of abovementioned models and their mathematic equation are listed in **Table IV-3**.

Thus, in order to provide a better point of view on the understanding of the thermal conductivity's enhancement mechanism, a model specifically designed for the PVDF composite samples of our study was developed in the thesis. This model is based on Eq. IV-4. This equation is chosen because it excludes the unknow parameters of our samples such as the aspect ratio of fillers. This parameter could change significantly during mixture with PVDF matrix and become inhomogeneous due to the breaks and fractures of MWCNTs. Another reason for using this equation is that it can be easily modified to take into consideration the effect of the crystalline phases of the PVDF matrix while the other models do not focus on such situation.

Table IV-3. Summary of some analytical and empirical models from literature.

Model	Equation	Comment
Russell's model	$k_c = k_m \frac{\phi^{\frac{2}{3}} + \frac{k_m}{k_f} \left(1 - \phi^{\frac{2}{3}}\right)}{\phi^{\frac{2}{3}} - \phi + \frac{k_m}{k_f} \left(1 - \phi^{\frac{2}{3}}\right)}$	no mutual interaction between fillers
Maxwell's model	$k_c = k_m \frac{2k_m + k_f + 2\phi(k_f - k_m)}{2k_m + k_f - \phi(k_f - k_m)}$	shape of the fillers be treated as identical cubes or homogenous spheres

Hamilton-Crosser's Model	$k_c = k_m \left[\frac{k_f + (n-1)k_m + (n-1)\Phi(k_f - k_m)}{(n-1)k_m + k_f - \Phi(k_f - k_m)} \right]$	introduced a factor of sphericity ($\psi \leq 1$) $n=3/\psi$
Hasselmann's model	$k_c = k_m \frac{k_f(1+2\alpha) + 2k_m + 2\Phi[k_f(1-\alpha) - k_m]}{k_f(1+2\alpha) + 2k_m - \Phi[k_f(1-\alpha) - k_m]}$	$\alpha = a_k/a$, a is the radius of spherical particles; a_k stand for Kapitza radius
Cheng-Vachon's model	$\frac{1}{k_c} = \frac{(1-B)}{k_m} + \frac{1}{\{C(k_f - k_m)[k_m + B(k_f - k_m)]\}^{1/2}} \ln \frac{[k_m + B(k_f - k_m)]^{1/2}}{[k_m + B(k_f - k_m)]^{1/2}}$	Dispersion factors B and C is in function of Φ

Consequently, in the interest of making the model fully applicable to our situation, it is worth to mention again that the formation of PVDF β phase is due to the nucleation effect. In this case it is reasonable to assume that all formed PVDF β phase is around MWCNTs, and these two components can be combined as a new filler MWCNTs- β as shown in **Figure IV-15**. MWCNTs- β could be also regarded as a composite where the polymer matrix is PVDF β phase and the filler are MWCNTs. This assumption is not entirely accurate especially when the volume fraction ratio between PVDF β phase and MWCNTs is low. Such situation is equivalent to a serious agglomeration of fillers which does not match what the model describes. This deviation between assumptions and reality has been taken into account as one of the possible sources of error in the results.

IV. B. 2. d. (ii) Proposed model and its application to sample analysis

The k_f in Eq. IV-4 can be used to indicate the effective thermal conductivity of MWCNTs- β and expressed as:

$$k_f = k_{MWCNTs}^{\Phi'} \cdot k_{\beta}^{(1-\Phi')} \quad (IV-5)$$

Here k_{MWCNTs} and k_{β} represent the thermal conductivity of PVDF β phase and MWCNTs respectively, Φ' is the volume fraction of MWCNTs normalized by volume of MWCNTs- β . Physically k_m in Eq. IV-4 represents the effective thermal conductivity of PVDF matrix which includes amorphous part and PVDF α phase. These two phases are contiguous and could be appropriately calculated using Eq. IV-2 also referred as mixture law [205]. k_m can be then expressed as:

$$k_m = k_{\alpha} \times \omega_{\alpha} + k_A \times (1 - \omega_{\alpha}) \quad (IV-6)$$

where k_{α} and k_A represent the thermal conductivity of PVDF α phase and amorphous part respectively, ω_{α} is the volume fraction of PVDF α phase normalized by the volume of PVDF matrix. Henceforth, Eq. IV-4 can be then rewritten as:

$$k_c = (k_{MWCNTs}^{\Phi'} \cdot k_{\beta}^{(1-\Phi')})^{\Phi} \cdot (k_{\alpha} \times \omega_{\alpha} + k_A \times (1 - \omega_{\alpha}))^{(1-\Phi)} \quad (IV-7)$$

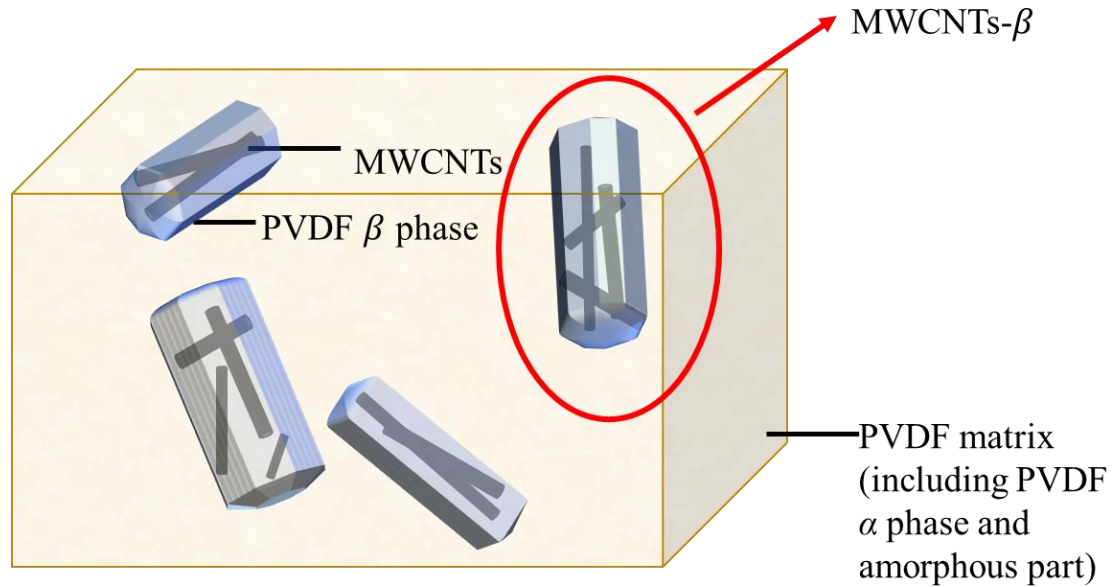


Figure IV-15. Schematic of PVDF composite filled with MWCNTs

This formula was used as the analytical model to fit the thermal conductivity measured by SThM in order to deduce the thermal conductivity of MWCNTs k_{MWCNTs} and of PVDF β phase k_{β} in composite.

Figure IV-16 shows the fitting result using the model. One should note that only the five experimental points, representing five of the studied samples, are adjusted using the model, i.e., the solid lines are just a guide for the eye in order to compare the tendencies of the results. From this modeling k_{MWCNTs} and k_{β} were found equal to 5.75 W/(m.K) and 1.32 W/(m.K), respectively. The residual norm of fitting is in the order of 1×10^{-5} . The reason of lower k_{MWCNTs} compared to theoretical values found in literature (generally considered as $\sim 3000 - 6000$ W/m . K [206]) is on one hand related to the fact that the quality of MWCNTs cannot be kept as high as the pristine ones, where their orientation is randomly distributed during the composite fabrication process. On the other hand, the interfacial thermal resistance is not independently separated in this model, and it will be correlated to the k_{MWCNTs} and k_{β} , which makes their values lower than expected. Even though a higher k_{β} compared to α phase and amorphous part of PVDF matrix is demonstrated and this corroborates our inference.

It is also interesting to note that by comparing the DSC results shown in **Figure IV-8**, it could be confirmed that the arise of γ crystallites melted at slightly higher temperature of 176 °C than α and β crystallites (T_m at 171 °C) while the cool rate is well controlled. This provides us the crystallization potential of PVDF composite samples. The increasing effect of MWCNTs is also visible in **Figure IV-8** where the growing of peaks corresponds to the γ phase. In addition, it has been demonstrated in literature that γ phase may enhance the thermal properties of PVDF more than β phase [193]. Hence, it is reasonable to suppose that the formation of β and γ phase PVDF together may facilitate/enhance the thermal transport further.

Using the fitted parameters k_{MWCNTs} and k_{β} , the thermal conductivity of fully crystallized PVDF/MWCNTs composite can be predicted. For the sample with 8 wt.% filler loading, the predicted thermal conductivity is approximate 0.373 W/(m.K). This suggest that the thermal conductivity of PVDF/MWCNTs composite could be enhanced by adjusting the cooling rate after fabrication to obtain a higher crystallinity of PVDF composite.

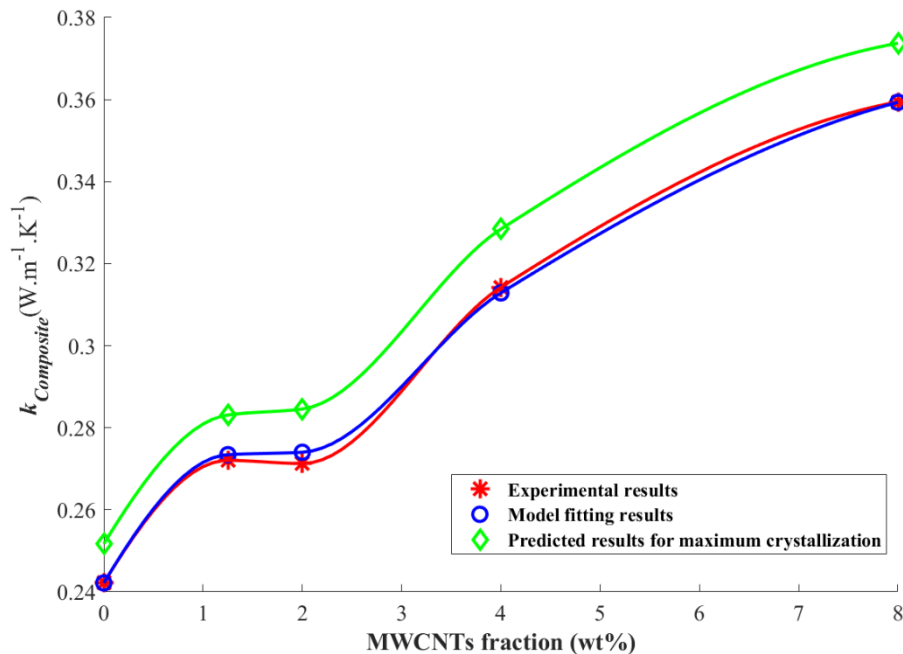


Figure IV-16. Experimental thermal conductivity, model fitting results and predicted results for fully crystallization of PVDF/MWCNTs composite versus weight fraction % of MWCNTs). Solid lines are not fitting curves but guides for eyes to compare the tendency of data.

Different k_{MWCNTs} have also been tested to simulate the thermal conductivity results as shown in **Figure IV-17**. It could be seen that a higher thermal conductivity of MWCNTs may result in a deviation of the fitting result from the experimental data. This suggests that the thermal conductivity of MWCNTs decreases significantly during the fabrication process. This is in agreement with the result proposed by Mohammad Nejad et al. by molecular dynamics (MD) that the thermal conductivity of MWCNTs may decrease with their length [207]. In addition, the interfacial thermal resistance between MWCNTs- MWCNTs and MWCNTs- PVDF plays a non-negligible role.

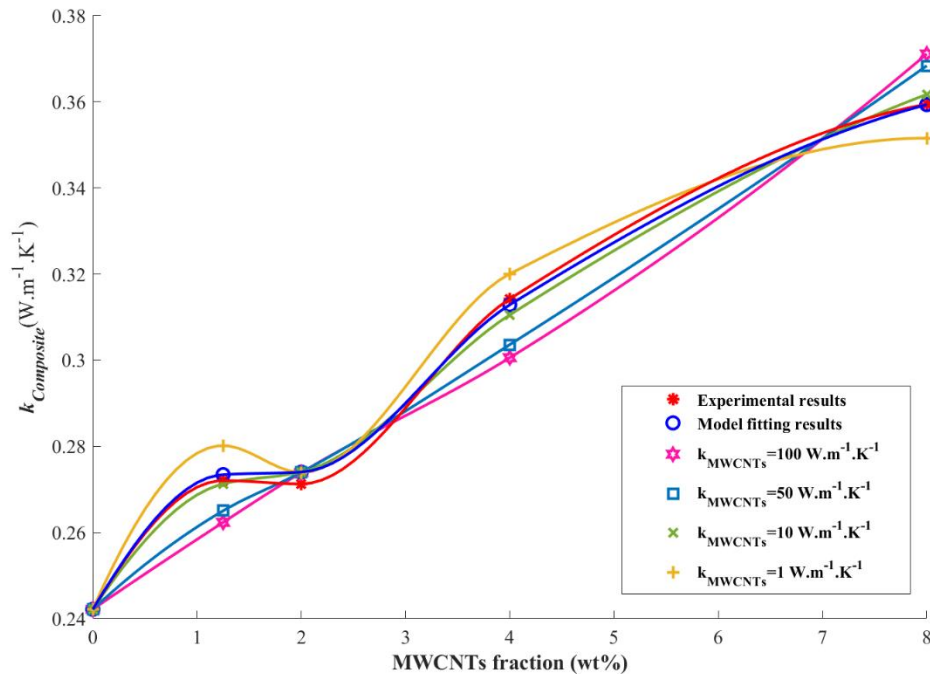


Figure IV-17. Model fitting results for four arbitrarily selected values of k_{MWCNTs} . Solid lines are not fitting curves but guides for eyes to compare the tendency of data.

IV. C. Conclusions and perspectives

Through SThM measurements the heat transfer enhancement mechanisms in two types of polymer-carbon filler composite i) HDPE filled with 50 μm EG composites and ii) PVDF/MWCNTs composites, versus carbon filler weight fraction within the polymer, were investigated. In principle, the characterization of the thermal conductivity of polymer

composites phenomena, such as agglomeration effect, can only be suggested from the combination of effective modeling with measurements at the macroscale. To this end, in this manuscript we proved that the SThM technique allows the local investigation of polymeric materials with a micrometric spatial resolution thermal image, providing some possibilities to demonstrate the aforementioned agglomeration effect.

For HDPE/EG samples SThM images allow the detection of zones with a thermal conductance larger than that of the matrix for the highest filler concentration studied. These zones correspond to EG filler agglomerates within the polymer and explain the observed enhancement of the thermal conductivity of the HDPE/EG composite. The k_{eff} results obtained by SThM are comparable but lower than those measured by PTR method, flash method and modeling. The reason may be that the inhomogeneous distribution of EG fillers can affect the representativeness of data collected by microscale probe. In this case, the k_{eff} account more heat transfer capability of polymer matrix than the real situation. This has been well demonstrated by the result of HDPE/EG composite with 2 wt.% fillers.

For PVDF/MWCNTs samples it is found from that thermal conductivity increases from 0.242 W/m.K for pristine PVDF to 0.359 W/m.K for PVDF nanocomposites filled with 8 wt.% MWCNTs. This variation versus filler concentration is found in good correspondence with that of the β phase relative percentage in the PVDF nanocomposites. This suggests that the observed heat transfer enhancement is rather due to the formation of β phase for PVDF/MWCNTs samples resulting of the addition of MWCNTs than the addition of MWCNTs itself. MWCNTs disperse well and form heat conduction network in the PVDF. MWCNTs can also promote the formation of β and γ phase crystallites, which increase the mean free path of energy carries and then the thermal conductivity of samples.

Additionally, a new analytical model was developed to better understand the impact of the β phase of PVDF on heat transport in PVDF/MWCNTs materials. The k_{MWCNTs} and k_{β} was found as 5.75 W/(m.K) and 1.32 W/(m.K), respectively.

Such thermally conductive polymer composites can help solving the current heat dissipation issues in different applications, using polymer-based material, like in automobile, packaging, aerospace, energy harvesting, electromagnetic interfaces (EMIs), fifth-generation mobile network, and electronic devices industries. The result of this study may provide a new point of view for the management and tuning of thermophysical properties of polymer-based composite.

Perspectives of this work include the application of the SThM technique to other polymer composites with carbon-based nanofillers such as graphene or rGO nanosheets for comparison and innovative 2D material nanoflakes. I started in the frame of my works the analysis of the effect of MWCNTs and a new type of MXene in polymethyl methacrylate (PMMA) on the heat conduction in PMMA. First results are given in the following chapter.



Chapter V. THERMAL CHARACTERIZATION OF POLYMER COMPOSITES WITH MXene-BASED FILLERS

This chapter presents the first results of an analysis of the effect of MWCNTs and a new type of two-dimensional material MXene on the thermal conductivity of polymethyl methacrylate (PMMA) via SThM technique. The synergistic effect between both kinds of fillers has also been studied.

V. A. Context

In addition to carbon fillers studied in previous chapter, a new type of 2D nanomaterials MXene, firstly reported in 2011 [208], has drawn increasing attention from scientific community due to its various high potential valuable properties such as combined metallic conductivity and hydrophilic surfaces [208].

MXene is a carbide or nitride with a multilayered structure and metallic properties. MXene have a general formula of $M_{n+1}X_nT_x$ ($n = 1, 2, \text{ or } 3$), where M denotes transition metal, X denotes carbon and/or nitrogen atom, and T denotes the surface terminations ($-OH$, $-O$, and/or $-F$) due to HF etching. MXene is considered as a highly promising material in various applications such as energy storage [209], transparent conductors [210], as well as thermal management domain [211]. Among the MXene family, $Ti_3C_2T_x$ has received widespread attention and research in recent years. The thermal conductivity of $Ti_3C_2T_x$ has been characterized as 55.8 W/(m.K) by temperature-dependent Raman spectroscopy and polarized-laser power-dependent Raman spectroscopy [212], making MXene a promising thermal filler for polymer materials. Several earlier research studies have reported the integration of MXene into various polymer matrices, including polyvinyl alcohol (PVA), epoxy, polypyrrole (PPy) and rubber [211]. In this study, PMMA will be used as polymer matrix to investigate the effect of $Ti_3C_2T_x$ MXene on its thermal conductivity.

In addition, synergistic hybrid effect between fillers with different shapes (such as graphene nanoplatelet (GNP) and multi-walled carbon nanotubes (MWCNTs)) on improving the thermal conductivity of polymeric composites has been demonstrated [213]. It is proposed that a prolate shape type filler may form conductive networks within the gaps between the 2D sheet materials, resulting in a synergistic effect [213]. In this study, MWCNTs are also incorporated with 2D MXene to investigate their synergistic hybrid effect on the tuning of PMMA thermal conductivity.

V. B. Sample description

PMMA is a transparent thermoplastic material (molecular formula shown in **Figure V-1**), making it an ideal substitute for traditional inorganic glass in various applications. PMMA is widely used in industries such as automotive, sensor, and conductive devices due to its unique optical transparency, lightweight and favorable manufacturing conditions [214].

PMMA pellets Plexiglas® 7N used in this study were obtained from Röhm GmbH. (Germany). Multi-layered MXene $Ti_3C_2T_x$ were received from Drexel University (Philadelphia, Pennsylvania, U.S.A.) (concentration 0.767g of MXene per 1g of MXene paste). Multi-walled carbon nanotubes (MWCNTs) Nanocyl 7000 were purchased from Nanocyl S.A. (Sambreville, Belgium). The delamination process of titanium carbide MXene and preparation process of composites are given in Appendix 8.

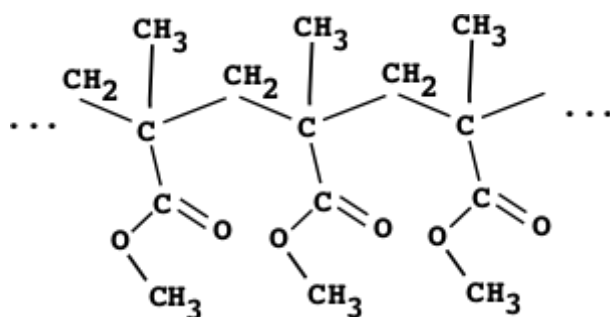


Figure V-1. Molecular formula of PMMA.

V. C. Thermal conductivity determination

The effect of carbon nanotubes and MXene on the thermal conductivity of PMMA based composite has been investigated via SThM technique and a TCU based on a balanced Wheatstone bridge. Measurement setup and procedure are explained in **Chapter II**.

V. C. 1. Roughness measurement

The roughness and the topography of a sample are crucial factors in determining the heat transfer that occurs through the mechanical contact between a SThM probe and a sample [84]. Thus, in order to evaluate its impact on SThM measurement, the roughness analysis of PMMA composite samples were performed firstly. The procedure for measuring surface roughness uses a conventional AFM probe and is described in **Chapter III**.

Sq values and their corresponding standard deviation are calculated by the same analysis procedure described in Chapter III and summarized in **Table V-1**. It could be seen that the averaged roughness *Sq* of PMMA composites is larger than 10 nm except 8 nm for PMMA matrix. It can be also observed that *Sq* value increases significantly with the characterized area size. This is mainly due to the fact that the surface of PMMA samples is not flat and has topography features with large height. The presence of these features cannot be neglected in the interpretation of SThM measurement results that are given in the next section.

Table V-1. Roughness of PMMA composite samples

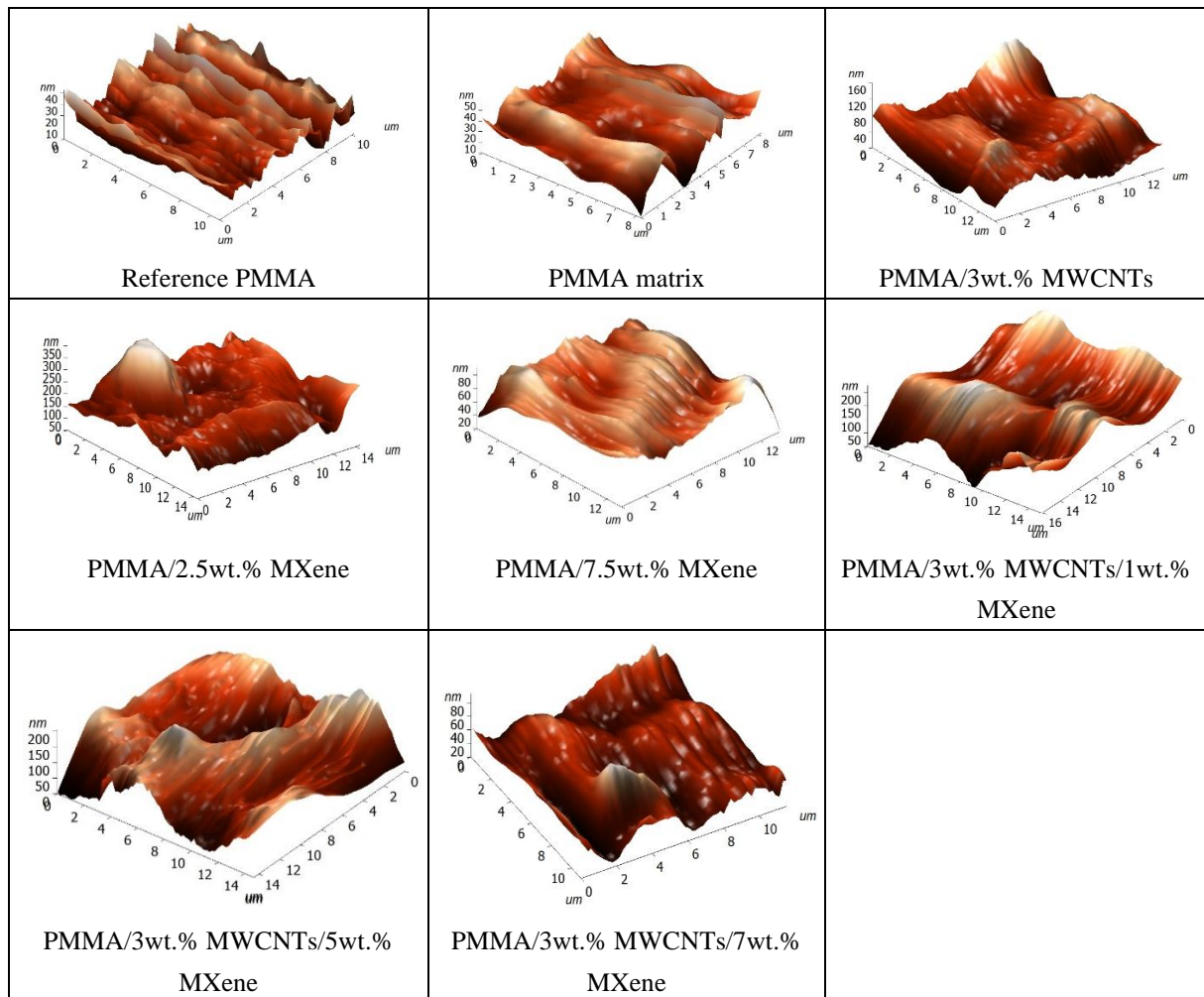
	Area [μm^2]	PMMA	PMMA/2.5	PMMA/7.5	PMMA/3	PMMA/3	PMMA/3	PMMA/3
			wt% MXene	wt% MXene	wt% CNTs	wt% CNTs/1 wt% MXene	wt% CNTs/5 wt% MXene	wt% CNTs/7 wt% MXene
<i>Sq</i> [nm]	1x1	6.80	8.16	7.44	9.02	18.43	10.47	14.68
<i>Sq</i> [nm]	2x2	6.42	14.26	13.99	22.19	28.60	10.61	20.51
<i>Sq</i> [nm]	2x2	7.09	7.87	20.73	14.52	32.13	18.17	16.15
<i>Sq</i> [nm]	2x2	10.49	18.71	17.73	11.59	28.51	17.52	15.36
<i>Sq</i> [nm]	20x20	24.55	38.03	46.28	76.53	147.84	83.30	43.33
<i>Sq</i> avg [nm]		8.00	13.61	17.48	16.10	29.75	15.43	17.34

std_{sq} [nm]		1.78	4.45	2.76	4.47	1.69	3.42	2.26
--------------------	--	------	------	------	------	------	------	------

V. C. 2. Measurement results for PMMA samples

Topography and thermal images were performed using a Wollaston probe operated at approximately 100°C on 10x10 μm^2 areas of PMMA composites and PMMA reference sample. **Table V-2** summarises topography results. Results show that while PMMA reference sample is rather flat, PMMA composite samples present valleys with sizes that are comparable to that of the apex of the Wollaston probe.

Table V-2. Topography of PMMA composite samples obtained by Wollaston probe.



The Wollaston probe used was calibrated using reference samples with thermal conductivity close to polymeric materials and following the protocol described in **Chapter II**. **Figure V-2** shows the calibration curve obtained and that could have been used for the estimation of the thermal conductivity of PMMA composites. Results are shown in **Figure V-3**.

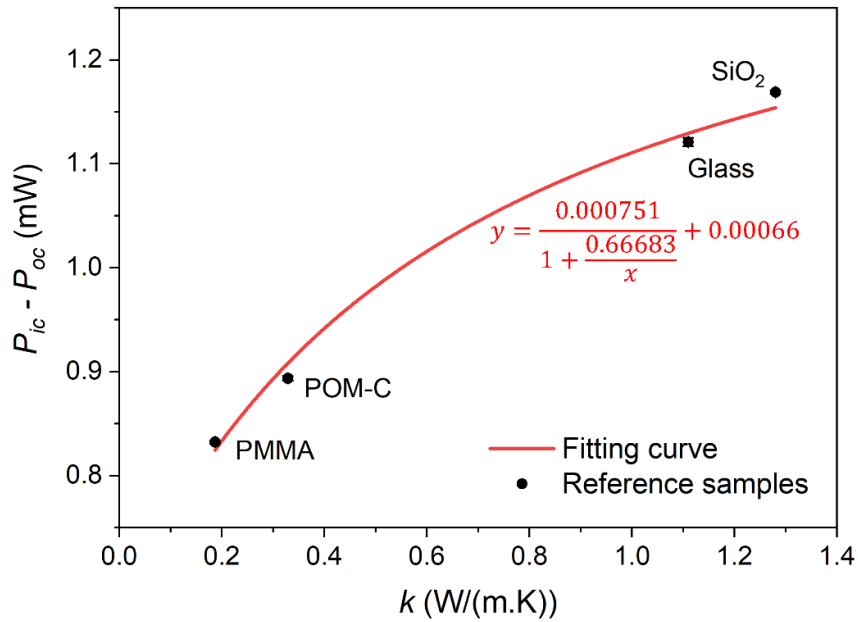


Figure V-2. Calibration curve obtained experimentally from the measurement of reference samples [83]: PMMA ($k_{PMMA} = 0.187 \text{ W} \cdot \text{m}^{-1} \cdot \text{K}^{-1}$), POM-C ($k_{POM-C} = 0.329 \text{ W} \cdot \text{m}^{-1} \cdot \text{K}^{-1}$), Glass ($k_{Glass} = 1.11 \text{ W} \cdot \text{m}^{-1} \cdot \text{K}^{-1}$) and SiO₂ ($k_{SiO_2} = 1.28 \text{ W} \cdot \text{m}^{-1} \cdot \text{K}^{-1}$). The equation in red is the expression of the fitting curve of the measurements.

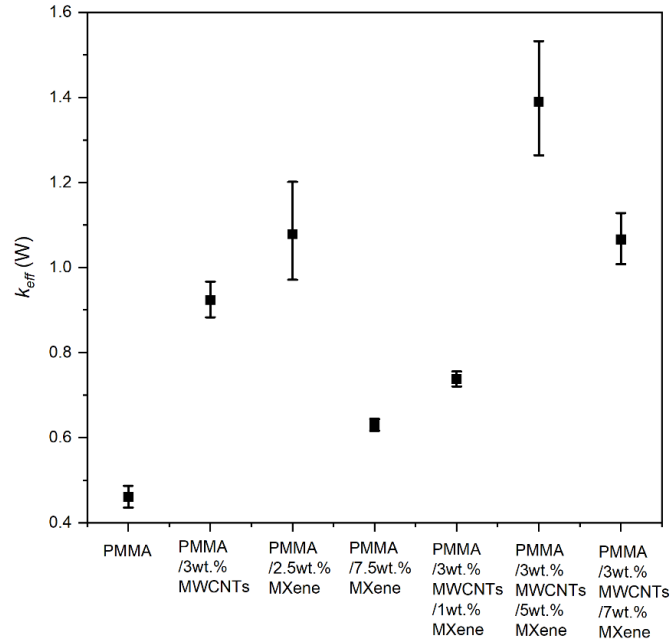


Figure V-3. Effective thermal conductivity of PMMA composites deduced by calibration curve.

The result for pristine PMMA samples is 0.46 W/(m.K) and is then larger than the one of reference PMMA sample (0.187 W/(m.K)). This value exceeds the possible range of k values for PMMA that have been reported in the scientific literature (0.167-0.25 W/(m.K) at RT) [215].

For Wollaston probe, the thermal contact radius with polymeric material may reach several micrometers because a large portion of heat is transferred from the heated microsensor to the sample by thermal conduction through air. The influence of roughness on overall heat transfer is primarily through affecting heat transfer through solid-solid contact.

However, the surface topography of the sample still has a significant impact on heat exchange between probe and samples due to the long range of thermal conduction by air. The schematic of such phenomenon is shown in **Figure V-4**. It could be seen that when probe is in contact with a sample that have comparable size valleys topography, the heat exchange towards sample is enlarged. This may explain the fact that the measured k_{eff} of neat PMMA is significantly higher than the value of the reference PMMA. Considering that all PMMA composite have a significant surface topography as observed in **Table V-2**, only qualitative

analysis could be made for obtained k_{eff} results.

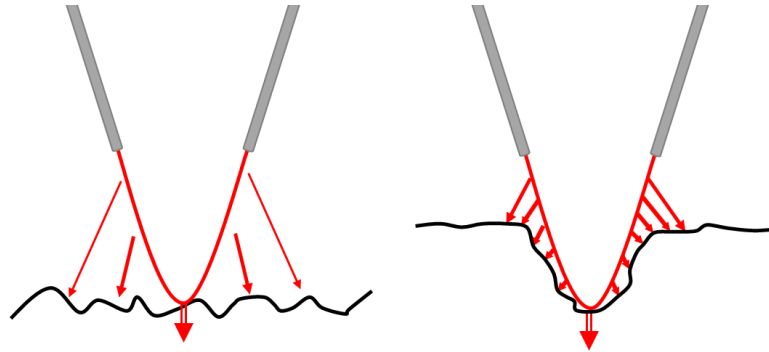


Figure V-4. Schematic of contact condition of a Wollaston probe with a sample without (left) or with (right) significant topography.

It could be observed that by add MWCNTs or MXene into PMMA, the thermal conductivity increase compared to neat PMMA. While the sample containing 7.5wt.% MXene have a lower k_{eff} than the counterpart containing 2.5wt.% MXene. This suggests a negative effect of MXene on thermal conductivity when MXene concentration exceeds a certain level. This may be due to the inter-flake thermal resistance when MXene flakes stack at high concentration [216]. Unfortunately, due to the limited number of samples, further analysis and discussion cannot be made at this time. Furthermore, no clear synergistic hybrid effect between MXene and MWCNTs could be observed.

V. D. Conclusions and perspectives

State of art shows that MXene has emerged as a promising nanomaterial due to its various potential properties such as metallic conductivity and hydrophilic surfaces. The effect of MXene as thermal conductive fillers on PMMA matrix is studied through SThM. Attempts were also made to investigate the synergistic hybrid effect on thermal conductivity tuning in PMMA polymer matrix between MXene and MWCNTs.

Due to the serious topography on the surface of PMMA composites, SThM cannot provide accurate information about the thermal conductivity of samples. Qualitatively speaking, addition of MWCNTs or MXene into PMMA may enhance the thermal conductivity compared

to neat PMMA. While high concentration of MXene may cause a decrease in thermal conductivity compared to PMMA containing low concentration.

The strong influence of topography and roughness of sample surface on SThM measurement results is also demonstrated clearly through this study. To further study these samples, a series of samples with a greater number of specimens and smoother sample surfaces would be necessary.

General conclusion and perspectives

These research works have been carried out in the frame of the establishment of treatment processes of materials dedicated to the tuning of the thermal conductivity (k) of materials for oriented applications that are in strong link with the thermal management of systems (**Chapter I**). The focus has been made on two types of materials:

(1) amorphous CrSi_2 , which is a semiconductor-like material and part of the TM-silicides studied for thermoelectric application. In this case, the material treatment process to be evaluated consisted in its implantation with ions of Ne and Al at room temperature and 250 °C and expected results are the decrease of the CrSi_2 thermal conductivity.

(2) polymeric based nanocomposites, that are involved in many applications where heat transfer must be enhanced or optimized depending on the concerned application. For these materials, the treatment is the introduction of highly conductive nanofillers in the polymer-based matrix.

For both the types of materials studied, the goals were to:

- improve the understanding of the mechanisms of the thermal conductivity variations observed as a function of the treatment conditions,
- measure the thermal conductivity of the materials previously treated in different conditions,
- develop new tools for the analysis of results when required,
- evaluate the treatment process and propose ways to improve it.

As reminded in the following, the works performed during the thesis bring results and highlight open questions to go further for all these research topics of the thesis. They also allow to analyze the methodology used to interpret the measurement by means of SThM (detailed in **Chapter II**) and to propose ways to improve this methodology for the analysis of thin films and polymeric bulk samples.

Results of the analysis of amorphous CrSi₂ thin films on substrate implanted with ions of Ne and Al at room temperature and 250 °C.

(Chapter III).

The main approaches used for tuning the thermal conductivity mainly consist for thermoelectric materials in introducing scattering centres for energy carriers for reducing k , but it is also found that nanocrystallites in an amorphous matrix can also contribute to the filtering of energy carriers and decrease the material thermal conductivity.

CrSi₂ is still a material that is not well known in its amorphous state. Scientific literature furthermore shows that the temperature of the material during irradiation is also a parameter to be exploited to decrease the thermal conductivity as in a range of temperature larger than RT a part of the amorphous material crystallizes due to a radiation-enhanced phase transformation process.

We studied using SThM amorphous chromium disilicide (CrSi₂) modified by Ne and Al ion implantations at RT and 250°C. Our results give a new estimation of the thermal conductivity for the amorphous CrSi₂ of about 6.5 W/m.K. As expected, it is lower than the thermal conductivity of the crystalline CrSi₂. The found k reduction is about 60% and heat conduction is shown mainly acting via phonons.

Changes of the microstructure of amorphous CrSi₂ as a function of the implantation irradiation conditions are in good accordance with those previously found elsewhere in the scientific literature. Identified thermal conductivity values show that ion implantation induces substantial modifications on the microstructure of amorphous CrSi₂, which induces the decrease of the material thermal conductivity k . The k reduction is more pronounced for the implantation at 250°C.

For Ne implantation at RT and 250°C Ne bubbles should act as efficient scattering centers for the phonons and phonon path should be disrupted by the atom mass contrast. For Al

implantation at RT results should be due to the phonon scattering by defect clusters and the disruption of the phonon path by the mass contrast. For implantation at 250°C, nanocrystallites formed during implantation mainly further reduces the heat conduction by electrons, which could be due to the presence of depletion zones located at the nanocrystallite boundaries. These nanocrystallites could lead to a decrease of the phonon contribution to heat conduction for both the studied implantations.

In a more general way, this work demonstrates that thermal conductivity behavior of amorphous structures can be tailored via ion implantation or irradiation techniques. This is done by exploring doping, amorphous to crystalline phase transitions and irradiation-induced void defects, providing new possibilities for applications in thermoelectrics.

One perspective could be to exploit the effect of the temperature during ion implantation for tuning the size of the induced crystallites in order to optimize the energy-filtering barrier at the crystallite boundaries for a more pronounced decrease of the material thermal conductivity.

Results of the analysis of polymeric based nanocomposites

(Chapters IV and V).

Thermally conductive polymer composites can help solving the current heat dissipation issues in different applications, using polymer-based material, like in automobile, packaging, aerospace, energy harvesting, electromagnetic interfaces (EMIs), fifth-generation mobile network, and electronic devices industries. Adding of highly thermally conductive charges and the improvement of the polymer crystallinity are considered as the main ways to improve k . Through SThM measurements the heat transfer enhancement in two types of polymer-carbon filler composite i) HDPE filled with 50 μm EG composites and ii) PVDF/MWCNTs composites, versus carbon filler weight fraction within the polymer, was investigated.

In principle, the characterization of the thermal conductivity of polymer composites phenomena, such as agglomeration effect, can only be suggested from the combination of

effective modeling with measurements at the macroscale. For HDPE/EG samples SThM images have allowed the detection of zones with a thermal conductance larger than that of the matrix for the highest filler concentration studied. These zones correspond to EG filler agglomerates within the polymer and explain the observed enhancement of the thermal conductivity of the HDPE/EG composite. The k_{eff} results obtained by SThM are comparable but lower than those elsewhere measured by PTR and flash methods. The reason may be that the inhomogeneous distribution of EG fillers can affect the representativeness of data collected by microscale probe. In this case, the k_{eff} account more heat transfer capability of polymer matrix than the real situation. This has been well demonstrated by the result of HDPE/EG composite with 2 wt.% fillers.

For PVDF/MWCNTs samples it is found from that thermal conductivity increases from 0.24 W/(m.K) for pristine PVDF to 0.36 W/(m.K) for PVDF nanocomposites filled with 8 wt.% MWCNTs. This variation versus filler concentration is found in good correspondence with that of the β phase relative percentage in the PVDF nanocomposites. This suggests that the observed heat transfer enhancement is rather due to the formation of β phase for PVDF/MWCNTs samples resulting of the addition of MWCNTs than the addition of MWCNTs itself. MWCNTs can promote the formation of β and γ phase crystallites, which increase the mean free path of energy carries and then the thermal conductivity of samples.

Additionally, an analytical model was developed to better understand the impact of the β phase of PVDF on heat transport in PVDF/MWCNTs materials. The k_{MWCNTs} and k_{β} was found as 5.75 W/(m.K) and 1.32 W/(m.K), respectively. The proposed model favors the understanding of the role of carbonous fillers in affecting the structural behavior of PVDF matrix and supply some strategies to improve the thermal conductivity of polymer composites.

For Mxene samples, because of the significant topography present on the surface of PMMA composites, SThM is unable to provide precise information regarding the thermal conductivity of samples. However, the incorporation of MWCNTs or MXene into PMMA may enhance the thermal conductivity qualitatively compared to neat PMMA. While high

concentration of MXene may cause a decrease in thermal conductivity compared to PMMA containing low concentration due to the high inter-flake thermal resistance between stacked MXene flakes.

This study also clearly demonstrates the significant impact of the topography and roughness of the sample surface on the measurement results obtained through SThM. To conduct further investigations on these samples, it would be necessary to have a larger number of specimens with smoother surfaces.

Perspectives of this work include the application of the SThM technique to other polymer composites with carbon-based nanofillers such as graphene or rGO nanosheets for comparison and innovative 2D material nanoflakes.

Results of the analysis of SThM measurements.

SThM technique equipped with the Wollaston probe was used in its active mode at steady state regime for the thermal conductivity measurements of both types of materials studied. The experimental setup and the methodology followed to perform the measurements are given in **Chapter II**. The thermal conductivity calibration and its associated model provides the calibration curve to be used for the determination of the thermal conductance G_s or the effective thermal conductivity k_{eff} of an unknown sample. In case of bulk samples, the material thermal conductivity equals k_{eff} . The ion implanted amorphous CrSi₂ samples that we studied are not thin films on a substrate. The modelling used to derive the film thermal conductivity from G_s or k_{eff} (determined with the calibration curve) is provided for this specific geometry of samples.

Based on the measurements obtained in the thesis, we have demonstrated that the SThM technique allows the local investigation of polymeric materials with a micrometric spatial resolution thermal image, providing some possibilities to localize agglomeration effects and their impact on the thermal conductance of a polymer material.

A complementary model has been developed to interpret the measurement by means of SThM based on Dryden's model. To improve this methodology for the analysis of thin films and polymeric bulk samples, the input parameters of the model could be more accurately characterized. As an example, the contact radius a could be obtained through an $a-k_{eff}$ calibration. This $a-k_{eff}$ relationship can be established by using a series of low thermal conductivity reference samples with varying thicknesses coated onto a substrate with a known thermal conductivity. Moreover, the interface between the reference samples and the substrate also needs to be thoroughly investigated. To maximize the calibration range, polymers with extremely low thermal conductivity can be used as reference samples. It should be noted that the selected polymer must have good thermal stability to ensure that the properties of the material do not change during the SThM experiment. In addition, using other techniques to determine input parameters is also a feasible approach.

References

- [1] E. v. Iyengar, “Review: An Inconvenient Truth: The Planetary Emergency of Global Warming and What We Can Do about It , by Al Gore ,” *Am Biol Teach*, vol. 69, no. 1, pp. 58–58, 2007, doi: 10.2307/4452094.
- [2] R. Mendelsohn, “The impact of climate change on agriculture in developing countries,” *J Nat Resour Policy Res*, vol. 1, no. 1, pp. 5–19, 2008, doi: 10.1080/19390450802495882.
- [3] S. M. Howden, J. F. Soussana, F. N. Tubiello, N. Chhetri, M. Dunlop, and H. Meinke, “Adapting agriculture to climate change,” *Proc Natl Acad Sci U S A*, vol. 104, no. 50, pp. 19691–19696, Dec. 2007, doi: 10.1073/pnas.0701890104.
- [4] T. W. Hertel and S. D. Rosch, “Climate change, agriculture, and poverty,” *Appl Econ Perspect Policy*, vol. 32, no. 3, pp. 355–385, 2010, doi: 10.1093/aep/ppq016.
- [5] M. R. Anwar, D. L. Liu, I. Macadam, and G. Kelly, “Adapting agriculture to climate change: A review,” *Theor Appl Climatol*, vol. 113, no. 1–2, pp. 225–245, Jul. 2013, doi: 10.1007/s00704-012-0780-1.
- [6] A. J. McMichael and R. E. Woodruff, “Climate change and human health,” *Encyclopedia of Earth Sciences Series*, vol. 353, no. 14, pp. 209–213, Oct. 2005, doi: 10.1007/1-4020-3266-8_41.
- [7] A. J. McMichael, “Globalization, Climate Change, and Human Health,” *New England Journal of Medicine*, vol. 368, no. 14, pp. 1335–1343, Apr. 2013, doi: 10.1056/nejmra1109341.
- [8] A. J. McMichael, R. E. Woodruff, and S. Hales, “Climate change and human health: Present and future risks,” *Lancet*, vol. 367, no. 9513, pp. 859–869, 2006, doi: 10.1016/S0140-6736(06)68079-3.

-
- [9] “Primary energy consumption measured in terawatt-hours (TWh),” *BP Statistical Review of World Energy*.
- [10] R. E. Nelson, “A brief history of thermophotovoltaic,” *Semiconductor Science and Technology A*, vol. 18, p. 141, 2003.
- [11] T. J. Coutts, “An overview of thermophotovoltaic generation of electricity,” *Solar Energy Materials & Solar Cells*, vol. 66, pp. 443–452, 2001.
- [12] T. J. Coutts, “Thermophotovoltaic principles, potential, and problems,” *AIP Conference Proceedings 404*, vol. 404, no. April 2008, pp. 217–234, 1997, doi: 10.1063/1.53449.
- [13] P.-O. CHAPUIS, C. LUCCHESI, and R. VAILLON, “THERMOPHOTOVOLTAÏQUE : DES CELLULES PV POUR CONVERTIR,” *Photoniques*, vol. 105, p. 37, 2020.
- [14] T. Bauer, *Thermophotovoltaics: basic principles and critical aspects of system design*. Springer, 2012. doi: 10.2174/97816080528511120101.
- [15] C. Melnick and M. Kaviani, “From thermoelectricity to phonoelectricity,” *Appl Phys Rev*, vol. 6, no. 2, p. 021305, 2019, doi: 10.1063/1.5031425.
- [16] G. J. Snyder and E. S. Toberer, “Complex thermoelectric materials,” *Nat Mater*, vol. 7, no. 2, pp. 105–114, Feb. 2008, doi: 10.1038/nmat2090.
- [17] X. Huang, P. Jiang, and T. Tanaka, “A review of dielectric polymer composites with high thermal conductivity,” *IEEE Electrical Insulation Magazine*, vol. 27, no. 4, pp. 8–16, 2011, doi: 10.1109/MEI.2011.5954064.
- [18] D. P. Almond and P. M. Patel, “Photothermal Science and Techniques,” p. 241, 1996, Accessed: Jan. 02, 2023. [Online]. Available: http://www.springer.com/physics/book/978-0-412-57880-9?cm_mmc=Google-_-Book Search-_-Springer-_-0#

-
- [19] G. Chen, *Nanoscale energy transport and conversion: a parallel treatment of electrons, molecules, phonons, and photons*. Oxford University Press, 2005.
- [20] D. G. Cahill *et al.*, “Nanoscale thermal transport,” *Journal of Applied Physics*, vol. 93, no. 2, pp. 793–818, 2003. doi: 10.1063/1.1524305.
- [21] G. P. Srivastava, *The physics of phonons*. CRC press., 1990.
- [22] A. A. Balandin, “Thermal properties of graphene and nanostructured carbon materials.,” *Nat. Mater.*, vol. 10, no. 8, p. 569, 2011, doi: 10.1038/nmat3064.
- [23] P. B. Allen, J. L. Feldman, J. Fabian, and F. Wooten, “Diffusons, locons and propagons: Character of atomic vibrations in amorphous Si,” *Philosophical Magazine B: Physics of Condensed Matter; Statistical Mechanics, Electronic, Optical and Magnetic Properties*, vol. 79, no. 11–12, pp. 1715–1731, 1999, doi: 10.1080/13642819908223054.
- [24] J. Ziman, *Principles of the Theory of Solids*. 1972. Accessed: Jan. 12, 2023. [Online]. Available: https://www.google.com/books?hl=zh-CN&lr=&id=o4woMNO-C3sC&oi=fnd&pg=PA1&dq=Ziman+JM.+1979.+Principles+of+the+Theory+of+Solids.+Cambridge,+UK:+Cambridge+Univ.+Press&ots=IONof54Bjg&sig=6pR3Q_LpfCq3sRLwXxPpQ9gtuLU
- [25] E. S. Toberer, L. L. Baranowski, and C. Dames, “Advances in thermal conductivity,” *Annu Rev Mater Res*, vol. 42, pp. 179–209, 2012, doi: 10.1146/annurev-matsci-070511-155040.
- [26] P. Brüesch, *Phonons: Theory and experiments I: Lattice dynamics and Models of interatomic forces*. 2012. Accessed: Jan. 12, 2023. [Online]. Available: https://www.google.com/books?hl=zh-CN&lr=&id=nq3xCAAQBAJ&oi=fnd&pg=PA1&dq=phonons+theory+and+experiments&ots=AMZNok6G7I&sig=iFeqTIuNaK4f9WJXGoICU19K_Pc

-
- [27] G. Chen, *Nanoscale energy transport and conversion: a parallel treatment of electrons, molecules, phonons, and photons*. 2005. Accessed: Jan. 12, 2023. [Online]. Available: <https://www.google.com/books?hl=zh-CN&lr=&id=M3n3IUJpYDYC&oi=fnd&pg=PR7&dq=+G.+Chen,+Nanoscale+Energy+Transport+and+Conversion:+A+Parallel+Treatment+of+Electrons,+Molecules,+Phonons,+and+Photons,+Oxford+University+Press,+NY+2005.&ots=kx2xirO7Wr&sig=OwlJvU>
- [28] J. Callaway, “Model for lattice thermal conductivity at low temperatures,” *Physical Review*, vol. 113, no. 4, pp. 1046–1051, 1959, doi: 10.1103/PhysRev.113.1046.
- [29] G. A. Slack, “The Thermal Conductivity of Nonmetallic Crystals,” *Solid State Physics - Advances in Research and Applications*, vol. 34, no. C, pp. 1–71, 1979, doi: 10.1016/S0081-1947(08)60359-8.
- [30] D. G. Cahill, S. K. Watson, and R. O. Pohl, “Lower limit to the thermal conductivity of disordered crystals,” *Phys Rev B*, vol. 46, no. 10, pp. 6131–6140, 1992, doi: 10.1103/PhysRevB.46.6131.
- [31] P. B. Allen and J. L. Feldman, “Thermal conductivity of disordered harmonic solids,” *Phys Rev B*, vol. 48, no. 17, pp. 12581–12588, 1993, doi: 10.1103/PhysRevB.48.12581.
- [32] P. B. Allen and J. L. Feldman, “Thermal conductivity of glasses: Theory and application to amorphous Si,” *Phys Rev Lett*, vol. 62, no. 6, pp. 645–648, 1989, doi: 10.1103/PhysRevLett.62.645.
- [33] J. L. Feldman, M. D. Kluge, P. B. Allen, and F. Wooten, “Thermal conductivity and localization in glasses: Numerical study of a model of amorphous silicon,” *Phys Rev B*, vol. 48, no. 17, pp. 12589–12602, 1993, doi: 10.1103/PhysRevB.48.12589.
- [34] W. X. Zhou, Y. Cheng, K. Q. Chen, G. Xie, T. Wang, and G. Zhang, “Thermal Conductivity of Amorphous Materials,” *Adv Funct Mater*, vol. 30, no. 8, Feb. 2020, doi:

10.1002/adfm.201903829.

- [35] P. L. Kapitza, “Heat transfer and superfluidity of helium II,” *Physical Review*, vol. 60, no. 4, pp. 354–355, 1941, doi: 10.1103/PhysRev.60.354.
- [36] K. Kadoya, N. Matsunaga, and A. Nagashima, “Viscosity and Thermal Conductivity of Dry Air in the Gaseous Phase,” *J Phys Chem Ref Data*, vol. 14, no. 4, pp. 947–970, 1985, doi: 10.1063/1.555744.
- [37] E. T. Swartz and R. O. Pohl, “Thermal boundary resistance,” *Rev Mod Phys*, vol. 61, no. 3, pp. 605–668, 1989, doi: 10.1103/RevModPhys.61.605.
- [38] K. Filippov, A. B.-M. O. P. L. (OPL), and undefined 2003, “Thermal boundary resistance and heat diffusion in AlGaN/GaN HFETs,” *cambridge.org*, Accessed: Jan. 10, 2023. [Online]. Available: <https://www.cambridge.org/core/journals/mrs-online-proceedings-library-archive/article/thermal-boundary-resistance-and-heat-diffusion-in-algangan-hfets/8A5C789E4AD282F3100ACD895E7CE6AD>
- [39] G. Chen, “Thermal conductivity and ballistic-phonon transport in the cross-plane direction of superlattices,” *Phys Rev B*, vol. 57, no. 23, p. 14958, Jun. 1998, doi: 10.1103/PhysRevB.57.14958.
- [40] W. A. Little, “the Transport of Heat Between Dissimilar Solids At Low Temperatures,” *Can J Phys*, vol. 37, no. 3, pp. 334–349, Mar. 1959, doi: 10.1139/p59-037.
- [41] A. Giri *et al.*, “Interfacial Defect Vibrations Enhance Thermal Transport in Amorphous Multilayers with Ultrahigh Thermal Boundary Conductance,” *Advanced Materials*, vol. 30, no. 44, p. 44, Nov. 2018, doi: 10.1002/adma.201804097.
- [42] M. Li, J. Zhang, X. Hu, and Y. Yue, “Thermal transport across graphene/SiC interface: effects of atomic bond and crystallinity of substrate,” *Appl Phys A Mater Sci Process*, vol. 119, no. 2, pp. 415–424, May 2015, doi: 10.1007/s00339-015-9066-7.

-
- [43] A. Giri, J. L. Braun, and P. E. Hopkins, “Effect of crystalline/amorphous interfaces on thermal transport across confined thin films and superlattices,” *J Appl Phys*, vol. 119, no. 23, Jun. 2016, doi: 10.1063/1.4953683.
- [44] A. Giri, P. E. Hopkins, J. G. Wessel, and J. C. Duda, “Kapitza resistance and the thermal conductivity of amorphous superlattices,” *J Appl Phys*, vol. 118, no. 16, p. 165303, Oct. 2015, doi: 10.1063/1.4934511.
- [45] K. Gordiz and A. Henry, “Phonon transport at interfaces between different phases of silicon and germanium,” *J Appl Phys*, vol. 121, no. 2, p. 793, Jan. 2017, doi: 10.1063/1.4973573.
- [46] A. Giri *et al.*, “Interfacial Defect Vibrations Enhance Thermal Transport in Amorphous Multilayers with Ultrahigh Thermal Boundary Conductance,” *Advanced Materials*, vol. 30, no. 44, p. 1804097, Nov. 2018, doi: 10.1002/adma.201804097.
- [47] S. Deng *et al.*, “Thermal boundary resistance measurement and analysis across SiC/SiO₂ interface,” *Appl Phys Lett*, vol. 115, no. 10, p. 101603, Sep. 2019, doi: 10.1063/1.5111157.
- [48] B. Deng, A. Chernatynskiy, M. Khafizov, D. H. Hurley, and S. R. Phillpot, “Kapitza resistance of Si/SiO₂ interface,” *J Appl Phys*, vol. 115, no. 8, p. 84910, 2014, doi: 10.1063/1.4867047.
- [49] Y. Yu, M. Cagnoni, O. Cojocaru-Mirédin, and M. Wuttig, “Chalcogenide Thermoelectrics Empowered by an Unconventional Bonding Mechanism,” *Adv Funct Mater*, vol. 30, no. 8, Feb. 2020, doi: 10.1002/adfm.201904862.
- [50] D. Rowe, *CRC handbook of thermoelectrics*. CRC Press, 1995. Accessed: Jan. 15, 2023. [Online]. Available: <https://www.google.com/books?hl=zh-CN&lr=&id=n4O1DwAAQBAJ&oi=fnd&pg=PA7&dq=CRC+handbook+of+thermoelctrics&ots=j7ShwmDahm&sig=augJhr62MzccYBTZnl4BuG89tEE>

-
- [51] S. Li *et al.*, “2D hetero-nanosheets to enable ultralow thermal conductivity by all scale phonon scattering for highly thermoelectric performance,” *Nano Energy*, vol. 30, pp. 780–789, Dec. 2016, doi: 10.1016/j.nanoen.2016.09.018.
- [52] Y. Nakamura, “Nanostructure design for drastic reduction of thermal conductivity while preserving high electrical conductivity,” *Sci Technol Adv Mater*, vol. 19, no. 1, pp. 31–43, 2018, doi: 10.1080/14686996.2017.1413918.
- [53] A. Desalvo, F. Zignani, R. Galloni, R. Rizzoli, and M. Ruth, “Doping of amorphous silicon by potassium ion implantation,” *Philosophical Magazine B: Physics of Condensed Matter; Statistical Mechanics, Electronic, Optical and Magnetic Properties*, vol. 67, no. 1, pp. 131–142, 1993, doi: 10.1080/13642819308230224.
- [54] Y. Wu, J. Nylén, C. Naseyowma, N. Newman, J. G. G. Francisco, and U. Häussermann, “Comparative study of the thermoelectric properties of amorphous Zn₄₁Sb₅₉ and crystalline Zn₄Sb₃,” *Chemistry of Materials*, vol. 21, no. 1, pp. 151–155, Jan. 2009, doi: 10.1021/cm802893v.
- [55] D. Rowe and B. Raton London New York, “Thermoelectrics Handbook,” *Thermoelectrics Handbook*, Oct. 2018, doi: 10.1201/9781420038903.
- [56] S. v. Novikov and A. T. Burkov, “Grain boundary scattering contribution to the thermopower in Cr-Si nanocrystalline films,” *J Phys Conf Ser*, vol. 769, no. 1, 2016, doi: 10.1088/1742-6596/769/1/012069.
- [57] G. J. Snyder and E. S. Toberer, “Complex thermoelectric materials,” *Nanoscience and Technology: A Collection of Reviews from Nature Journals*, vol. 7, pp. 50–59, 2009, doi: 10.1142/9789814287005_0006.
- [58] G. S. Nolas, D. T. Morelli, and T. M. Tritt, “Skutterudites: a phonon-glass-electron crystal approach to advanced thermoelectric energy conversion applications,” *Annual Review of Materials Science*, vol. 29, pp. 89–116, 1999, doi: 10.1146/annurev.matsci.29.1.89.

-
- [59] Y. Shi, A. Assoud, S. Ponou, S. Lidin, and H. Kleinke, “A New Material with a Composite Crystal Structure Causing Ultralow Thermal Conductivity and Outstanding Thermoelectric Properties: $Tl_2Ag_{12}Te_{7+\delta}$,” *J Am Chem Soc*, vol. 140, no. 27, pp. 8578–8585, Jul. 2018, doi: 10.1021/jacs.8b04639.
- [60] X. Zhou *et al.*, “Routes for high-performance thermoelectric materials,” *Materials Today*, vol. 21, no. 9, pp. 974–988, Nov. 2018, doi: 10.1016/j.mattod.2018.03.039.
- [61] H. Han, L. G. Potyomina, A. A. Darinskii, S. Volz, and Y. A. Kosevich, “Phonon interference and thermal conductance reduction in atomic-scale metamaterials,” *Phys Rev B Condens Matter Mater Phys*, vol. 89, no. 18, May 2014, doi: 10.1103/PhysRevB.89.180301.
- [62] R. Lu *et al.*, “High carrier mobility and ultralow thermal conductivity in the synthetic layered superlattice $Sn_4Bi_{10}Se_{19}$,” *Mater Adv*, vol. 2, no. 7, pp. 2382–2390, 2021, doi: 10.1039/d0ma00912a.
- [63] X. He and Y. Wang, “Recent advances in the rational design of thermal conductive polymer composites,” *Ind Eng Chem Res*, vol. 60, no. 3, pp. 1137–1154, Jan. 2021, doi: 10.1021/acs.iecr.0c05509.
- [64] C. I. Idumah, “Recently emerging advancements in thermal conductivity and flame retardancy of MXene polymeric nanoarchitectures,” *Polymer-Plastics Technology and Materials*, 2022, doi: 10.1080/25740881.2022.2121220.
- [65] D. M. Price and M. Jarratt, “Thermal conductivity of PTFE and PTFE composites,” *Thermochim Acta*, vol. 392–393, pp. 231–236, 2002, doi: 10.1016/S0040-6031(02)00105-3.
- [66] M. Hareesha, B. Yogesha, L. L. Naik, and D. Saravanabavan, “Development on graphene based polymer composite materials and their applications - A recent review,” *AIP Conf Proc*, vol. 2316, no. 1, p. 030016, Feb. 2021, doi: 10.1063/5.0036854.

-
- [67] M. Chirtoc, N. Horny, I. Tavman, A. Turgut, I. Kökey, and M. Omastová, “Preparation and photothermal characterization of nanocomposites based on high density polyethylene filled with expanded and unexpanded graphite: Particle size and shape effects,” *International Journal of Thermal Sciences*, vol. 62, pp. 50–55, 2012, doi: 10.1016/j.ijthermalsci.2012.02.015.
- [68] S. A. Putnam, D. G. Cahill, B. J. Ash, and L. S. Schadler, “High-precision thermal conductivity measurements as a probe of polymer/nanoparticle interfaces,” *J Appl Phys*, vol. 94, no. 10, pp. 6785–6788, Oct. 2003, doi: 10.1063/1.1619202.
- [69] S. Gomès, A. Assy, and P. O. Chapuis, “Scanning thermal microscopy: A review,” *Physica Status Solidi (A) Applications and Materials Science*, vol. 212, no. 3. Wiley-VCH Verlag, pp. 477–494, 2015. doi: 10.1002/pssa.201400360.
- [70] E. Guen, “Microscopie thermique à sonde locale : étalonnages, protocoles de mesure et applications quantitatives sur des matériaux nanostructurés,” 2020. Accessed: Apr. 06, 2021. [Online]. Available: <https://tel.archives-ouvertes.fr/tel-03078527>
- [71] A. Hammiche, H. M. Pollock, M. Song, and D. J. Hourston, “Sub-surface imaging by scanning thermal microscopy,” *Meas Sci Technol*, vol. 7, no. 2, pp. 142–150, 1996, doi: 10.1088/0957-0233/7/2/004.
- [72] S. Gomès, L. David, V. Lysenko, A. Descamps, T. Nychyporuk, and M. Raynaud, “Application of scanning thermal microscopy for thermal conductivity measurements on meso-porous silicon thin films,” *J Phys D Appl Phys*, vol. 40, no. 21, pp. 6677–6683, 2007, doi: 10.1088/0022-3727/40/21/029.
- [73] A. Assy, S. Lefèvre, P. O. Chapuis, and S. Gomès, “Analysis of heat transfer in the water meniscus at the tip-sample contact in scanning thermal microscopy,” *J Phys D Appl Phys*, vol. 47, no. 44, 2014, doi: 10.1088/0022-3727/47/44/442001.
- [74] E. Guen *et al.*, “Scanning thermal microscopy on samples of varying effective thermal

-
- conductivities and identical flat surfaces,” *J Appl Phys*, vol. 128, no. 23, p. 235301, 2020, doi: 10.1063/5.0020276.
- [75] S. Lefèvre, “Modélisation et élaboration des métrologies de microscopie thermique a sonde locale résistive,” p. 216, 2004, Accessed: Oct. 04, 2021. [Online]. Available: <https://tel.archives-ouvertes.fr/tel-00007145/>
- [76] A. Alkurdi and E. Guen, “Resistive-thermometry scanning thermal microscopy: combined experimental/numerical approaches for thermal studies of nano-objects,” *J. Phys. Cond. Mat.*.
- [77] L. David, S. Gomès, and M. Raynaud, “Modelling for the thermal characterization of solid materials by dc scanning thermal microscopy,” *J Phys D Appl Phys*, vol. 40, no. 14, pp. 4337–4346, 2007, doi: 10.1088/0022-3727/40/14/032.
- [78] A. Assy, “Development of two techniques for thermal characterization of materials: Scanning Thermal Microscopy (SThM) and 2ω method,” 2015. Accessed: May 09, 2021. [Online]. Available: <http://edeea.ec-lyon.fr>
- [79] T. P. Nguyen, L. Thiery, S. Euphrasie, S. Gomès, B. Hay, and P. Vairac, “Calibration of thermocouple-based scanning thermal microscope in active mode (2ω method),” *Review of Scientific Instruments*, vol. 90, no. 11, Nov. 2019, doi: 10.1063/1.5119044.
- [80] M. Massoud, “Experimental characterization of heat transfer in nanostructured silicon-based materials,” 2016. Accessed: May 06, 2021. [Online]. Available: <http://theses.insa-lyon.fr/publication/2016LYSEI063/these.pdf>
- [81] A. A. Wilson and T. Borca-Tasciuc, “Quantifying non-contact tip-sample thermal exchange parameters for accurate scanning thermal microscopy with heated microprobes,” *Review of Scientific Instruments*, vol. 88, no. 7, p. 74903, Jul. 2017, doi: 10.1063/1.4991017.

-
- [82] S. Lefèvre, S. Volz, J. B. Saulnier, C. Fuentes, and N. Trannoy, “Thermal conductivity calibration for hot wire based dc scanning thermal microscopy,” *Review of Scientific Instruments*, vol. 74, no. 4, pp. 2418–2423, Apr. 2003, doi: 10.1063/1.1544078.
- [83] “QUANTIHEAT EUROPEAN PROJECT Prototype Application Note Page 1 | 5 Thermal reference samples.”
- [84] E. Guen, P. O. Chapuis, N. J. Kaur, P. Klapetek, and S. Gomés, “Impact of roughness on heat conduction involving nanocontacts,” *Appl Phys Lett*, vol. 119, no. 16, p. 161602, Oct. 2021, doi: 10.1063/5.0064244.
- [85] V. v. Tsukruk, V. v. Gorbunov, and N. Fuchigami, “Microthermal analysis of polymeric materials,” *Thermochim Acta*, vol. 395, no. 1–2, pp. 151–158, Jan. 2002, doi: 10.1016/S0040-6031(02)00139-9.
- [86] Y. Zhang *et al.*, “A Review on Principles and Applications of Scanning Thermal Microscopy (SThM),” *Adv Funct Mater*, vol. 30, no. 18, p. 1900892, May 2020, doi: 10.1002/ADFM.201900892.
- [87] K. Kim, J. Chung, G. Hwang, O. Kwon, and J. S. Lee, “Quantitative measurement with scanning thermal microscope by preventing the distortion due to the heat transfer through the air,” *ACS Nano*, vol. 5, no. 11, pp. 8700–8709, Nov. 2011, doi: 10.1021/NN2026325.
- [88] J. R. Dryden, “The effect of a surface coating on the constriction resistance of a spot on an infinite half-plane,” *J Heat Transfer*, vol. 105, no. 2, pp. 408–410, 1983, doi: 10.1115/1.3245596.
- [89] S. P. Murarka, “Silicide thin films and their applications in microelectronics,” *Intermetallics (Barking)*, vol. 3, pp. 173–186, 1995.
- [90] X. Chen and C. Liang, “Transition metal silicides: fundamentals, preparation and catalytic applications,” *Catal Sci Technol*, vol. 9, pp. 4785–4820, 2019, doi:

10.1039/c9cy00533a.

- [91] S. Jin, A. L. Schmitt, L. Zhu, Y. Song, and J. Szczech, “Synthesis, Characterization and Physical Properties of Transition Metal Silicide Nanowires,” *Proc. SPIE 6370, Nanomaterial Synthesis and Integration for Sensors, Electronics, Photonics, and Electro-Optics*, vol. 63700O, pp. 1–10, 2006, doi: 10.1117/12.687206.
- [92] M. I. Fedorov and V. K. Zaitsev, “Thermoelectrics of transition metal silicides,” in *Thermoelectrics Handbook: macro to nano*, D. M. Rowe, Ed. CRC Press, 2009.
- [93] A. Nozariasbmarz *et al.*, “Thermoelectric silicides : A review,” *Jpn J Appl Phys*, vol. 56, no. 05DA04, 2017.
- [94] M. C. Bost and J. E. Mahan, “Semiconducting silicides as potential materials for electro-optic very large scale integrated circuit interconnects,” *Journal of Vacuum Science & Technology B*, vol. 4, no. 6, pp. 1336–1338, 1986, doi: 10.1116/1.583454.
- [95] M. Barus and D. Donoval, “Analysis of I-V measurements on CrSi₂-Si Schottky structures in a wide temperature range,” *Solid State Electronics*, vol. 36, no. 7, pp. 969–974, 1993.
- [96] O. S. Anilturk and R. Turan, “Electrical transport at a non-ideal CrSi₂-Si junction,” *Solid State Electronics*, vol. 44, pp. 41–48, 2000.
- [97] M. C. Bost, J. E. Mahan, M. C. B. S, and J. E. Mahan, “An investigation of the optical constants and band gap of chromium disilicide,” *J Appl Phys*, vol. 63, pp. 839–844, 1988, doi: 10.1063/1.340078.
- [98] D. Goroshko *et al.*, “Enhancement of near IR ensitivity of silicon-based photodetectors,” *Physica Status Solidi C*, vol. 10, no. 12, pp. 1844–1846, 2013, doi: 10.1002/pssc.201300402.

-
- [99] M. Abd El Qader *et al.*, “Structural, electrical, and thermoelectric properties of CrSi₂ thin films,” *Thin Solid Films*, vol. 545, pp. 100–105, 2013, doi: 10.1016/j.tsf.2013.07.040.
- [100] T. Dasgupta, J. Etourneau, B. Chevalier, S. F. Matar, and A. M. Umarji, “Structural, thermal, and electrical properties of CrSi₂,” *J Appl Phys*, vol. 103, no. 11, 2008, doi: 10.1063/1.2917347.
- [101] D. Goroshko, E. Chusovitin, D. Bezbabniy, L. Dózsa, B. Pécz, and N. Galkin, “Formation and Thermoelectric Properties of Si/CrSi₂/Si (001) Heterostructures with Stressed Chromium Disilicide Nanocrystallites,” *Electron. Mater. Lett.*, vol. 11, no. 3, pp. 424–428, 2015, doi: 10.1007/s13391-015-4475-5.
- [102] I. Nishida, “The crystal growth and thermoelectric properties of chromium disilicide,” *J Mater Sci*, vol. 7, pp. 1119–1124, 1972.
- [103] S. Perumal, S. Gorsse, U. Ail, R. Decourt, and A. M. Umarji, “Effect of composition on thermoelectric properties of polycrystalline CrSi₂,” *J Electron Mater*, vol. 42, no. 6, pp. 1042–1046, Jun. 2013, doi: 10.1007/s11664-013-2510-6.
- [104] T. Pandey and A. K. Singh, “Origin of enhanced thermoelectric properties of doped CrSi₂,” *RSC Adv*, vol. 4, no. 7, pp. 3482–3486, 2014, doi: 10.1039/c3ra44822c.
- [105] A. T. Burkov, S. V. Novikov, V. V. Khovaylo, and J. Schumann, “Energy filtering enhancement of thermoelectric performance of nanocrystalline Cr_{1-x}Si_x composites,” *J Alloys Compd*, vol. 691, pp. 89–94, 2017, doi: 10.1016/j.jallcom.2016.08.117.
- [106] F. Nava, T. Tien, and K. N. Tu, “Temperature dependence of semiconducting and structural properties of Cr Si thin films,” *J Appl Phys*, vol. 57, pp. 2018–2025, 1985, doi: 10.1063/1.334389.
- [107] A. P. Caricato, G. Leggieri, A. Luches, and F. Romano, “Morphological and structural

-
- characterizations of CrSi₂ nanometric films deposited by laser ablation,” *Appl Surf Sci*, vol. 254, pp. 1224–1227, 2007, doi: 10.1016/j.apsusc.2007.09.026.
- [108] S. V Novikov, A. T. Burkov, and J. Schumann, “Crystallization and Transport Properties of Amorphous Cr-Si Thin Film Thermoelectrics,” *J Electron Mater*, vol. 43, no. 6, pp. 2420–2424, 2014, doi: 10.1007/s11664-014-3101-x.
- [109] C. Kim, “Electrical properties of CrSi₃, Cr/CrSi₃/Cr/CrSi₃, and CrSi₃/Si/CrSi₃/Si sputtered on alumina plates,” *Thin Solid Films*, vol. 479, pp. 182–187, 2005, doi: 10.1016/j.tsf.2004.12.019.
- [110] S. V Novikov, A. T. Burkov, and J. Schumann, “Enhancement of thermoelectric properties in nanocrystalline M – Si thin film composites (M = Cr , Mn),” *J Alloys Compd*, vol. 557, pp. 239–243, 2013, doi: 10.1016/j.jallcom.2012.12.088.
- [111] G. S. Nolas and H. J. Goldsmid, “The figure of merit in amorphous thermoelectrics,” *Physica Status Solidi A Appl Res*, vol. 194, no. 1, pp. 271–276, 2002, doi: 10.1002/1521-396X(200211)194:1<271::AID-PSSA271>3.0.CO;2-T.
- [112] G. S. Nolas and H. J. Goldsmid, “Amorphous Thermoelectrics,” in *21st International Conference on Thermoelectrics*, 2002, pp. 296–298.
- [113] Y. Wu, J. Nyle, C. Naseyowma, N. Newman, and F. J. Garcia-garcia, “Comparative Study of the Thermoelectric Properties of Amorphous Zn₄₁Sb₅₉ and Crystalline Zn₄Sb₃,” *Chem. Mater.*, vol. 21, pp. 151–155, 2009.
- [114] S. Kim *et al.*, “Transparent Amorphous Oxide Semiconductor as Excellent Thermoelectric Materials,” *Coatings*, vol. 8, no. 462, 2018, doi: 10.3390/coatings8120462.
- [115] I. R. Sanders, J. Stephen, G. W. Hinder, B. D. Williams, and B. J. Smith, “The effect of argon implantation on the conductivity of boron implanted silicon,” *Solid State Electron*,

vol. 20, no. 8, pp. 703–707, 2002, doi: 10.1016/0038-1101(77)90047-8.

- [116] C. Uzan-Saguy *et al.*, “Electrical isolation of GaN by ion implantation damage: Experiment and model,” *Appl Phys Lett*, vol. 74, no. 17, pp. 2441–2443, 2002, doi: 10.1063/1.123874.
- [117] R. Choudhary and R. P. Chauhan, “Nitrogen ion implantation effects on the structural, optical and electrical properties of CdSe thin film,” *Journal of Materials Science: Materials in Electronics*, vol. 29, no. 15, pp. 12595–12602, 2018, doi: 10.1007/s10854-018-9376-6.
- [118] P. F. P. Fichtner, M. Behar, J. R. Kaschny, A. Peeva, R. Koegler, and W. Skorupa, “Copper gettering at half the projected ion range induced by low-energy channeling He implantation into silicon;,” *Appl Phys Lett*, vol. 77, pp. 972–974, 2000, doi: 10.1063/1.1289062.
- [119] D. A. Brett, D. J. Llewellyn, and M. C. Ridgway, “Trapping of Pd, Au, and Cu by implantation-induced nanocavities and dislocations in Si,” *Appl Phys Lett*, vol. 88, no. 222107, 2006, doi: 10.1063/1.2208382.
- [120] T. Isoda, M. Uematsu, and K. M. Itoh, “Observation of silicon self-diffusion enhanced by the strain originated from end-of-range defects using isotope multilayers,” *J Appl Phys*, vol. 118, no. 115706, 2015, doi: 10.1063/1.4931421.
- [121] M. Kato, K. Arimoto, J. Yamanaka, K. Nakagawa, and K. Sawano, “Fabrication of high-quality strain relaxed SiGe(110) films by controlling defects via ion implantation,” *J Cryst Growth*, vol. 477, pp. 197–200, 2017, doi: 10.1016/j.jcrysgro.2017.05.022.
- [122] M. Luysberg *et al.*, “Effect of helium ion implantation and annealing on the relaxation behavior of pseudomorphic Si_{1-x}Ge_x buffer layers on Si (100) substrates,” *J Appl Phys*, vol. 92, pp. 4290–4295, 2002.

-
- [123] M. de M. Timm, “Ion implantation and ion irradiation effects on nuclear and thermoelectric materials,” 2019. Accessed: Feb. 02, 2023. [Online]. Available: <https://www.lume.ufrgs.br/handle/10183/204277>
- [124] A. Moll, “Elaboration et étude des propriétés thermoélectriques du disiliciure de chrome sous forme de monocristal, de couche mince et de nanofil,” Université de Montpellier, 2018.
- [125] F. A. G. R.E. Stoller, M.B. Toloczko, G.S. Was, A.G. Certain, S. Dwaraknath, “On the use of SRIM for computing radiation damage exposure,” *Nucl. Instr. Meth. Phys. Res. B*, vol. 310, pp. 75–80, 2013, doi: <http://dx.doi.org/10.1016/j.nimb.2013.05.008>.
- [126] J. F. Ziegler and J. P. Biersack, “Stopping and range of ions in matter: SRIM.” p. <http://www.srim.org/>, 2003.
- [127] J. A. Thornton, “Influence of apparatus geometry and deposition conditions on the structure and topography of thick sputtered coatings,” *Journal of Vacuum Science & Technology*, vol. 11, no. 666, pp. 2–7, 1974, doi: 10.1116/1.1312732.
- [128] E. Alfonso, J. Olaya, and G. Cubillos, “Thin Film Growth Through Sputtering Technique and Its Applications,” in *Crystallization - Science and Technology*, M. Andreetta, Ed. São Paulo, 2012.
- [129] A. Hirata and M. Chen, “Angstrom-beam electron diffraction of amorphous materials,” *J Non Cryst Solids*, vol. 383, pp. 52–58, 2014, doi: 10.1016/j.jnoncrsol.2013.03.010.
- [130] W. Buckel, “Elektronenbeugungs-Aufnahmen von dünnen Metallschichten bei tiefen Temperaturen,” *Zeitschrift für Physik*, vol. 138, no. 2, pp. 136–150, Apr. 1954, doi: 10.1007/BF01337905.
- [131] A. T. Burkov, S. v. Novikov, V. v. Khovaylo, and J. Schumann, “Energy filtering enhancement of thermoelectric performance of nanocrystalline Cr_{1-x}Si_xcomposites,” *J*

Alloys Compd, vol. 691, pp. 89–94, 2017, doi: 10.1016/j.jallcom.2016.08.117.

- [132] S. Perumal, S. Gorsse, U. Ail, M. Prakasam, B. Chevalier, and A. M. Umarji, “Thermoelectric properties of chromium disilicide prepared by mechanical alloying,” *J Mater Sci*, vol. 48, no. 17, pp. 6018–6024, Sep. 2013, doi: 10.1007/s10853-013-7398-2.
- [133] D. L. da Silva, M. J. Mörschbacher, P. F. P. Fichtner, E. Oliviero, and M. Behar, “Formation of bubbles and extended defects in He implanted (1 0 0) Si at elevated temperatures,” *Nuclear Inst. and Methods in Physics Research, B*, vol. 219–220, pp. 713–717, 2004, doi: 10.1016/j.nimb.2004.01.148.
- [134] E. Oliviero *et al.*, “Damage accumulation in neon implanted silicon,” *J Appl Phys*, vol. 100, no. 2006, 2006, doi: 10.1063/1.2220644.
- [135] E. Oliviero, S. Peripolli, P. F. P. Fichtner, and L. Amaral, “Characterization of neon implantation damage in silicon,” vol. 112, pp. 111–115, 2004, doi: 10.1016/j.mseb.2004.05.014.
- [136] Qiang-Li, W. Kesternich, H. Schroeder, D. Schwahn, and H. Ullmaier, “Gas densities in helium bubbles in nickel measured by small angle neutron scattering,” *Acta Metall. Mater.*, vol. 38, no. 12, pp. 2383–2392, 1990.
- [137] E. Oliviero *et al.*, “Damage accumulation in neon implanted silicon,” *J Appl Phys*, vol. 100, no. 043505, 2006, doi: 10.1063/1.2220644.
- [138] T. Dasgupta, J. Etourneau, B. Chevalier, S. F. Matar, and A. M. Umarji, “Structural, thermal, and electrical properties of CrSi₂,” *J Appl Phys*, vol. 103, no. 11, 2008, doi: 10.1063/1.2917347.
- [139] D. M. Rowe, Ed., *Thermoelectrics Handbook: macro to nano*. New York: Taylor & Francis Group, 2006.

-
- [140] G. S. Was, *Fundamentals of Radiation Materials Science*. Springer, 2007.
- [141] S. Perumal, S. Gorsse, U. Ail, B. Chevalier, R. Decourt, and A. M. Umarji, “Effect of co-substitution of Mn and Al on thermoelectric properties of chromium disilicide,” *J Mater Sci*, vol. 48, no. 1, pp. 227–231, 2013, doi: 10.1007/s10853-012-6732-4.
- [142] M. M. Timm *et al.*, “Ion implantation effects on the microstructure, electrical resistivity and thermal conductivity of amorphous CrSi₂ thin films,” *J Mater Sci*, vol. 57, no. 2, pp. 1174–1185, Jan. 2022, doi: 10.1007/s10853-021-06674-8.
- [143] N. Tureson *et al.*, “Effect of ion-implantation-induced defects and Mg dopants on the thermoelectric properties of ScN,” *Phys Rev B*, vol. 98, no. 20, p. 205307, 2018, doi: 10.1103/PhysRevB.98.205307.
- [144] S. Lefèvre and S. Volz, “3 Ω -Scanning Thermal Microscope,” *Review of Scientific Instruments*, vol. 76, no. 3, Mar. 2005, doi: 10.1063/1.1857151.
- [145] E. Puyoo, S. Grauby, J. M. Rampnoux, E. Rouvire, and S. Dilhaire, “Thermal exchange radius measurement: Application to nanowire thermal imaging,” *Review of Scientific Instruments*, vol. 81, no. 7, p. 73701, 2010, doi: 10.1063/1.3455214.
- [146] T. Beechem, S. Graham, P. Hopkins, and P. Norris, “Role of interface disorder on thermal boundary conductance using a virtual crystal approach,” *Appl Phys Lett*, vol. 90, no. 5, p. 54104, 2007, doi: 10.1063/1.2437685.
- [147] R. J. Stoner and H. J. Maris, “Kapitza conductance and heat flow between solids at temperatures from 50 to 300 K,” *Phys Rev B*, vol. 48, no. 22, pp. 16373–16387, 1993, doi: 10.1103/PhysRevB.48.16373.
- [148] R. Burcea *et al.*, “Influence of Generated Defects by Ar Implantation on the Thermoelectric Properties of ScN,” *ACS Appl Energy Mater*, vol. 2022, pp. 11025–11033, 2022, doi: 10.1021/acsaem.2c01672.

-
- [149] A. Zenji, J. M. Rampnoux, S. Grauby, and S. Dilhaire, “Ultimate-resolution thermal spectroscopy in time domain thermoreflectance (TDTR),” *J Appl Phys*, vol. 128, no. 6, p. 065106, Aug. 2020, doi: 10.1063/5.0015391.
- [150] O. (Otfried) Madelung, *Semiconductors. Group IV elements and III-V compounds*. Springer-Verlag, 1991.
- [151] H. Nakasawa, T. Takamatsu, Y. Iijima, K. Hayashi, and Y. Miyazaki, “Thermoelectric Properties of Mo and Ge co-substituted CrSi₂,” *Transactions of the Materials Research Society of Japan*, vol. 43, no. 2, pp. 85–91, Apr. 2018, doi: 10.14723/tmrsj.43.85.
- [152] B. K. Voronov, L. D. Dudkin, and N. N. Trusova, “Characteristic Features of the Physicochemical Structure of Chromium Disilicide,” *Chemical Bonds in Solids*, pp. 21–26, 1972, doi: 10.1007/978-1-4684-8682-7_4.
- [153] M. Yamasaki, S. Kagao, and Y. Kawamura, “Thermal diffusivity and conductivity of Zr₅₅Al₁₀Ni₅Cu₃₀ bulk metallic glass,” *Scr Mater*, vol. 53, no. 1, pp. 63–67, Jul. 2005, doi: 10.1016/j.scriptamat.2005.03.021.
- [154] U. Harms, T. D. Shen, and R. B. Schwarz, “Thermal conductivity of Pd₄₀Ni_{40-x}Cu_xP₂₀ metallic glasses,” *Scr Mater*, vol. 47, no. 6, pp. 411–414, 2002, doi: 10.1016/S1359-6462(02)00160-4.
- [155] C. L. Choy, K. W. Tong, H. K. Wong, and W. P. Leung, “Thermal conductivity of amorphous alloys above room temperature,” *J Appl Phys*, vol. 70, no. 9, pp. 4919–4925, 1991, doi: 10.1063/1.349037.
- [156] A. Reza, H. Yu, K. Mizohata, and F. Hofmann, “Thermal diffusivity degradation and point defect density in self-ion implanted tungsten,” *Acta Mater*, vol. 193, pp. 270–279, 2020, doi: 10.1016/j.actamat.2020.03.034.
- [157] G. J. Snyder and E. S. Toberer, “Complex thermoelectric materials,” *Nat Mater*, vol. 7,

-
- no. February, pp. 105–114, 2008.
- [158] S. Perumal, S. Gorsse, U. Ail, B. Chevalier, R. Decourt, and A. M. Umarji, “Effect of co-substitution of Mn and Al on thermoelectric properties of chromium disilicide,” *J Mater Sci*, vol. 48, no. 1, pp. 227–231, 2013, doi: 10.1007/s10853-012-6732-4.
- [159] A. T. Burkov, S. v. Novikov, V. v. Khovaylo, and J. Schumann, “Energy filtering enhancement of thermoelectric performance of nanocrystalline Cr_{1-x}Si_xcomposites,” *J Alloys Compd*, vol. 691, pp. 89–94, 2017, doi: 10.1016/j.jallcom.2016.08.117.
- [160] Z. Han and A. Fina, “Thermal conductivity of carbon nanotubes and their polymer nanocomposites: A review,” *Progress in Polymer Science (Oxford)*, vol. 36, no. 7, pp. 914–944, 2011, doi: 10.1016/j.progpolymsci.2010.11.004.
- [161] Y. S. Jun, J. G. Um, G. Jiang, G. Lui, and A. Yu, “Ultra-large sized graphene nanoplatelets (GnPs) incorporated polypropylene (PP)/GnPs composites engineered by melt compounding and its thermal, mechanical, and electrical properties,” *Compos B Eng*, vol. 133, pp. 218–225, Jan. 2018, doi: 10.1016/j.compositesb.2017.09.028.
- [162] S. Y. Yang *et al.*, “Synergetic effects of graphene platelets and carbon nanotubes on the mechanical and thermal properties of epoxy composites,” *Carbon N Y*, vol. 49, no. 3, pp. 793–803, Mar. 2011, doi: 10.1016/j.carbon.2010.10.014.
- [163] E. M. Jackson, P. E. Laibinis, W. E. Collins, A. Ueda, C. D. Wingard, and B. Penn, “Development and thermal properties of carbon nanotube-polymer composites,” *Compos B Eng*, vol. 89, pp. 362–373, Mar. 2016, doi: 10.1016/j.compositesb.2015.12.018.
- [164] Y. Zhang and S. J. Park, “Imidazolium-optimized conductive interfaces in multilayer graphene nanoplatelet/epoxy composites for thermal management applications and electroactive devices,” *Polymer (Guildf)*, vol. 168, pp. 53–60, Apr. 2019, doi: 10.1016/j.polymer.2019.01.086.

-
- [165] H. Ye, B. Han, H. Chen, and L. Xu, “The liquid-exfoliation of graphene assisted with hyperbranched polyethylene-g-polyhedral oligomeric silsesquioxane copolymer and its thermal property in polydimethylsiloxane nanocomposite,” *Nanotechnology*, vol. 30, no. 35, p. 355602, Jun. 2019, doi: 10.1088/1361-6528/ab200b.
- [166] G. Georgousis *et al.*, “Strain sensing in polymer/carbon nanotube composites by electrical resistance measurement,” *Compos B Eng*, vol. 68, pp. 162–169, 2015, doi: 10.1016/j.compositesb.2014.08.027.
- [167] C. W. Nan, R. Birringer, D. R. Clarke, and H. Gleiter, “Effective thermal conductivity of particulate composites with interfacial thermal resistance,” *J Appl Phys*, vol. 81, no. 10, pp. 6692–6699, Aug. 1997, doi: 10.1063/1.365209.
- [168] M. S. S. A. Saraswathi, D. Rana, P. Vijayakumar, S. Alwarappan, and A. Nagendran, “Tailored PVDF nanocomposite membranes using exfoliated MoS₂ nanosheets for improved permeation and antifouling performance,” *New Journal of Chemistry*, vol. 41, no. 23, pp. 14315–14324, 2017, doi: 10.1039/c7nj03193a.
- [169] M. S. Sri Abirami Saraswathi, D. Rana, K. Divya, S. Alwarappan, and A. Nagendran, “Fabrication of anti-fouling PVDF nanocomposite membranes using manganese dioxide nanospheres with tailored morphology, hydrophilicity and permeation,” *New Journal of Chemistry*, vol. 42, no. 19, pp. 15803–15810, 2018, doi: 10.1039/C8NJ02701C.
- [170] “No Title.”
- [171] A. I. Buzin, P. Kamasa, M. Pyda, and B. Wunderlich, “Application of a Wollaston wire probe for quantitative thermal analysis,” *Thermochim Acta*, vol. 381, no. 1, pp. 9–18, Jan. 2002, doi: 10.1016/S0040-6031(01)00648-7.
- [172] M. Chirtoc *et al.*, “Photothermal characterization of nanocomposites based on high density polyethylene (HDPE) filled with expanded graphite,” *Int J Thermophys*, vol. 33, no. 10–11, pp. 2110–2117, Sep. 2012, doi: 10.1007/s10765-012-1305-y.

-
- [173] C. A. Coulson, “Valence Angles in Group II Dihalide Molecules,” *Isr J Chem*, vol. 11, no. 5, pp. 683–690, 1973, doi: 10.1002/ijch.197300065.
- [174] J. Bian, X. W. Wei, H. L. Lin, L. Wang, and Z. P. Guan, “Comparative Study on the Exfoliated Expanded Graphite Nanosheet-PES Composites Prepared via Different Compounding Method,” *J Appl Polym Sci*, vol. 124, no. 5, pp. 3547–3557, 2011, doi: 10.1002/app.35531.
- [175] M. J. Mochane and A. S. Luyt, “The Effect of Expanded Graphite on the Thermal Stability, Latent Heat, and Flammability Properties of EVA/Wax Phase Change Blends,” *Polym Eng Sci*, vol. 55, no. 6, pp. 1255–1262, 2015, doi: 10.1002/pen.24063.
- [176] J. Jacob, G. Ae, and A. K. Bhowmick, “Ethylene vinyl acetate/expanded graphite nanocomposites by solution intercalation: preparation, characterization and properties,” *J Mater Sci*, vol. 43, no. 2, pp. 702–708, 2008, doi: 10.1007/s10853-007-2193-6.
- [177] S. K. Karan *et al.*, “Effect of γ -PVDF on enhanced thermal conductivity and dielectric property of Fe-rGO incorporated PVDF based flexible nanocomposite film for efficient thermal management and energy storage applications,” *RSC Adv*, vol. 6, no. 44, pp. 37773–37783, 2016, doi: 10.1039/c6ra04365h.
- [178] H. Pan, B. Na, R. Lv, C. Li, J. Zhu, and Z. Yu, “Polar phase formation in poly(vinylidene fluoride) induced by melt annealing,” *J Polym Sci B Polym Phys*, vol. 50, no. 20, pp. 1433–1437, Oct. 2012, doi: 10.1002/polb.23146.
- [179] E. Kabir, M. Khatun, L. Nasrin, M. J. Raihan, and M. Rahman, “Pure β -phase formation in polyvinylidene fluoride (PVDF)-carbon nanotube composites,” *J Phys D Appl Phys*, vol. 50, no. 16, p. 163002, Mar. 2017, doi: 10.1088/1361-6463/aa5f85.
- [180] P. Martins, A. C. Lopes, and S. Lanceros-Mendez, “Electroactive phases of poly(vinylidene fluoride): Determination, processing and applications,” *Prog Polym Sci*, vol. 39, no. 4, pp. 683–706, 2014, doi: 10.1016/j.progpolymsci.2013.07.006.

-
- [181] L. Ruan, X. Yao, Y. Chang, L. Zhou, G. Qin, and X. Zhang, “Properties and applications of the β phase poly(vinylidene fluoride),” *Polymers (Basel)*, vol. 10, no. 3, Feb. 2018, doi: 10.3390/polym10030228.
- [182] K. Nakagawa and Y. Ishida, “Dielectric relaxations and molecular motions in poly(vinylidene fluoride) with crystal form II,” *Journal of Polymer Science Part A-2: Polymer Physics*, vol. 11, no. 8, pp. 1503–1533, Aug. 1973, doi: 10.1002/pol.1973.180110804.
- [183] A. Gradys and P. Sajkiewicz, “Determination of the melting enthalpy of β phase of poly(vinylidene fluoride),” *E-Polymers*, May 2013, doi: 10.1515/epoly-2013-0119.
- [184] S. Yu, W. Zheng, W. Yu, Y. Zhang, Q. Jiang, and Z. Zhao, “Formation mechanism of β -phase in PVDF/CNT composite prepared by the sonication method,” *Macromolecules*, vol. 42, no. 22, pp. 8870–8874, Nov. 2009, doi: 10.1021/ma901765j.
- [185] K. Ke, P. Pötschke, D. Jehnichen, D. Fischer, and B. Voit, “Achieving β -phase poly(vinylidene fluoride) from melt cooling: Effect of surface functionalized carbon nanotubes,” *Polymer (Guildf)*, vol. 55, no. 2, pp. 611–619, 2014, doi: 10.1016/j.polymer.2013.12.014.
- [186] C. L. Choy, “Thermal conductivity of polymers,” *Polymer (Guildf)*, vol. 18, no. 10, pp. 984–1004, Oct. 1977, doi: 10.1016/0032-3861(77)90002-7.
- [187] J. Yu, X. Huang, C. Wu, and P. Jiang, “Permittivity, thermal conductivity and thermal stability of poly(vinylidene fluoride)/graphene nanocomposites,” *IEEE Transactions on Dielectrics and Electrical Insulation*, vol. 18, no. 2, pp. 478–484, 2011, doi: 10.1109/TDEI.2011.5739452.
- [188] M. J. Biercuk, M. C. Llaguno, M. Radosavljevic, J. K. Hyun, A. T. Johnson, and J. E. Fischer, “Carbon nanotube composites for thermal management,” *Appl Phys Lett*, vol. 80, no. 15, pp. 2767–2769, 2002, doi: 10.1063/1.1469696.

-
- [189] N. Shenogina, S. Shenogin, L. Xue, and P. Koblinski, “On the lack of thermal percolation in carbon nanotube composites,” *Appl Phys Lett*, vol. 87, no. 13, pp. 1–3, 2005, doi: 10.1063/1.2056591.
- [190] P. Bonnet, D. Sireude, B. Garnier, and O. Chauvet, “Thermal properties and percolation in carbon nanotube-polymer composites,” *Appl Phys Lett*, vol. 91, no. 20, 2007, doi: 10.1063/1.2813625.
- [191] J. Yu and P. Jiang, “Enhanced Thermal Conductivity for PVDF Composites with a Hybrid Functionalized Graphene Sheet-Nanodiamond Filler Thermal conductivity of polymer/ceramic View project economics View project,” *Fibers and Polymers*, vol. 14, no. 8, pp. 1317–1323, 2017, doi: 10.1007/s12221-013-1317-7.
- [192] R. Ram, V. Soni, and D. Khastgir, “Electrical and thermal conductivity of polyvinylidene fluoride (PVDF) – Conducting Carbon Black (CCB) composites: Validation of various theoretical models,” *Compos B Eng*, vol. 185, p. 107748, Mar. 2020, doi: 10.1016/j.compositesb.2020.107748.
- [193] S. K. Karan *et al.*, “Effect of γ -PVDF on enhanced thermal conductivity and dielectric property of Fe-rGO incorporated PVDF based flexible nanocomposite film for efficient thermal management and energy storage applications,” *RSC Adv*, vol. 6, no. 44, pp. 37773–37783, 2016, doi: 10.1039/c6ra04365h.
- [194] E. Pukada, “History and recent progress in piezoelectric polymers,” *IEEE Trans Ultrason Ferroelectr Freq Control*, vol. 47, no. 6, pp. 1277–1290, 2000, doi: 10.1109/58.883516.
- [195] A. Patti, P. Russo, D. Acierno, and S. Acierno, “The effect of filler functionalization on dispersion and thermal conductivity of polypropylene/multi wall carbon nanotubes composites,” *Compos B Eng*, vol. 94, pp. 350–359, Jun. 2016, doi: 10.1016/j.compositesb.2016.03.072.

-
- [196] C. W. Nan, G. Liu, Y. Lin, and M. Li, “Interface effect on thermal conductivity of carbon nanotube composites,” *Appl Phys Lett*, vol. 85, no. 16, pp. 3549–3551, Oct. 2004, doi: 10.1063/1.1808874.
- [197] Y. Agari and T. Uno, “Estimation on thermal conductivities of filled polymers,” *J Appl Polym Sci*, vol. 32, no. 7, pp. 5705–5712, 1986, doi: 10.1002/app.1986.070320702.
- [198] M. X. Shen, Y. X. Cui, J. He, and Y. M. Zhang, “Thermal conductivity model of filled polymer composites,” *International Journal of Minerals, Metallurgy and Materials*, vol. 18, no. 5, pp. 623–631, Oct. 2011, doi: 10.1007/s12613-011-0487-9.
- [199] J. Z. Xu, B. Z. Gao, and F. Y. Kang, “A reconstruction of Maxwell model for effective thermal conductivity of composite materials,” *Appl Therm Eng*, vol. 102, pp. 972–979, 2016, doi: 10.1016/j.applthermaleng.2016.03.155.
- [200] R. L. Hamilton, “Thermal conductivity of heterogeneous two-component systems,” *Industrial and Engineering Chemistry Fundamentals*, vol. 1, no. 3, pp. 187–191, Aug. 1962, doi: 10.1021/i160003a005.
- [201] H. Bhatt, K. Y. Donaldson, D. P. H. Hasselman, and R. T. Bhatt, “Role of the Interfacial Thermal Barrier in the Effective Thermal Diffusivity/Conductivity of SiC-Fiber-Reinforced Reaction-Bonded Silicon Nitride,” *Journal of the American Ceramic Society*, vol. 73, no. 2, pp. 312–316, 1990, doi: 10.1111/j.1151-2916.1990.tb06511.x.
- [202] S. C. Cheng and R. I. Vachon, “A technique for predicting the thermal conductivity of suspensions, emulsions and porous materials,” *Int J Heat Mass Transf*, vol. 13, no. 3, pp. 537–546, Mar. 1970, doi: 10.1016/0017-9310(70)90149-3.
- [203] L. H. Liang, Y. G. Wei, and B. Li, “Thermal conductivity of composites with nanoscale inclusions and size-dependent percolation,” *Journal of Physics Condensed Matter*, vol. 20, no. 36, p. 365201, Aug. 2008, doi: 10.1088/0953-8984/20/36/365201.

-
- [204] T. B. Lewis and L. E. Nielsen, “Dynamic mechanical properties of particulate-filled composites,” *J Appl Polym Sci*, vol. 14, no. 6, pp. 1449–1471, Jun. 1970, doi: 10.1002/app.1970.070140604.
- [205] W. D. KINGERY, “Thermal Conductivity: XIV, Conductivity of Multicomponent Systems,” *Journal of the American Ceramic Society*, vol. 42, no. 12, pp. 617–627, Dec. 1959, doi: 10.1111/J.1151-2916.1959.TB13583.X.
- [206] Y. J. Kwon, J. bin Park, Y. P. Jeon, J. Y. Hong, H. S. Park, and J. U. Lee, “A review of polymer composites based on carbon fillers for thermal management applications: Design, preparation, and properties,” *Polymers (Basel)*, vol. 13, no. 8, 2021, doi: 10.3390/polym13081312.
- [207] S. Mohammad Nejad, R. Srivastava, F. M. Bellussi, H. Chávez Thielemann, P. Asinari, and M. Fasano, “Nanoscale thermal properties of carbon nanotubes/epoxy composites by atomistic simulations,” *International Journal of Thermal Sciences*, vol. 159, p. 106588, 2021, doi: 10.1016/j.ijthermalsci.2020.106588.
- [208] M. Naguib *et al.*, “Two-Dimensional Nanocrystals: Two-Dimensional Nanocrystals Produced by Exfoliation of Ti_3AlC_2 (Adv. Mater. 37/2011),” *Advanced Materials*, vol. 23, no. 37, pp. 4207–4207, Oct. 2011, doi: 10.1002/adma.201190147.
- [209] X. Wang *et al.*, “Pseudocapacitance of MXene nanosheets for high-power sodium-ion hybrid capacitors,” *Nat Commun*, vol. 6, no. 1, pp. 1–6, Apr. 2015, doi: 10.1038/ncomms7544.
- [210] K. Hantanasirisakul *et al.*, “Fabrication of Ti_3C_2Tx MXene Transparent Thin Films with Tunable Optoelectronic Properties,” *Adv Electron Mater*, vol. 2, no. 6, p. 1600050, Jun. 2016, doi: 10.1002/aelm.201600050.
- [211] J. Wang, M. Shen, Z. Liu, and W. Wang, “MXene materials for advanced thermal management and thermal energy utilization,” *Nano Energy*, vol. 97, 2022, doi:

10.1016/j.nanoen.2022.107177.

- [212] R. Liu and W. Li, “High-Thermal-Stability and High-Thermal-Conductivity Ti₃C₂T_x MXene/Poly(vinyl alcohol) (PVA) Composites,” *ACS Omega*, vol. 3, no. 3, pp. 2609–2617, Mar. 2018, doi: 10.1021/acsomega.7b02001.
- [213] J. Yu, H. K. Choi, H. S. Kim, and S. Y. Kim, “Synergistic effect of hybrid graphene nanoplatelet and multi-walled carbon nanotube fillers on the thermal conductivity of polymer composites and theoretical modeling of the synergistic effect,” *Compos Part A Appl Sci Manuf*, vol. 88, pp. 79–85, Sep. 2016, doi: 10.1016/j.compositesa.2016.05.022.
- [214] U. Ali, K. J. B. A. Karim, and N. A. Buang, “A Review of the Properties and Applications of Poly (Methyl Methacrylate) (PMMA),” *Polymer Reviews*, vol. 55, no. 4, pp. 678–705, Oct. 2015, doi: 10.1080/15583724.2015.1031377.
- [215] D. G. Cahill and R. O. Pohl, “Thermal conductivity of amorphous solids above the plateau,” *Phys Rev B*, vol. 35, no. 8, pp. 4067–4073, 1987, doi: 10.1103/PhysRevB.35.4067.
- [216] L. Chen, X. Shi, N. Yu, X. Zhang, X. Du, and J. Lin, “Measurement and analysis of thermal conductivity of Ti₃C₂T_x MXene films,” *Materials*, vol. 11, no. 9, 2018, doi: 10.3390/ma11091701.
- [217] M. M. Yovanovich, J. R. Culham, and P. Teertstra, “Analytical modeling of spreading resistance in flux tubes, half spaces, and compound disks,” *IEEE Transactions on Components Packaging and Manufacturing Technology Part A*, vol. 21, no. 1, pp. 168–176, 1998, doi: 10.1109/95.679046.
- [218] B. Mattsson, H. Ericson, L. M. Torell, and F. Sundholm, “Micro-Raman Investigations of PVDF-Based Proton-Conducting Membranes,” *J Polym Sci A: Polym Chem*, vol. 37, pp. 3317–3327, 1999, doi: 10.1002/(SICI)1099-0518(19990815)37:16.

-
- [219] N. Betz *et al.*, “A FTIR study of PVDF irradiated by means of swift heavy ions,” *J Polym Sci B Polym Phys*, vol. 32, no. 8, pp. 1493–1502, Jun. 1994, doi: 10.1002/polb.1994.090320821.
- [220] S. Lanceros-Méndez, J. F. Mano, A. M. Costa, and V. H. Schmidt, “FTIR and DSC studies of mechanically deformed β -PVDF films,” *J Macromol Sci Phys*, vol. 40 B, no. 3–4, pp. 517–527, May 2001, doi: 10.1081/MB-100106174.

Appendix 1: Theoretical calculations

As introduced in the introduction, layered samples were studied in the thesis. This section regroups the thermal model that was used for the SThM measurement of a sample in the form of a thin layer deposited on substrate. A thermal resistance at the interface between layers is taken into account. Ballistic effect due to a confined heat source is neglected and the coating is assumed diffusive.

i. Studied system

In this model the limited source heating the sample is described by a heating disk with an effective radius a at the sample surface as seen in **Figure A1. 1**.

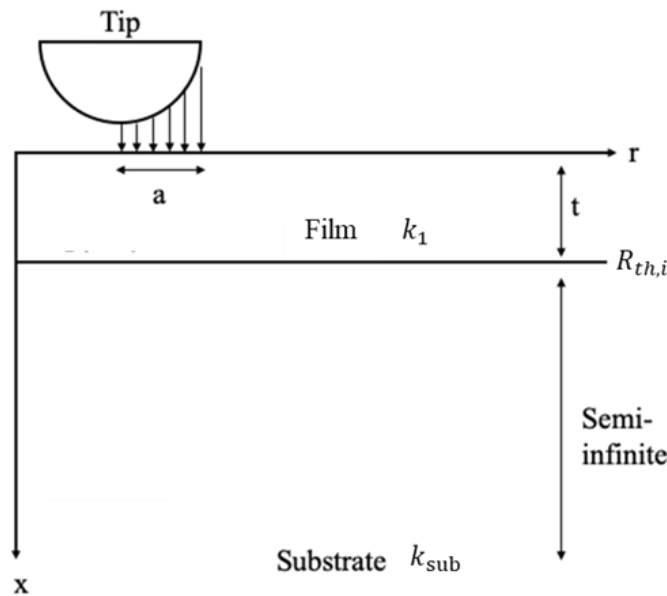


Figure A1. 1. Contact spot of radius a , on an infinite half-plane with surface coating of thickness t .

ii. Analytical resolution

It is assumed that the thermal constriction of each spot is unaffected by neighboring spots. It is then appropriate to consider the effect of a surface coating upon the constriction

resistance of a spot on an infinite half-plane.

As described by Dryden [88], both coating and substrate respective temperatures T_1 and T_2 must satisfy the Laplace equation ($\nabla^2 T_1 = \nabla^2 T_2 = 0$) in their respective regions (inside the coating and substrate). Consequently, for an axisymmetric heat flow the Laplacian is given as follow:

$$\nabla^2 \frac{\partial^2}{\partial r^2} + \frac{1}{r} \frac{\partial}{\partial r} + \frac{\partial^2}{\partial x^2} \quad (\text{A1.1})$$

where x and r are the axial and radial coordinates, respectively.

In order to resolve Eq.A1.1, boundary conditions should be chosen as to follow for an isothermal contact:

1. Temperature and heat flux continuities at the interface between the coating and substrate:

$$T_1 = T_2 \quad \begin{array}{l} r > 0 \\ \text{and } x = t \end{array} \quad (\text{A1.2})$$

$$k_1 \frac{\partial T_1}{\partial x} = k_2 \frac{\partial T_2}{\partial x} \quad \begin{array}{l} r > 0 \\ \text{and } x = t \end{array} \quad (\text{A1.3})$$

2. Boundary condition at the surface ($x = 0$)

$$\frac{\partial T_1}{\partial x} = f(r) \quad \begin{array}{l} a > r > 0 \\ \text{and } x = 0 \end{array} \quad (\text{A1.4})$$

$$= 0 \quad r > a \quad (\text{A1.5})$$

Thus, after a Hankel transform (where ξ is a dummy of variable integration):

$$\bar{T}_1(\xi, x) = A(\xi)e^{\xi x} + B(\xi)e^{-\xi x} \quad (\text{A1.6})$$

$$\bar{T}_2(\xi, x) = C(\xi)e^{-\xi x} \quad (\text{A1.7})$$

$C(\xi)$ can then be found using Eq. A1.2, A1.3 and A1.4 and will be equal to:

$$C(\xi) = \frac{Q}{2k_1\pi a} \frac{\sin(\xi a)}{\xi^2} \frac{1}{\lambda_2 - \lambda_1 e^{-\xi t}} \quad (\text{A1.8})$$

With $\lambda_1 = \frac{(1 - \frac{k_{sub}}{k_1})}{2}$ and $\lambda_2 = \frac{(1 + \frac{k_{sub}}{k_1})}{2}$ and Q the heat flux. Then $A(\xi)$ and $B(\xi)$ can be expressed in term of $C(\xi)$, which leads to:

$$\bar{T}_1(\xi, x) = C(\xi)(\lambda_1 e^{\xi(x-2t)} + \lambda_2 e^{-\xi x}) \quad (\text{A1.9})$$

And then:

$$T_1(r, x) = \int_{\xi=0}^{\infty} \xi \bar{T}_1(\xi, x) J_0(\xi r) d\xi \quad (\text{A1.10})$$

Where J_0 and J_1 are the Bessel functions of the first kind of order 0 and 1, respectively. To further simplify Eq. A1.10, it can be expressed including Eq. A1.8 and Eq. A1.9 as follow:

$$T_1(r, x) = \frac{Q}{2k_1\pi a} \int_{\xi=0}^{\infty} \frac{K e^{\xi(x-2t)} + e^{-\xi x}}{1 - K e^{-2\xi x}} J_0(\xi r) \frac{\sin(\xi)}{\xi} d\xi \quad (\text{A1.11})$$

Knowing that $K = \frac{1 - \frac{k_{sub}}{k_1}}{1 + \frac{k_{sub}}{k_1}}$.

After the calculation of the surface temperature the constriction resistance of a spot on a half-plane can be given by:

$$R = \frac{\Delta T}{Q} = \frac{\hat{T}}{Q} \quad (\text{A1.12})$$

Where ΔT is the temperature change due to the thermal constriction, and Q is the total flux passing through the spot. Since both T_1 and T_2 approach zero at a sufficiently large distance from the contact spot, ΔT will be equal to the average temperature \hat{T} of the contact spot.

$$\hat{T} = \frac{1}{\pi a^2} \int_{r=0}^a T_1(r, 0) 2\pi r dr \quad (\text{A1.13})$$

The resulting expression of R is given as explained in literature [88]:

$$R = \frac{1}{\pi k_1 a} \int_{\xi=0}^{\infty} \frac{1 + K e^{-2\xi t/a}}{1 - K e^{-2\xi t/a}} J_1(\xi) \frac{\sin(\xi)}{\xi^2} d\xi \quad (\text{A1.14})$$

Including a TBR (R_{th}), the effective thickness of the first layer will be equal to:

$$t_{eff} = t + R_{th} k_{1eff} \quad (\text{A1.15})$$

Where t is the lattice difference between the layers (i.e. the thickness).

Thus Eq. A1.14 will be considered a follow:

$$R = \frac{1}{\pi k_{1eff} a} \int_{\xi=0}^{\infty} \frac{1 + K e^{-2\xi t_{eff}/a}}{1 - K e^{-2\xi t_{eff}/a}} J_1(\xi) \frac{\sin(\xi)}{\xi^2} d\xi \quad (\text{A1.15})$$

In the general case, Eq. A1.15 will be used in order to calculate the spreading resistance due of the tip-sample contact. But it is still possible to simplify such an equation as already explained in literature [88], [217]. Thus, two cases arise:

1. For a Thin coating where $0 < t_{eff}/a < 0.1$:

$$R \approx \frac{1}{4k_{sub}a} + \frac{1}{\pi k_{1eff}a} \left(\frac{t_{eff}}{a} \right) \left[1 - \left(\frac{k_{1eff}}{k_{sub}} \right)^2 \right] \quad (\text{A1.16})$$

The first term on the right-hand side of Eq. A1.16 represents the constriction resistance for a spot of radius a on a half-plane with no surface coating. The second term represents the effect of the coating upon the constriction resistance. The ratio $\frac{k_{1eff}}{k_{sub}}$ determines whether this term causes a positive or negative change in the constrictive resistance. Note that for a given spot size, a , the constriction resistance, R , depends linearly upon the coating thickness, t_{eff} .

2. For a Thick coating where $0.1 < t_{eff}/a$

$$R \approx \frac{1}{4k_{1\,eff}a} - \frac{1}{2\pi k_{1\,eff}a} \left(\frac{a}{t_{eff}} \right) \ln \left(\frac{2}{1 + \frac{k_{1\,eff}}{k_{sub}}} \right) \quad (A1.17)$$

The first term on the right-hand side represents the constriction resistance for a spot of radius a on a half-plane of thermal conductivity $k_{1\,eff}$. The second term represents the effect of the substrate material with thermal conductivity k_{sub} . There is a logarithmic dependence on the ratio $\frac{k_{1\,eff}}{k_{sub}}$.

A simulation based on Eq. A1.15 is developed using Matlab, and especially, simplified Eq. A1.16 and Eq. A1.17 is used to reduce the computation work.

Appendix 2. Uncertainty calculation of unbalanced TCU

However, in real case there is a small distinction between the current flow into two branched. In this TCU, ΔV indicate the dissipated voltage difference between R_v and $R_{el,p}$, $\Delta V = \pm(R_v I_v - R_{el,p} I_p)$, where I_v and I_p represent the current flow through R_v and $R_{el,p}$ respectively. The tropism of symbol \pm depends on the connection socket of point A and B on multimeter. Because of the variation of $R_{el,p}$ during measurement, a difference between I_v and I_p arises, thus,

$$I_v = \frac{I(R_2 + R_{el,p})}{R_1 + R_v + R_2 + R_{el,p}} \quad (\text{A2.1})$$

$$I_p = \frac{I(R_1 + R_v)}{R_1 + R_v + R_2 + R_{el,p}} \quad (\text{A2.2})$$

ΔV can then be written as:

$$\Delta V = \pm \frac{I(R_{el,p} R_1 - R_v R_2)}{R_1 + R_v + R_2 + R_{el,p}} \quad (\text{A2.3})$$

As R_1 and R_2 are set equal, above equation can be given by:

$$\Delta V = \pm \frac{I(R_{el,p} - R_v) R_1}{2R_1 + R_v + R_{el,p}} \quad (\text{A2.4})$$

$$R_{el,p} - R_v = \pm \Delta V / \frac{R_1 I}{2R_1 + R_v + R_{el,p}} \quad (\text{A2.5})$$

Here an example of all parameters for the probe used in chapter III is given: $R_1 = R_2 = 100 \Omega$, $R_v = 5.08 \Omega$, $R_{el,p}$ is approximatively equal to R_v during measurement. Thus $R_{el,p} - R_v = \pm \Delta V / 0.48I$. Therefore, an uncertainty of approximately 4% must be considered

for the calculation of $R_{el,p} - R_v$.

Appendix 3. Previous techniques used for the sample analysis from ref [123]

The composition and stoichiometry of the as-deposited CrSi₂ film are accessed via Rutherford Backscattering Spectrometry (RBS). The RBS measurements were made using a 1.5 MeV He⁺ beam from a 3 MeV HVEE Tandem accelerator at the Laboratório de Implantação Iônica, Instituto de Física (UFRGS, Brazil). The microstructure evolution of the samples was analyzed via Transmission Electron Microscopy (TEM) using cross-sectional samples prepared by focused ion beam (FIB) with the FEI Strata DB 235 equipment available at the IEMN (Lille, France). TEM observations were performed using a JEOL JEM 2200FS TEM operating at 200 kV (Platform Microscopie Électronique et Analytique (MEA), Université de Montpellier, France). Ne and Al distributions along the CrSi₂ film were assessed via Scanning Transmission Electron Microscopy - Energy Dispersive X-ray spectrometry (STEM-EDX). The STEM-EDX measurements were done using a 100 mm² Oxford Xmax TLE windowless detector. The crystallinity of the CrSi₂ samples considered in this study was assessed via the Selected Area Electron Diffraction (SAED) technique. The electrical resistivity ρ measurements on implanted and non-implanted CrSi₂ thin layers were carried out between 80 K and 330 K with a magnetic field of 0.5T by the Van der Pauw method. The electric contacts were made using in droplets, and the measurements were done with an Ecopia HMS 5000 four-point probe equipment (CTM, Université de Montpellier, France).

Appendix 4. Sensitivity of fitted k of CrSi₂ layer by analytical model

i. k in function of contact radius

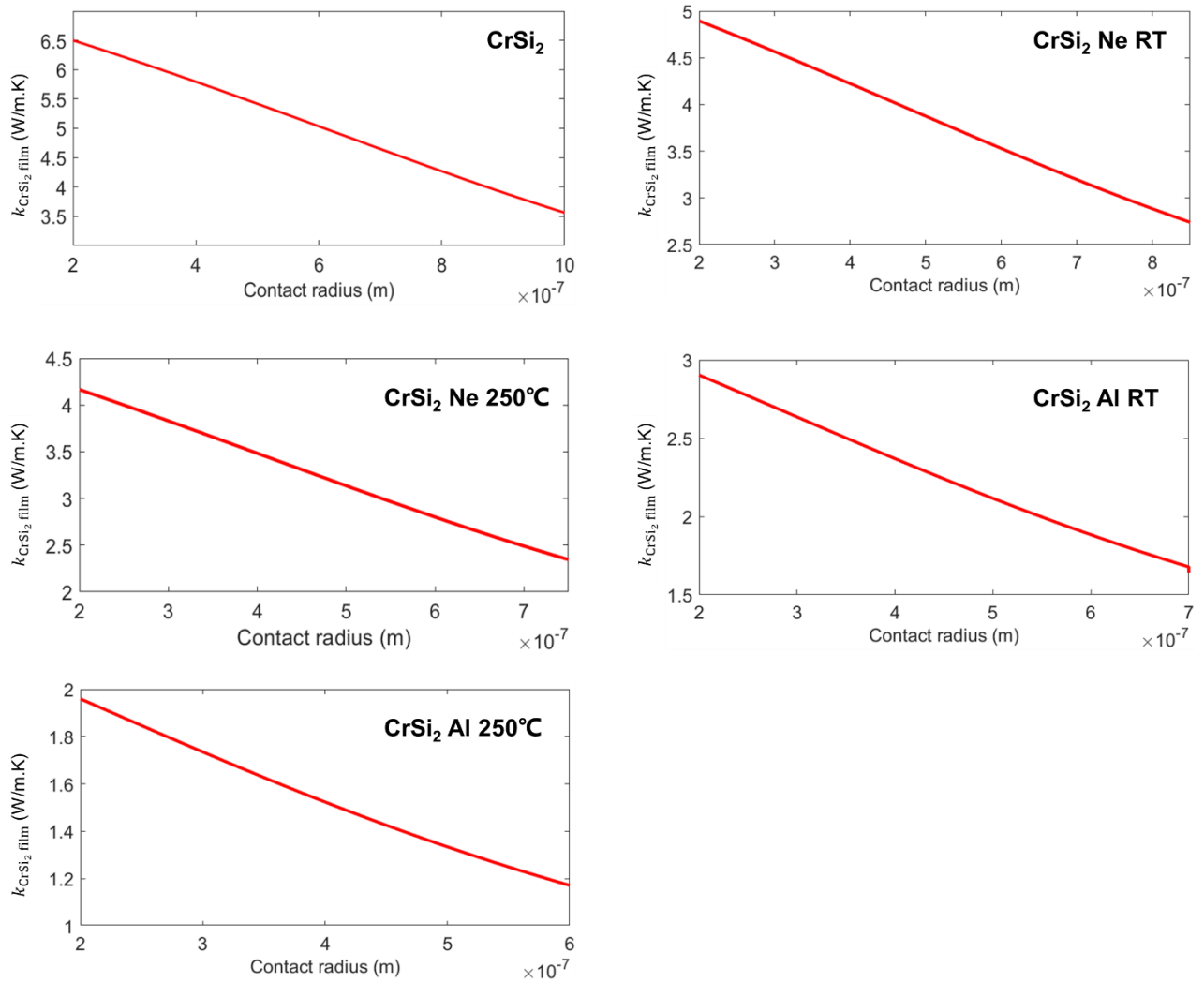


Figure A4. 1. Fitted k of CrSi₂ layer by analytical model in function of input contact radius a .

ii. k in function of TBR

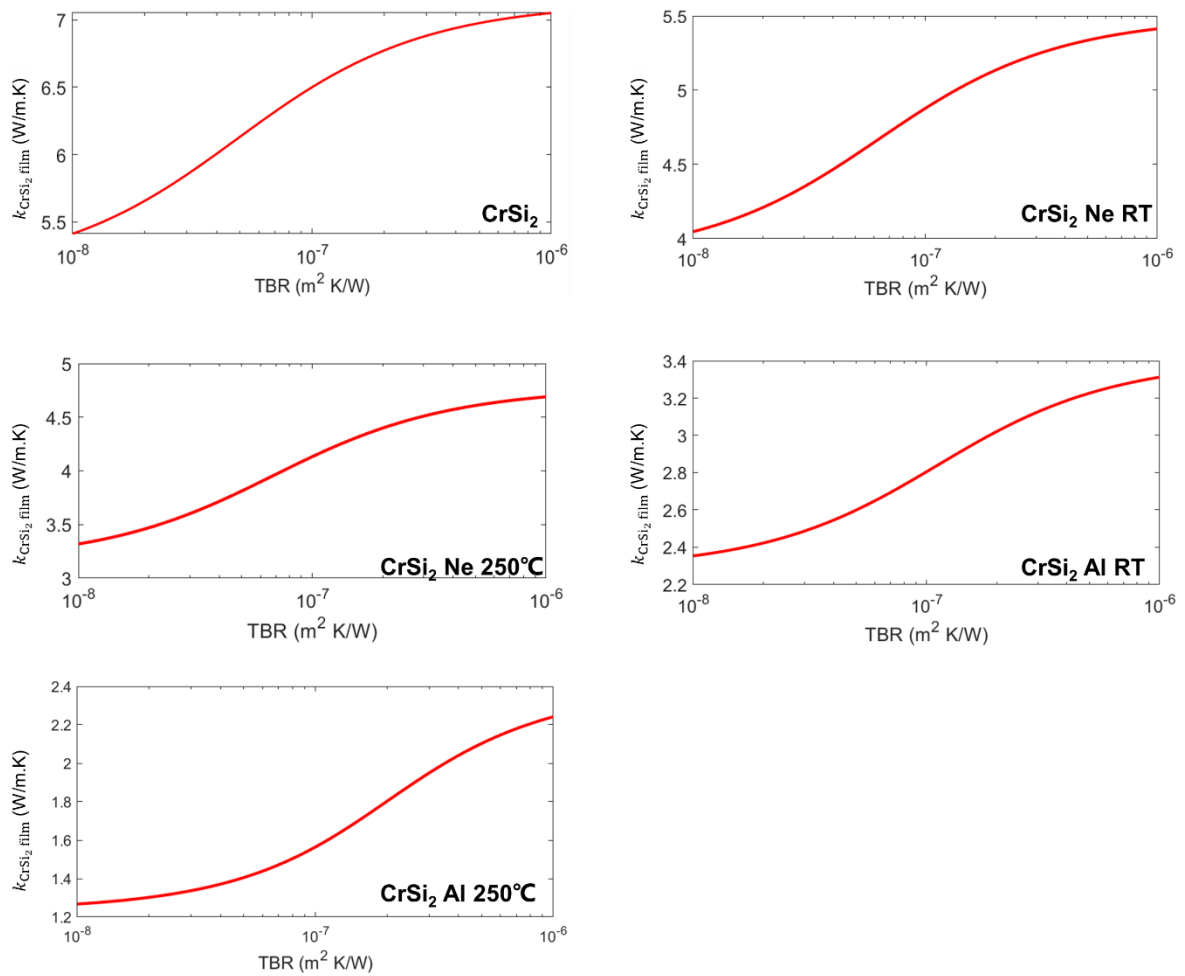


Figure A4. 2. Fitted k of CrSi_2 layer by analytical model in function of input TBR.

iii. k in function of thickness

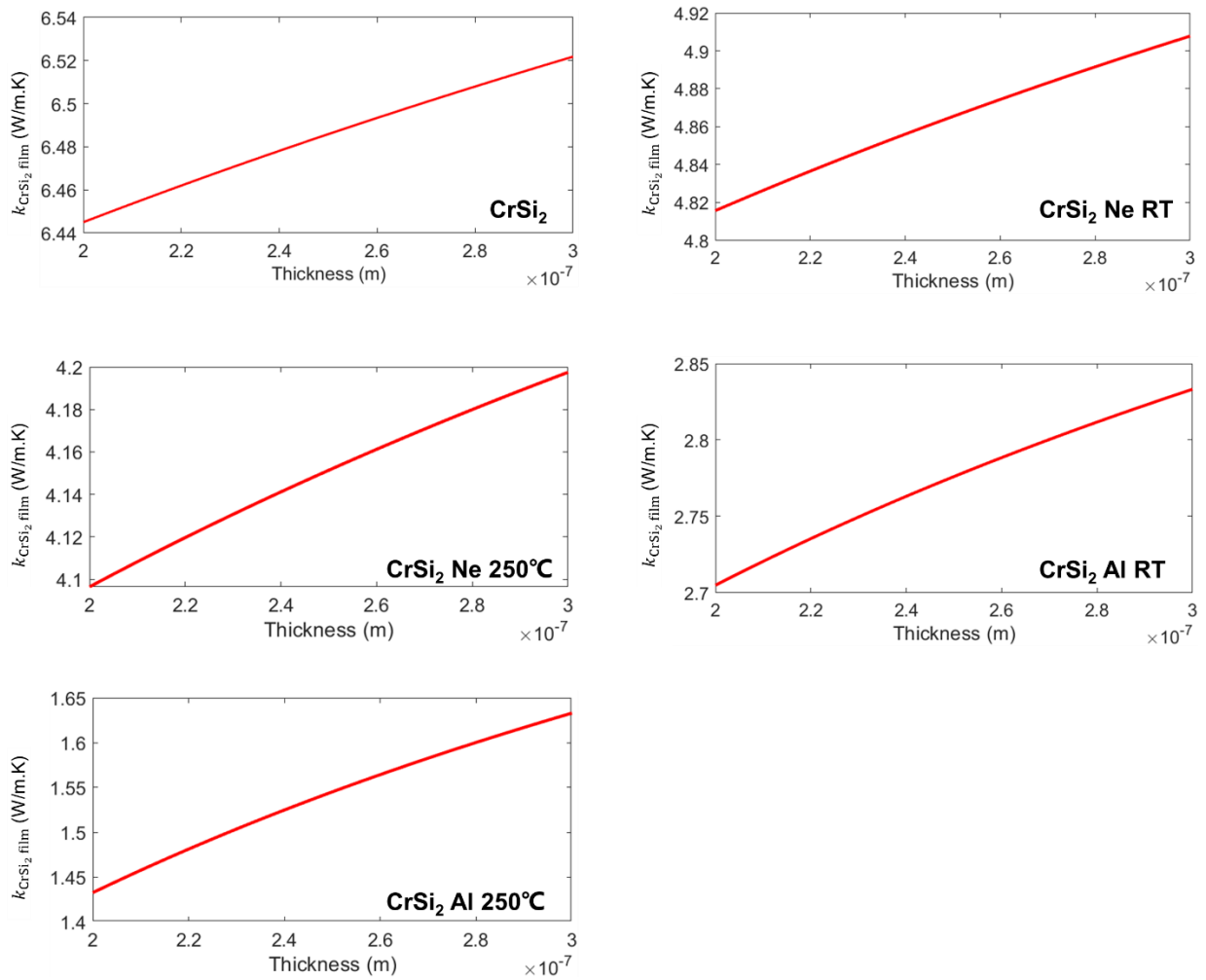


Figure A4. 3. Fitted k of CrSi₂ layer by analytical model in function of input thickness.

iv. k in function of thermal conductivity of Si substrate

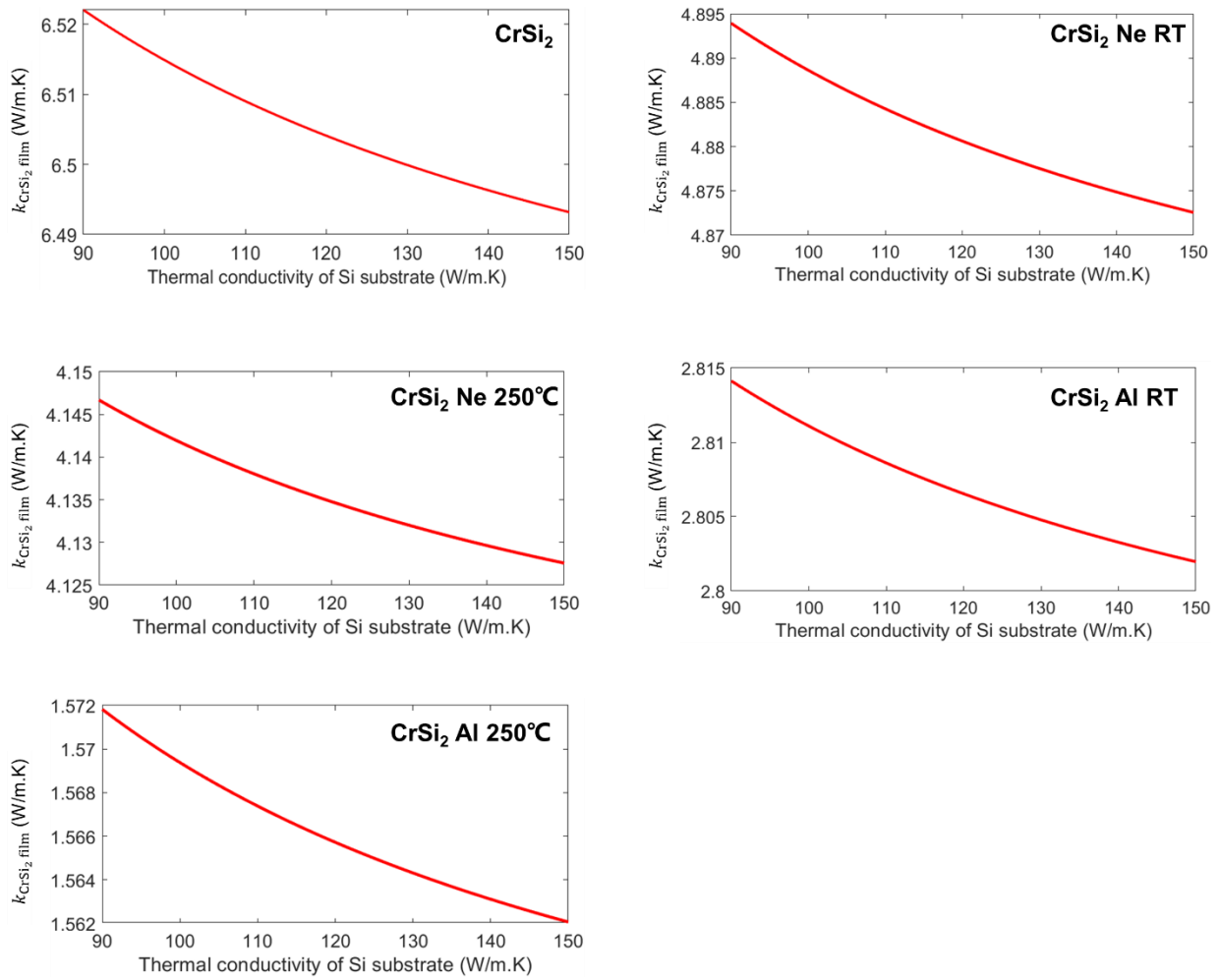


Figure A4. 4. Fitted k of CrSi₂ layer by analytical model in function of input k_{Si} .

Appendix 5. SEM image of PVDF composites

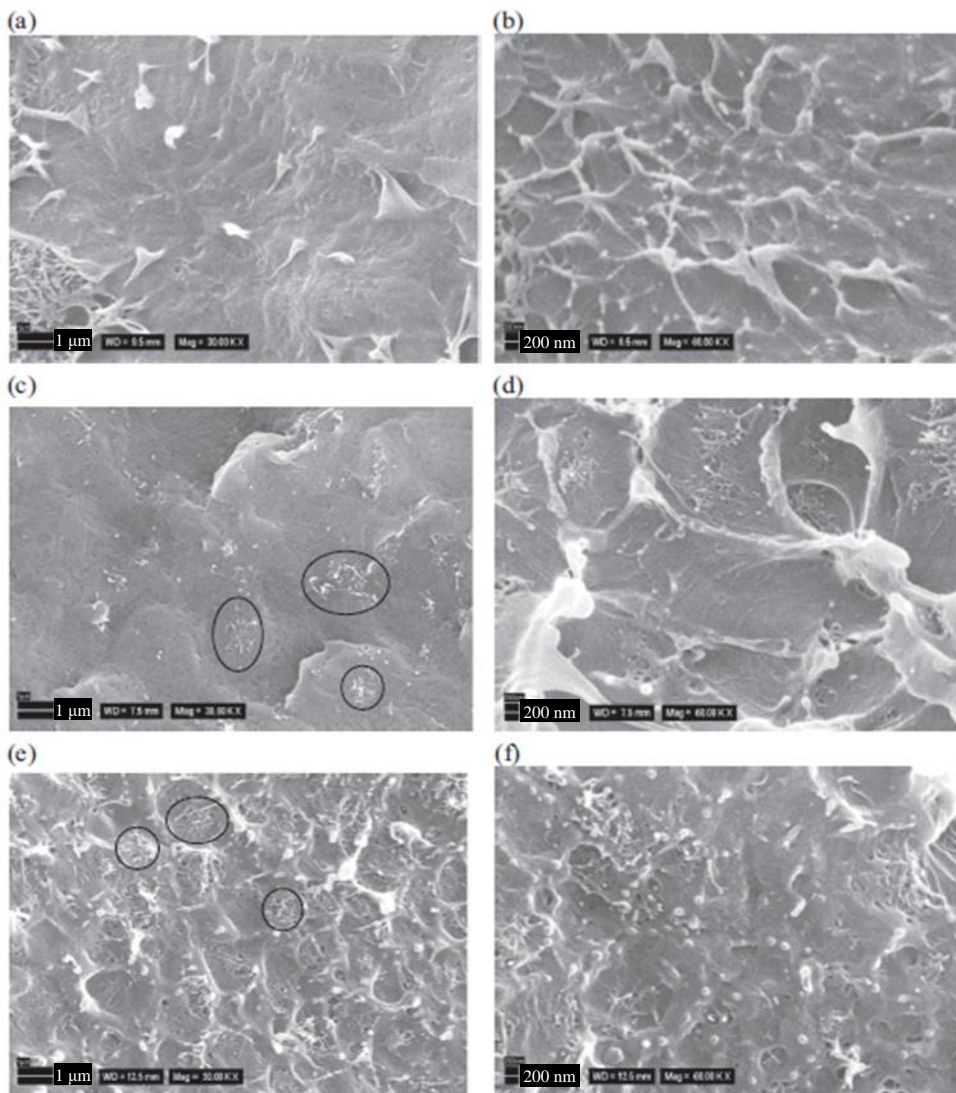


Figure A5. 1. SEM picture of (a), (b) PVDF matrix; (c), (d) PVDF/1.25 wt.% MWCNTs composite and (e), (f) PVDF/3.0 wt.% MWCNTs composite.

Appendix 6. FT-IR spectra of PVDF composites

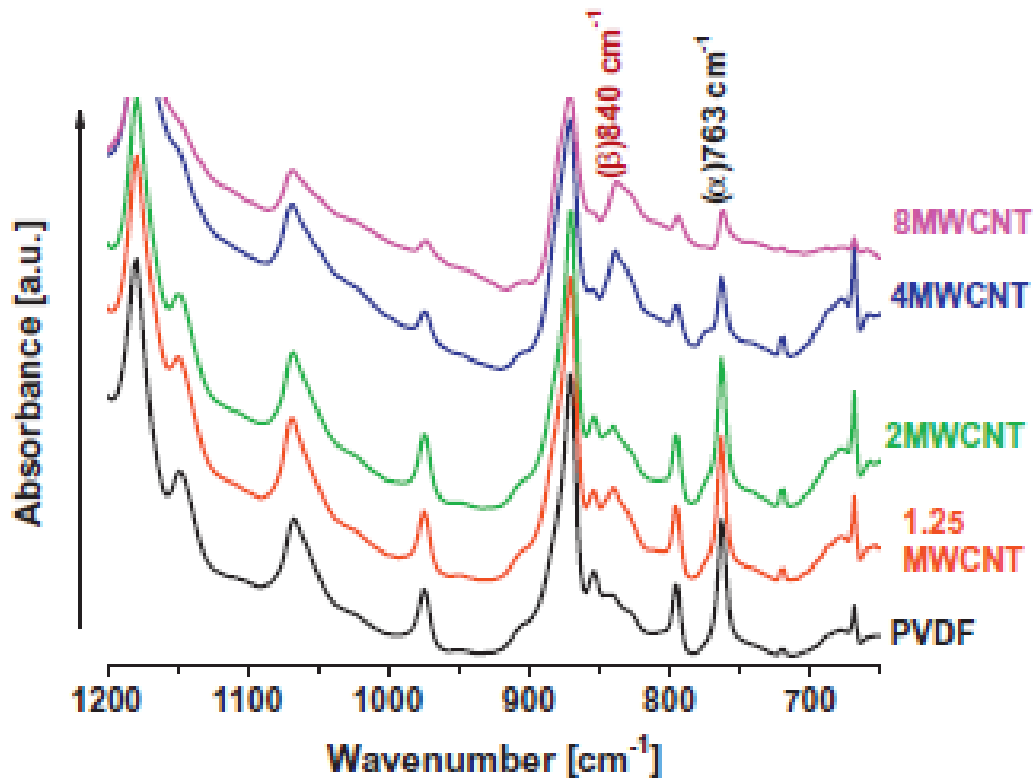
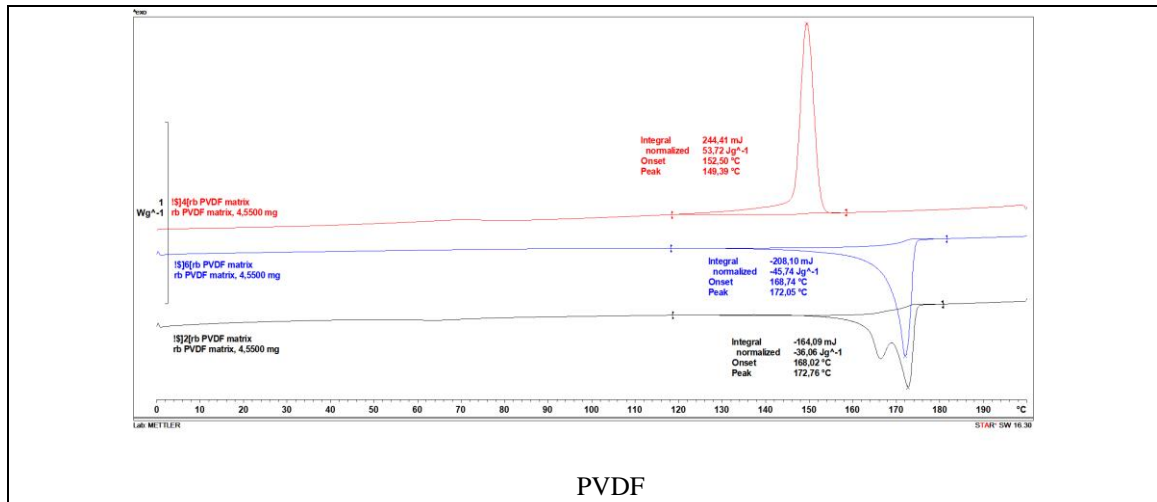


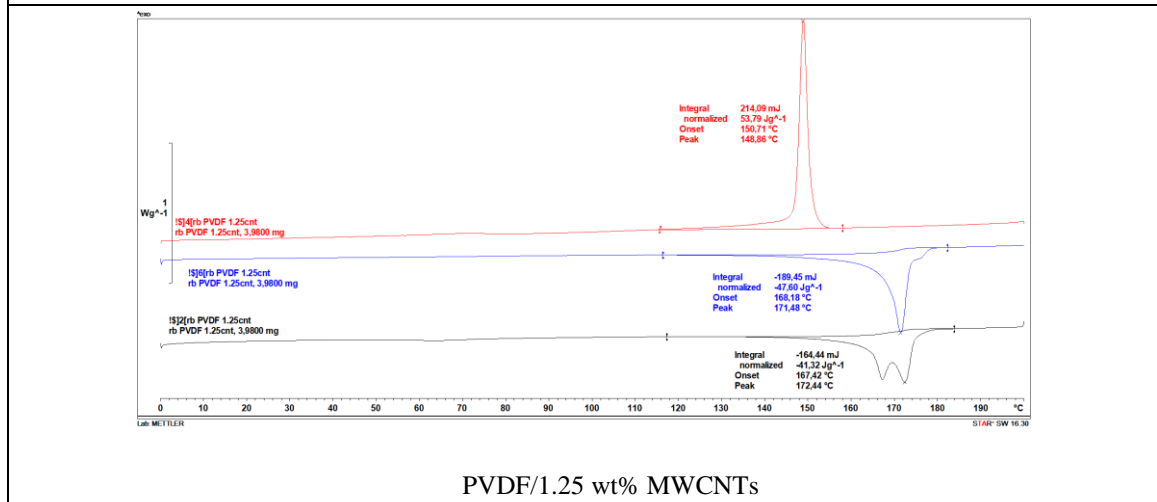
Figure A6. 1. IR image of PVDF matrix and composites with MWCNTs fillers.

Peaks at 763 cm^{-1} is assigned to the rocking vibration, a mixed mode of CF_2 bending and CCC skeletal vibration, respectively [218], [219]. The absorbance of vibration band at this wavenumber is corresponding to PVDF α phase. The bands observed at 840 cm^{-1} , is assigned to a mixed mode of CH_2 rocking and CF_2 asymmetric stretching vibration (parallel to the chain axis), and a rocking mode and CF_2 bending mode (perpendicular to the chain axis and parallel to the polar b -axis), respectively [219], [220]. This band is corresponding to PVDF β phase.

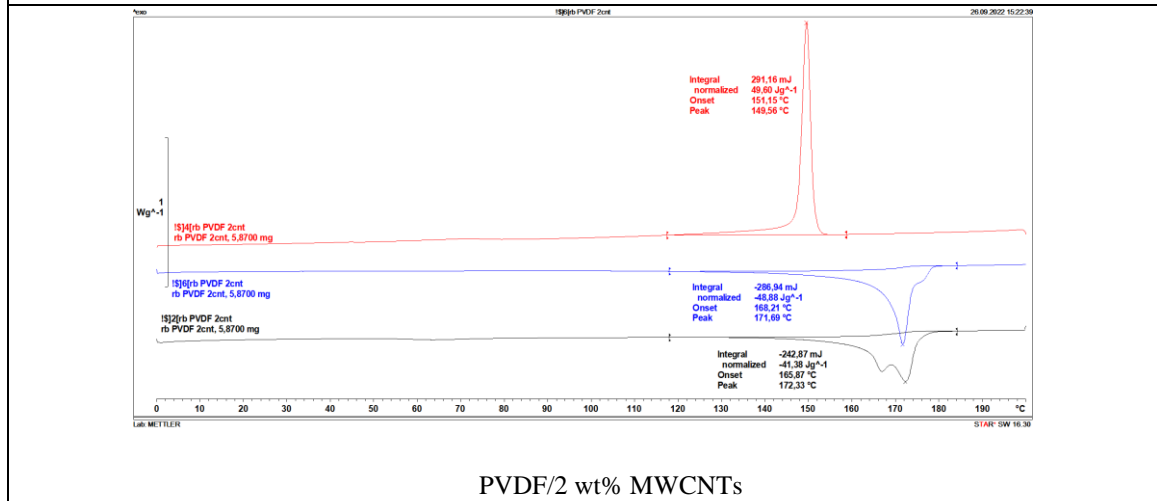
Appendix 7. DSC results of PVDF composites



PVDF



PVDF/1.25 wt% MWCNTs



PVDF/2 wt% MWCNTs

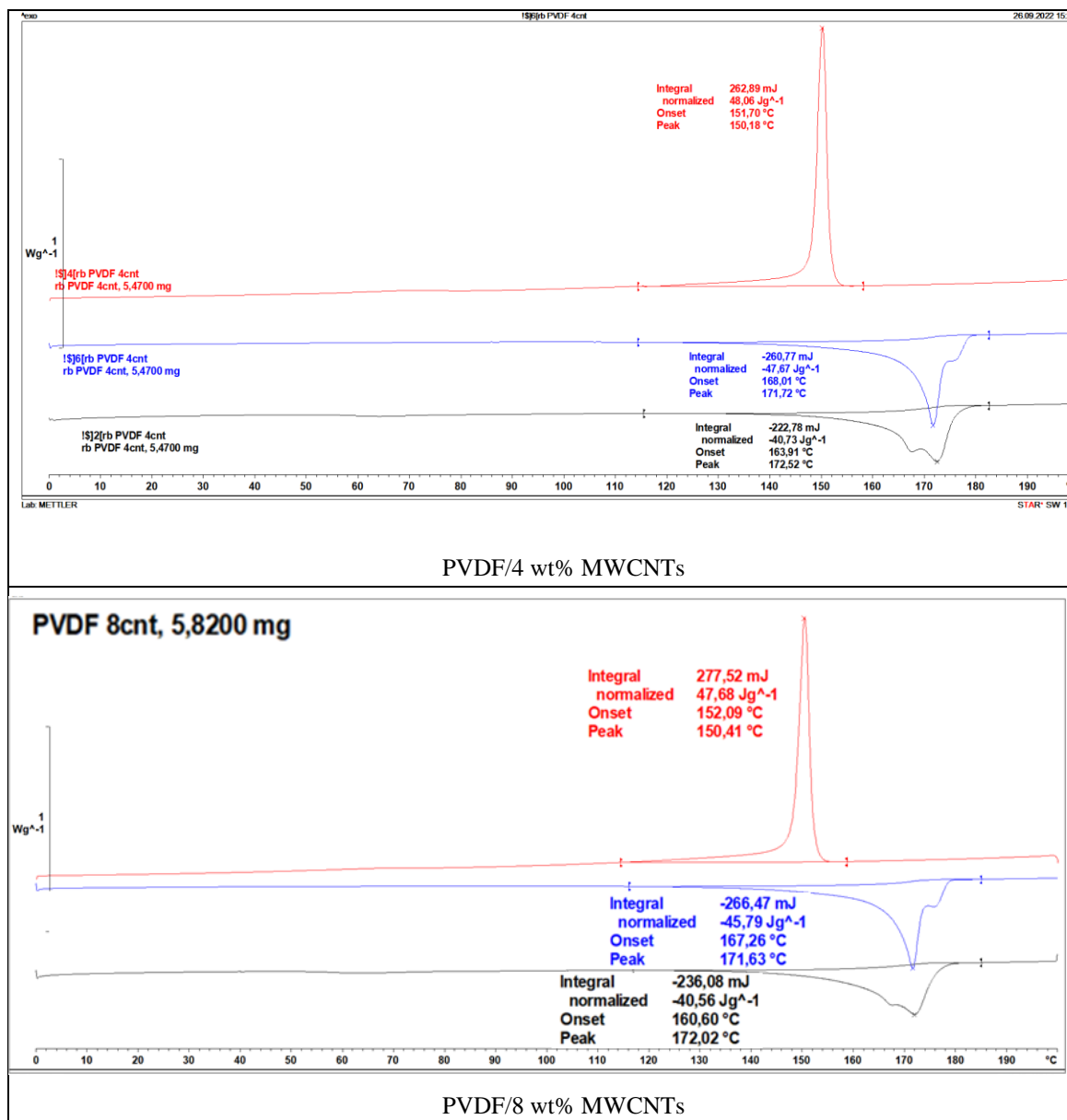


Figure A7. 1. DSC results of PVDF composites, line 2 (black), 4 (red) and 6 (blue) indicate the first heating process, cooling process and the second heating process, respectively.

Appendix 8. Preparation procedure of PMMA composites filled with MXene and MWCNTs

i. Delamination process of titanium carbide MXene

To obtain delaminated MXene solution, MXene paste was mixed with LiCl in DI water. The beaker was put into water bath and placed onto magnetic stirrer. Mixture was left for stirring for 18-24 h. On the next day it was split into 2 centrifugation tubes. Then it was centrifuged until the supernatant became black instead of transparent. When supernatant was dark green and it contained delaminated MXene sheets, and solution was collected. The concentration of prepared solution was calculated with free-standing film made vacuum-assisted filtration (VAF) The concentration of MXene in solution is usually within 0.1-0.5 mg/ml.

ii. Preparation of composites:

For the preparation of PMMA/MXene composites MXene water solution was changed into acetone. Then PMMA pellets were dissolved in acetone. Solutions were mixed together and left for mixing on a stirrer to evaporate some amount of acetone. This mixture was transferred into metal container of mechanical stirrer for further stirring. After mixing the mixture was poured out into PTFE Petri dish and left for drying on the open air, and later it was put into vacuum drying oven.

For PMMA/MWCNTs composites PMMA pellets were dissolving in chloroform under continuous stirring on magnetic stirrer. Appropriate calculated amount of MWCNTs were added to chloroform and placed for sonication with ultrasonic probe. Then MWCNTs mixture was added to PMMA solution and left for stirring. After that it was transferred into container of mechanical stirrer and left for stirring again. Next steps were repeated as above.

To obtain PMMA/MWCNTs/MXene composite samples, PMMA pellets were put for stirring in acetone. Respective amount of MWCNTs were mixed also with acetone and put for

sonication with ultrasonic probe. When PMMA pellets were dissolved, MWCNTs mixture and calculated amount of MXene solution (in acetone) were added to PMMA and left for solvent evaporation during continuous mixing on the magnetic stirrer. Further protocol steps were the same as aforementioned.





FOLIO ADMINISTRATIF

THESE DE L'INSA LYON, MEMBRE DE L'UNIVERSITE DE LYON

NOM : SUN
Prénoms : Wenxiang

DATE de SOUTENANCE : 11/05/2023

TITRE : Investigation of the thermal conductivity tuning of solid materials for energy-efficient systems using scanning thermal microscopy

NATURE : Doctorat
Ecole doctorale : MEGA de Lyon
Spécialité: Thermique Energétique

Numéro d'ordre : 2023INSAL0031

RESUME :

One potential solution for system thermal management is to utilize or create nanostructured or nanocomposite materials, as they can exhibit a tuned thermal conductivity. Two types of materials developed in this direction were studied in this thesis. They are amorphous chromium disilicide (CrSi_2) thin films on substrate that were modified by implantation with Ne and Al ions at room temperature and at 250°C for thermoelectric applications, and bulk polymer nanocomposites where nanofillers (expanded graphite (EG), multiwall carbon nanotubes (MWCNTs), and MXene) are used to enhance the polymer thermal conductivity for electronic applications (as an example). Scanning thermal microscopy (SThM) is used to analyze the heat conduction within both the types of material as a function of their microstructure change. Estimations of the contribution of phonons and electrons to the heat conduction in CrSi_2 in its amorphous phase and for ion-implanted amorphous CrSi_2 were obtained. These results combined with the analyses of the material microstructure show a decrease of the material thermal conductivity for all the studied CrSi_2 samples, more pronounced for ion-implantation at 250°C . Based on scientific literature this decrease is attributed to implantation induced defects clusters that are energy carrier scattering centers, phonon path disruption by atom mass contrast and nanocrystallites, created due to a radiation-enhanced phase transformation process at 250°C , with depletion zones for electrons located at their boundaries. For the case of Ne-implantations, observed Ne bubbles that are additionally induced by the ion-implantation also lead to phonon scattering. For polymer nanocomposites, thermal conductivity SThM measurements combined with the analyses of the material microstructure allow to verify that the introduction of carbonaceous fillers increases the heat conduction in materials while the filler concentration increases. A new analytical model, which allows the thermal conductivity estimation in the case of MWCNTs- multiphase PVDF based composites, is proposed and results are compared with SThM measurements. Main findings show that the β phase of PVDF, created because MWCNTs introduced in the PVDF matrix act as nucleation centers for β phase-PVDF, explains the increase of the thermal conductivity of the nanocomposite.

MOTS-CLÉS : thermal conduction tuning, amorphous chromium disilicide, carbon filler-based polymer nanocomposites, scanning thermal microscopy

Laboratoire (s) de recherche : Centre d'Énergétique et de Thermique de Lyon (CETHIL)

Directeur de thèse: GOMÈS Séverine

Président de jury : GRAUBY Stéphane

Composition du jury : GRAUBY Stéphane, YASSAR Abderrahim, DELMAS Agnès, PERNOT Gilles, GOMÈS Séverine, HAMAOUI Georges